

Carbon-Based Materials at Nanoscale

Guest Editors: Dan Xia, Michal Otyepka, Xi Li, Wei Liu,
and Qingbin Zheng





Carbon-Based Materials at Nanoscale

Journal of Nanomaterials

Carbon-Based Materials at Nanoscale

Guest Editors: Dan Xia, Michal Otyepka, Xi Li, Wei Liu,
and Qingbin Zheng



Copyright © 2015 Hindawi Publishing Corporation. All rights reserved.

This is a special issue published in "Journal of Nanomaterials." All articles are open access articles distributed under the Creative Commons Attribution License, which permits unrestricted use, distribution, and reproduction in any medium, provided the original work is properly cited.

Editorial Board

Domenico Acierno, Italy
Katerina Aifantis, USA
Sheikh Akbar, USA
Nageh K. Allam, USA
Margarida Amaral, Portugal
Martin Andersson, Sweden
Raul Arenal, Spain
Ilaria Armentano, Italy
Vincenzo Baglio, Italy
Lavinia Balan, France
Thierry Baron, France
Andrew R. Barron, USA
Reza Bayati, USA
Hongbin Bei, USA
Daniel Bellet, France
Stefano Bellucci, Italy
Enrico Bergamaschi, Italy
Samuel Bernard, France
D. Bhattacharyya, New Zealand
Sergio Bietti, Italy
Giovanni Bongiovanni, Italy
Theodorian Borca-Tasciuc, USA
Mohamed Bououdina, Bahrain
Torsten Brezesinski, Germany
C. Jeffrey Brinker, USA
Christian Brosseau, France
Philippe Caroff, Australia
Victor M. Castaño, Mexico
Albano Cavaleiro, Portugal
Bhanu P. S. Chauhan, USA
Shafiu Chowdhury, USA
Jin-Ho Choy, Republic of Korea
Kwang-Leong Choy, UK
Yu-Lun Chueh, Taiwan
Elisabetta Comini, Italy
Giuseppe Compagnini, Italy
David Cornu, France
Miguel A. Correa-Duarte, Spain
P. Davide Cozzoli, Italy
Shadi A. Dayeh, USA
Luca Deseri, USA
Yong Ding, USA
Philippe Dubois, Belgium
Alain Dufresne, France
Zehra Durmus, Turkey
Joydeep Dutta, Oman
Ali Eftekhari, USA
Jeffrey Elam, USA
Samy El-Shall, USA
Ovidiu Ersen, France
Claude Estournès, France
Andrea Falqui, KSA
Matteo Ferroni, Italy
E. Johan Foster, USA
Ilaria Fratoddi, Italy
Wolfgang Fritzsche, Germany
Alan Fuchs, USA
Miguel A. Garcia, Spain
Siddhartha Ghosh, Singapore
P. K. Giri, India
Russell E. Gorga, USA
Jihua Gou, USA
Jean M. Greneche, France
Smrati Gupta, Germany
Kimberly Hamad-Schifferli, USA
Simo-Pekka Hannula, Finland
Michael Harris, USA
Yasuhiko Hayashi, Japan
F. Hernandez-Ramirez, Spain
Michael Z. Hu, USA
Nay Ming Huang, Malaysia
Shaoming Huang, China
David Hui, USA
Zafar Iqbal, USA
Balachandran Jeyadevan, Japan
Xin Jiang, Germany
Rakesh Joshi, Australia
Jeong-won Kang, Korea
Hassan Karimi-Maleh, Iran
Antonios Kelarakis, UK
Alireza Khataee, Iran
Ali Khorsand Zak, Iran
Philippe Knauth, France
Ralph Krupke, Germany
Christian Kübel, Germany
Prashant Kumar, UK
Michele Laus, Italy
Eric Le Bourhis, France
Burtrand Lee, USA
Jun Li, Singapore
Meiyong Liao, Japan
Shijun Liao, China
Silvia Licocchia, Italy
Wei Lin, USA
Nathan C. Lindquist, USA
Jun Liu, USA
Zainovia Lockman, Malaysia
Nico Lovergine, Italy
Jim Low, Australia
Jue Lu, USA
Songwei Lu, USA
Ed Ma, USA
Laura M. Maestro, Spain
Gaurav Mago, USA
Muhamamd A. Malik, UK
Devanesan Mangalaraj, India
Sanjay R. Mathur, Germany
Tony McNally, UK
Yogendra Mishra, Germany
Paulo Cesar Morais, Brazil
Paul Munroe, Australia
Jae-Min Myoung, Republic of Korea
Rajesh R. Naik, USA
Albert Nasibulin, Russia
Toshiaki Natsuki, Japan
Koichi Niihara, Japan
Natalia Noginova, USA
Sherine Obare, USA
Won-Chun Oh, Republic of Korea
Atsuto Okamoto, Japan
Abdelwahab Omri, Canada
Ungyu Paik, Republic of Korea
Piersandro Pallavicini, Italy
Edward A. Payzant, USA
Alessandro Pegoretti, Italy
Ton Peijs, United Kingdom
Oscar Perales-Pérez, Puerto Rico
Jorge Pérez-Juste, Spain
Alexey P. Popov, Finland
Philip D. Rack, USA
Peter Reiss, France
Orlando Rojas, USA
Marco Rossi, Italy
Ilker S. Bayer, Italy
Cengiz S. Ozkan, USA

Sudipta Seal, USA
Shu Seki, Japan
Vladimir Šepelák, Germany
Huaiyu Shao, Japan
Prashant Sharma, USA
Donglu Shi, USA
Bhanu P. Singh, India
Surinder Singh, USA
Vladimir Sivakov, Germany
Ashok Sood, USA
Adolfo Speghini, Italy
Marinella Striccoli, Italy
Xuping Sun, KSA
Ashok K. Sundramoorthy, USA

Angelo Taglietti, Italy
Bo Tan, Canada
Leander Tapfer, Italy
Valeri P. Tolstoy, Russia
Muhammet S. Toprak, Sweden
Ramon Torrecillas, Spain
Achim Trampert, Germany
Takuya Tsuzuki, Australia
Tamer Uyar, Turkey
Bala Vaidhyanathan, UK
Luca Valentini, Italy
Rajender S. Varma, USA
Ester Vazquez, Spain
Antonio Villaverde, Spain

Ajayan Vinu, Australia
Ruibing Wang, Macau
Shiren Wang, USA
Yong Wang, USA
Magnus Willander, Sweden
Ping Xiao, UK
Zhi Li Xiao, USA
Yangchuan Xing, USA
Doron Yadlovker, Israel
Yoke K. Yap, USA
Kui Yu, Canada
William Yu, USA
Michele Zappalorto, Italy
Renyun Zhang, Sweden

Contents

Carbon-Based Materials at Nanoscale, Dan Xia, Michal Otyepka, Xi Li, Wei Liu, and Qingbin Zheng
Volume 2015, Article ID 750242, 2 pages

Catalytic Activity of Co₃O₄ Nanomaterials with Different Morphologies for the Thermal Decomposition of Ammonium Perchlorate, Li-Na Jin, Jian-Guo Wang, Xin-Ye Qian, Dan Xia, and Ming-Dong Dong
Volume 2015, Article ID 854310, 7 pages

Relationship between Polymer Dielectric Constant and Percolation Threshold in Conductive Poly(styrene)-Type Polymer and Carbon Black Composites, Mariana Castro Martínez, Susana Hernández López, and Enrique Viguera Santiago
Volume 2015, Article ID 607896, 9 pages

Conductive Polymeric Composites Based on Multiwalled Carbon Nanotubes and Linseed Oil Functionalized and Cross-Linked with Diacetylenes from Propargyl Alcohol, Alejandro Ramírez-Jiménez, Susana Hernández-López, and Enrique Viguera-Santiago
Volume 2015, Article ID 531249, 7 pages

Tuning Electronic Structures of BN and C Double-Wall Hetero-Nanotubes, Xueran Liu, Meijun Han, Xinjiang Zhang, Haijun Hou, Shaoping Pang, and Qisheng Wu
Volume 2015, Article ID 326294, 9 pages

A Review on the Efficiency of Graphene-Based BHJ Organic Solar Cells, Alejandro Manzano-Ramírez, Edgar J. López-Naranjo, Wole Soboyejo, Yunny Meas-Vong, and Bertrand Vilquin
Volume 2015, Article ID 406597, 15 pages

Synthesis of Carbon Encapsulated Mono- and Multi-Iron Nanoparticles, M. Reza Sanaee and Enric Bertran
Volume 2015, Article ID 450183, 10 pages

Synthesis and Properties of Magnetic Carbon Nanocages Particles for Dye Removal, Hengfei Qin, Yongkui Huang, Siyu Liu, Yao Fang, Xi Li, and Shifei Kang
Volume 2015, Article ID 604201, 8 pages

Highly Sensitive CO Gas Sensor from Defective Graphene: Role of van der Waals Interactions, Yingda Jiang, Sha Yang, Shuang Li, Wei Liu, and Yonghao Zhao
Volume 2015, Article ID 504103, 7 pages

Substrate Temperature Effect on the Microstructure and Properties of (Si, Al)/a-C:H Films Prepared through Magnetron Sputtering Deposition, Xiaoqiang Liu, Junying Hao, Hu Yang, Xiuzhou Lin, and Xianguang Zeng
Volume 2015, Article ID 194308, 9 pages

Editorial

Carbon-Based Materials at Nanoscale

Dan Xia,¹ Michal Otyepka,² Xi Li,³ Wei Liu,⁴ and Qingbin Zheng⁵

¹*Interdisciplinary Nanoscience Center, Aarhus University, 8000 Aarhus, Denmark*

²*Department of Physical Chemistry, Palacký University, 771 46 Olomouc, Czech Republic*

³*Department of Environmental Science and Engineering, Fudan University, Shanghai 200433, China*

⁴*School of Materials Science and Engineering, Nanjing University of Science and Technology, Nanjing 210094, China*

⁵*Leibniz Institute of Polymer Research Dresden, 01005 Dresden, Germany*

Correspondence should be addressed to Dan Xia; xiadan@inano.au.dk

Received 30 September 2015; Accepted 1 October 2015

Copyright © 2015 Dan Xia et al. This is an open access article distributed under the Creative Commons Attribution License, which permits unrestricted use, distribution, and reproduction in any medium, provided the original work is properly cited.

Carbon-based nanomaterials (CBNs), namely, fullerene, carbon nanotubes, and graphene, have attracted significant attention since their discoveries, and in these days they play significant role in nanoscience and nanotechnology [1]. The unique properties of CBNs make them widely used in many fields ranging within material science [2], energy [3], environment [4, 5], biology [6–9], medicine [10, 11], and so forth. Articles published in this special issue reflect the broad application potential of CBNs and provide some overview of the recent progress in this field.

The paper by M. R. Sanaee and E. Bertran is focused on iron nanoparticles encapsulated by carbon shell. The authors present a synthesis of core/shell nanostructures by using a new modified arc discharge reactor. Different iron cores including spherical, oval, and multiple cores were synthesized. The carbon shell protecting the iron cores against oxidation shows high degree of crystallinity. Due to the carbon shell spherical shape and iron superparamagnetic behavior, the authors conclude that the carbon encapsulated iron nanoparticles can be potentially used in drug delivery. X. Li et al. showed that magnetic carbon nanocages synthesized from a cheap carbon source material lignin using low temperature carbonization process can be used as efficient and recycled adsorbents in the removal of dye staff from textile wastewater.

The conductive polymeric composites based on multi-walled carbon nanotubes were studied by E. V. Santiago et al. By tailoring the epoxidized linseed oil matrix with groups rich in nonpolar electric density, as diacetylene, capable of

interacting by van der Waals forces, it was possible to improve the dispersion of carbon nanotubes without necessity of some modification knowing that those treatments usually affect lowering their electrical properties. The authors conclude that these composites may have potential application in vapor sensors. The effect of dielectric constant of some polystyrene-type polymer matrix on the percolation threshold in conductive polymer composites with carbon black is also studied. It is confirmed that the percolation threshold decreases while the dielectric constant increases.

The hybrid materials based on CBNs are usually stabilized by noncovalent interactions with dominating van der Waals forces. The theoretical simulations of the CBNs provide useful insight into stability and nature of such interactions [12]. W. Liu et al. studied the interactions between CO molecule and the pristine and defective graphene layers using the state-of-the-art density-function theory calculations. The results clearly demonstrate that the defective graphene could be a good sensor for CO. Using theoretical calculations Q. Wu et al. showed that band gap of carbon and boron nitride double-wall heteronanotubes (C/BN-DWHNTs) with different chirality and size could be tuned by intertube distance. Imposing an external electric field of zigzag DWHNTs provides further possibility for future electronic and electrooptic nanodevice applications.

Heterogeneous catalysis belongs to extensively studied disciplines with a huge application potential in industry. The catalytic activity of nanomaterials synthesized from carbon precursor nanomaterials was studied by M.-D. Dong

et al. The synthesized Co_3O_4 nanomaterials with different morphologies showed excellent catalytic activity for thermal decomposition of ammonium perchlorate and the Co_3O_4 nanorods with large BET surface area and pore volume had the highest catalytic activity. Organic solar cells are also extensively studied materials because they can be applied as sustainable source of energy. A. Manzano-Ramírez et al. reviewed the efficiency of graphene-based bulk heterojunction (BHJ) organic solar cells. The various applications of graphene as a constituent of BHJ organic solar cells were discussed focusing on the PCE achieved by the graphene-based devices.

Radio frequency magnetron sputtering was used for deposition of hydrogenated amorphous carbon films codoped with Si and Al ((Si, Al)/a-C:H) on Si (100) substrate at different temperatures. The substrate temperature effect on microstructure, mechanical, and tribological properties of the (Si, Al)/a-C:H films was studied and the correlation between the structure, mechanical, and tribological properties was also discussed by X. Liu et al.

We are confident that this special issue will provide new insights and inspiration to the interested reader for further work in the field of CBNs. Many individuals contributed to the success of this special issue.

Acknowledgments

We would like to thank all authors who submitted their papers for publication in this special issue. We would also like to acknowledge the referees who have put in the hard work and their valuable time to review each paper in a timely and professional way.

Dan Xia
Michal Otyepka
Xi Li
Wei Liu
Qingbin Zheng

References

- [1] V. Georgakilas, J. A. Perman, J. Tucek, and R. Zboril, "Broad family of carbon nanoallotropes: classification, chemistry, and applications of fullerenes, carbon dots, nanotubes, graphene, nanodiamonds, and combined superstructures," *Chemical Reviews*, vol. 115, no. 11, pp. 4744–4822, 2015.
- [2] Q. Li, J. Song, F. Besenbacher, and M. Dong, "Two-dimensional material confined water," *Accounts of Chemical Research*, vol. 48, no. 1, pp. 119–127, 2015.
- [3] D. Yu, K. Goh, H. Wang et al., "Scalable synthesis of hierarchically structured carbon nanotube-graphene fibres for capacitive energy storage," *Nature Nanotechnology*, vol. 9, no. 7, pp. 555–562, 2014.
- [4] Q. Xue, H. Chen, Q. Li, K. Yan, F. Besenbacher, and M. Dong, "Room-temperature high-sensitivity detection of ammonia gas using the capacitance of carbon/silicon heterojunctions," *Energy & Environmental Science*, vol. 3, no. 3, pp. 288–291, 2010.
- [5] H. Sun, X. You, J. Deng et al., "Novel graphene/carbon nanotube composite fibers for efficient wire-shaped miniature energy devices," *Advanced Materials*, vol. 26, no. 18, pp. 2868–2873, 2014.
- [6] C. Ge, J. Du, L. Zhao et al., "Binding of blood proteins to carbon nanotubes reduces cytotoxicity," *Proceedings of the National Academy of Sciences of the United States of America*, vol. 108, no. 41, pp. 16968–16973, 2011.
- [7] X. Zhang, W. Hu, J. Li, L. Tao, and Y. Wei, "A comparative study of cellular uptake and cytotoxicity of multi-walled carbon nanotubes, graphene oxide, and nanodiamond," *Toxicology Research*, vol. 1, no. 1, pp. 62–68, 2012.
- [8] M. V. Khodakovskaya, K. de Silva, A. S. Biris, E. Dervishi, and H. Villagarca, "Carbon nanotubes induce growth enhancement of tobacco cells," *ACS Nano*, vol. 6, no. 3, pp. 2128–2135, 2012.
- [9] Y. Liu, X. Dong, and P. Chen, "Biological and chemical sensors based on graphene materials," *Chemical Society Reviews*, vol. 41, no. 6, pp. 2283–2307, 2012.
- [10] M. Adeli, R. Soleyman, Z. Beiranvand, and F. Madani, "Carbon nanotubes in cancer therapy: a more precise look at the role of carbon nanotube-polymer interactions," *Chemical Society Reviews*, vol. 42, no. 12, pp. 5231–5256, 2013.
- [11] M. Zheng, S. Liu, J. Li et al., "Integrating oxaliplatin with highly luminescent carbon dots: an unprecedented theranostic agent for personalized medicine," *Advanced Materials*, vol. 26, no. 21, pp. 3554–3560, 2014.
- [12] M. Pykal, P. Jurečka, F. Karlický, and M. Otyepka, "Modelling of graphene functionalization," *Physical Chemistry Chemical Physics*, 2015.

Research Article

Catalytic Activity of Co_3O_4 Nanomaterials with Different Morphologies for the Thermal Decomposition of Ammonium Perchlorate

Li-Na Jin,¹ Jian-Guo Wang,¹ Xin-Ye Qian,¹ Dan Xia,² and Ming-Dong Dong²

¹Institute for Advanced Materials and School of Materials Science and Engineering, Jiangsu University, Zhenjiang 212013, China

²Center for DNA Nanotechnology (CDNA), Interdisciplinary Nanoscience Center (iNANO), Aarhus University, 8000 Aarhus, Denmark

Correspondence should be addressed to Li-Na Jin; jinln@mail.ujs.edu.cn and Ming-Dong Dong; dong@inano.au.dk

Received 9 March 2015; Accepted 20 April 2015

Academic Editor: P. Davide Cozzoli

Copyright © 2015 Li-Na Jin et al. This is an open access article distributed under the Creative Commons Attribution License, which permits unrestricted use, distribution, and reproduction in any medium, provided the original work is properly cited.

Nano- Co_3O_4 with different morphologies was successfully synthesized by annealing $\text{CoC}_2\text{O}_4 \cdot 2\text{H}_2\text{O}$ precursors. The as-obtained samples were characterized by powder X-ray diffraction (XRD), scanning electron microscopy (SEM), and low-temperature nitrogen adsorption-desorption. It was found that the volume ratio of N,N-dimethylformamide (DMF) and water played an important role in the formation of cobalt oxalate precursors with different morphologies. After calcination in air, cobalt oxalate precursors converted to Co_3O_4 nanomaterials while their original morphologies were maintained. The catalytic effect was investigated for nano- Co_3O_4 with different morphologies on the thermal decomposition of ammonium perchlorate (AP) by differential scanning calorimeter (DSC). The results indicated that all products showed excellent catalytic activity for thermal decomposition of AP and the Co_3O_4 nanorods with larger BET surface area and pore volume had the highest catalytic activity.

1. Introduction

Morphology-controlled synthesis of inorganic nanomaterials is of extensive research interest in materials science because the electronic, optical, magnetic, and catalytic properties of nanocrystals are highly dependent on not only their composition, but also their structure [1], shape [2], and size [3]. Therefore, many efforts have been made to develop cost-effective synthesis methods of nanomaterials with different structures and morphologies for enabling novel intrinsic properties and applications of nanomaterials.

Co_3O_4 , as one of the most intriguing magnetic p-type semiconductors, is of special interest due to its potential applications in heterogeneous catalyst [4], lithium-ion battery [5], supercapacitor [6], gas sensor [7], and many other aspects [8]. Up to now, shape-controlled Co_3O_4 nanostructures have been prepared by various approaches, in which morphology-conserved transformation of precursors has proved to be a promising approach for the synthesis of Co_3O_4

nanostructures [9–12]. For example, Zhu et al. reported the shape-controlled synthesis of cobalt carbonate/hydroxide intermediates via a solvothermal method at 220°C for 18 h [9]. Hu et al. synthesized $\beta\text{-Co}(\text{OH})_2$ nanosheet at 180°C for 12 h and $\text{Co}(\text{CO}_3)_{0.5}(\text{OH})_{0.11}\text{H}_2\text{O}$ nanobelt at 140°C for 12 h via a solvothermal method [10]. Wang et al. prepared one-dimensional and layered parallel folding of cobalt oxalate nanostructures using N,N-dimethylacetamide (DMA) and dimethyl sulfoxide (DMSO) as solvents at ambient temperature [11]. In our past work, we prepared shape-controlled synthesis of Co_3O_4 nanostructures derived from coordination polymer precursors [12]. However, for some shape-controlled synthesis methods, special instruments, complicated processes, long reaction times, and relatively high temperatures are required. Therefore, it is important to design a simple, rapid, low-temperature, and low-cost synthesis route to synthesize morphology-controlled cobalt precursors.

Over the past decades, ammonium perchlorate (AP) has received considerable attention because AP is an important

oxidizer in solid composite propellants for solid fueled rockets and the combustion behavior of propellants is highly relevant to the thermal decomposition of AP. The lower the temperature at which AP begins to decompose, the higher the burning rate of propellants [13–15]. Recently, Co_3O_4 nanomaterials with various morphologies have been used as effective catalyst to accelerate thermal decomposition of AP [12, 16–19].

In the present work, we report morphology-controlled preparation of cobalt oxalate precursors from the reaction of cobalt(II) nitrate hexahydrate and oxalic acid under mild conditions. It was found that the volume ratio of N,N-dimethylformamide (DMF) and water played a crucial role in the formation of cobalt oxalate with different morphologies. After calcination in air, the as-prepared cobalt oxalate precursors subsequently converted to porous Co_3O_4 nanomaterials while their original morphologies had been well maintained. To study their potential applications, the as-prepared nano- Co_3O_4 with different morphologies had been applied in the thermal decomposition of AP, which exhibited good activity.

2. Experimental

All chemicals and solvents are of analytical grade and were used as received without further purification. In a typical experiment, 1 mmol $\text{Co}(\text{NO}_3)_2 \cdot 6\text{H}_2\text{O}$ was dissolved in a mixed solution of DMF and deionized water at room temperature (the total volume is 20 mL), followed by addition of 1 mmol $\text{H}_2\text{C}_2\text{O}_4 \cdot 2\text{H}_2\text{O}$ under vigorous stirring. After 5 min, the as-obtained precipitates were centrifuged, washed with distilled water and absolute ethanol several times, and dried in vacuum at 60°C for 5 h. In addition, a calcination process (350°C for 1 h in air with a heating rate of 2°C min^{-1}) was performed to transform cobalt oxalate to black Co_3O_4 crystals. In the experiments, to obtain products with different morphologies, the volume ratio of DMF and water was adjusted while all other conditions were keeping unaltered.

The products were characterized by powder X-ray diffraction (XRD) on a Rigaku D/max 2500PC diffractometer with graphite monochromator and $\text{Cu K}\alpha$ radiation ($\lambda = 0.15406 \text{ nm}$) at a step width of 0.02° . SEM images of the products were obtained on scanning electron micro analyzers (HITACHI S-3400N.). Nitrogen adsorption-desorption isotherms, pore size distributions, and surface areas of the samples were measured by the instrument of NOVA 2000e using N_2 adsorption.

To test the catalytic effect of Co_3O_4 nanostructures with different morphologies on the thermal decomposition of AP, the mixture of AP and Co_3O_4 was ground carefully for 10 min and was detected by a differential scanning calorimeter (DSC) using STA 449C thermal analyzer with a heating rate of $10^\circ\text{C min}^{-1}$ in N_2 atmosphere over the temperature range of $30\text{--}500^\circ\text{C}$. The mass percentage of Co_3O_4 nanostructures to AP in the mixture was 2%.

3. Results and Discussion

Figure 1 shows the XRD patterns of the precursors prepared under the different volume ratio of DMF and water. All of

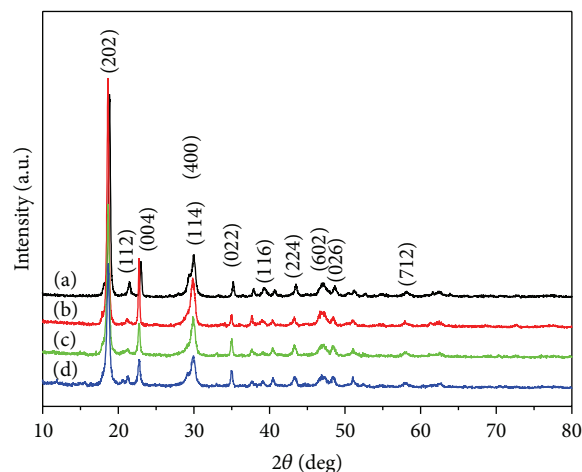


FIGURE 1: XRD patterns of the as-prepared precursors under the different volume ratio of DMF and water: (a) 0:20, (b) 4:16, (c) 8:12, and (d) 12:8.

the diffraction peaks in Figure 1(a), 1(b), 1(c), and 1(d) can be indexed as the orthorhombic phase of $\text{CoC}_2\text{O}_4 \cdot 2\text{H}_2\text{O}$ by comparison with the data of JCPDS card files number 25-0250. No impurity peaks are detected in the XRD pattern.

Morphologies of all the precursors were characterized by SEM and the images of the samples are shown in Figure 2. When 20 mL of H_2O was used without addition of DMF, the result shown in Figure 2(a) reveals that sample is composed of $\text{CoC}_2\text{O}_4 \cdot 2\text{H}_2\text{O}$ microrods with diameter of about $2\text{--}5 \mu\text{m}$. When 16 mL of H_2O and 4 mL of DMF were used, spindle-like $\text{CoC}_2\text{O}_4 \cdot 2\text{H}_2\text{O}$ nanostructures were obtained, shown in Figure 2(b). Figure 2(c) shows the morphology of sample prepared in the presence of 12 mL of H_2O and 8 mL of DMF. It was observed that the sample consisted of nanorod bundles. Figure 2(d) illustrates nanorods in sample prepared by using 8 mL of H_2O and 12 mL of DMF. In addition, when 4 mL of H_2O and 16 mL of DMF were used or 20 mL of DMF was used without addition of H_2O , no products could be obtained. The above facts showed that DMF/water volume ratio played an important role in the information of $\text{CoC}_2\text{O}_4 \cdot 2\text{H}_2\text{O}$. According to the previously reported studies, when only water was used as solvent, $\text{CoC}_2\text{O}_4 \cdot 2\text{H}_2\text{O}$ microrods were obtained because the ion-exchange reaction between the cobalt ion and the oxalate ion was very rapid in aqueous solution. In organic solvent medium, oxalic acid is a weak electrolyte that cannot be electrolytically dissociated into ions, so the cobalt ion and the oxalic acid do not react immediately. Therefore, when DMF and water were used, the reaction rate slowed down leading to smaller products, including spindle-like architectures, nanorod bundles, and nanorods. Furthermore, when the amount of DMF was increased to 16 mL or 20 mL, no products were obtained because the ion-exchange reaction was restrained [11].

The thermal behavior of $\text{CoC}_2\text{O}_4 \cdot 2\text{H}_2\text{O}$ microrods was investigated by thermogravimetric analysis (TGA) in static air atmosphere. From Figure 3, it can be seen that there are two distinct weight loss steps. The first weight loss

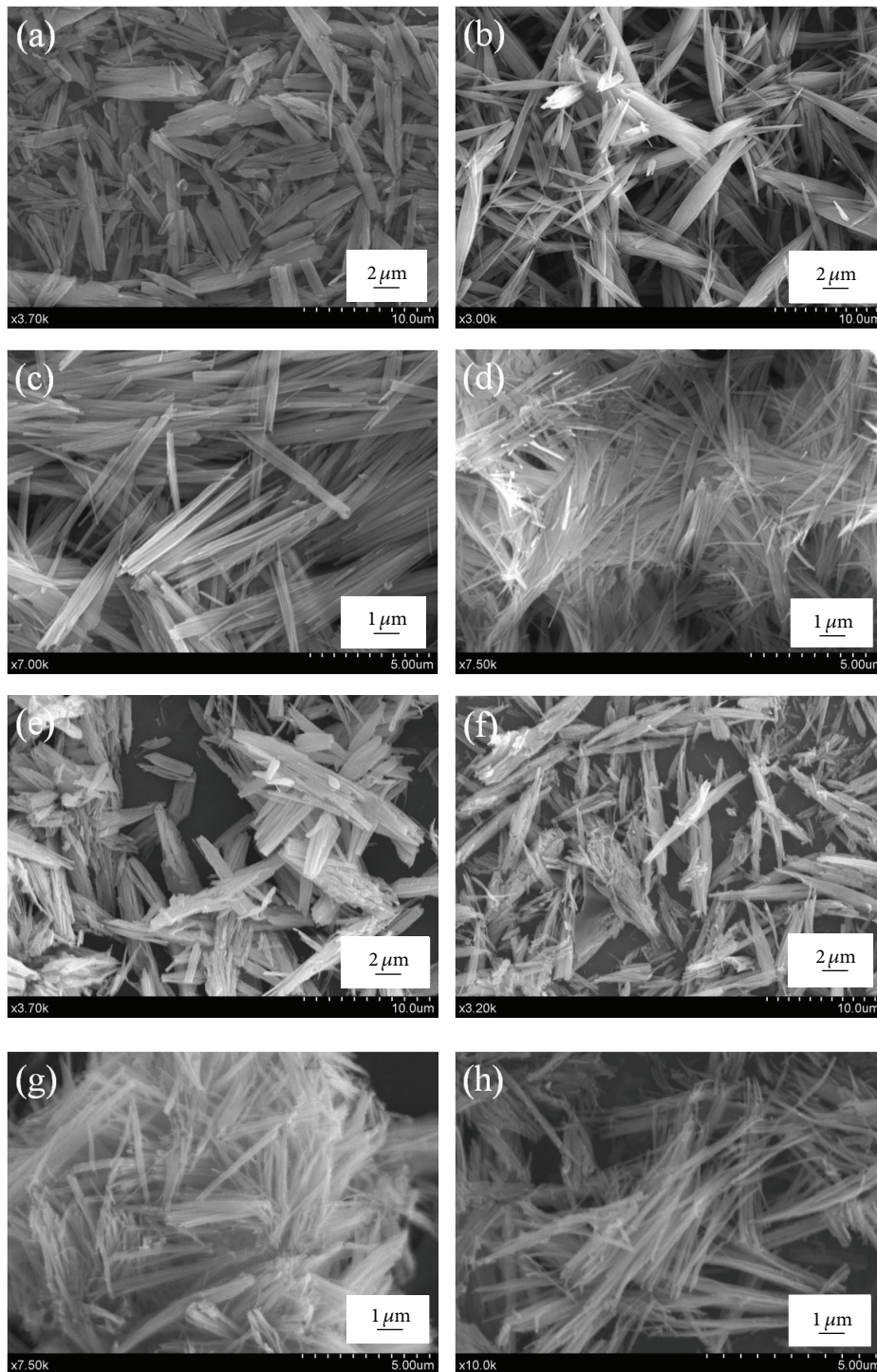
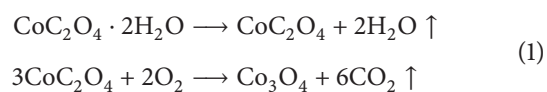


FIGURE 2: SEM images of the as-prepared cobalt oxalate precursors and Co_3O_4 nanostructures: (a, e) microrods, (b, f) spindle-like architectures, (c, g) nanorod bundles, and (d, h) nanorods.

occurs at $110\text{--}220^\circ\text{C}$, which corresponds to the evaporation of crystallized water. When the temperature is above 300°C , the second weight loss was observed, which is attributed to the decomposition of anhydrous oxalate into Co_3O_4 . The weight loss of two steps is about 19.7% and 53.3%, which is close to

the theoretical value. The decomposition of $\text{CoC}_2\text{O}_4 \cdot 2\text{H}_2\text{O}$ can be expressed as the following reaction:



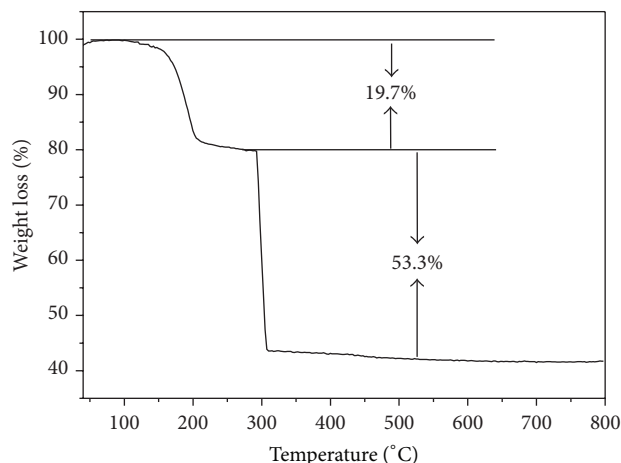


FIGURE 3: TGA curve of the as-obtained $\text{CoC}_2\text{O}_4 \cdot 2\text{H}_2\text{O}$ microrods.

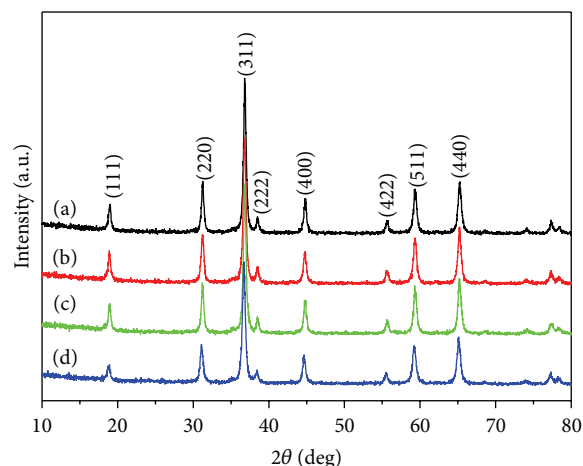


FIGURE 4: XRD patterns of the as-prepared Co_3O_4 nanostructures: (a) microrods, (b) spindle-like architectures, (c) nanorod bundles, and (d) nanorods.

According to the results of TGA, the thermal decomposition of the corresponding $\text{CoC}_2\text{O}_4 \cdot 2\text{H}_2\text{O}$ was performed at 350°C . After being annealed at 350°C for 1 h in air, the as-synthesized $\text{CoC}_2\text{O}_4 \cdot 2\text{H}_2\text{O}$ with different morphologies were completely converted to phase-pure spinel Co_3O_4 . The morphology of the Co_3O_4 products is shown in Figures 2(e)–2(h), from which it can be seen that the original shape has been maintained after calcination. The crystallographic phase of all the samples is again examined by XRD (Figure 4). All diffraction peaks can be well indexed to the pure cubic phase of Co_3O_4 (JCPDS 43-1003), indicating that the pure phase of Co_3O_4 was obtained by annealing $\text{CoC}_2\text{O}_4 \cdot 2\text{H}_2\text{O}$ precursor directly. Figure 5 shows TEM images of the Co_3O_4 products, revealing that the Co_3O_4 products were composed of numerous Co_3O_4 nanoparticles with a size of several tens of nanometers and abundant pore structures were formed among the nanoparticles.

Nitrogen adsorption-desorption isotherms of nano- Co_3O_4 are shown in Figure 6, and the insets illustrate the corresponding Barrett-Joyner-Halenda (BJH) pore size distribution plots. The isotherms can be categorized as type IV with an H3 hysteresis loop, which is characteristic of mesoporous materials. The BJH pore size distribution indicates that all of the samples contain mesoscale pores. The Brunauer-Emmett-Teller (BET) surface areas and pore volumes of the samples are $42 \text{ m}^2/\text{g}$ and $190.3 \text{ mm}^3/\text{g}$, $61 \text{ m}^2/\text{g}$ and $226.3 \text{ mm}^3/\text{g}$, $62 \text{ m}^2/\text{g}$ and $241.3 \text{ mm}^3/\text{g}$, and $83 \text{ m}^2/\text{g}$ and $277.1 \text{ mm}^3/\text{g}$ for the Co_3O_4 with microrods, spindle-like architectures, nanorod bundles, and nanorods, respectively.

Considering the porous structures and high BET surface area, we investigated the application of the synthesized nano- Co_3O_4 for the thermal decomposition of AP. Figure 7 shows DSC curves for thermal decomposition of pure AP and its mixture with nano- Co_3O_4 with different morphologies.

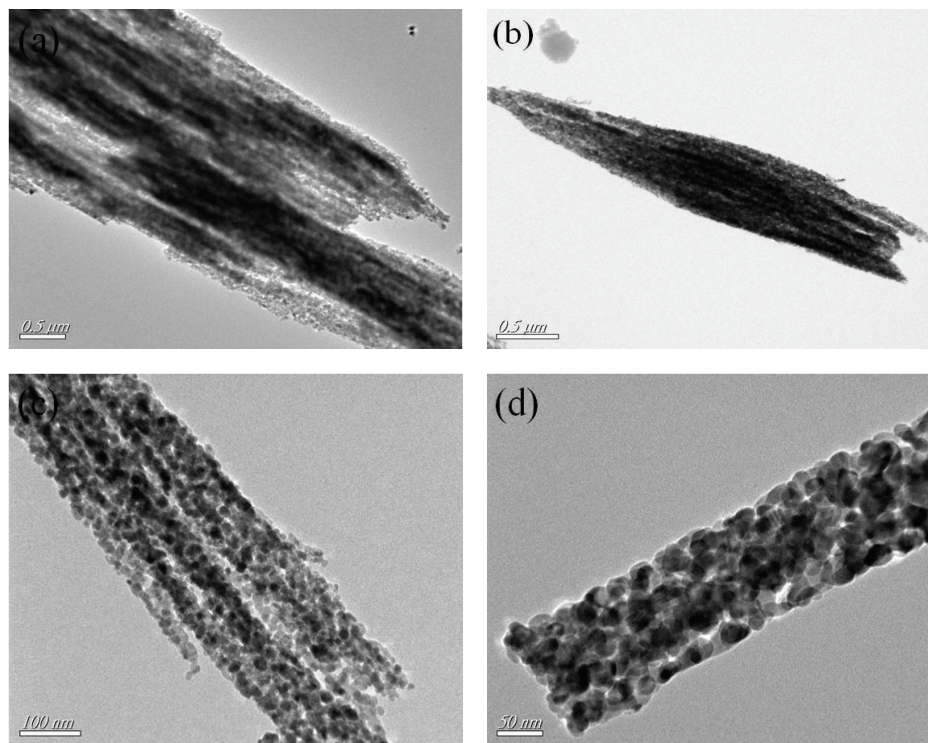


FIGURE 5: TEM images of the as-prepared Co_3O_4 nanostructures: (a) microrods, (b) spindle-like architectures, (c) nanorod bundles, and (d) nanorods.

For pure AP, an endothermic peak was observed at about 250°C , which is due to the crystal transformation of AP from orthorhombic to cubic phase (Figure 7(e)) [13]. When nano- Co_3O_4 with different morphologies as catalyst was added to AP, all samples have similar endothermic peaks at about 250°C , indicating that the catalysts have little effect on the crystallographic transition temperature of AP. However, in the relatively high temperature region, the samples containing catalysts have dramatic changes in the exothermic peaks of AP decomposition. When 2 wt% catalysts were added to AP, the original exothermic peak of pure AP at 445.0°C disappeared and only one exothermic peak was observed. The exothermic peak temperature was 305.1 , 299.7 , 297.4 , and 296.2°C for Co_3O_4 microrods, spindle-like architectures, nanorod bundles, and nanorods, respectively (Figure 7(a)–7(d)). The present catalytic activity of Co_3O_4 nanorods was higher than Co_3O_4 nanoparticles, nanosheets, and octahedral particles [12, 18, 19]. The above results indicate that Co_3O_4 particles have a significant effect on the decomposition temperature of AP and Co_3O_4 nanomaterials with different morphologies for decreasing the decomposition of AP are proportional to their BET surface area and pore volume. It is known that specific surface area and pore volume can be the primary reasons for the catalytic role, since more reactive sites can be generated [12, 20, 21]. Thus, Co_3O_4 nanorods with larger BET surface area and pore volume have the most effective catalytic activity and the thermal

decomposition temperature of AP shifted downward about 148.8°C .

4. Conclusions

In summary, we synthesized porous nano- Co_3O_4 with different morphologies via annealing $\text{CoC}_2\text{O}_4 \cdot 2\text{H}_2\text{O}$ precursors prepared under ambient condition without the assistance of template or surfactant. The as-prepared porous nano- Co_3O_4 with different morphologies have good catalytic properties for the thermal decomposition of AP due to their large BET surface area and pore volume. Co_3O_4 nanorods with larger BET surface area and pore volume show better catalytic activity than others and shifted the AP thermal decomposition temperature downwardly to about 148.8°C .

Conflict of Interests

The authors declare that there is no conflict of interests regarding the publication of this paper.

Acknowledgments

The authors acknowledge the financial support by National Natural Science Foundation of China (no. 21401081), China Postdoctoral Science Foundation (no. 2014M560397), Jiangsu Natural Science Funds for Distinguished Young Scholars

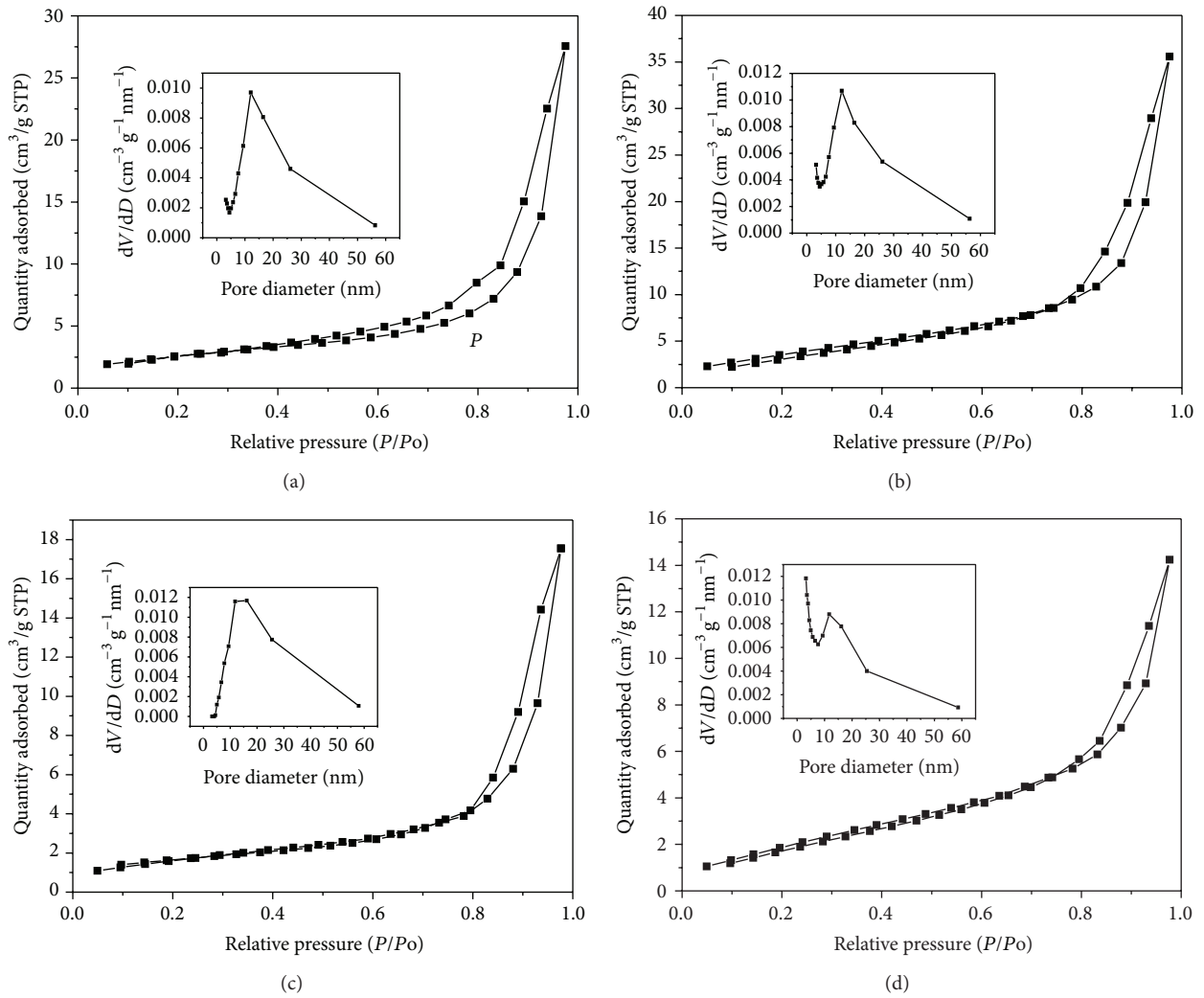


FIGURE 6: N_2 adsorption-desorption isotherms of as-prepared Co_3O_4 nanostructures at 77 K: (a) microrods, (b) spindle-like architectures, (c) nanorod bundles, and (d) nanorods. Inset in each isotherm is the corresponding pore size distributions.

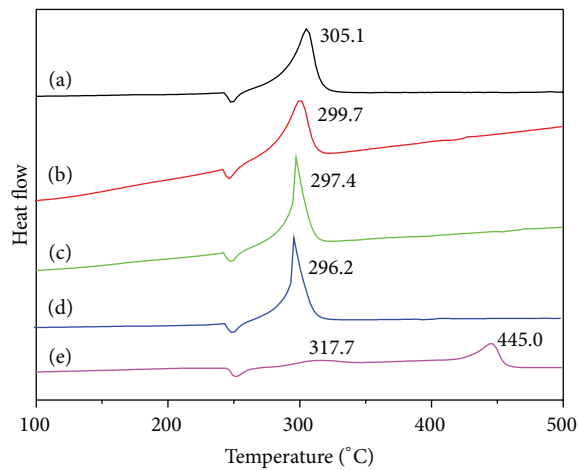


FIGURE 7: DSC curves of the AP samples after addition of various Co_3O_4 nanostructures: (a) 2 wt% Co_3O_4 microrods, (b) 2 wt% Co_3O_4 spindle-like architectures, (c) 2 wt% Co_3O_4 nanorod bundles, (d) 2 wt% Co_3O_4 nanorods, and (e) pure AP.

(no. BK20140013), Jiangsu Postdoctoral Science Foundation (no. 1401051C), and the Senior Intellectuals Fund of Jiangsu University (nos. 14JDG058 and 11JDG098).

References

- [1] Q. Hua, T. Cao, X.-K. Gu et al., "Crystal-plane-controlled selectivity of Cu_2O catalysts in propylene oxidation with molecular oxygen," *Angewandte Chemie—International Edition*, vol. 53, no. 19, pp. 4856–4861, 2014.
- [2] Y. Zhong, J. Wang, R. Zhang et al., "Morphology-controlled self-assembly and synthesis of photocatalytic nanocrystals," *Nano Letters*, vol. 14, no. 12, pp. 7175–7179, 2014.
- [3] Y. Li and Y. Huang, "Morphology-controlled synthesis of platinum nanocrystals with specific peptides," *Advanced Materials*, vol. 22, no. 17, pp. 1921–1925, 2010.
- [4] L. Chen, J. Hu, R. Richards, S. Prikhodko, and S. Kodambaka, "Synthesis and surface activity of single-crystalline Co_3O_4 (111) holey nanosheets," *Nanoscale*, vol. 2, no. 9, pp. 1657–1660, 2010.
- [5] B. Yan, L. Chen, Y. Liu et al., " Co_3O_4 nanostructures with a high rate performance as anode materials for lithium-ion batteries, prepared via book-like cobalt-organic frameworks," *CrystEngComm*, vol. 16, no. 44, pp. 10227–10234, 2014.
- [6] H. Wang, L. Zhang, X. Tan et al., "Supercapacitive properties of hydrothermally synthesized Co_3O_4 nanostructures," *The Journal of Physical Chemistry C*, vol. 115, no. 35, pp. 17599–17605, 2011.
- [7] Y. Lü, W. Zhan, Y. He et al., "MOF-templated synthesis of porous Co_3O_4 concave nanocubes with high specific surface area and their gas sensing properties," *ACS Applied Materials and Interfaces*, vol. 6, no. 6, pp. 4186–4195, 2014.
- [8] Y. Du, W. Huang, Z. Hua et al., "A facile ultrasonic process for the preparation of Co_3O_4 nanoflowers for room-temperature removal of low-concentration NO_x ," *Catalysis Communications*, vol. 57, pp. 73–77, 2014.
- [9] T. Zhu, J. S. Chen, and X. W. Lou, "Shape-controlled synthesis of porous Co_3O_4 nanostructures for application in supercapacitors," *Journal of Materials Chemistry*, vol. 20, no. 33, pp. 7015–7020, 2010.
- [10] L. Hu, Q. Peng, and Y. Li, "Selective synthesis of Co_3O_4 nanocrystal with different shape and crystal plane effect on catalytic property for methane combustion," *Journal of the American Chemical Society*, vol. 130, no. 48, pp. 16136–16137, 2008.
- [11] D. Wang, Q. Wang, and T. Wang, "Morphology-controllable synthesis of cobalt oxalates and their conversion to mesoporous Co_3O_4 nanostructures for application in supercapacitors," *Inorganic Chemistry*, vol. 50, no. 14, pp. 6482–6492, 2011.
- [12] L.-N. Jin, Q. Liu, and W.-Y. Sun, "Shape-controlled synthesis of Co_3O_4 nanostructures derived from coordination polymer precursors and their application to the thermal decomposition of ammonium perchlorate," *CrystEngComm*, vol. 14, no. 22, pp. 7721–7726, 2012.
- [13] S. Chaturvedi and P. N. Dave, "A review on the use of nanometals as catalysts for the thermal decomposition of ammonium perchlorate," *Journal of Saudi Chemical Society*, vol. 17, no. 2, pp. 135–149, 2013.
- [14] W. Wang and J. Yao, "Catalytic activity of magnetite with different shapes for the thermal decomposition of ammonium perchlorate," *Chemistry Letters*, vol. 43, no. 10, pp. 1554–1556, 2014.
- [15] L.-N. Jin, Q. Liu, and W.-Y. Sun, "Room temperature solution-phase synthesis of flower-like nanostructures of $[\text{Ni}_3(\text{BTC})_2 \cdot 12\text{H}_2\text{O}]$ and their conversion to porous NiO ," *Chinese Chemical Letters*, vol. 24, no. 8, pp. 663–667, 2013.
- [16] S. Jamil, M. R. Janjua, and T. Ahmad, "The synthesis of flower shaped microstructures of Co_3O_4 by solvothermal approach and investigation of its catalytic activity," *Solid State Sciences*, vol. 36, pp. 73–79, 2014.
- [17] X. Guan, G. Li, L. Zhou, L. Li, and X. Qiu, "Template-free approach to core-shell-structured Co_3O_4 microspheres," *Chemistry Letters*, vol. 38, no. 3, pp. 280–281, 2009.
- [18] E. Alizadeh-Gheshlaghi, B. Shaabani, A. Khodayari, Y. Azizian-Kalandaragh, and R. Rahimi, "Investigation of the catalytic activity of nano-sized CuO , Co_3O_4 and CuCo_2O_4 powders on thermal decomposition of ammonium perchlorate," *Powder Technology*, vol. 217, pp. 330–339, 2012.
- [19] H. Zhou, B. Lv, D. Wu, and Y. Xu, "Synthesis and properties of octahedral Co_3O_4 single-crystalline nanoparticles enclosed by (111) facets," *CrystEngComm*, vol. 15, no. 41, pp. 8337–8344, 2013.
- [20] X. Guan, L. Li, J. Zheng, and G. Li, " MgAl_2O_4 nanoparticles: a new low-density additive for accelerating thermal decomposition of ammonium perchlorate," *RSC Advances*, vol. 1, no. 9, pp. 1808–1814, 2011.
- [21] X.-J. Shen, J.-P. Yang, Y. Liu, Y.-S. Luo, and S.-Y. Fu, "Facile surfactant-free synthesis of monodisperse Ni particles via a simple solvothermal method and their superior catalytic effect on thermal decomposition of ammonium perchlorate," *New Journal of Chemistry*, vol. 35, no. 7, pp. 1403–1409, 2011.

Research Article

Relationship between Polymer Dielectric Constant and Percolation Threshold in Conductive Poly(styrene)-Type Polymer and Carbon Black Composites

Mariana Castro Martínez,¹ Susana Hernández López,² and Enrique Viguera Santiago²

¹Programa de Posgrado en Ciencia de Materiales de la UAEM, Facultad de Química, Universidad Autónoma del Estado de México, Paseo Colón Esquina con Paseo Toluca, 50000 Toluca, MEX, Mexico

²Laboratorio de Investigación y Desarrollo de Materiales Avanzados (LIDMA), Facultad de Química, Universidad Autónoma del Estado de México, Paseo Colón Esquina con Paseo Toluca, 50000 Toluca, MEX, Mexico

Correspondence should be addressed to Enrique Viguera Santiago; eviguera@uaemex.mx

Received 4 June 2015; Revised 4 August 2015; Accepted 5 August 2015

Academic Editor: Wei Liu

Copyright © 2015 Mariana Castro Martínez et al. This is an open access article distributed under the Creative Commons Attribution License, which permits unrestricted use, distribution, and reproduction in any medium, provided the original work is properly cited.

We study the effect of dielectric constant of some poly(styrene)-type polymer matrix on the percolation threshold in conductive polymer composites with carbon black (CB). We demonstrate that percolation threshold diminishes with an increment of the dielectric constant of polymer matrix. We chose polystyrene and other three polymers similar in structure and molecular weight but with different chemical nature. The corresponding dielectric constant and critical concentration, X_c , in volume fraction of carbon black, v/v CB, were the following: 4MePS ($\epsilon = 2.43$; $X_c = 0.058$), PS ($\epsilon = 2.60$; $X_c = 0.054$), 4BrPS ($\epsilon = 2.82$; $X_c = 0.051$), and 4ClPS ($\epsilon = 2.77$; $X_c = 0.047$). The correlation between both parameters confirms that the percolation threshold decreases while the dielectric constant increases. At microscopic level, this effect is attributed to an enhanced physical interaction of the CB particles with the asymmetric electric density produced by electronegative or inductive atoms/groups. Therefore, by controlling the chemical structure of the polymer matrix, the attraction forces between the polar groups on the carbon black surface particles with those of the polymer matrix can be improved, which in turn induces a better disaggregation and dispersion of those particles into the polymer matrix, allowing the percolation threshold reached at a lower filling fraction.

1. Introduction

Polymer composites with electrical properties have received attention during the last 60 years for scientific and technological reasons [1–7]. From the theoretical point of view, the electrical conductivity of these materials can be explained very well by the percolation approach. This predicts the formation of electrical pathways at the critical filling fraction X_c , and for larger filler fractions the electrical properties fit very well with the following equation [8]:

$$\rho(X) \approx (X - X_c)^{-\beta}. \quad (1)$$

With X being the volume fraction of the conductive particles, β is the critical exponent and X_c is percolation concentration or critical concentration. Characteristics of the shape and

spatial distribution of the conductive particles used for the composite system can be related to the value of the critical parameters [8–12].

For these materials, both the fillers and the polymer are very important for designing and good performance. Some factors concerning the conductive particle nature must be considered in conjunction with the polymer properties such as thermodynamic and rheological ones and with the processing conditions employed for the composite preparation. The filler content must be as low as possible to avoid problems such as poor processability, poor mechanical properties, high cost, and particle-polymer incompatibility, which lead to weakening of some properties including the electrical ones. In order to decrease the three-dimensional percolation threshold and optimize the polymer-particles compatibility,

several studies have been realized considering the conductive particles and/or the polymer matrix. Studies related to conductive particles are *nature* (metallic, carbonaceous, polymeric, etc.), geometry and size, surface functionalization, and so forth [5]. The main problem during the construction of the conductive network when carbonaceous particles are used, such as carbon black [6], graphite [7, 13, 14], fibers [15, 16], or carbon nanotubes (NTC) [17, 18], is the van der Waals interactions among carbon particles in the macroscopic agglomerates, which has a crucial effect for obtaining an optimal dispersion of them into the polymer matrix and in turn in the percolation threshold. Then, the compatibility is related to composition and surface chemistry [19]; *geometry*: a high aspect ratio of the conductive particles allows reaching lower percolation concentrations [14, 20]; *structure* [10, 21–23]: a higher structure of the primary aggregates of elementary carbon particles reduces percolation threshold due to a better electric path interconnection at microscopic level [10]; *surface area* [22, 23]: surface functionalization of the NTC [24–28], graphite [14, 29], and CB particles [22] has been used to enhance the dispersion and compatibility with polymer matrixes. However, chemical modification is used to reduce electrical properties of conducting particles.

Some other studies have taken into account the polymer matrix characteristics as *viscosity*, *molecular weight*, and *superficial tension*. Matrix melt viscosity has two effects: it can either reduce or increase percolation threshold, depending on particle size and shape. In carbon black filled polymers, percolation threshold increases with melt viscosity [30–34]. (2) The *crystalline degree* [18, 35, 36] of the polymer matrix becomes important for the percolation threshold in carbon black polymer composites, and segregation occurs preferably on the amorphous phase. For this reason, percolation threshold could be reached at lower volume fraction of carbon particles in semicrystalline than in amorphous polymers; (3) *cross-linking*; (4) *elastic modulus* [37], and (5) *immiscible blends* in which composites show enhanced interparticle connectivity around the incompatible region and consequent decreasing of the percolation threshold due to a preferential distribution of the conductive carbon along the interface of those immiscible polymers [20, 38–42].

The preparation method also has an influence in the dispersion process of the conductive particles and as a consequence in the reproducibility of the electric properties of the respective polymer composites. Most of the polymer composites are produced in liquid phase, in a melt stage, or in monomer or polymer dissolution. In both cases, a suspension is always formed and it has been studied that the resistivity control for melt polymer composites is also dependent on processing parameters such as mixing time, temperature, rotor speed, molding time, temperature, and pressure at molding [43–49]. For a composite obtained by *in situ* method that consists in making first a dispersion of carbon particles into the monomer and then a subsequent polymerization of that suspension, the optimization of the processing parameters is more difficult. In solution, particles are immersed in a viscous fluid and they are submitted to interactions which may strongly change their distribution [50] depending on the stirring speed, solvent proportion, temperature, ultrasonic

time, ultrasonic oscillation frequency, and external variables like electric fields [51, 52].

For electrical properties of polymer composites, a variable of interest that has not been deeply studied is the role of the structure (chemical nature) of the polymer matrix that surely plays in junction with the aforementioned parameters during the dispersion/distribution process of carbon particles. Due to the existence of secondary interactions between the superficial functional groups on carbon black and the chemical groups on the polymer, that interaction could be improved or maximized with the presence of certain function on the polymer. At the end, any functional group(s) could modify the electronic density of the molecules in some magnitude which could have a positive or negative effect on the formation of conductive paths for the formation of polymeric compound as will be shown below. There are few studies that show a qualitative effect of the chemical influence of the polymer matrix on the percolation threshold [39, 53–56] but without any clear tendency. Because we are interested in evaluating it in terms of a macroscopic property of the polymers, the dielectric constant and the results are interpreted in terms of the existing theories. The magnitude of the dielectric constant is dependent on the ability of the polarizable units in a polymer to orient fast enough to keep up with the oscillations of an alternating electric field. At optical frequencies (10^{14} Hz), only the lowest mass species, electrons, are efficiently polarized. At lower frequencies, atomic polarization of heavier, more slowly moving nuclei also contributes to the dielectric constant. Atomic polarization of induced dipoles can occur in the infrared (10^{12} Hz) or lower frequency regimes. Dipole polarization is the reorientation and alignment of permanent dipoles in response to the electric field. The three modes of polarization can interact, but, in most cases, they act essentially separately and are therefore additives. The dielectric constant measured at frequencies lower than optical frequency can lead to a basic understanding of the influence of molecular structure on dielectric properties in polymers [57–60]. It is because we propose to study this polymer property in the control of the electric percolation threshold on polymer composites using one type of CB particles, Vulcan XC72, which has polar nature and is widely used by other authors for its high structure and some surface oxidation. The proposal consists in obtaining polymer composites from polymer matrix of different dielectric constant produced by the presence of electronegative or inductive atoms/groups into the aromatic ring which is the base of the polystyrene polymer. These polymers were synthesized by the same method in order to have very close molecular masses. The preparation method for CB polymer composites was in solution by ultrasonic shaking (solution) [56]. Carbon black particles were dispersed in polymer solutions at the same viscosity and they were shaken in the same time depending on the CB amount in order to control the processing parameters and to obtain them in reproducible way. From the microscopic point of view, CB particles should be attracted and better distributed by more polarizable (higher dielectric constant) polymers producing conductive networks at lower CB concentration than those

composites based on polymers with a reduced dielectric constant. We demonstrate a close correlation between the CB percolation threshold and the dielectric constant of some poly(styrene)-derivatives polymer matrixes, which make the electronic affinity between polymeric matrix and CB particles clear, evidencing a better dispersion and a preferential distribution of the carbon particles in highly polarizable polymer matrixes. This effect has a positive consequence in the electrical properties by lowering the concentration threshold. In order to avoid, as much as possible, the influence of other factors on the percolation threshold, such as molecular weight and density among others, polymer matrixes were synthesized via free radicals in bulk medium for producing amorphous polymers under the same reaction conditions. Structural and electric characterizations were also complemented by thermal analysis as differential scanning calorimetry, DSC, and thermogravimetric analysis, TGA, and density and molecular mass. Dielectric constant was evaluated as a function of temperature at a low frequency (850 MHz) in order to analyze the dipole effect of the repetitive polymer units.

2. Materials and Methods

2.1. Materials. Styrene, 4-methylstyrene, 4-chlorostyrene, and 4-bromostyrene monomers were purchased from Aldrich. Inhibitor was eliminated by surpassing the liquid monomers through a chromatographic type WB2-basic Alumina packed column. Tetrahydrofuran (THF) and benzoyl peroxide (BPO) were also supplied by Aldrich. CB Vulcan XC72, with a size of 32 nm and a density of 1.8 g/cm³, was donated by Cabot Co. and it was used as received.

2.2. Synthesis of Matrix Polymers. Polymerization of monomers after being free of inhibitor was carried out in mass via free radicals using benzoyl peroxide (400:1 mol monomer : BPO) as initiator, and the following temperatures were used in an oil bath under a nitrogen flux: first, monomer was left at 70°C for 12 h; then, the high viscose product was left for 8 h at a temperature of 90°C and finally temperature was elevated at 110°C and the solid product was left for 8 h. After cooling to room temperature, the solid polymer was solved in THF and reprecipitated from methanol in order to remove residual monomer and initiator. The white solid was filtered, washed with methanol, and dried under vacuum for 72 h. Polymers (Figure 1) obtained were characterized by DSC, TGA, Gel Permeation Chromatography, GPC, and density, and dielectric constant was measured at 850 MHz.

2.3. Composite Preparation. All composite samples were prepared by the same procedure to avoid fluctuations in the evaluation of critical CB concentration. Composites from 2 to 16 weight percent (wt%) (or 0.034–0.13 volumetric fraction, v/v) of CB were prepared using an ultrasonic shaking bath (23°C) at the same initial relative viscosity (2.6 ± 0.05) of the polymer solutions, using THF as a solvent. A general procedure is described for a poly(styrene)-based composite [61]. Polymer was dissolved in the necessary volume of THF until

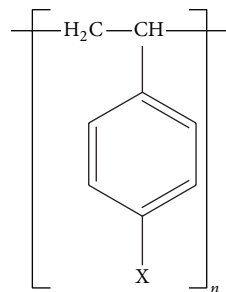


FIGURE 1: Polymer structures and acronyms. Poly(styrene): PS, with X = H; 4-methyl-poly(styrene): 4MePS, with X = CH₃; 4-chloro-poly(styrene): 4ClPS, with X = Cl; and 4-bromo-poly(styrene): 4BrPS, with X = Br.

it achieves the mentioned viscosity and it was sonicated, using an ultrasonic processor Ultrasonik 28X (50/60 Hz), until the polymer was completely dissolved; it takes around 30 min. After the polymer is dissolved, the appropriate quantity of CB is added gradually without interrupting the sonication. It takes between 6 and 9 h, depending on the amount of CB: 2–4 wt% (6 hr), 5–7 wt% (7 h), 8–10 wt% (8 h), and higher than 10 wt% (9 h). The THF solvent was evaporated by distillation under reduced pressure. The composite was well dried under vacuum for 24 h. The electrical resistance of the composites was evaluated and resistivity was calculated in order to build the percolation curves. Composites were prepared by triplicate and the specimens were processed for electrical characterization. Finally, percolation threshold was numerically computed by fitting experimental data according to (1).

2.4. Polymer and Composite Characterization

2.4.1. Differential Scanning Calorimetry (DSC) and Thermogravimetric Analysis (TGA). Differential scanning calorimetry (DSC) and thermogravimetric analysis (TGA) were carried out simultaneously using a SDT Q600 modulus from TA Instruments, under nitrogen atmosphere, a heating rate of 10°C/min, from 30 to 600°C. Glass transition temperature, T_g , and decomposition temperature or temperature at which the polymer lost 10% of its weight, T_{10} , were obtained, respectively.

2.4.2. The Weight-Average Molecular Weight (M_w) and Polydispersity Index (I). A GPC Agilent 100 Series was used in order to obtain the weight molecular mass and the polydispersity, using a Zorbax Eclipse XBD-C8 column 150 × 4.6 mm of internal diameter at 60°C, a flux of 1.6 mL/min, and HPLC THF as solvent.

2.4.3. Density. Polymer density was measured by two techniques: by direct relationship of mass/volume which in turns was measured for pure polymer cylinders prepared by thermocompression molding. And the second method was by the displacement of water in a calibrated probe at 23°C. The measurements were very close and their average was taken.

TABLE 1: Thermal, mass, and electronic properties of polymers.

Characterization	Property	Polymer			
		PS	4MePS	4BrPS	4ClPS
Thermal	$T_g/^\circ\text{C}$	106	115	136	131
	$T_{10}/^\circ\text{C}$	385	370	387	382
GPC	Mass of the repetitive unit	80	118	182.9	138.5
	$M_w \times 10^5$ g/mol	1.43	2.45	2.55	2.48
	PD	1,788	2,076	1,394	1,791
	I	2.024	1.506	1.370	1.452
Electric	Pauling electronegativity of the 4-substituent	2.1	2.4	2.8	3.2
	magnitude of dipole moment (D) ^a	0.25	0.084	1.45	1.38
	Dielectric constant (17°C, 850 MHz)	2.60	2.43	2.82	2.77

^aCalculated by MOPAC PM3.

2.4.4. Relative Viscosity. The initial viscosity of the polymer solutions used for dispersing CB particles was measured using an Ostwald capillary viscometer previously calibrated with water at 23°C, and then the pure solvent (THF) was measured and finally the polymer solutions. As mentioned before, the initial viscosity of the polymer solution for each composite preparation was 2.3 ± 0.05 .

2.4.5. Dielectric Constant. Pure polymers were molded to disks of 2 cm diameter \times 0.9–1.1 mm thickness by compression molding. A steel mold was heated at 10°C above polymer's T_g , it was filled with the polymer cut in small pieces, and a pressure of 12 Kg/cm² was applied for 30 min. Then, the mold was cooled down to 60°C, mechanical compression was removed, and sample was cooled at room temperature (23°C). The dimensions of the transparent plates were measured with a micrometer and then the dielectric constant was evaluated. Polymer dielectric constant was measured using an Agilent 4991A RF Impedance/Material Analyzer at 850 MHz of frequency range from 17°C to five degrees below the corresponding polymer matrix T_g into a controllable oven. The dielectric constant (κ) was calculated by the formula of a parallel plate capacitor as $\kappa = Ct/\epsilon_0 A$, where C is the capacitance of the capacitor, ϵ_0 is the vacuum dielectric permittivity, A is the area of the electrode, and t is the thickness of the capacitor.

2.4.6. Resistivity Measurements. Cylinder shaped samples of 1 \times 1 cm were prepared by thermomechanical molding from all polymers and composites. 1 g of sample was introduced into a steel mold heated from room temperature to ten grades up to polymer's T_g , and it was pressed at 12 Kg/cm². The heating was made at a rate of 10°C/min. Finally, molding system was cooled with air to 50°C, pressure was released, and the sample was removed [61, 62]. Resistivity measurements were made with an electrometer Keithley 6517A following the methodology pointed out in [56, 61, 62]. For each composition, the plotted resistivity is the average of nine samples, obtaining a deviation standard of 3% for the conductive zone and 10% for the percolation zone in the percolation curve.

2.4.7. Percolation Threshold. For determination of the percolation threshold, numerical fit was carried out on Origin 6 software according to (1). For all cases, three free parameters ρ_0 , X_c , and β were considered, where ρ_0 is the proportionality constant. 0.99 of data correlation were reached for running numerical interactions. Best fitting curves were obtained for β very close to 2, and then β was fixed to this value and numerical interactions were run again. The value of the critical exponent agrees with the universal values for 3D media [9].

3. Results and Discussion

Thermal properties as T_g and decomposition of the polymers were evaluated by DSC and TGA, respectively, and they are shown in Table 1. The decomposition temperature of polymers is higher than 380°C for the PS and the halogenated ones. However, 4-methyl-poly(styrene) (4MePS) shows a lower decomposition temperature probably due to the benzyl hydrogen of the CH₃ substituent. These hydrogens need lower energy to break and build up resonance-stabilized species with the aromatic ring. DSC and TGA analyses were a reference to establish the processing conditions of the polymers. There is a large range of temperature between T_g and T_{10} , giving us a broad range of work above the T_g without the decomposition of the polymer.

The weight-average molecular weight (M_w) and polydispersity (I) were evaluated by GPC. The results are shown in Table 1. It was important to minimize the parameters that could affect the threshold percolation of the studied polymers. As it is shown in Table 1, 4MePS, 4-bromo-poly(styrene) (4BrPS), and 4-chloro-poly(styrene) (4ClPS) have differences in M_w less than 10,000 g/mol and a polydispersity less than 1.5, with polystyrene (PS) being an exception to this. PS has a different M_w by 100,000 g/mol compared to the other polymers and a lightly higher dispersion. However, by calculating the polymerization degree (PD), we notice that PS and 4ClPS have almost the same value (1,790), followed by 4MePS with approximately 2,000 repetitive units and finally 4BrPS with only 1,400 units, approximately. If these results had a relevant incidence on the percolation threshold,

we could anticipate that PS and 4BrPS would have the lowest percolation threshold because 4BrPS has the smallest polymer chains and PS has both, the smallest and the largest chains, as indicated by its dispersion.

To avoid the side effects on the percolation threshold, one initial solution viscosity for each polymer (2.3 ± 0.05) was established for preparing the respective composites using THF as a solvent and 23°C temperature. Such viscosity requires preparing polymer solutions with the following concentrations: PS: 6 g/mL, 4MePS: 8 g/mL, 4BrPS: 5 g/mL, and 4ClPS: 4 g/mL. Obviously, this viscosity is lightly modified by the CB incorporation, but it was compensated with the shaking time. For preparing the polymer composites at the volume fraction of CB, it was necessary to evaluate the polymer density. The average results of the two mentioned methods are PS: 1.048 g/cm^3 , 4MePS: 1.015 g/cm^3 , 4BrPS: 1.53 g/cm^3 , and 4ClPS: 1.22 g/cm^3 and are according to the values published in other sources [63–65].

Pauli electronegativity of the 4-bonded atoms is shown in Table 1, calculus of the magnitude of the dipole moment was made numerically using MOPAC PM3 software, and the dielectric constant is taken at 17°C . As it is shown, the dipole moment is 0.25 D for PS due to the ethyl group regarded as the equivalent of the polymer's backbone. This group is an inductor electronic donor, meaning that the electronic density is displaced from the backbone chain to the aromatic ring, producing a small dipole moment. When the hydrogen in position 4 from the main chain is replaced by a methyl (CH_3) group, the dipole moment decreases almost to zero. This dipole moment reduction is produced because both groups on the benzene ring (ethyl and methyl) have the same inductor electronic effect in such a way that the vector of dipole moment is almost canceled (0.084 D). The opposite and higher change in dipole moment is observed when a halogen atom is sited in the same 4-aromatic ring position. From a microscopic point of view, the dipole moment (Table 1) has no direct correlation with the electronegativity of those atoms. We expected that 4ClPS had a higher dipole moment than 4BrPs due to its higher electronegativity, even though this is not the only factor that affects it. From a macroscopic view, the dielectric constant (κ) at 17°C and 850 MHz only reflects a partial dipole orientation of the polar repetitive units due to the dipole movement that is restricted by the glassy state, whose temperature (17°C) is lower than the corresponding T_g . However, it shows a difference in polarity at this temperature, the least polar polymer being the 4MePS ($\kappa = 2.44$) and the most one the 4BrPS ($\kappa = 2.82$) and very close one the 4ClPS ($\kappa = 2.77$).

The dielectric properties of a polymer are determined by the charge distribution and also by statistical thermal motion of its polar groups. The dipole units cannot orient themselves below the T_g ; however, as the temperature increases, the orientation of dipoles is ameliorated, increasing the dielectric constant. Dielectric constant was also evaluated at some predetermined temperatures: 17°C (as the initial), 70°C , 90°C , and 100°C , for PS. However, 4MePS was increased to 105°C , 4ClPS to 120°C and 125°C , and 4BrPS to 130°C . The upper limit for those temperatures was five degrees below

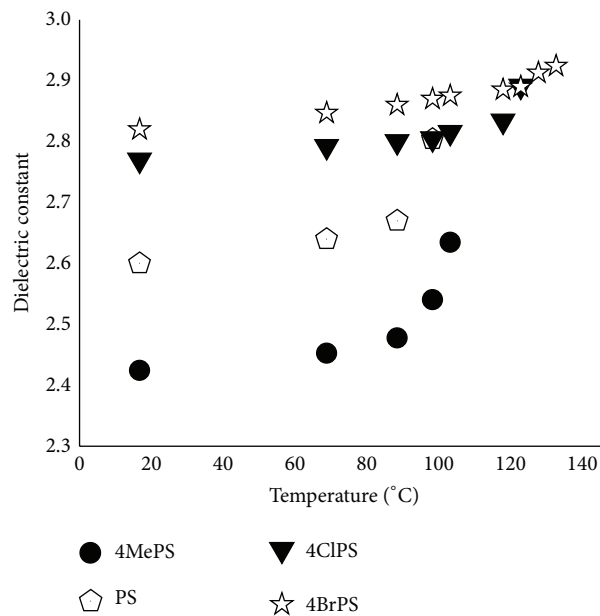


FIGURE 2: Dielectric behavior of polymers related to temperature.

the corresponding T_g 's. The dielectric constant behavior with respect to temperature is plotted in Figure 2. As we can see, the dielectric constant of PS and 4MePS increases with temperature. At 100°C , PS and 4ClPS have the same dielectric constant, but PS has reached its maximum (an increase of 7%). 4MePS increases by 6.5% from its initial value. Although 4ClPS shows the same tendency of increasing the dielectric constant with temperature, the increasing percentage is not as high as that for PS; it only increases by 4.2% reaching 4BrPS at its maximum. 4BrPS presents the less important increase of dielectric constant; it remains almost constant with changing temperature (3.2%). 4BrPS resulted to be the less "orientable" polymer maybe due to the heavy repetitive unit.

The polymer composites were prepared as described; polymer and CB aforesaid densities were taken into account for the composition calculus. Results of electrical resistivity depending on CB in wt% and fraction volume, v/v , for each composite are plotted in Figure 3. The corresponding values of the percolation threshold and the dielectric constant are listed in Table 2. A critical exponent of $\beta = 2$ (Figure 3) was obtained for resistivity as a function of the volumetric fraction, while the numerical fit of the percolation curves in terms of the wt% CB rendered a $\beta = 2.3$ value. These values indicate that percolation networks are interconnected giving a 3D-fractal structure, which is consistent with the used percolation model (1).

On the other hand, a decrease of the percolation threshold is an evidence that it is linked to the polymer polar nature. A decrease in the percolation threshold means the construction of conductive networks with low concentration of carbon particles due to their good disaggregation and distribution through the entire polymer matrix. The carbon black agglomeration renders an increase in the percolation threshold and a secondary effect as follows: at concentrations higher than

TABLE 2: Analysis of the percolation threshold related to the dielectric constant measured between 17°C and 5°C below the corresponding polymer T_g .

Polymer	Percolation threshold		Dielectric constant	
	v/v CB	wt% CB	(17°C, 850 MHz)	($T_g - 5^\circ\text{C}$, 850 MHz)
4MePS	0.058	9.4	2.43	2.64
PS	0.054	8.9	2.60	2.80
4ClPS	0.047	6.9	2.77	2.89
4BrPS	0.051	5.9	2.82	2.92

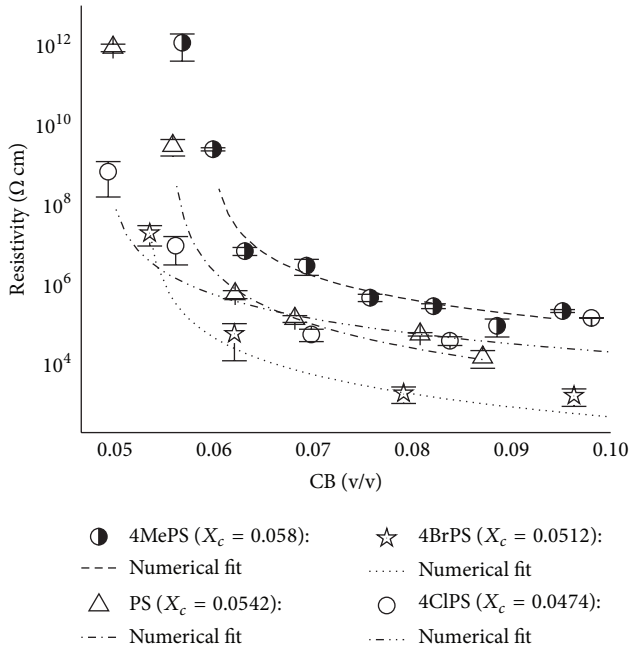


FIGURE 3: Electrical resistivity of composites as a function of carbon black volume fraction.

percolation threshold, it could be noticed that the changes in resistivity related to the CB concentration (Figure 3) also depend on the chemical nature of the polymer matrix.

As the carbon particles used for composite preparation were the same, it should be expected that the resistivity of each compound converges in the same limit value independent of the polymer matrix at CB concentrations higher than percolation threshold. However, the maximum resistivity reached has different value for each composite, as it is shown in Figure 3. For 4MePS, the maximum resistivity is in the order of $10^6 \Omega\text{-cm}$, whereas, for 4ClPS composites, it is barely $10^3 \Omega\text{-cm}$, which is a difference of 3 orders of magnitude. Above the percolation threshold, the conductive networks are interconnected among them. This interconnection could be modified if the CB disaggregation and dispersion are not homogeneous, producing agglomeration of the particles. A better distribution of the carbon black particles could allow a superior interconnection between the different chains of the same CB filler fraction in such a way that the composite reaches a lower electrical resistivity. The polymer matrix role is relevant because, for the same carbon black particle

composition, there is a great difference in the resistivity values, as shown in Figure 3. Therefore, the critical parameter values suggest the three-dimensional conductive chains in all the studied polymer matrixes due to the dipolar moment of the lateral groups on the backbone, in such a way that the presence of polar groups facilitates the CB dispersion, the building of electrical networks, and the faster achievement of the percolation threshold. These results match the qualitative observations made by [39], in which the polar side groups have an influence on the preferential construction of conductive networks.

The behavior of percolation threshold related to the polymer dielectric constant in weight percent and volume fraction is shown in Figure 4. The difference in dielectric constant at 17°C is very subtle between PS-4MePS and 4ClPS-4BrPS. However, we can appreciate that a real difference in the percolation threshold exists. A clear tendency in diminishing the percolation threshold as the dielectric constant of the polymer increases is shown in the wt% CB curves. However, when the CB volume fraction is calculated, the 4BrPS did not render the lowest percolation. Maybe the high density of this polymer makes CB particles get more volume than 4ClPS. Despite this unpredicted behavior, the tendency seems to be the same: both polymers with the highest dielectric constant also produce the formation of CB composites with less percolation concentration.

Those behaviors are the evidence that an asymmetric electronic density has an important effect on favoring the dispersion and distribution of the CB particles, having as a consequence a lower percolation threshold. An increase in the polymer dielectric constant results in a decrease of the percolation threshold. Curves of M_w , PD, and I versus percolation threshold do not show a similar behavior as the dielectric constant versus percolation threshold. In the extreme cases, for 4MePS, the percolation concentration, X_c , was calculated at 9.4 wt% CB (0.0584 v/v) and, for 4BrPS, it was 5.9 wt% CB (0.051 v/v CB). This is an important difference since, at molecular level, the chemical structure of both polymers is different only by the presence of a halogen atom or a methyl group into the 4-position of the aromatic ring. For each repetitive unit in 4MePS, the dipole moment is only 0.084 D, whereas, for 4BrPS, it is 1.45 D, the substantial difference which is reflected in the percolation threshold. At a macroscopic scale, the dielectric constant also increases by the presence of the halogen atom being only 2.42 for 4MePS and 2.82 for 4BrPS. The dielectric constant measured below T_g , at which no orientation order is achieved and being only the atomic polarization that contributes to this dielectric

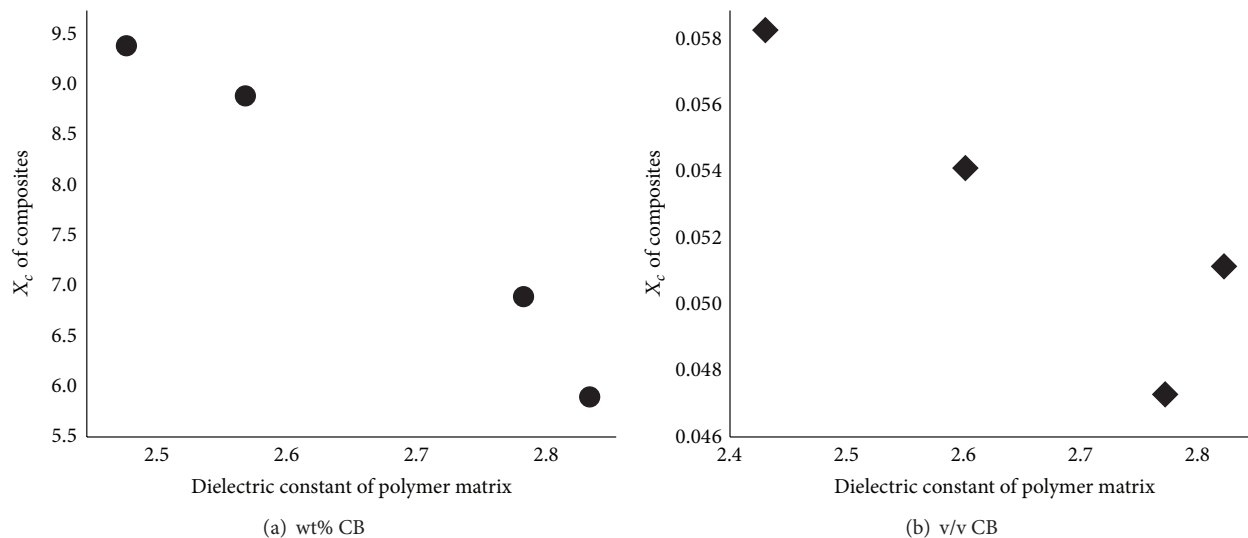


FIGURE 4: Dielectric constant versus percolation threshold in (a) wt% CB and (b) volume fraction CB.

constant, evidences the effect of the substituent atom nature on the aromatic ring.

For explaining such results, the fact that the presence of a dipole moment generated by the presence of electronegative atoms or acceptor functional groups on the polymer is important in order to achieve a good dispersion of the CB particles by creating a better interaction between the groups of the carbon particles and the polar moieties of the main polymer chain could be considered. Then, electrostatic interaction between total electronegative species and carbon black particles is very important while sonication procedure is carried out. Composites were obtained by dissolution method. In this stage, interactions between chains can be depreciated and the mobility is higher than that in the rubber state. Consequently, interaction among CB particles and the repetitive units produce a better disaggregation and distribution of carbon particles. In others words, an appropriate growth of the interconnection of the percolation paths by preferential distribution of the carbon particles in that type of polymers is possible. According to the numerical approximations of CB polymer composites based on PS, 4MePS, 4CIPS, and 4BrPS, high structure percolation chains are built. However, clear effects on percolation threshold are evident for the chemical modified polymer matrix. This is an evidence that there are electrostatic interactions between CB particles and the polar groups on the main polymer chain that promote a much better setting up of the conduction networks as the polarity (dielectric constant) of the polar matrix increases, having as a result a low electric percolation threshold.

4. Conclusions

According to the results, it was proved that a polymer with a dipole moment in the repetitive units has a determinant effect on the percolation threshold. It produces a decrease of the percolation threshold since an asymmetric electronic

density produces a disaggregation and preferential dispersion of the CB particles in order to achieve the network conductive paths with less CB particles. At a macroscopic level, the subtle differences of the dielectric constant at room temperature by the presence of atoms with different electronegativity on the aromatic ring encourage the hypothesis that an increase in the dielectric constant results in a decrease of the percolation threshold. This demonstrates the relevance of the electronic nature of both, polymer and conductive particles, if we want to control the percolation threshold. Electronic nature of polymer, evaluated as dielectric constant, offers the possibility to use this property in the new design of conductive polymer composites. Of course, there is an implication between the chemical nature of the polymer and other properties like the mechanical and thermal ones, which is important to take into account for a potential application.

Conflict of Interests

The authors declare that there is no conflict of interests regarding the publication of this paper.

Acknowledgment

The authors are grateful to the support provided by PRODEP-SEP 2015 “Red de Compuestos Poliméricos, Propiedades y Aplicaciones” Project.

References

- [1] F. El-Tantawy, K. Kamada, and H. Ohnabe, “In situ network structure, electrical and thermal properties of conductive epoxy resin-carbon black composites for electrical heater applications,” *Materials Letters*, vol. 56, no. 1-2, pp. 112–126, 2002.
- [2] M. F. Appel, W. E. Van der Veer, and T. Benter, “Conductive carbon filled polymeric electrodes: novel ion optical elements for time-of-flight mass spectrometers,” *Journal of the American Society for Mass Spectrometry*, vol. 13, no. 10, pp. 1170–1175, 2002.

- [3] J. W. Hu, S. G. Chen, M. Q. Zhang, M. W. Li, and M. Z. Rong, "Low carbon black filled polyurethane composite as candidate for wide spectrum gas-sensing element," *Materials Letters*, vol. 58, no. 27-28, pp. 3606-3609, 2004.
- [4] J. F. Feller and Y. Grohens, "Evolution of electrical properties of some conductive polymer composite textiles with organic solvent vapours diffusion," *Sensors and Actuators B: Chemical*, vol. 97, no. 2-3, pp. 231-242, 2004.
- [5] F. Hussain, M. Hojjati, M. Okamoto, and R. E. Gorga, "Polymer-matrix nanocomposites, processing, manufacturing, and application: an overview," *Journal of Composite Materials*, vol. 40, no. 17, pp. 1511-1575, 2006.
- [6] J.-C. Huang, "Carbon black filled conducting polymers and polymer blends," *Advances in Polymer Technology*, vol. 21, no. 4, pp. 299-313, 2002.
- [7] S. S. Azim, A. Satheesh, K. K. Ramu, S. Ramu, and G. Venkatachari, "Studies on graphite based conductive paint coatings," *Progress in Organic Coatings*, vol. 55, no. 1, pp. 1-4, 2006.
- [8] D. Stauffer and A. Aharony, *Introduction to Percolation Theory*, Taylor & Francis, New York, NY, USA, 2nd edition, 1994.
- [9] F. Carmona, "Conducting filled polymers," *Physica A: Statistical Mechanics and Its Applications*, vol. 157, no. 1, pp. 461-469, 1989.
- [10] L. Salomé, "Structure of percolating carbon black fractal aggregates dispersed in a polymer," *Journal de Physique II*, vol. 3, no. 11, pp. 1647-1656, 1993.
- [11] I. Webman, J. Jortner, and M. H. Cohen, "Critical exponents for percolation conductivity in resistor networks," *Physical Review B*, vol. 16, no. 6, pp. 2593-2596, 1977.
- [12] F. Lux, "Models proposed to explain the electrical conductivity of mixtures made of conductive and insulating materials," *Journal of Materials Science*, vol. 28, no. 2, pp. 285-301, 1993.
- [13] W. Thongruang, R. J. Spontak, and C. M. Balik, "Correlated electrical conductivity and mechanical property analysis of high-density polyethylene filled with graphite and carbon fiber," *Polymer*, vol. 43, no. 8, pp. 2279-2286, 2002.
- [14] W. P. Wang, C. Y. Pan, and J. S. Wu, "Electrical properties of expanded graphite/poly (styrene-co-acrylonitrile) composites," *Journal of Physics and Chemistry of Solids*, vol. 66, no. 10, pp. 1695-1700, 2005.
- [15] P. Tsotra and K. Friedrich, "Short carbon fiber reinforced epoxy resin/polyaniline blends: their electrical and mechanical properties," *Composites Science and Technology*, vol. 64, no. 15, pp. 2385-2391, 2004.
- [16] Y. Biryulin, D. Kurdybaylo, V. Shamanin et al., "Strongly non-linear carbon nanofibre influence on electrical properties of polymer composites," *Fullerenes Nanotubes and Carbon Nanostructures*, vol. 16, no. 5-6, pp. 629-633, 2008.
- [17] Z. Wang, M. Lu, H.-L. Li, and X.-Y. Guo, "SWNTs-polystyrene composites preparations and electrical properties research," *Materials Chemistry and Physics*, vol. 100, no. 1, pp. 77-81, 2006.
- [18] H. Deng, T. Skipa, R. Zhang et al., "Effect of melting and crystallization on the conductive network in conductive polymer composites," *Polymer*, vol. 50, no. 15, pp. 3747-3754, 2009.
- [19] D. Pantea, H. Darmstadt, S. Kaliaguine, and C. Roy, "Electrical conductivity of conductive carbon blacks: influence of surface chemistry and topology," *Applied Surface Science*, vol. 217, no. 1-4, pp. 181-193, 2003.
- [20] W. Thongruang, R. J. Spontak, and C. M. Balik, "Bridged double percolation in conductive polymer composites: an electrical conductivity, morphology and mechanical property study," *Polymer*, vol. 43, no. 13, pp. 3717-3725, 2002.
- [21] S. N. Lawandy, S. F. Halim, and N. A. Darwish, "Structure aggregation of carbon black in ethylene-propylene diene polymer," *Express Polymer Letters*, vol. 3, no. 3, pp. 152-158, 2009.
- [22] P. J. Mather and K. M. Thomas, "Carbon black/high density polyethylene conducting composite materials. Part I Structural modification of a carbon black by gasification in carbon dioxide and the effect on the electrical and mechanical properties of the composite," *Journal of Materials Science*, vol. 32, no. 2, pp. 401-407, 1997.
- [23] E. Petrach, I. Abu-Isa, and X. Wang, "Investigation of elastomer graphite composite material for proton exchange membrane fuel cell bipolar plate," *Journal of Fuel Cell Science and Technology*, vol. 6, no. 3, Article ID 031005, 2009.
- [24] W. K. Park, J. H. Kim, S.-S. Lee, J. Kim, G.-W. Lee, and M. Park, "Effect of carbon nanotube pre-treatment on dispersion and electrical properties of melt mixed multi-walled carbon nanotubes/poly(methyl methacrylate) composites," *Macromolecular Research*, vol. 13, no. 3, pp. 206-211, 2005.
- [25] A. Eitan, K. Jiang, D. Dukes, R. Andrews, and L. S. Schadler, "Surface modification of multiwalled carbon nanotubes: toward the tailoring of the interface in polymer composites," *Chemistry of Materials*, vol. 15, no. 16, pp. 3198-3201, 2003.
- [26] Y. Dror, W. Salalha, R. L. Khalfin, Y. Cohen, A. L. Yarin, and E. Zussman, "Carbon nanotubes embedded in oriented polymer nanofibers by electrospinning," *Langmuir*, vol. 19, no. 17, pp. 7012-7020, 2003.
- [27] Y. J. Kim, T. S. Shin, H. D. Choi, J. H. Kwon, Y.-C. Chung, and H. G. Yoon, "Electrical conductivity of chemically modified multiwalled carbon nanotube/epoxy composites," *Carbon*, vol. 43, no. 1, pp. 23-30, 2005.
- [28] Y. Lin, B. Zhou, K. A. S. Fernando, P. Liu, L. F. Allard, and Y.-P. Sun, "Polymeric carbon nanocomposites from carbon nanotubes functionalized with matrix polymer," *Macromolecules*, vol. 36, no. 19, pp. 7199-7204, 2003.
- [29] G. Zheng, J. Wu, W. Wang, and C. Pan, "Characterizations of expanded graphite/polymer composites prepared by in situ polymerization," *Carbon*, vol. 42, no. 14, pp. 2839-2847, 2004.
- [30] M. Sumita, H. Abe, H. Kayaki, and K. Miyasaka, "Effect of melt viscosity and surface tension of polymers on the percolation threshold of conductive-particle-filled polymeric composites," *Journal of Macromolecular Science B: Physics*, vol. B25, no. 1-2, pp. 171-184, 1986.
- [31] R. Socher, B. Krause, M. T. Müller, R. Boldt, and P. Pötschke, "The influence of matrix viscosity on MWCNT dispersion and electrical properties in different thermoplastic nanocomposites," *Polymer*, vol. 53, no. 2, pp. 495-504, 2012.
- [32] C. Zhang, C.-A. Ma, P. Wang, and M. Sumita, "Temperature dependence of electrical resistivity for carbon black filled ultrahigh molecular weight polyethylene composites prepared by hot compaction," *Carbon*, vol. 43, no. 12, pp. 2544-2553, 2005.
- [33] G. R. Kasaliwal, A. Gödel, P. Pötschke, and G. Heinrich, "Influences of polymer matrix melt viscosity and molecular weight on MWCNT agglomerate dispersion," *Polymer*, vol. 52, no. 4, pp. 1027-1036, 2011.
- [34] K. Miyasaka, K. Watanabe, E. Jojima, H. Aida, M. Sumita, and K. Ishikawa, "Electrical conductivity of carbon-polymer composites as a function of carbon content," *Journal of Materials Science*, vol. 17, no. 6, pp. 1610-1616, 1982.
- [35] S. G. Beaucage, S. Rane, D. W. Schaefer, G. Long, and D. Fischer, "Morphology of polyethylene-carbon black composites," *Journal of Polymer Science Part B: Polymer Physics*, vol. 37, no. 11, pp. 1105-1119, 1999.

- [36] Y.-J. Li, M. Xu, J.-Q. Feng, X.-L. Cao, Y.-F. Yu, and Z.-M. Dang, "Effect of the matrix crystallinity on the percolation threshold and dielectric behavior in percolative composites," *Journal of Applied Polymer Science*, vol. 106, no. 5, pp. 3359–3365, 2007.
- [37] S.-P. Rwei, F.-H. Ku, and K.-C. Cheng, "Dispersion of carbon black in a continuous phase: electrical, rheological, and morphological studies," *Colloid and Polymer Science*, vol. 280, no. 12, pp. 1110–1115, 2002.
- [38] Y. S. Kim, J. B. Wright, and J. C. Grunlan, "Influence of polymer modulus on the percolation threshold of latex-based composites," *Polymer*, vol. 49, no. 2, pp. 570–578, 2008.
- [39] S. H. Foulger, "Reduced percolation thresholds of immiscible conductive blends," *Journal of Polymer Science Part B: Polymer Physics*, vol. 37, no. 15, pp. 1899–1910, 1999.
- [40] K. Cheah, M. Forsyth, and G. P. Simon, "Processing and morphological development to carbon black filled conducting blends using a binary host of poly(styrene-co-acrylonitrile) and poly(styrene)," *Journal of Polymer Science Part B: Polymer Physics*, vol. 38, no. 23, pp. 3106–3119, 2000.
- [41] M. Q. Zhang, G. Yu, H. M. Zeng, H. B. Zhang, and Y. H. Hou, "Two-step percolation in polymer blends filled with carbon black," *Macromolecules*, vol. 31, no. 19, pp. 6724–6726, 1998.
- [42] P. J. Brigandi, J. M. Cogen, C. A. Wolf, J. R. Reffner, and R. A. Pearson, "Kinetic and thermodynamic control in conductive PP/PMMA/EAA carbon black composites," *Journal of Applied Polymer Science*, vol. 132, no. 25, pp. n/a–n/a, 2015.
- [43] J. F. Feller, "Conductive polymer composites: influence of extrusion conditions on positive temperature coefficient effect of poly(butylene terephthalate)/poly(olefin)—carbon black blends," *Journal of Applied Polymer Science*, vol. 91, no. 4, pp. 2151–2157, 2004.
- [44] Q. Yuan and D. Wu, "Low percolation threshold and high conductivity in carbon black filled polyethylene and polypropylene composites," *Journal of Applied Polymer Science*, vol. 115, no. 6, pp. 3527–3534, 2010.
- [45] J. F. Feller and É. Petitjean, "Conductive polymer composites (CPC): influence of processing conditions, shear rate and temperature on electrical properties of poly(butylene terephthalate)/poly(amide 12-b-tetramethyleneglycol)," *Macromolecular Symposium*, vol. 203, no. 1, pp. 309–316, 2003.
- [46] N. C. Das, T. K. Chaki, and D. Khastgir, "Effect of processing parameters, applied pressure and temperature on the electrical resistivity of rubber-based conductive composites," *Carbon*, vol. 40, no. 6, pp. 807–816, 2002.
- [47] M. Leboeuf, N. Ghamri, B. Brulé, T. Coupez, and B. Vergnes, "Influence of mixing conditions on rheological behavior and electrical conductivity of polyamides filled with carbon black," *Rheologica Acta*, vol. 47, no. 2, pp. 201–212, 2008.
- [48] O. S. Carneiro, J. A. Covas, R. Reis, B. Brulé, and J. J. Flat, "The effect of processing conditions on the characteristics of electrically conductive thermoplastic composites," *Journal of Thermoplastic Composite Materials*, vol. 25, no. 5, pp. 607–629, 2012.
- [49] J. M. Ibarrola, S. H. Lopez, E. V. Santiago, J. Alaniz-Perez, and M. I. Perez-Valverde, "Experimental study of the processing parameters of polymer conductive semicrystalline polymer composites with carbon black: optimizations and reproducibility," *Journal of Thermoplastic Composite Materials*, vol. 28, no. 4, pp. 574–590, 2015.
- [50] A. L. R. Bug, S. A. Safran, G. S. Grest, and I. Webman, "Do interactions raise or lower a percolation threshold?" *Physical Review Letters*, vol. 55, no. 18, pp. 1896–1899, 1985.
- [51] T. Prasse, L. Flandin, K. Schulte, and W. Bauhofer, "In situ observation of electric field induced agglomeration of carbon black in epoxy resin," *Applied Physics Letters*, vol. 72, no. 22, pp. 2903–2905, 1998.
- [52] M.-K. Schwarz, W. Bauhofer, and K. Schulte, "Alternating electric field induced agglomeration of carbon black filled resins," *Polymer*, vol. 43, no. 10, pp. 3079–3082, 2002.
- [53] X. Wu, C. Lu, X. Zhang, and Z. Zhou, "Conductive natural rubber/carbon black nanocomposites via cellulose nanowhisker templated assembly: tailored hierarchical structure leading to synergistic property enhancements," *Journal of Materials Chemistry A*, vol. 3, no. 25, pp. 13317–13323, 2015.
- [54] K. Cheah, G. P. Simon, and M. Forsyth, "Effects of polymer matrix and processing on the conductivity of polymer blend," *Polymer International*, vol. 50, no. 1, pp. 27–36, 2001.
- [55] R. Tchoudakov, O. Breuer, M. Narkis, and A. Siegmann, "Conductive polymer blends with low carbon black loading: polypropylene/polyamide," *Polymer Engineering and Science*, vol. 36, no. 10, pp. 1336–1346, 1996.
- [56] S. Hernández López, E. Viguera Santiago, J. Mercado Posadas, and V. Sánchez-Mendieta, "Electrical properties of acrylated-epoxidized soybean oil polymers-based composites," *Advances in Technology of Materials and Materials Processing Journal*, vol. 8, no. 2, pp. 214–219, 2006.
- [57] T. Blythe and D. Bloor, *Electrical Properties of Polymers*, Cambridge University Press, Cambridge, UK, 2nd edition, 2005.
- [58] G. Hougham, G. Tesoro, A. Viehbeck, and J. D. Chapple-Sokol, "Polarization effects of fluorine on the relative permittivity in polyimides," *Macromolecules*, vol. 27, no. 21, pp. 5964–5971, 1994.
- [59] Y. Wang, J. Wang, F. Wang, S. Li, and J. Xiao, "PVDF based all-organic composite with high dielectric constant," *Polymer Bulletin*, vol. 60, no. 5, pp. 647–655, 2008.
- [60] Y. C. Li, R. Kwok, Y. Li, and S. C. Tjong, "Frequency and temperature dependences of dielectric dispersion and electrical properties of polyvinylidene fluoride/expanded graphite composites," *Journal of Nanomaterials*, vol. 2010, Article ID 261748, 10 pages, 2010.
- [61] R. San Juan-Farfán, S. Hernández-López, G. Martínez-Barrera, M. A. Camacho-López, and E. Viguera-Santiago, "Electrical characterization of polystyrene-carbon black composites," *Physica Status Solidi C*, vol. 2, no. 10, pp. 3762–3765, 2005.
- [62] S. Hernández-López, E. Viguera-Santiago, M. Mayorga-Rojas, and D. Reyes-Contreras, "Thickness effect on electric resistivity on polystyrene and carbon black-based composites," *Journal of Physics: Conference Series*, vol. 167, Article ID 012059, 2009.
- [63] J. E. Mark, *Polymer Data Handbook*, Oxford University Press, New York, NY, USA, 2nd edition, 1989.
- [64] R. Corneliussen, S. A. Rice, and H. Yamakawa, "On the thermodynamic properties of solutions of polar polymers. A comparison of experiment and theory," *The Journal of Chemical Physics*, vol. 38, no. 7, pp. 1768–1778, 1963.
- [65] D. Slep, J. Asselta, M. H. Rafailovich et al., "Phase separation of polystyrene and bromo-polystyrene mixtures in equilibrium structures in thin films," *Langmuir*, vol. 14, no. 17, pp. 4860–4864, 1998.

Research Article

Conductive Polymeric Composites Based on Multiwalled Carbon Nanotubes and Linseed Oil Functionalized and Cross-Linked with Diacetylenes from Propargyl Alcohol

Alejandro Ramírez-Jiménez, Susana Hernández-López, and Enrique Viguera-Santiago

Laboratorio de Investigación y Desarrollo de Materiales Avanzados (LIDMA), Facultad de Química,
Universidad Autónoma del Estado de México, Paseo Colón Esquina con Paseo Tolloca, 50000 Toluca, MEX, Mexico

Correspondence should be addressed to Alejandro Ramírez-Jiménez; alejandro.ramirez@nucleares.unam.mx,
Susana Hernández-López; shernandezl@uaemex.mx, and Enrique Viguera-Santiago; enriqueviguera@uaemex.mx

Received 5 June 2015; Accepted 11 August 2015

Academic Editor: Dan Xia

Copyright © 2015 Alejandro Ramírez-Jiménez et al. This is an open access article distributed under the Creative Commons Attribution License, which permits unrestricted use, distribution, and reproduction in any medium, provided the original work is properly cited.

Diacetylene-functionalized epoxidized linseed oil (DAELO) matrix was synthesized in order to improve the dispersion of multiwalled carbon nanotubes (MWCNTs) without the necessity of some chemical or physical modification of them. That fact was evidenced by the low critical concentration of DAELO-based composites in comparison (1.0 wt% MWCNTs) with the epoxidized linseed oil- (ELO-) based composites (5 wt% MWCNTs). For this, both series of composites were prepared by the ultrasonic dispersion method using the same conditions of solvent, dilution, and sonication time. It was shown that, tailoring the polymer matrix with groups rich in nonpolar electric density, as diacetylene, and capable of interacting by van der Waals forces, it is possible to improve the dispersion of carbon nanotubes (CNTs) without necessity of some modification knowing that those treatments usually affect lowering their electrical properties.

1. Introduction

Carbon nanotubes (CNTs) have excellent electrical and mechanical properties [1, 2], which makes them ideal candidates for several applications, for example, as nanofiller material in conductive polymeric compounds [3]; CNTs are quite effective compared to carbon black microparticles, due to the large aspect ratio. Incorporation of CNTs into polymeric compounds gives rise to new opportunities for electronic applications, for example, in conductive films [4, 5], photovoltaic devices [6], or sensors [7–9]. Their advantages are that they may be flexible, easy to mold, and cheap; nonetheless they have the drawbacks of the polymers from fossil sources. In this context, polymers from natural sources, for example, from vegetable oils, represent a good alternative for the cost, environment, and chemical transformation, making them tailored structures [10–12]. As an example, linseed oil is a triglyceride consisting of three fatty acids condensed onto a glycerol unit; its composition is mainly of

linolenic acid (56.6%), linoleic acid (15.3%), and oleic acid (19.1%) moieties [13] (Figure 1), so it has on average 6.4 double bonds per triglyceride unit [14]; this feature makes it easy to modify by chemical conversion to other functional groups as epoxides. After the epoxidation, these groups could be used as cross-linker site or could be chemically modified in order to have a specific group in their structure [15, 16]. For an effective and reproducible utilization of CNTs in these composites, it is very important to have a good and homogeneous dispersion of the conductive particles throughout the polymer matrix. However, this is likely the main drawback owing to van der Waals forces between them along with their structure; they form clusters or tight long bundles and these might form a dense and entangled network; therefore in order to improve their dispersion, surface modifications have been made [17, 18]; one of them is the noncovalent attachment of molecules although their disadvantage is that the forces between the molecules and the CNTs might be weak; another one is the covalent attachment of functional groups to the walls of

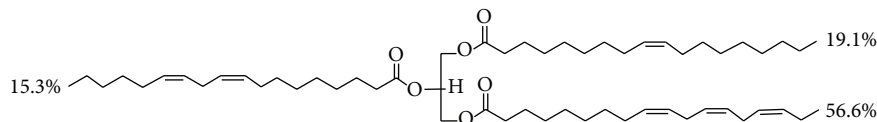


FIGURE 1: Chemical structure and main composition of linseed oil (LO).

CNTs; however this decreases the conductivity because the groups might introduce defects on the graphitic structure [19, 20]. Functionalization with divalent adducts represents an option which alters less the electrical transport owing to unaltered sp^2 conjugation [21]. Other options have been the dispersion by shear mixing, using surfactants [22], or by sonication in different solvents [23, 24]. In order to avoid any modification to the CNT and some loss of the electrical properties, we thought in synthesizing a matrix with functional groups rich in electrical density without dipole moment, as the diacetylenes, but that it may interact with the electrical density of the CNTs via van der Waals forces, assisting the dispersion.

The proposal was the functionalization of the epoxidized linseed oil with propargyl alcohol by a catalytic ring opening reaction in order to have terminal acetylenes groups (APELO), followed by an oxidative coupling reaction C–C to form diacetylene groups which also serve as cross-linkers of the oil. Finally, solutions of DAELO and MWCNTs at different loads were mixed using an ultrasonic bath, the percolation curve was built, and the critical concentration for diacetylene linseed oil was lower than ELO, demonstrating that rich electron groups have a positive effect on the dispersion of MWCNTs as compared with ELO.

2. Materials and Methods

Lipase acrylic resin from *Candida antarctica*, MWCNTs $D \times L$ 110–170 nm \times 5–9 μm , density 1.7–2.1 g/cm^3 , linseed oil (LO), hydrogen peroxide, alumina, anhydrous zinc chlorine, propargyl alcohol (PA), copper chlorine, and tetramethyl ethylene diamine (TMEDA) were obtained from Sigma Aldrich Co.; sodium carbonate and magnesium sulphate anhydrous were obtained from J. T. Baker, Mexico. All the reactants were used as received. SEM images were obtained in a JEOL JSM-6510LV microscope at acceleration voltage of 30 kV, at 5000, 10000, and 20000x, with backscattered electrons detector. ^1H NMR spectra were recorded at room temperature using CDCl_3 as solvent on a Bruker Avance 300 MHz NMR. Chemical shifts are relative to $(\text{CH}_3)_4\text{Si}$ and are given in ppm. FTIR-ATR spectra were recorded on an Avatar FTIR-ATR spectrophotometer, into a range between 550 and 4000 cm^{-1} and spectra were acquired at 4 cm^{-1} resolution and signals averaged over 32 scans. DSC and TGA analysis were recorded under nitrogen atmosphere (100 mL/min) using a SDT-Q600 TA Instruments modulus from 20 to 600 $^\circ\text{C}$ and heating rate of 20 $^\circ\text{C}/\text{min}$. Electrical resistance was measured on a digital multimeter ASYC II 5390.

ELO was synthesized using the chemoenzymatic method described in previous report [25]; a toluene solution, 100 g of LO, 8 g of oleic acid, and 10 g of lipase were put into a precipitate glass using 120 mL of solvent; the reaction mixture was warmed at 42 $^\circ\text{C}$ and mixed by stirring at 355 rpm; then 160 mL of hydrogen peroxide at 30% drop by drop was added. After 24 hours, the reaction was filtered to recover the enzyme. The product was purified by successive extractions of 3 \times 20 mL of Na_2CO_3 solution at 10% and 1 \times 20 mL of water; finally ELO was dried using MgSO_4 anhydrous. The product was characterized by FTIR-ATR, ^1H NMR, DSC, and TGA.

For synthesis of functionalized ELO with propargyl alcohol (PAELO), a mixture of 0.5 g of ELO, ZnCl_2 at different percentages (5–20%), and 0.5 mL of propargyl alcohol was heated at different temperatures (60–90 $^\circ\text{C}$) and times (3–20 h); a change of color was observed from white to amber or red. PA and ZnCl_2 were extracted with water; the product was filtered and solved in acetone; finally it was dried by a rotary evaporator and by a vacuum line. These conditions were carried out in order to found those that render the maximal functionalization without side reactions. Products were characterized by FTIR-ATR, ^1H NMR, DSC, and TGA.

In order to form the diacetylene groups, a coupling C–C of terminal acetylenes was carried out at room temperature by the Hay reaction [26, 27]. PAELO was dissolved in chloroform, while an aqueous solution of CuCl and TMEDA in stoichiometric ratio 1:1 was prepared; both solutions were placed together and mixed by magnetic stirring under an air flow. After 40 min the reaction was stopped and a solid was observed; the organic solvent was evaporated. The catalyst obtained *in situ* $\text{Cu}(\text{TMEDA})$ [28] was extracted with water many times as necessary until the characteristic blue color was not observed. The final product was a yellow solid which was dried and characterized by FTIR-ATR, DSC, TGA, and UV-Vis spectroscopy.

The diacetylene-polymer composites (DAELO-MWCNTs) were prepared in three steps: first a polymer solution of 10 mg/mL in chloroform was made and MWCNTs at concentrations between 0.1 and 1.2 mg/mL were dispersed in chloroform by an ultrasonic bath for 30 minutes at 35 MHz and 70 W. On the second step, equal volumes were mixed and sonicated for 30 minutes more; finally 1 mL of the final solution was placed inside stainless steel cylinders of 14 mm diameter mounted on glass plates. Once the solvent was evaporated slowly (casting technique), the films were placed in an oven at 70 $^\circ\text{C}$; once the samples were dried, two parallel lines of silver contacts on the surface were placed using conductive silver paint. In order to compare the effect of diacetylenes in the polymeric structure, ELO-polymer composites were made under the same conditions,

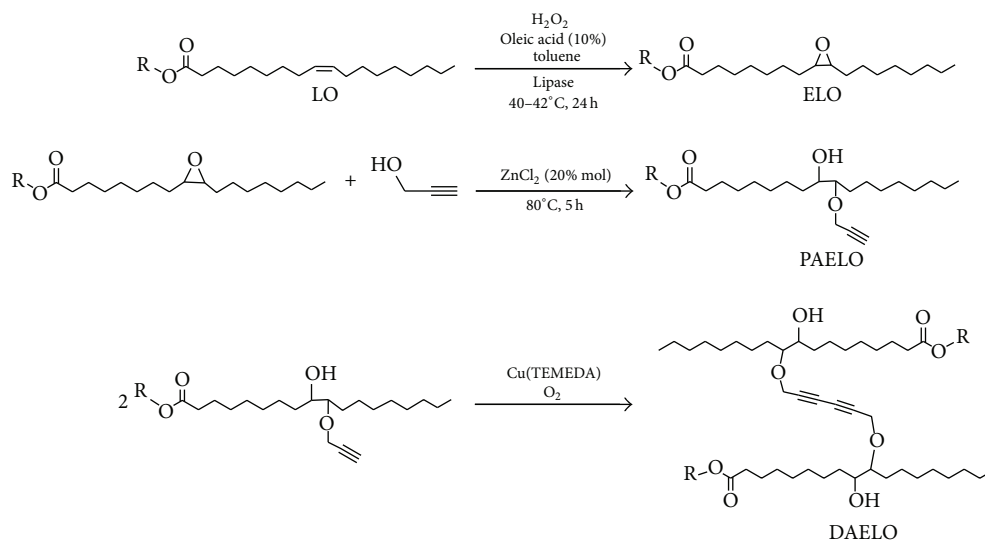


FIGURE 2: Simplified scheme for the synthesis of the polymeric matrix.

but because ELO is a liquid monomer, films of the mixture on glass substrates were cured at 220°C for 2 h.

For electrical characterization, I - V relationship was measured by the two-point technique with an electrometer Keithley 6717A. Samples with 1, 3, 4, 5, 8, 10, and 12% (W/W) of MWCNTs were measured; for this polymer's MWCNTs composites, an I - V lineal correlation was observed at potentials between 10 and 100 mV. The electrical resistance and the resistivity of the films were calculated and plotted against MWCNTs percentage (W/W). The thicknesses of the layers were measured using a profilometer Sloan Dektak IIA. Four samples were averaged for each point of the electrical resistance. The percolation theory was applied in order to calculate the percolation threshold, at the onset of the network; electrical resistivity obeys the power law relation:

$$\sigma = \sigma_m (\phi - \phi_c)^\beta, \quad (1)$$

where σ is the electrical resistivity of the polymeric compound, ϕ is the filler concentration, ϕ_c is the critical filler concentration or percolation threshold, and β and σ_m are fitting constant. The adjustment was made using Origin 6.0 software. Three free parameters σ_m , ϕ_c , and β were considered, where σ_m is the proportionality constant. Best fitting curves were obtained for β very close to -1.65 ; then β was fixed to this value and numerical interactions were run again until reaching 0.99 of data correlation.

3. Results and Discussion

ELO was synthesized by a chemoenzymatic reaction (Figure 2). The epoxy rings formation was confirmed by FTIR-ATR, ^1H NMR, and DCS. By FTIR-ATR, the band at 821 cm^{-1} corresponding to the $\nu(\text{C}-\text{O})$ from epoxy groups was observed (Figure 3(b)), whereas those corresponding to the double bonds at 1650 and 3008 do not (Figure 3(a)). The ^1H NMR spectrum also showed the signals from epoxy

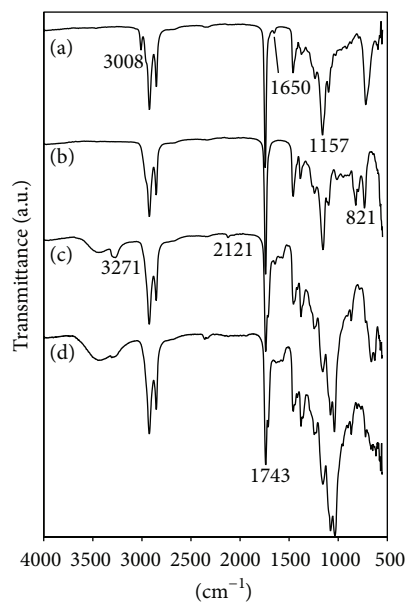


FIGURE 3: FTIR-ATR spectra of (a) LO, (b) ELO, (c) APELO, and (d) DAELO.

rings between 2.90 and 3.21 ppm, integrating 11.5 hydrogens (Figure 4(b)); these signals allowed calculating the epoxy groups percentage; it was 96% with respect to the signals from the double bonds between 5.23 and 5.42 ppm in the ^1H NMR spectrum of LO integrating 12 hydrogens (Figure 4(a)). The signal of hydrogens from double bonds in the ELO spectrum integrates only 0.56. Molecular weight of LO and ELO was calculated by integration of their respective spectra; for the first one it was 879 g/mol and for the second one it was 970 g/mol. In DSC an exothermic peak between 205 and 275°C was observed which corresponds to the ring opening of epoxy groups (Figure 5(a)) [29].

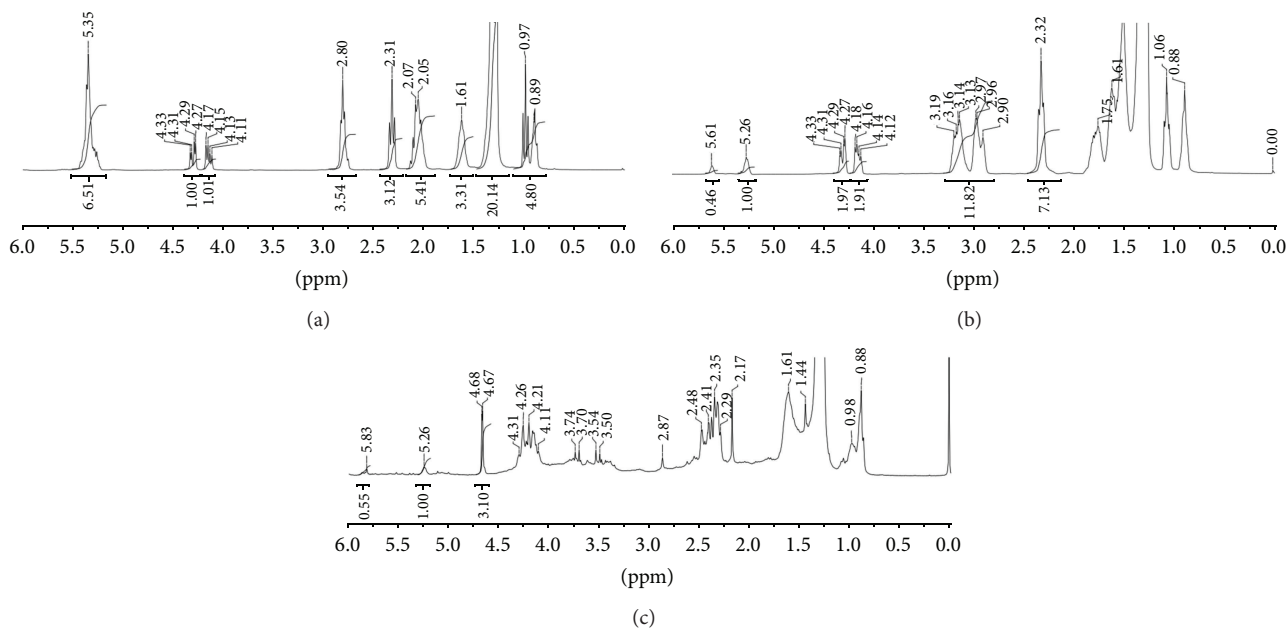


FIGURE 4: ^1H NMR 300 MHz, CDCl_3 of (a) LO, (b) ELO, and (c) APELO.

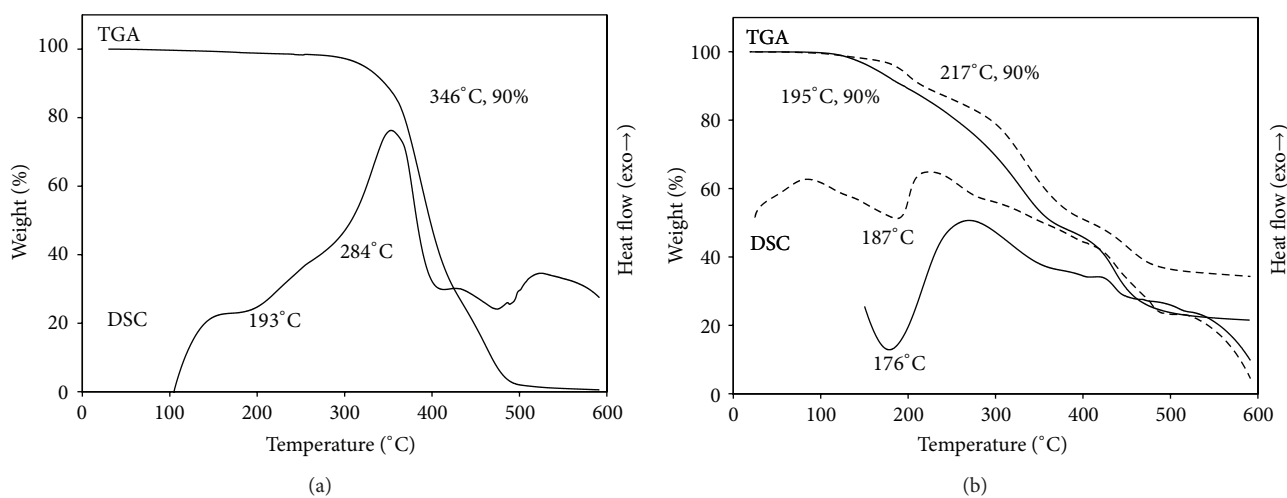


FIGURE 5: DSC and TGA runs of (a) ELO and (b) APELO (solid lines) and DAELO (dashed lines). Heating rate of $20^\circ\text{C}/\text{min}$ under nitrogen atmosphere.

ELO was functionalized with PA by an epoxy ring opening reaction catalyzed by ZnCl_2 ; PA was used as reactant and solvent in order to obtain better results. The higher percent of functionalization (27%) was obtained when the reaction was carried out at 80°C , 20 h, and 20 mol percent of catalyst. The products were characterized by FTIR-ATR and ^1H NMR. In the FTIR-ATR spectra the bands of $\nu(\text{C}\equiv\text{C}-\text{H})$ at 3271 cm^{-1} and $\nu(\text{C}\equiv\text{C})$ at 2121 cm^{-1} were observed as well as the characteristic band centered around 3450 cm^{-1} from hydroxyl groups (Figure 3(c)); the band from epoxy groups was not observed. On the other hand, in the ^1H NMR spectrum of APELO, the signal of methylene from PA appeared as a doublet at 4.68 ppm; $J = 3\text{ Hz}$ (Figure 4(c)); the integration

allowed calculating the percent of functionalization with respect to the epoxy groups; for the highest functionalization (28%) the integral had a value of 3.20, corresponding to 1.6 acetylene groups. When the reaction was carried out for only 5 h, the functionalization was of 26%; therefore, these conditions were used for the APELO synthesis. Results for other conditions are shown in Table 1. Low values should be due to hydroxyl group formation which attack epoxy rings to form ethers. This is evidenced by IR (Figure 3), where the band of $\nu(\text{C}-\text{O})$ at 1037 cm^{-1} is more intense than in ELO and LO spectra.

Cross-linking of acetylenes of PAELO was carried out by the Hay reaction. The product obtained (DAELO) was

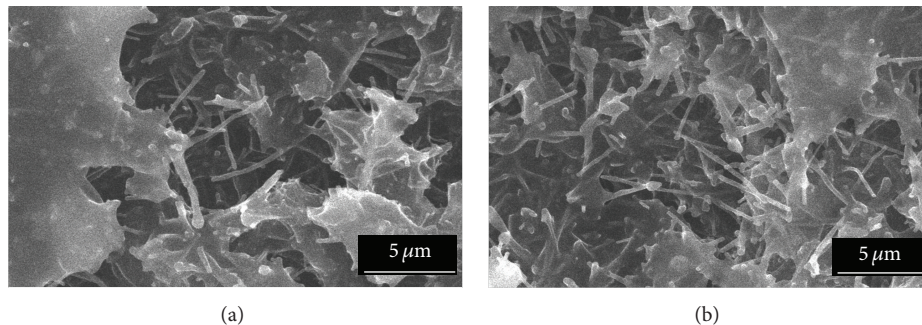


FIGURE 6: SEM micrographs of polymeric composites with (a) 5% and (b) 10% of MWCNTs, 30 kV, and 5000x.

TABLE 1: Results of the functionalization of ELO with PA at different conditions.

Catalyst (%)	Reaction time	Temperature (°C)	Functionalization (%)
10	5	80	8
20	3	80	19
20	5	80	26
20	20	80	27
20	5	70	22
20	8	70	20
30	5	70	20

a yellow solid which was characterized by FTIR-ATR, DSC, and TGA. In FTIR, the band of $\nu(\text{C}\equiv\text{C}-\text{H})$ at 3270 cm^{-1} diminished with respect to PAELO which confirm the C-C coupling (Figure 3(d)). This coupling improves thermal stability as shown by TGA (Figure 5(b)). The T_{10} for DAELO was 216°C , whereas for PAELO it was 154°C . In DSC an exothermic peak starts at 176 and 187°C for PAELO and DAELO, respectively, owing to their corresponding decomposition.

Once the resin is obtained, the polymeric compounds were prepared according to the experimental section. Chloroform was chosen as solvent due to the fact that it has been used at high MWCNTs concentrations [30]. Interestingly, only one hour of ultrasound was enough to disperse the MWCNTs inasmuch as longer times might cause fractures on CNTs [24]. Dispersion was confirmed by images from SEM (Figure 6) for samples with 5 and 10% at 5000x.

The electrical resistance of DAELO-MWCNTs compounds was measured for samples with 1, 3, 4, 5, 8, 10, and 12% (W/W) of MWCNTs at potentials between 10 and 100 mV; in all cases a lineal relation was obtained, indicating an adequate electric contact between the network of MWCNTs and a very good distribution of them in the matrix. It is also noted that a good tendency of resistivity is obtained in the limits of the percolation theory; this is difficult to reach for other particles if the synthesis conditions are not optimized. Resistivity values are shown in Figure 7; these

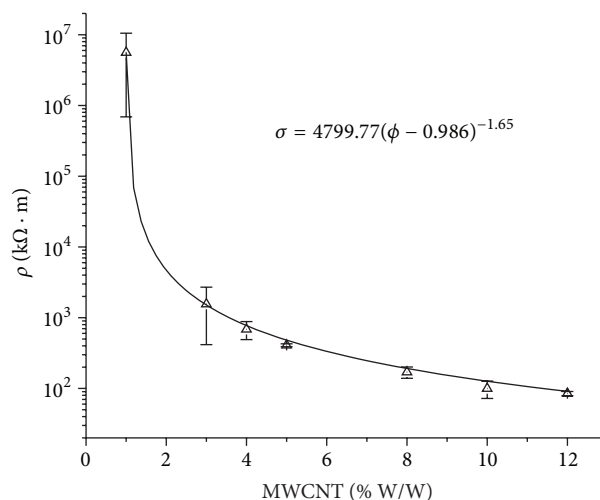


FIGURE 7: Resistivity as a function of MWCNTs percentage (W/W), mean value \pm SD ($n = 4$), and their adjusted curve.

were adjusted by percolation threshold equation finding the critical concentration at 0.99% (W/W) which is similar to other polymer MWCNTs compounds; for example, the percolation threshold for polystyrene-single walled carbon nanotubes composites was at 1.5% (W/W) [31], whereas for polyvinylidene fluoride MWCNTs it was at 0.95% [32]. Although the density of DAELO was slightly lower than ELO, the volumetric fraction of MWCNTs was similar in both compounds. In comparison, the measured compositions of ELO-composites always had a higher value of resistivity and a higher error, indicating a major problem of dispersion of CNTs in that molecule; even if it is true, the resistivity of ELO without CNTs is higher than DAELO; results are given in Table 2. This result could be explained in terms of π interactions between the electrical density of diacetylenes groups (1 per molecule in average) and electrical density of MWCNTs allowing a better dispersion [33]. By tailoring the polymer matrix, it is possible to improve the interactions between the electronic density of the functional groups in the polymers and the CNTs reaching a low critical concentration in the electrical conductive composites.

TABLE 2: Comparison of resistivity of composites at different percentage of MWCNTs.

MWCNTs (W/W)	ρ (k Ω -m)	
	DAELO-MWCNTs	ELO-MWCNTs
0	7.1×10^7	1.7×10^9
1	$9.08 \times 10^6 \pm 4.9 \times 10^6$	—
3	1559 ± 1143	—
4	686 ± 196	—
5	408 ± 19	4697 ± 1642
8	170 ± 31	5711 ± 3658
10	99.7 ± 27.5	3160 ± 944
12	81.6 ± 5.7	3101 ± 1392

Densities of ELO, DAELO, and MWCNTs were 0.99, 0.89, and 1.9 g/cm³, respectively.

4. Conclusions

In this work, the functionalization of ELO with PA was only 27%; however it was possible to make a resin by oxidative coupling of the terminal alkynes; this resin was used as matrix for the polymer MWCNTs composites formation where the introduction of a few diacetylenes groups allows the dispersion of MWCNTs with a short time of sonication. The percolation threshold was at low concentration of conductive particles; these decreased the electrical resistivity in five orders of magnitude from 1% to 10% in weight of MWCNTs. Because the combination of CNTs and polymers with π electrons had been of interest for electronic devices, we think that these composites may have potential application, for example, in vapor sensors.

Conflict of Interests

The authors declare that there is no conflict of interests regarding the publication of this paper.

Acknowledgments

The authors are grateful to the Universidad Autónoma del Estado de México for the support under Project 3540/2013 CHT and to the CONACyT for the fellowship for the post-doctoral stance of Ph.D. Alejandro Ramírez-Jiménez. The authors thank M. C. Maria de las Nieves Zavala Segovia, Ph.D. Gustavo López-Tellez from CCIQS UAEM-UNAM, and M. S. Alejandro Esparza from CECADET-UNAM for their technical support with NMR, SEM analysis, and thickness measurements, respectively.

References

- [1] P. G. Collins, A. Zettl, H. Bando, A. Thess, and R. E. Smalley, "Nanotube nanodevice," *Science*, vol. 278, no. 5335, pp. 100–103, 1997.
- [2] E. T. Thostenson, Z. Ren, and T.-W. Chou, "Advances in the science and technology of carbon nanotubes and their composites: a review," *Composites Science and Technology*, vol. 61, no. 13, pp. 1899–1912, 2001.
- [3] R. H. Baughman, A. A. Zakhidov, and W. A. de Heer, "Carbon nanotubes the route toward applications," *Science*, vol. 297, no. 5582, pp. 787–792, 2002.
- [4] T. Sekitani, H. Nakajima, H. Maeda et al., "Stretchable active-matrix organic light-emitting diode display using printable elastic conductors," *Nature Materials*, vol. 8, no. 6, pp. 494–499, 2009.
- [5] L. Hu, M. Pasta, F. La Mantia et al., "Stretchable, porous, and conductive energy textiles," *Nano Letters*, vol. 10, no. 2, pp. 708–714, 2010.
- [6] H. Ago, K. Petritsch, M. S. P. Shaffer, A. H. Windle, and R. H. Friend, "Composites of carbon nanotubes and conjugated polymers for photovoltaic devices," *Advanced Materials*, vol. 11, no. 15, pp. 1281–1285, 1999.
- [7] A. Merkoçi, M. Pumera, X. Llopis, B. Pérez, M. Del Valle, and S. Alegret, "New materials for electrochemical sensing VI: carbon nanotubes," *Trends in Analytical Chemistry*, vol. 24, no. 9, pp. 826–838, 2005.
- [8] W. Obityayo and T. Liu, "A review: carbon nanotube-based piezoresistive strain sensors," *Journal of Sensors*, vol. 2012, Article ID 652438, 15 pages, 2012.
- [9] N. Sinha, J. Ma, and J. T. W. Yeow, "Carbon nanotube-based sensors," *Journal of Nanoscience and Nanotechnology*, vol. 6, no. 3, pp. 573–590, 2006.
- [10] U. Biermann, U. Bornscheuer, M. A. R. Meier, J. O. Metzger, and H. J. Schäfer, "Oils and fats as renewable raw materials in chemistry," *Angewandte Chemie*, vol. 50, no. 17, pp. 3854–3871, 2011.
- [11] M. A. Mosiewicki and M. I. Aranguren, "A short review on novel biocomposites based on plant oil precursors," *European Polymer Journal*, vol. 49, no. 6, pp. 1243–1256, 2013.
- [12] G. Lligadas, J. C. Ronda, M. Galià, and V. Cádiz, "Renewable polymeric materials from vegetable oils: a perspective," *Materials Today*, vol. 16, no. 9, pp. 337–343, 2013.
- [13] L. Montero de Espinosa and M. A. R. Meier, "Plant oils: the perfect renewable resource for polymer science?!" *European Polymer Journal*, vol. 47, no. 5, pp. 837–852, 2011.
- [14] Y. Xia, R. L. Quirino, and R. C. Larock, "Bio-based thermosetting polymers from vegetable oils," *Journal of Renewable Materials*, vol. 1, no. 1, pp. 3–27, 2013.
- [15] A. Köckritz and A. Martin, "Oxidation of unsaturated fatty acid derivatives and vegetable oils," *European Journal of Lipid Science and Technology*, vol. 110, no. 9, pp. 812–824, 2008.
- [16] R. Andrews and M. C. Weisenberger, "Carbon nanotube polymer composites," *Current Opinion in Solid State & Materials Science*, vol. 8, no. 1, pp. 31–37, 2004.
- [17] A. Eitan, K. Jiang, D. Dukes, R. Andrews, and L. S. Schadler, "Surface modification of multiwalled carbon nanotubes: toward the tailoring of the interface in polymer composites," *Chemistry of Materials*, vol. 15, no. 16, pp. 3198–3201, 2003.
- [18] N. Roy, R. Sengupta, and A. K. Bhowmick, "Modifications of carbon for polymer composites and nanocomposites," *Progress in Polymer Science*, vol. 37, no. 6, pp. 781–819, 2012.
- [19] J. E. Moreno-Marcelino, E. Viguera-Santiago, G. López-Téllez, and S. Hernández-López, "Chemical functionalization of carbon nanotubes and its effects on electrical conductivity," *Journal of Nano Research*, vol. 28, pp. 51–61, 2014.
- [20] A. López-Bezanilla, F. Triozon, S. Latil, X. Blase, and S. Roche, "Effect of the chemical functionalization on charge transport in

- carbon nanotubes at the mesoscopic scale,” *Nano Letters*, vol. 9, no. 3, pp. 940–944, 2009.
- [21] D. Bouilly, J. Cabana, and R. Martel, “Unaltered electrical conductance in single-walled carbon nanotubes functionalized with divalent adducts,” *Applied Physics Letters*, vol. 101, no. 5, Article ID 053116, 2012.
- [22] J. Yu, N. Grossiord, C. E. Koning, and J. Loos, “Controlling the dispersion of multi-wall carbon nanotubes in aqueous surfactant solution,” *Carbon*, vol. 45, no. 3, pp. 618–623, 2007.
- [23] K. D. Ausman, R. Piner, O. Lourie, R. S. Ruoff, and M. Korobov, “Organic solvent dispersions of single-walled carbon nanotubes: toward solutions of pristine nanotubes,” *Journal of Physical Chemistry B*, vol. 104, no. 38, pp. 8911–8915, 2000.
- [24] Y. Y. Huang and E. M. Terentjev, “Dispersion of carbon nanotubes: mixing, sonication, stabilization, and composite properties,” *Polymers*, vol. 4, no. 1, pp. 275–295, 2012.
- [25] G. López-Tellez, E. Viguera-Santiago, and S. Hernández-López, “Characterization of linseed oil epoxidized at different percentages,” *Superficies y Vacío*, vol. 22, no. 1, pp. 5–10, 2009.
- [26] A. S. Hay, “Oxidative coupling of acetylenes. II¹,” *The Journal of Organic Chemistry*, vol. 27, no. 9, pp. 3320–3321, 1962.
- [27] B. Maaten, J. Moussa, C. Desmaretz et al., “Cu-modified hydroxy-apatite as catalyst for Glasser-Hay C-C homo-coupling reaction of terminal alkynes,” *Journal of Molecular Catalyst A: Chemical*, vol. 393, pp. 112–116, 2014.
- [28] P. Lahtinen, E. Lankinen, M. Leskelä, and T. Repo, “Insight into copper oxidation catalysts: kinetics, catalytic active species and their deactivation,” *Applied Catalysis A: General*, vol. 295, no. 2, pp. 177–184, 2005.
- [29] G. López Téllez, E. Viguera-Santiago, S. Hernández-López, and B. Bilyeu, “Synthesis and thermal cross-linking study of partially-aminated epoxidized linseed oil,” *Designed Monomers and Polymers*, vol. 11, no. 5, pp. 435–445, 2008.
- [30] C.-X. Liu and J.-W. Choi, “Improved dispersion of carbon nanotubes in polymers at high concentrations,” *Nanomaterials*, vol. 2, no. 4, pp. 329–347, 2012.
- [31] V. Antonucci, G. Faiella, M. Giordano, L. Nicolais, and G. Pepe, “Electrical properties of single walled carbon nanotube reinforced polystyrene composites,” *Macromolecular Symposia*, vol. 247, pp. 172–181, 2007.
- [32] R. Rizvi and H. E. Naguib, “Carbon nanotube network evolution during deformation of PVDF-MWNT nanocomposites,” in *Electroactive Polymer Actuators and Devices*, vol. 8687 of *Proceedings of SPIE*, International Society for Optics and Photonics, San Diego, Calif, USA, March 2013.
- [33] X. Dai, Z. Liu, B. Han et al., “Carbon nanotube/poly(2,4-hexadiyne-1,6-diol) nanocomposites prepared with the aid of supercritical CO₂,” *Chemical Communications*, vol. 10, no. 19, pp. 2190–2191, 2004.

Research Article

Tuning Electronic Structures of BN and C Double-Wall Hetero-Nanotubes

Xueran Liu, Meijun Han, Xinjiang Zhang, Haijun Hou, Shaoping Pang, and Qisheng Wu

School of Materials Engineering, Yancheng Institute of Technology, Yancheng, Jiangsu 224051, China

Correspondence should be addressed to Shaoping Pang; psp800@126.com and Qisheng Wu; qishengwu@ycit.cn

Received 8 April 2015; Revised 15 June 2015; Accepted 2 July 2015

Academic Editor: Dan Xia

Copyright © 2015 Xueran Liu et al. This is an open access article distributed under the Creative Commons Attribution License, which permits unrestricted use, distribution, and reproduction in any medium, provided the original work is properly cited.

First principle calculations based on density functional theory with the generalized gradient approximation were carried out to investigate the energetic and electronic properties of carbon and boron nitride double-wall hetero-nanotubes (C/BN-DWHNTs) with different chirality and size, including an armchair (n, n) carbon nanotube (CNT) enclosed in (m, m) boron nitride nanotube (BNNT) and a zigzag ($n, 0$) CNT enclosed in ($m, 0$) BNNT. The electronic structure of these DWHNTs under a transverse electric field was also investigated. The ability to tune the band gap with changing the intertube distance (d_i) and imposing an external electric field (F) of zigzag DWHNTs provides the possibility for future electronic and electrooptic nanodevice applications.

1. Introduction

Carbon nanotubes (CNTs) play a very important role in nanodevice applications due to their novel properties. By comparison with CNTs, boron nitride nanotubes (BNNTs) are formed with similar structures, however, of very distinctive properties [1]. Of similar crystalline structure, hexagonal boron nitride (h-BN) has been considered as a potential substrate material for graphene [1, 2]. Recently, the structures of bilayer and trilayer graphene/h-BN have been reported with tunable band gaps for electronic device applications [3–5].

Hexagonal boron nitride shares similar crystalline structure with graphene, and it is slightly lattice-mismatched from graphene by about 1.5%, which implies that it is possible to form hetero-nanostructures. BNNTs' growth on CNT has successfully been applied to nanowires [6]. Several studies have also been conducted on BN-coated CNTs [7, 8]. The BNNT around the CNTs effectively helps to protect them and makes them more stable; for example, oxidation degradation of CNTs is reduced by coating with BNNTs, and the thermal stability of CNT@BNNTs is far superior to CNTs [9].

An efficient way to modify the band gap of nanotubes is to apply an external electric field F [10]. The response of the nanotube to F is of interest for studying its future application, such as that in logic gates, static memory cells, and sensor

devices [11–13]. Ab initio calculation showed that band gaps of both CNTs and BNNTs can be greatly reduced by a transverse electric field [14, 15]. An intriguing question to answer is whether external electric fields can also be an efficient way to modulate the electronic properties of C/BN-DWHNTs.

However, a first-principles study on the stability as well as the electronic properties modulated with d_i and F of C/BN-DWHNTs is not available. To fill the deficiency, in this work, we performed a series of first-principles calculations to study the coaxial CNT@BNNT and to examine the electric field shielding effect of BNNT on the inside CNT. We calculated the band structures of coaxial CNT@BNNT consisting of armchair and zigzag CNT cores and BNNT sheaths, focusing on the band structure variations with d_i and F . The relative insensitivity of armchair CNT@BNNT to F , at least for the few cases considered here, suggests that zigzag CNT@BNNT would be a suitable candidate for double-wall hetero-nanotubes devices.

2. Calculation Methods

The geometric structure optimization and calculation of the related electrical properties of the CNT@BNNT with no F were conducted using SIESTA [16, 17] and adopted norm-conserving nonlocal pseudopotentials for the atomic core.

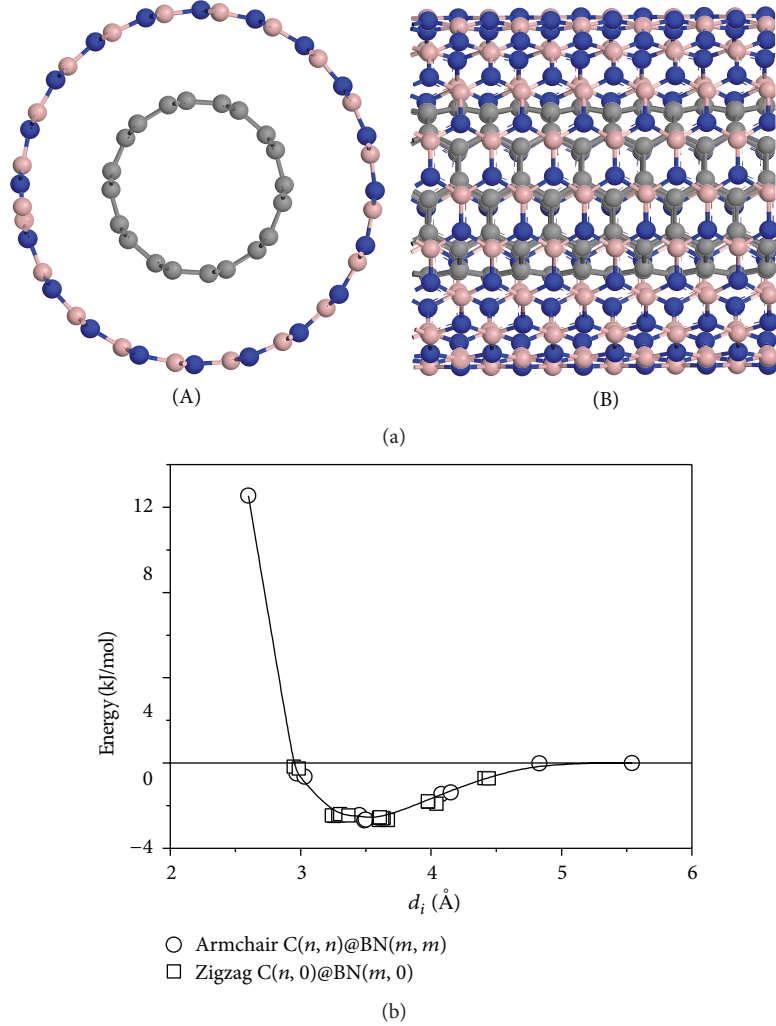


FIGURE 1: Structure of the optimized CNT(5,5)@BNNT(10,10): (a) top view (A) and side view (B). (b) The formation energy E_f variation versus intertube distance d_i . ○ and □ are the formation energy of calculated armchair and zigzag DWHNTs, respectively. The solid line was plotted in eyes.

The Perdew, Burke, and Ernzerhof (PBE) form generalized gradient approximation (GGA) corrections were employed for the exchange-correlation potential energy [18]. The atomic orbital basis set employed throughout was double- ζ plus polarization functions (DZP). Periodic boundary condition along the axis was employed for nanotubes. Brillouin zones were sampled by a set of k -points grid ($1 \times 1 \times 8$) according to the Monkhorst-Pack approximation [19].

When electric field was imposed, the calculation was using density functional theory available in DMol3 code [20, 21]. The PBE function [22] of GGA was used to calculate the exchange-correlation potential energy, the all electron approach was used, and the orbit population parameter smearing was set at 0.0005 a.u.

Our models were constructed within a tetragonal super cell with lattice constants of a and b equaling 40 Å to avoid the interaction between two adjacent nanotubes and c , the lattice constant in z direction along the tube axis, equaling one-dimensional (1D) lattice parameter of the nanotubes.

The tube was taken along the z direction and the circular cross section was lying in the (x, y) plane. Both the CNT and BNNTs structures were fully optimized until the force on each atom was less than $0.005 \text{ eV \AA}^{-1}$ during relaxation.

The van der Waals interactions are very important in two-dimensional materials [23], especially in layered structures. The van der Waals force has obvious effect on the adsorption energy and adsorption position and height [24–26]. In this paper, the distances of the CNT and BNNT are fixed, and the optimization does not change the C/BN-DWHNTs structures. The van der Waals interactions could increase the value of E_f , but they should not affect the electronic properties of C/BN-DWHNTs [10].

3. Results and Discussion

Two types of C/BN-DWHNTs were investigated, zigzag and armchair. The zigzag C/BN-DWHNTs are studies that include CNT($n, 0$)@BNNT($m, 0$) ($n = 6-10$, $m = 14-20$).

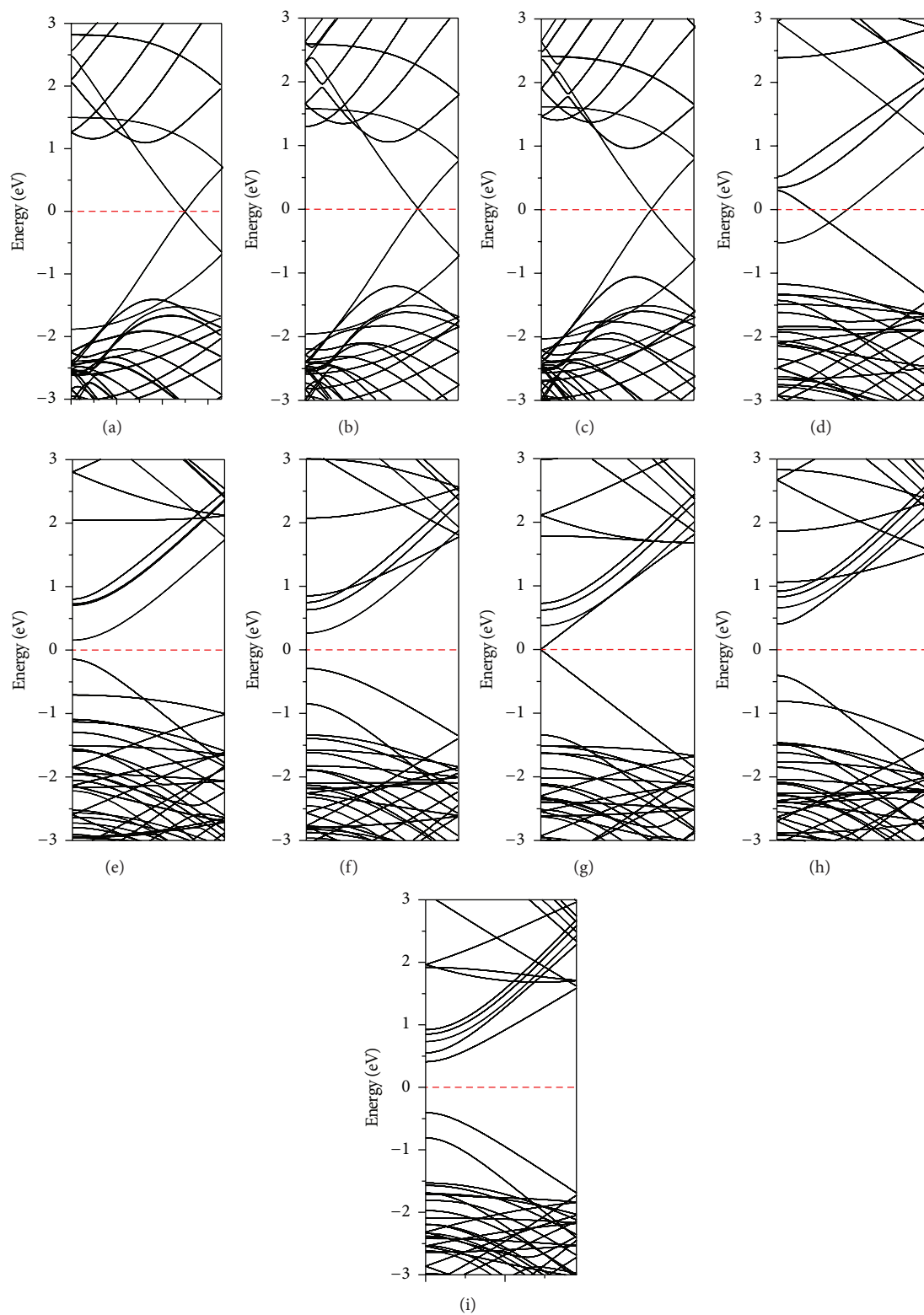


FIGURE 2: Band structures of (a) armchair CNT(5, 5)@BNNT(10, 10), (b) armchair CNT(6, 6)@BNNT(11, 11), (c) armchair CNT(7, 7)@BNNT(12, 12), (d) zigzag CNT(6, 0)@BNNT(15, 0), (e) zigzag CNT(7, 0)@BNNT(16, 0), (f) zigzag CNT(8, 0)@BNNT(17, 0), (g) zigzag CNT(9, 0)@BNNT(18, 0), (h) zigzag CNT(10, 0)@BNNT(19, 0), and (i) zigzag CNT(11, 0)@BNNT(20, 0).

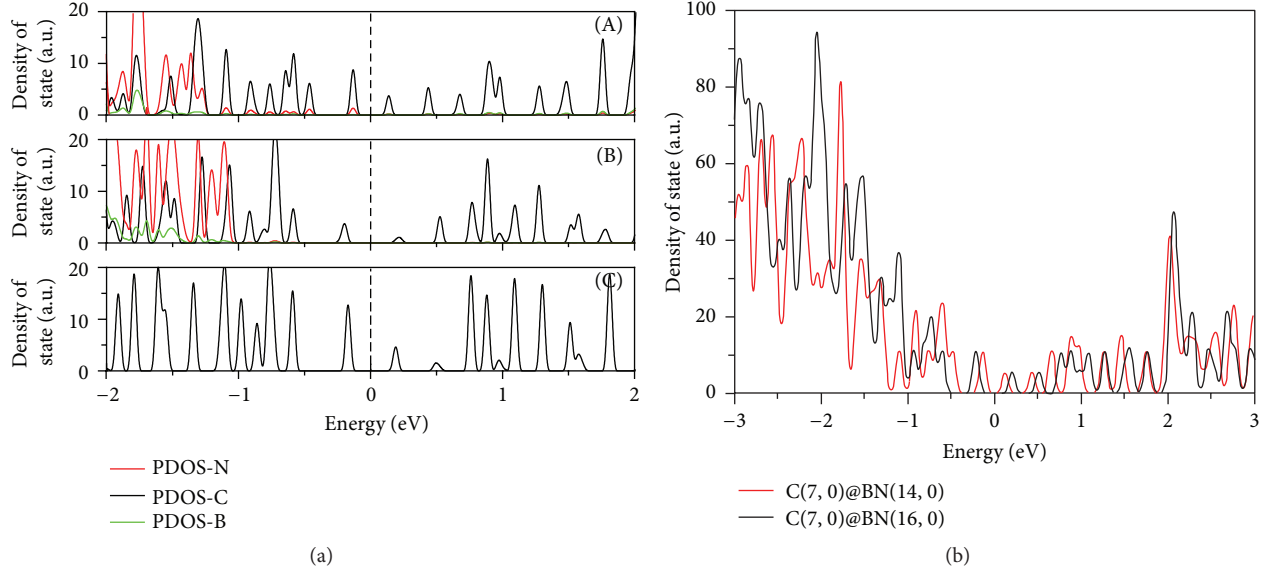


FIGURE 3: (a) (A) Partial density of state of zigzag CNT(7, 0)@BNNT(14, 0), (B) partial density of state of zigzag CNT(7, 0)@BNNT(16, 0), and (C) density of state of single-wall CNT (7, 0). The Fermi level lies at 0 eV (dash line). (b) Density of state of CNT(7, 0)@BNNT(14, 0) and CNT(7, 0)@BNNT(16, 0) DWHNTs.

The armchair C/BN-DWHNTs considered are CNT(n , n)@BNNT(m , m) ($n = 5-7$, $m = 8-13$). Figure 1(a) gives an illustration of the coaxial armchair CNT(5, 5) inside armchair BNNT(10, 10), the left (right) panel for the top (lateral) view of the initial structure.

The calculated covalent bond lengths of the various C/BN-DWHNTs in the fully optimized structures are listed in Table 1. For any C/BN-DWHNTs, we define the binding energy per atom as $E_b = [E_t^@ - xE^C - y(E^B + E^N)]/(x + y)$, where E^C , E^B , and E^N are the energy of isolated carbon, boron, and nitride atoms, respectively. $E_t^@$ is the total energy of a C/BN-DWHNT, x is the number of C atoms, and y is the number of B and N atoms. The formation energy E_f ($E_f = E_b^@ - E_b^C - E_b^{BN}$) of each C/BN-DWHNT is also calculated, in which the E_b^C and E_b^{BN} are the binding energy of free standing CNT and BNNT, respectively.

The stability of C/BN-DWHNTs is determined by the interaction force between the inner and outer nanotubes, as shown in Table 1. The formation energy E_f varying with d_i was plotted in Figure 1(b). When $d_i = \sim 2.60$ Å, E_f is positive, which means the free standing CNT and BNNT are favorite in energy. When $d_i = \sim 3.5$ Å, the armchair C/BN-DWHNTs have the lowest binding energy and formation energy, meaning that the armchair C/BN-DWHNTs at $d_i = \sim 3.5$ Å are more possible to exist. This result is in agreement with the literature [27], in which Yuan and Liew have studied the coaxial CNT@BNNT nanocables and found that the optimal intertube distances between inner C tube and the outer BN are about 3.5 Å for armchair nanocables.

The distance d_i of the armchair C/BN-DWHNTs can be approximately evaluated by the expression as $d_i = 3(ma_{B-N} - na_{C-C})/2\pi$; here a_{B-N} and a_{C-C} are the bond lengths of outer BNNT and inner CNT, respectively. Let $d_i = 3.5$ Å;

the possible stable structures are CNT(n , n)@BNNT(m , m) ($m - n = 5$), for example, CNT(5, 5)@BNNT(10, 10), CNT(6, 6)@BNNT(11, 11), and CNT(7, 7)@BNNT(12, 12) DWHNTs (see Table 1(a)). Taking the armchair CNT(5, 5)@BNNT(m , m) ($m = 8-13$) nanotubes as examples, the covalent bond lengths in the fully optimized CNT and BNNT are 1.43 and 1.45 Å, respectively. When $d_i = \sim 2.60$ Å, the bond length of inner CNT was suppressed to 1.385 Å and the bond length of outer BNNT was extended to 1.540 Å in the perpendicular direction. This result indicates the occurrence of greater repulsive interactions between the inner CNT and the outer BNNT.

The calculated covalent bond lengths of the various zigzag DWHNTs in fully optimized structures are listed in Table 1(b). When $d_i = \sim 3.6$ Å, the zigzag C/BN-DWHNTs have the lowest binding energy and formation energy. It means that the C/BN-DWHNTs at $d_i = \sim 3.6$ Å are more possible to exist. For zigzag configurations, the distance d_i is as follows: $d = \sqrt{3}(ma_{B-N} - na_{C-C})/2\pi$; letting $d = 3.6$ Å, the possible stable structures are CNT(n , 0)@BNNT(m , 0) ($m - n = 9$), for example, CNT(6, 0)@BNNT(15, 0), CNT(7, 0)@BNNT(16, 0) DWHNTs.

The calculated band structures of C/BN-DWHNTs are shown in Figure 2. The armchair C/BN-DWHNTs are metallic, with the lowest conduction band and the highest valence band crossing over the Fermi level at $\sim 2/3$ along Γ -Z direction in reciprocal space. The electric band structure near the Fermi level is very similar to the CNTs because the lowest conduction band and the highest valence band are determined by the carbon atoms. We also found that changing d_i cannot be an efficient way to open the band gap for armchair C/BN-DWHNTs.

The calculated band gaps (E_g) of the single-wall CNT(n , 0) are 0.19, 0.58, 0.04, 0.78, and 0.87 eV for $n = 7-11$,

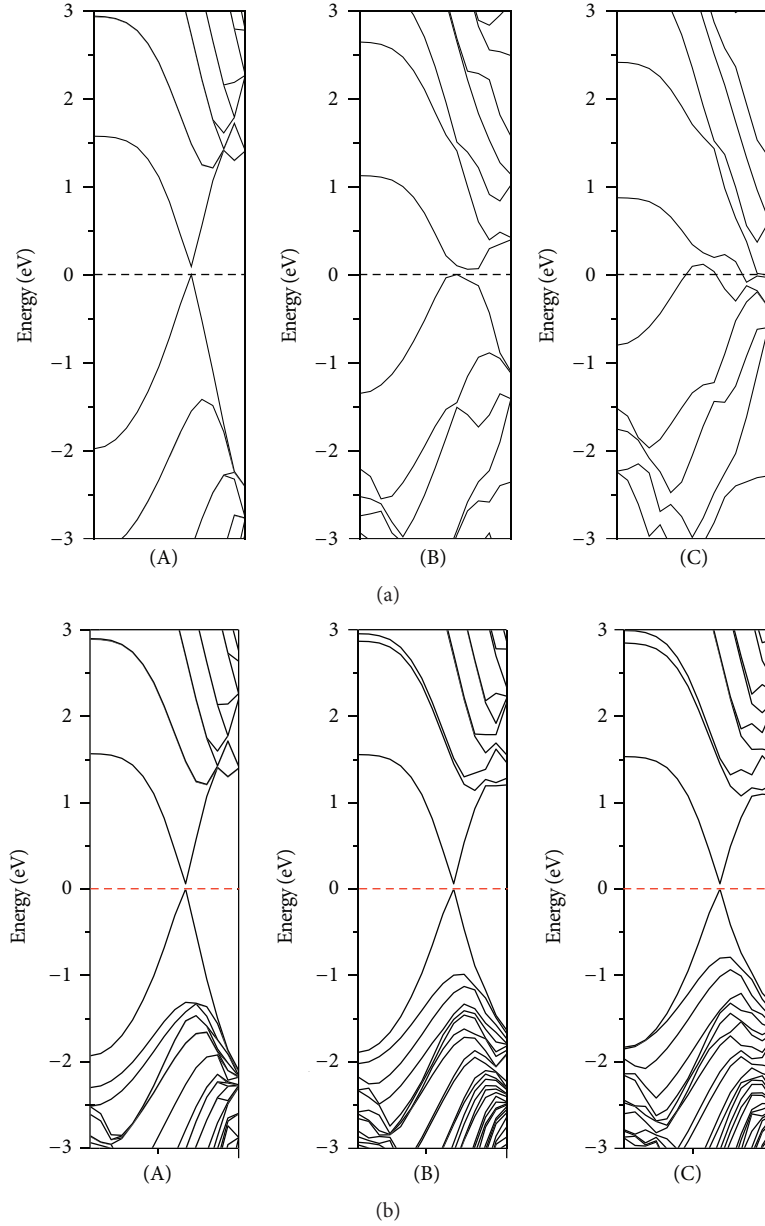


FIGURE 4: (a) Band structures of CNT(5, 5) under an external electric field of (A) $F = 0 \text{ V/\AA}$, (B) $F = 0.1 \text{ V/\AA}$, and (C) $F = 0.15 \text{ V/\AA}$ along y -axis, respectively. (b) Band structures for CNT(5, 5)@BNNT(10, 10) under (A) $F = 0 \text{ V/\AA}$, (B) $F = 0.1 \text{ V/\AA}$, and (C) $F = 0.15 \text{ V/\AA}$ along y -axis, respectively.

respectively, which are consistent with results of similar studies [28]. For the zigzag DWHNTs, d_i affects the band gap of C/BN-DWHNTs. A different size CNT(7, 0) was considered as the inner tube of the zigzag C/BN-DWHNTs. The calculated band gaps are listed in Table 1(b). All the zigzag CNT(7, 0)@BNNT structures are found to be direct gap semiconductors with both the valence band top and conduction band bottom at the Γ point. In Figure 3(a), analysis of the PDOS of CNT(7, 0)@BNNT indicated that p orbitals of the carbon atoms dominate the band near Fermi level. However, for CNT(7, 0)@BNNT(14, 0), the p orbitals of the nitrogen atoms have a contribution to the bands near

the Fermi level, which also proved the stronger interaction when the d_i strayed from $\sim 3.6 \text{ \AA}$. Figure 3(b) shows the DOS of CNT(7, 0)@BNNT(14, 0) and CNT(7, 0)@BNNT(16, 0) DWHNTs. The band gap of CNT(7, 0)@BNNT(14, 0) became small when comparing with the CNT(7, 0)@BNNT(16, 0) during the stronger intertube interactions.

After the CNTs were encapsulated into the BNNT, for the stable structure such as CNT(5, 5)@BNNT(10, 10), their geometries changed little. To study the effect of the transverse electric field on the electronic structure of the nanotubes, F along y direction (perpendicular to the tube axis) was imposed. We first examined the electronic properties of

TABLE 1: (a) Calculated bond lengths (a_{C-C} and a_{B-N}) in the direction of the tube axis (z) and in the perpendicular direction (r), intertube spacing (d_i), the unit being Å, the binding energy (E_b), and the forming energy (E_f) in kJ/mol of different geometrically optimized armchair double-wall hetero-nanotube optimizations. (b) Calculated bond lengths (a_{C-C} and a_{B-N}) in the perpendicular direction (r), intertube spacing (d_i), the unit being Å, the binding energy (E_b kJ/mol) and the forming energy (E_f kJ/mol) kJmol⁻¹, and GGA band gap (E_g eV) of different geometrically optimized zigzag double-wall hetero-nanotube optimizations. (c) The calculated bond lengths (a_{C-C} and a_{B-N}) of various double-wall hetero-nanotubes, in the direction of the tube axis (z) and in the perpendicular direction (r), and intertube spacing (d_i) of different geometrically optimized double-wall hetero-nanotube optimizations; the unit is Å.

(a)							
	a_{C-C}		a_{B-N}		d_i	E_b	E_f
	r	z	r	z			
CNT(5, 5)@BNNT(8, 8)	1.385	1.418	1.540	1.471	2.60	-761.89	12.537
CNT(5, 5)@BNNT(9, 9)	1.420	1.434	1.473	1.453	2.97	-773.74	-0.493
CNT(5, 5)@BNNT(10, 10)	1.435	1.441	1.439	1.441	3.45	-774.41	-2.450
CNT(5, 5)@BNNT(11, 11)	1.441	1.443	1.438	1.441	4.08	-772.29	-1.455
CNT(5, 5)@BNNT(12, 12)	1.436	1.440	1.444	1.442	4.83	-769.60	-0.023
CNT(5, 5)@BNNT(13, 13)	1.434	1.440	1.448	1.444	5.54	-768.83	-0.013
CNT(6, 6)@BNNT(10, 10)	1.416	1.431	1.473	1.453	3.03	-777.50	-0.641
CNT(6, 6)@BNNT(11, 11)	1.433	1.440	1.446	1.445	3.49	-778.17	-2.689
CNT(6, 6)@BNNT(12, 12)	1.440	1.444	1.439	1.441	4.15	-775.66	-1.376
CNT(7, 7)@BNNT(12, 12)	1.431	1.438	1.448	1.445	3.50	-780.77	-2.657

(b)						
	a_{C-C}	a_{B-N}	d_i	E_b	E_f	E_g
	r	r				
CNT(6, 0)@BNNT(13, 0)	1.439	1.466	2.947	-763.81	-0.173	Metallic
CNT(6, 0)@BNNT(14, 0)	1.450	1.452	3.260	-765.74	-2.488	Metallic
CNT(6, 0)@BNNT(15, 0)	1.450	1.447	3.601	-765.55	-2.678	Metallic
CNT(6, 0)@BNNT(16, 0)	1.458	1.445	4.043	-764.40	-1.919	Metallic
CNT(6, 0)@BNNT(17, 0)	1.458	1.443	4.412	-762.85	-0.705	Metallic
CNT(7, 0)@BNNT(14, 0)	1.431	1.466	2.987	-768.25	-0.271	0.146
CNT(7, 0)@BNNT(15, 0)	1.440	1.453	3.240	-769.60	-2.457	0.247
CNT(7, 0)@BNNT(16, 0)	1.446	1.446	3.670	-769.50	-2.685	0.302
CNT(7, 0)@BNNT(17, 0)	1.449	1.443	3.979	-768.25	-1.829	0.281
CNT(7, 0)@BNNT(18, 0)	1.449	1.442	4.444	-766.51	-0.731	0.262
CNT(8, 0)@BNNT(16, 0)	1.439	1.453	3.288	-773.45	-2.467	0.492
CNT(8, 0)@BNNT(17, 0)	1.444	1.446	3.636	-772.49	-2.581	0.558
CNT(9, 0)@BNNT(17, 0)	1.436	1.453	3.305	-775.66	-2.395	0.034
CNT(9, 0)@BNNT(18, 0)	1.443	1.445	3.627	-775.09	-2.608	0.027
CNT(10, 0)@BNNT(18, 0)	1.434	1.452	3.368	-777.78	-2.471	0.805
CNT(10, 0)@BNNT(19, 0)	1.441	1.444	3.603	-777.11	-2.571	0.811
CNT(11, 0)@BNNT(20, 0)	1.442	1.444	3.610	-776.15	-2.558	0.814
CNT(11, 0)@BNNT(21, 0)	1.441	1.442	3.976	-777.30	-1.799	0.808

(c)			
CNT(5, 5)@BNNT(10, 10)			
E (V/Å)	0	0.1	0.25
a_{C-C}^z	1.435	1.433-1.437	1.439-1.431
a_{C-C}^r	1.435	1.434-1.436	1.433-1.440
a_{B-N}^z	1.439	1.434-1.440	1.429-1.447
a_{B-N}^r	1.441	1.447-1.472	1.438-1.508
d_{ix}	3.592	3.614	3.697
d_{iy}	3.602	3.597	3.581

CNT(5, 5)			
E (V/Å)	0	0.1	0.25 (distortion)
a_{C-C}^z	1.425	1.424-1.428	1.421-1.437
a_{C-C}^r	1.426	1.426-1.431	1.392-1.476

BNNT(10, 10)			
E (V/Å)	0	0.1	0.25
a_{C-C}^z	1.436	1.435-1.437	1.436-1.444
a_{C-C}^r	1.452	1.447-1.452	1.432-1.457

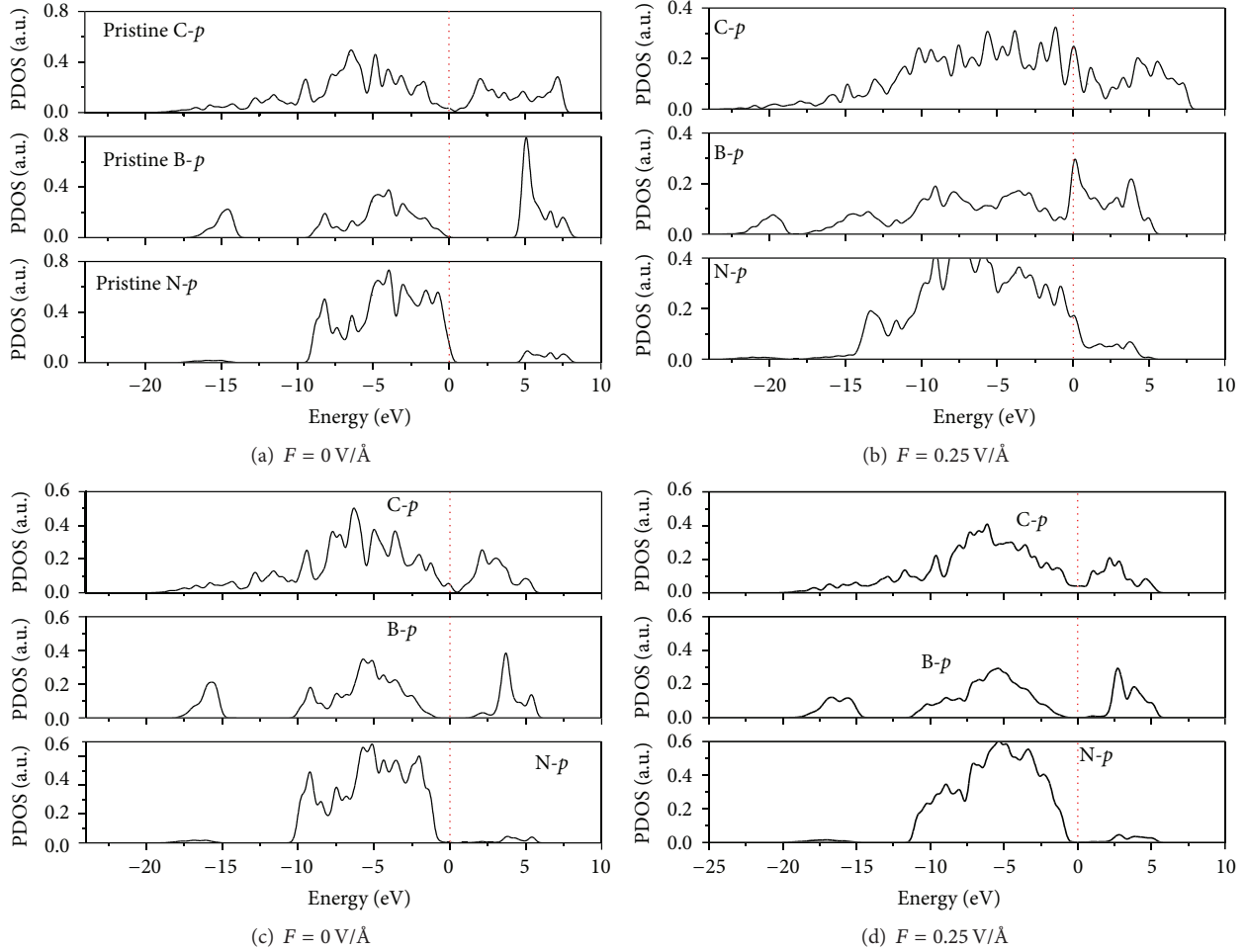


FIGURE 5: PDOS of CNT(5,5) and BNNT(10,10) under an external electric field of (a) $F = 0 \text{ V/\AA}$ and (b) $F = 0.25 \text{ V/\AA}$, respectively. PDOS of CNT(5,5)@BNNT(10,10) under an external electric field of (c) $F = 0 \text{ V/\AA}$ and (d) $F = 0.25 \text{ V/\AA}$, respectively. The Fermi level lies at 0 eV (dotted line). The solid line corresponds to p -state of C, B, and N at pristine CNT(5,5) and BNNT(10,10), respectively.

the CNT(5,5) under an external electric field (see Figure 4(a)). The CNT(5,5) remains semimetallic with an enhancement of density of states around the Fermi level with increasing the external electrical field. Two linear bands became flat (localized) around the Fermi level in CNT(5,5) with increasing field strengths. It can therefore be inferred that the conductance will be greatly enhanced. And the results were well consistent with the literature [29]. The calculated values of the band structures for the armchair CNT(5,5)@BNNT(10,10) at $F = 0, 0.1$ and 0.15 V/\AA are presented in Figure 4(b). There is no distinct difference between the electronic structures of the CNT(5,5)@BNNT(10,10) under different transverse electric fields. It shows that the transverse field does not affect the electronic structures evidently. Whereas the band structures for CNT(5,5) under $F = 0$ and $F = 0.25 \text{ V/\AA}$ show a striking contrast, the band structures for the CNT(5,5)@BNNT(10,10) under $F = 0$ and $F = 0.25 \text{ V/\AA}$ are quite similar. The same phenomenon has been found for CNT(6,6)@BNNT(10,10) and CNT(7,7)@BNNT(12,12) DWHNTs when F is smaller than critical F_c (here F_c is a boundary when $F > F_c$, the band structure of armchair

CNT@BNNT would change abruptly, when $F < F_c$, and the band structure of armchair CNT@BNNT would keep original shape). See the results in Table 1(c); both CNT and BNNT single-walled nanotubes experience large structural changes after geometric optimization with increasing F . When $F = 0.25 \text{ V/\AA}$, optimized CNT(5,5) was distorted.

However, with increasing F , the DOS of the CNT@BNNT is not a simple superposition of the DOS for the individual CNT and pristine BNNT under F . The peak heights for several particular states on the DOS are moderately strengthened or weakened due to the tube-tube interaction. To explore the origin of this phenomenon, the PDOS for C, B, and N in pristine CNT(5,5), BNNT(10,10), and CNT(5,5)@BNNT(10,10) under electric fields $F = 0$ and 0.25 V/\AA was plotted, respectively, as shown in Figure 5. The calculated PDOS indicates that the p -states of carbon atoms contribute mainly to the energy levels near the Fermi level. The p -states of boron and nitrogen in pristine BNNT are very sensitive to the F . However, the change is not obvious in the heterostructure, which maybe caused by the effect of the tube-tube interaction.

We also examined the electronic properties of the zigzag CNT (7, 0)@BNNT(16, 0) and CNT(10, 0)@BNNT(18, 0) under an electronic field. We found that with increasing F the band gap of zigzag CNT (7, 0)@BNNT(16, 0) decreases gradually, and the phenomena are similar to the single-wall CNT (7, 0) under an electronic field. Though the band structure of zigzag CNT(10, 0)@BNNT(18, 0) also decreases gradually with increasing F , it is different from the single-wall CNT(10, 0), because of the increasing intertube interactions.

4. Conclusions

The electronic structures of the double-wall heteronanotubes near the Fermi level are dominated by the p -electrons of carbon atoms; the band structure of the armchair DWHNTs is difficult to modulate with changing intertube distance. However, either changing intertube distance or imposing electric field is the efficient way to modulated the band structure of zigzag DWHNTs. Our results suggest an interesting avenue of exploring novel heterostructure of CNT@BNNT for potentially important applications in CNT@BNNT-based nanodevices.

Conflict of Interests

The authors declare that there is no conflict of interests regarding the publication of this paper.

Acknowledgments

This project was supported by the Natural Science Foundation of China (Grant no. 51402251), the Natural Science Foundation of Jiangsu Province of China (Grant no. BK20140471), and Talent Introduction Project of Yancheng Institute of Technology (nos. XKR2011009 and XKR2011001).

References

- [1] C. R. Dean, A. F. Young, I. Meric et al., "Boron nitride substrates for high-quality graphene electronics," *Nature Nanotechnology*, vol. 5, no. 10, pp. 722–726, 2010.
- [2] D. Usachov, V. K. Adamchuk, D. Haberer et al., "Quasifree-standing single-layer hexagonal boron nitride as a substrate for graphene synthesis," *Physical Review B*, vol. 82, no. 7, Article ID 075415, 2010.
- [3] G. Giovannetti, P. A. Khomyakov, G. Brocks, P. J. Kelly, and J. Van Den Brink, "Substrate induced band gap in graphene on hexagonal boron nitride: *Ab initio* density functional calculations," *Physical Review B*, vol. 76, no. 7, Article ID 073103, 2006.
- [4] J. Sławińska, I. Zasada, and Z. Klusek, "Energy gap tuning in graphene on hexagonal boron nitride bilayer system," *Physical Review B*, vol. 81, no. 15, Article ID 155433, 2010.
- [5] A. Ramasubramaniam, D. Naveh, and E. Towe, "Tunable band gaps in bilayer graphene-BN heterostructures," *Nano Letters*, vol. 11, no. 3, pp. 1070–1075, 2011.
- [6] R. Nakanishi, R. Kitaura, J. H. Warner et al., "Thin single-wall BN-nanotubes formed inside carbon nanotubes," *Scientific Reports*, vol. 3, article 1385, 2013.
- [7] A. Gomathi, M. Ramya Harika, and C. N. R. Rao, "Urea route to coat inorganic nanowires, carbon fibers and nanotubes by boron nitride," *Materials Science and Engineering A*, vol. 476, no. 1-2, pp. 29–33, 2008.
- [8] M. Das, A. K. Basu, S. Ghatak, and A. G. Joshi, "Carbothermal synthesis of boron nitride coating on PAN carbon fiber," *Journal of the European Ceramic Society*, vol. 29, no. 10, pp. 2129–2134, 2009.
- [9] L. Chen, H. Ye, Y. Gogotsi, and M. J. McNallan, "Carbothermal synthesis of boron nitride coatings on silicon carbide," *Journal of the American Ceramic Society*, vol. 86, no. 11, pp. 1830–1837, 2003.
- [10] S. Li, Y. F. Wu, W. Liu, and Y. H. Zhao, "Control of band structure of van der Waals heterostructures: silicene on ultrathin silicon nanosheets," *Chemical Physics Letters*, vol. 609, pp. 161–166, 2014.
- [11] P. Avouris, R. Martel, V. Derycke, and J. Appenzeller, "Carbon nanotube transistors and logic circuits," *Physica B: Condensed Matter*, vol. 323, no. 1–4, pp. 6–14, 2002.
- [12] C. L. Phillips, C. S. Yah, S. E. Iyuke, K. Rumbold, and V. Pillay, "The cellular response of *Saccharomyces cerevisiae* to multi-walled carbon nanotubes (MWCNTs)," *Journal of Saudi Chemical Society*, vol. 19, no. 2, pp. 147–154, 2015.
- [13] K. Chikkadi, M. Muoth, W. Liu, V. Maiwald, and C. Hierold, "Enhanced signal-to-noise ratio in pristine, suspended carbon nanotube gas sensors," *Sensors and Actuators, B: Chemical*, vol. 196, pp. 682–690, 2014.
- [14] A. Freitas, S. Azevedo, and J. R. Kaschny, "Effects of a transverse electric field on the electronic properties of single- and multi-wall BN nanotubes," *Solid State Communications*, vol. 153, no. 1, pp. 40–45, 2013.
- [15] C.-W. Chen, M.-H. Lee, and S. J. Clark, "Band gap modification of single-walled carbon nanotube and boron nitride nanotube under a transverse electric field," *Nanotechnology*, vol. 15, no. 12, pp. 1837–1843, 2004.
- [16] P. Ordejón, E. Artacho, and J. M. Soler, "Self-consistent order- N density-functional calculations for very large systems," *Physical Review B*, vol. 53, no. 16, Article ID R10441, 1996.
- [17] D. Sánchez-Portal, P. Ordejón, E. Artacho, and J. M. Soler, "Density-functional method for very large systems with LCAO basis sets," *International Journal of Quantum Chemistry*, vol. 65, no. 5, pp. 453–461, 1997.
- [18] J. P. Perdew, K. Burke, and M. Ernzerhof, "Generalized gradient approximation made simple," *Physical Review Letters*, vol. 77, no. 18, pp. 3865–3868, 1996.
- [19] H. J. Monkhorst and J. D. Pack, "Special points for Brillouin-zone integrations," *Physical Review B*, vol. 13, no. 12, pp. 5188–5192, 1976.
- [20] B. Delley, "An all-electron numerical method for solving the local density functional for polyatomic molecules," *The Journal of Chemical Physics*, vol. 92, no. 1, pp. 508–517, 1990.
- [21] B. Delley, "From molecules to solids with the DMol³ approach," *Journal of Chemical Physics*, vol. 113, no. 18, pp. 7756–7764, 2000.
- [22] J. P. Perdew and Y. Wang, "Accurate and simple analytic representation of the electron-gas correlation energy," *Physical Review B*, vol. 45, no. 23, pp. 13244–13249, 1992.
- [23] S. Li, Y. Wu, Y. Tu et al., "Defects in silicene: vacancy clusters, extended line defects, and di-adatoms," *Scientific Reports*, vol. 5, article 7881, 2015.
- [24] W. Liu, A. Tkatchenko, and M. Scheffler, "Modeling adsorption and reactions of organic molecules at metal surfaces," *Accounts of Chemical Research*, vol. 47, no. 11, pp. 3369–3377, 2014.

- [25] W. Liu, S. N. Filimonov, J. Carrasco, and A. Tkatchenko, "Molecular switches from benzene derivatives adsorbed on metal surfaces," *Nature Communications*, vol. 4, article 2569, 2013.
- [26] W. Liu, J. Carrasco, B. Santra, A. Michaelides, M. Scheffler, and A. Tkatchenko, "Benzene adsorbed on metals: concerted effect of covalency and van der Waals bonding," *Physical Review B*, vol. 86, no. 24, Article ID 245405, 2012.
- [27] J. Yuan and K. M. Liew, "Structural stability of a coaxial carbon nanotube inside a boron-nitride nanotube," *Carbon*, vol. 49, no. 2, pp. 677–683, 2011.
- [28] V. Zólyomi and J. Kúrti, "First-principles calculations for the electronic band structures of small diameter single-wall carbon nanotubes," *Physical Review B*, vol. 70, no. 8, Article ID 85403, 2004.
- [29] S. V. Tishchenko, "Electronic structure of zigzag carbon nanotubes," *Low Temperature Physics*, vol. 32, no. 10, pp. 953–956, 2006.

Review Article

A Review on the Efficiency of Graphene-Based BHJ Organic Solar Cells

**Alejandro Manzano-Ramírez,¹ Edgar J. López-Naranjo,²
Wole Soboyejo,³ Yunny Meas-Vong,⁴ and Bertrand Vilquin⁵**

¹CINVESTAV-IPN Unidad Querétaro, 76230 Santiago de Querétaro, QRO, Mexico

²Universidad Autónoma de Nayarit, Ciudad de la Cultura Amado Nervo s/n, 63190 Tepic, NAY, Mexico

³Princeton Institute of Science and Technology of Materials (PRISM), Bowen Hall, 70 Prospect Street, Princeton, NJ 08544, USA

⁴CIDETEQ, Parque Tecnológico Querétaro Sanfandila, 76703 Pedro Escobedo, QRO, Mexico

⁵Univertisté de Lyon, École Centrale de Lyon, Institut des Nanotechnologies de Lyon, 36 Avenue Guy de Collongue, 69134 Ecully Cedex, France

Correspondence should be addressed to Alejandro Manzano-Ramírez; amanzano@cinvestav.mx

Received 19 May 2015; Revised 30 August 2015; Accepted 31 August 2015

Academic Editor: Michal Otyepka

Copyright © 2015 Alejandro Manzano-Ramírez et al. This is an open access article distributed under the Creative Commons Attribution License, which permits unrestricted use, distribution, and reproduction in any medium, provided the original work is properly cited.

Graphene, a material composed of one-atom-thick planar sheets of sp^2 -bonded carbon atoms with a two-dimensional honeycomb structure, has been proposed for many applications due to its remarkable electronic, optical, thermal, and mechanical properties. Its high transparency, conductivity, flexibility, and abundance make it an excellent material to be applied in the field of organic photovoltaic cells, especially as a replacement for transparent conducting oxide electrodes. However, graphene has been demonstrated to be useful not only as substitute for indium tin oxide electrodes, but also as cathode, electron acceptor, hole transport, and electron extraction material. Thus, in this work, we summarize and discuss the efficiency of bulk heterojunction devices using graphene as a main constituent.

1. Introduction

Organic solar cells (OSCs) belong to the class of photovoltaic devices known as excitonic solar cells, which are characterized by strongly bound electron-hole pairs (excitons) that are formed after excitation with light. Strongly bound excitons exist in these materials as a consequence of the low dielectric constants in the organic components, which are insufficient to affect direct electron-hole dissociation, as it is found in their high dielectric inorganic counterparts. In excitonic solar cells, exciton dissociation occurs almost exclusively at the interface between two materials of different electron affinities (and/or ionization potentials): the electron donor and the electron acceptor. To generate an effective photocurrent in these organic solar cells, an appropriate donor-acceptor pair and device architecture must be selected. Two main approaches have been explored in the effort to

develop viable devices: the donor-acceptor bilayer and the so-called bulk heterojunction (BHJ), which is represented in the ideal case as a bicontinuous composite of donor and acceptor phases, thereby not only maximizing the donor/acceptor interface for efficient exciton dissociation, but also forming a nanoscale interpenetrating network for charge transport to the electrodes [1, 2] (Figure 1). Organic solar cell research and device development still have a long way to go to compete with inorganic solar cells. The efficiency of inorganic devices can top 20% and the development of inorganic thin-layer and multijunction instruments will likely lead to even better performance. In contrast, the best OSCs, based on the BHJ concept, operate at a maximum of ~8.0% efficiency. However, due to its low cost, lightweight, high availability of materials, and easy manufacturing, the OSCs technology turns very appealing as it could theoretically produce highly efficient devices [3–5].

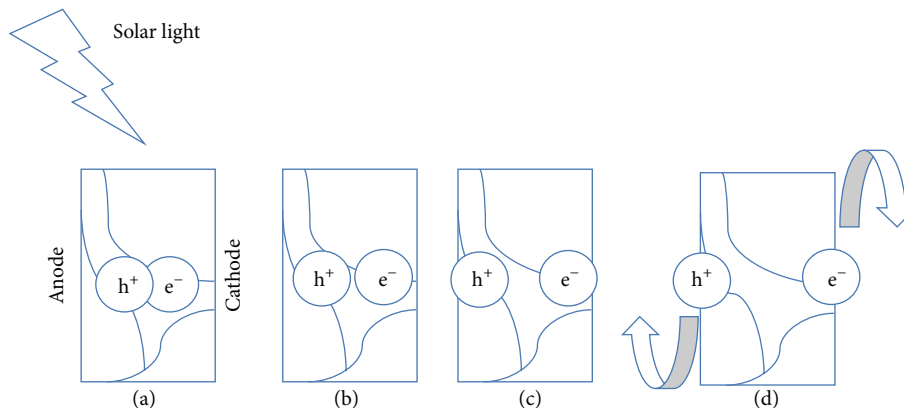


FIGURE 1: BHJ cell operation mechanism. (a) Exciton generation, (b) exciton dissociation, (c) charge formation, and (d) charge transport and collection.

Based on the simple consideration that low band gap materials have the possibility to improve the efficiency of photovoltaic devices due to a better overlap with the solar spectrum, it is expected that, for a maximum photon harvesting in the OSCs, low band gap materials will be employed. The use of this type of materials results in higher currents that can lead to higher power conversion efficiency (PCE). Poly-3-hexylthiophene (P3HT), one of the most used materials as donor in a BHJ device, exhibits a band gap of 650 nm (1.9 eV) and thus only has the possibility to harvest up to 22.4% of the available photons giving a maximum theoretical current density of 14.3 mAcm^{-2} . If P3HT is applied in a BHJ device, coupled with the most commonly used acceptor (i.e., phenyl- C_{61} -butyric acid methyl ester, PCBM), the band gap extends to 1000 nm allowing for absorption of 53% of the available photons giving a maximum current density of 33.9 mAcm^{-2} . However, in practical terms these values cannot be achieved and the real performance of a P3HT : PCBM system is around its optimal of about 5% which is lower than a quarter of a silicon solar cell's optimal [6, 7].

Graphene, a zero-band-gap semiconductor is a rising star in materials science (Figure 2). It shows a two-dimensional (2D) structure consisting of sp^2 -hybridized carbon and it is also the thinnest known material in the universe and the strongest ever measured [8–11]. It exhibits remarkable electronic and mechanical properties and a considerable number of new optical effects that have not been observed in other materials [12, 13]. Its remarkably high carrier mobility, wide absorption spectral range, and high optical transparency indicate graphene as a cost-effective and abundant material that qualifies for application in optoelectronic devices such as displays, light-emitting diodes, and solar cells [14–17].

Different routes are available for the preparation of graphene [12, 18, 19]. The first involves chemical vapor deposition (CVD) of monolayer of graphite on transition metal surfaces [20, 21]. The second route is the micromechanical exfoliation of graphite and involves peeling of the graphene from graphite using “Scotch” tape [22]. The “Scotch” tape is then dipped in acetone to release the graphene, which is subsequently captured on a silicon wafer with a SiO_2

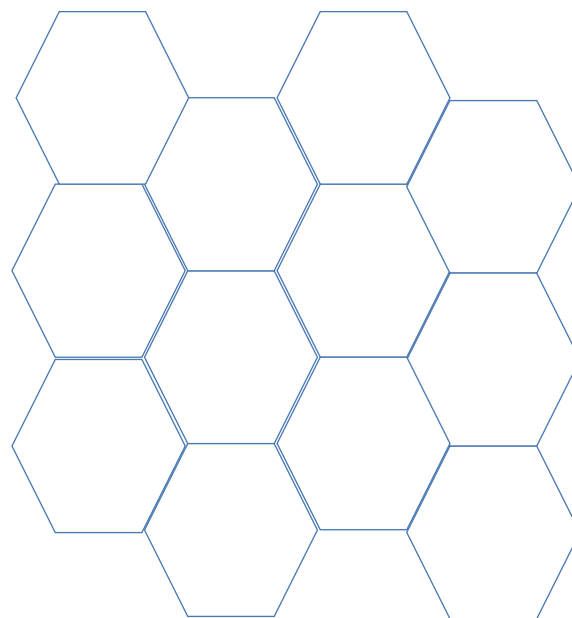


FIGURE 2: Representation of graphene structure.

(silicon dioxide) layer on top. The third route involves the epitaxial growth of graphene on electrically insulating substrates like silicon carbide [23]. However, the second and third methods are unsuitable for large-scale preparation of graphene for the fabrication of polymer nanocomposites [19]. Thus, it appears that the only routes to prepare bulk quantities of graphene and chemically modified graphene (CMG) are from graphene oxide (GO) and graphite intercalation compounds (GICs). The presence of hydroxyl and epoxide groups on the graphitic basal planes and carboxyl and carbonyl groups on the edges of layers makes GO water dispersible [24]. Thus, on sonication in aqueous media, GO exfoliates readily into colloidal suspensions of single graphene oxide layers. Chemical reduction of GO present in the colloidal suspension with reducing agents is necessary to convert the electrically insulating GO layers back to conducting graphene

suitable for composite applications. The final route by which bulk quantities of graphene can be prepared is by thermally reducing GO. This technique involves rapidly heating GO in inert (argon or nitrogen) environment to produce thermally reduced expanded graphene oxide (TRGO) [25, 26]. Due to its wrinkled nature, TRGO do not collapse back to GO but remain highly agglomerated. However, McAllister et al. [27] observed that, after TRGO was dispersed by ultrasonication in appropriate solvents, 80% of the flakes were single graphene sheets.

Derivatives of graphene, such as GO and reduced graphene oxide (rGO), are also being widely investigated from the point of view of primary and practical applications [16]. rGO can be easily prepared by wet processes such as spin-, dip-, and spray-coating to give large-area GO films and by hydrazine vapor treatment to reduce the GO films. Secondary treatments, such as thermal annealing, have been indicated to increase the photocurrent and device efficiency by removing defects and optimizing the morphology of graphene-based cell constituents [2, 16].

Regarding the PCE in BHJ devices, the highest value was observed to be ~7.4% for the device with ITO/PEDOT:PSS/PBTTT-3:PC₇₀BM/Ca/Al (indium tin oxide/poly(3,4-ethylenedioxythiophene):poly(styrenesulfonate)/poly(2,5-bis(3-tetradecylthiophen-2-yl)thieno(3,2-b)thiophene)/3:phenyl-C₇₀-butyric acid methyl ester/calcium/aluminum) structure [16]. Photovoltaic devices based on graphene are still not as efficient as, for example, devices with ITO electrodes or organic acceptors mainly because the conductivities of graphene are relatively low [9, 28]. Theoretical PCEs as high as 12% have been calculated for graphene-based organic devices [29], and it has also been proposed that graphene may favor charge carrier multiplication [30]. Graphene has proved to be useful not only as substitute for ITO electrodes, but also as cathode, electron acceptor, hole transport, and electroextraction material (Figure 3) [15, 31, 32]. Therefore, this review is intended to examine the efficiency of different graphene-based devices and the newest trends in order to maximize their efficiencies.

2. Electrode Material

In BHJ devices, the conventional transparent conductive electrode used to couple photons into the active layer is extensively the ITO-based electrode that shows a sheet resistance of less than 100 Ω /sq and an optical transparency of ~90% [2, 33]. ITO electrodes consume as much as 30% of the fabrication cost in solar cells and their use seems to be increasingly problematic due to the limited indium source, susceptibility to ion diffusion into polymer layers, instability in acid or base, and the brittle nature of metal oxide [34–36]. Additionally, Krebs et al. reported that the energy involved in processing the ITO electrode accounts for 87% in roll-to-roll based OSCs fabrication [37]. Thus, a substitute for ITO with similar performance but lower cost is clearly needed. In this regard, graphene has risen as a promising electrode material due to its high theoretical surface area of 2630 m²/g and ability to facilitate electron or hole transfer along its two-dimensional

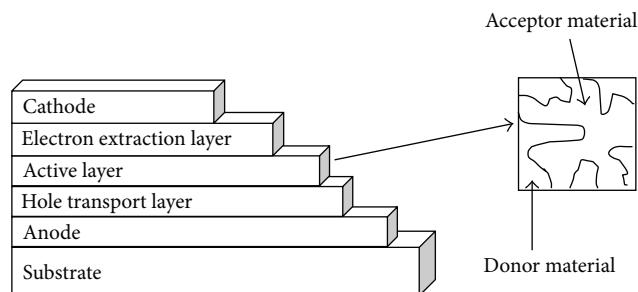


FIGURE 3: Configuration of a typical BHJ solar cell.

surface [13, 22, 35]. The high transparency, conductivity, flexibility, and elemental abundance of graphene indicate that it is an excellent replacement for transparent conducting oxide electrodes [38–40]. Graphene transparent electrodes can be expected to be applied not only for the substitution of ITO that is usually used as anode but also for cathode for which low work function metals are used [41, 42].

However, for chemically processed graphene, mainly the contact resistance of the small graphene flakes and the insulating property of the graphene chemically reduced from graphene oxide limit the device performance. The structural defects and lateral disorder of such chemically exfoliated graphite affect the carrier mobility of the film negatively [43]. Therefore, although graphene could provide a low-cost alternative for ITO, there is still tremendous room for improvement in terms of enlarging the lateral scale of graphene in these devices [44].

2.1. Anode. Xu et al. [45] reported on polymer organic photovoltaic cells using pure graphene films as the transparent anode directly fabricated from graphene solutions by spin-coating, with P3HT as the electron donor and PCBM as the acceptor. The graphene films reduced with hydrazine and annealed at temperatures of 300, 500, and 700°C had transmittance of 75%, 73%, and 69% at a wavelength of 550 nm, respectively. Under these experimental conditions, the reduced graphene films could have a sheet resistance of 17.9 k Ω /sq and a conductivity of 22.3 S/cm which is comparable with that obtained using more complicated graphene composites. The current density-voltage (J - V) characteristic of the device (hydrazine + 700°C) under illumination of simulated solar light shows a short-circuit photocurrent density (J_{sc}) of 1.18 mA/cm² with an open circuit voltage (V_{oc}) of 0.46 V, a calculated filling factor (FF) of 24.58%, and an overall PCE of 0.13%. The ITO device used as a reference was fabricated under the same conditions and had a PCE of 3.59%. The low PCE of the graphene-based device is likely due to the hydrophobic graphene film surface which makes it rather hard to get a uniform poly(3,4-ethylenedioxythiophene):poly(styrenesulfonate) (PEDOT:PSS) layer. So, it is highly possible that, with optimized graphene-electrode conductivity and graphene film surface wetting property, the performance of these graphene-electrodes cells could be improved significantly [45]. Although this approach provides a cost-effective, simple

solution-based process, the overall PCE of the graphene-based device is lower than that reported for the best OSCs based on the BHJ concept (~8.0%).

Yin et al. [34] indicated that the performance of the organic devices mainly depends on the charge transport efficiency through rGO electrodes when the optical transmittance of rGO is above 65%. However, if the transmittance of rGO is less than 65%, the performance of the device is dominated by the light transmission efficiency, that is, the transparency of rGO films. In this work, highly conductive rGO film was transferred onto a polyethylene terephthalate (PET) substrate, which was used as the transparent electrode. The authors reported that lowering the rGO sheet resistance via increasing the rGO thickness notably enhanced the current density of devices and thus the overall PCE. In order to study the effect of rGO thickness on the performance of the devices, rGO films with different thickness were prepared (4 nm, 10 nm, 16 nm, and 21 nm). The highest optical transmittance, 88%, was obtained in the 4 nm thick rGO films, but the sheet resistance dramatically increased to 16.0 k Ω /sq. The highest PCE obtained in the flexible rGO/PET devices was 0.78% and corresponded to the 16 nm thick rGO cells, which showed the highest J_{sc} and V_{oc} . These devices showed an excellent stability after applying the bending-induced tension stress, and their performance was well maintained even after bending a thousand times [34].

Wang et al. [46] described the fabrication and characterization of transparent graphene-constructed films (TGFs) to be used as hole collecting electrodes in organic solar cells. The transparency of TGFs on quartz was tuned by controlling the film thickness by varying the solution concentration. Different thicknesses (30, 22, 12, and 4 nm) had transmittance of 55, 66, 80, and 90, respectively, at a wavelength of 500 nm. The electrical characteristics of the as-prepared 30 nm thick TGFs were evaluated by a four-point probe measurement, which showed resistance of 1.6 k Ω /sq and a conductivity of 206 S cm⁻¹. To demonstrate how the TGFs performed as anodes, organic solar cells were fabricated using a blend of P3HT and PCBM. The photoactive composite layer was sandwiched between TGFs/quartz and Ag electrode. The TGFs on quartz had a sheet resistance of 18 k Ω /sq and a transmittance of 85% at 500 nm. The devices were illuminated with monochromatic light and the highest external quantum efficiency (EQE) of around 43% was achieved at a wavelength of 520 nm. This efficiency is comparable to the highest EQE value of 47% for a reference device fabricated under similar conditions but with ITO/glass as the anode. The current-voltage (I - V) characteristics of the device showed a distinct diode behavior under monochromatic light with a wavelength of 510 nm. In this case, PCE was of 1.53%, and under simulated solar light PCE was 0.29% [46].

Wang et al. [44] produced large area, continuous, transparent, and highly conducting few-layered graphene films (FLGFs) by chemical vapor deposition method to be used as anode for application in photovoltaic devices. In the solution-processed organic solar cells, the anode layer should possess good hydrophilicity to allow the spreading of the hole transport layer. In order to tune the surface wettability without

degrading the conductivity, the graphene film was noncovalently modified with pyrene butanoic acid succidimidyl ester (PBASE) as a result; the PCE was of 1.71%. This performance corresponds to ~55.2% of the PCE of a control device based on an ITO anode. The electronic energy levels of graphene before and after modification with PBASE were investigated; the results indicated that graphene maintained a nearly zero-gap condition after the treatment. Thus, since the main drawback of graphene film is its poor hydrophilicity, which led to a negative effect on the construction of solution-processed devices, PBASE treatment resulted to be an effective method to overcome this issue successfully [44].

Gómez De Arco et al. [47] reported on the implementation of continuous, highly flexible, and transparent graphene films obtained by CVD and used as transparent conductive electrodes. The thickness of CVD graphene was on the order of 1–3 nm. According to the authors, the use of CVD graphene is more attractive than the other graphene films, for example, those that are formed by stacked micrometer sized flakes that suffer from flake to flake contact resistance and high roughness. In the case of CVD graphene, the grain boundaries have the advantage of being formed *in situ* during synthesis; such process is expected to minimize contact resistance between neighboring graphene domains and may result in smoother films with better conducting properties. Solar cells made with CVD graphene exhibited performance that compares to ITO device and surpasses that of ITO devices under bending conditions, exhibiting PCE of 1.18%, which is nearly 93% of that shown by the ITO device. Contrary to the conventional materials used in BHJ OSCs, in this case, the multilayered configuration employed a copper phthalocyanine (CuPc), fullerene (C₆₀), and bathocuproine (BCP) mixture as active layer [47].

Jung et al. [48] reported the characteristics of two different types of OSCs fabricated on HNO₃- (nitric acid-) treated and untreated multilayer graphene (MLG) transparent electrodes prepared using chemical vapor deposition and a multitransfer process. MLG films were formed by stacking graphene films three times on the same substrate and were used as the device anodes. OSCs fabricated on untreated transparent electrodes had a V_{oc} of 0.575 V, a J_{sc} of 8.08 mA/cm², FF of 43.5%, and a PCE of 2.02%. In contrast, application of HNO₃-treated films as transparent electrodes led to an improved performance with a V_{oc} of 0.602 V, a J_{sc} of 8.26 mA/cm², FF of 5.75%, and a PCE of 2.68%. The results suggested that HNO₃ treatment is a promising method improving the performance of large-area OSCs [48].

Choe et al. [49] presented the results of applying multilayer graphene (MLG) films as transparent conductive electrodes. The MLG films were synthesized into a CVD chamber under a flow of H₂ in Ar gas mixture at different growth temperatures. MLG films prepared at 800, 900, and 1000 °C showed the sheet resistances of 1730 ± 600, 990 ± 400, and 610 ± 140 Ω /sq and the mobility of 660 ± 270, 1030 ± 440, and 1180 ± 260 cm²/V s, respectively. The performance of the devices with 1000 °C grown MLG films was found to be the best with a PCE of ~1.3%. The PCE was further enhanced when a hole-blocking titanium suboxide (TiO_x) layer was

TABLE 1: PCE of BHJ OSCs using graphene as anode.

Material	Device conformation	Highest PCE	Reference
TGFs	Quartz/TGFs/P3HT : PCBM/Ag	1.53%	[46]
FLGFs	FLGFs/PEDOT : PSS/P3HT : PCBM/LiF/Al	1.71%	[44]
Graphene	Quartz/graphene/PEDOT : PSS/P3HT : PCBM/LiF/Al	0.13%	[45]
rGO	PET : rGO : PEDOT : PSS/P3HT : PCBM/TiO ₂ /Al	0.78%	[34]
Graphene	PET : CVD graphene/PEDOT : PSS/CuPc/C ₆₀ /BCP/Al	1.18%	[47]
MLG	Glass/MLG/PEDOT : PSS/P3HT : PCBM/TiO _x /Al	2.6%	[49]
CCG	CCG/PEDOT : PSS/P3HT : PCBM/Al	1.01%	[51]
MLG	MLG/MoO ₃ + PEDOT : PSS/P3HT : PCBM/LiF/Al	2.5%	[36]
MLG	MLG/PEDOT : PSS/P3HT : PCBM/Ca/Al	2.68%	[48]
MLG	Glass/MLG/PEDOT : PSS/P3HT : PCBM/Ca/Al	1.17%	[50]

inserted in the device structure, resulting in a PCE of ~2.6% which is a significantly higher efficiency compared to the other graphene-based photovoltaic cells [49].

Choi et al. [50] fabricated OSCs based on MLG electrodes, which were prepared using the CVD method and a multitransfer process on a glass substrate. The MLG electrode transferred onto a glass substrate showed a sheet resistance of $374 \pm 3 \Omega/\text{sq}$ and an optical transparency of 84.2%. The sheet resistance of the MLG (4 layers) film was higher than those reported elsewhere because in this case no chemical treatment was performed on the film. The transparency of the MLG film was fairly constant regardless of wavelength, unlike the conventional ITO film showing transparency modulation in the blue wavelength region. To prepare the MLG electrode on glass, a thin layer of graphene was grown on Cu foils using CVD; the transfer process was repeated four times on the transparent glass substrate until the MLG film was obtained. The PCE of the BHJ device was 1.17%, indicating that MLG films are a promising indium-free transparent electrode substitute for the conventional ITO electrode for use in cost-efficient OSCs [50].

Wang et al. [36] developed a direct layer-by-layer (LBL) transfer method of graphene sheets to fabricate MLG films. Stacking multilayers together and doping them rendered higher extrinsic conductivity. HCl was used to dope the individual layers during the transfer process, followed by HNO₃ doping at the surface. Different types of devices were fabricated to evaluate the effect of the various treatments proposed in this work. To improve the hydrophilicity of graphene, a thin layer of (~20 Å) molybdenum oxide (MoO₃) was evaporated on the graphene. The as-grown graphene-based devices showed a poor performance, yielding a low PCE of 0.35%. After modifying the graphene with MoO₃ + PEDOT : PSS double interfacial layer, the PCE was dramatically increased and 1.23% was achieved. Finally, the 4-layer acid-doped graphene solar cell exhibited the best performance in this work with PCE of 2.5%, which is about 83.3% that of the control device fabricated on ITO. The LBL, acid-doped, four-layer graphene film has a sheet resistance of ~80 Ω/sq and a transmittance of ~90% at 550 nm [36].

Geng et al. [51] reported a simple method for preparing transparent conductive films using a chemically converted graphene (CCG) suspension via controlled chemical

reduction of exfoliated GO in the absence of dispersant to be used as transparent electrodes in BHJ devices. After vacuum filtration of the reduction-controlled CCG suspension and subsequent thermal annealing (optimal conditions were 15 min at 800°C) of the CCG films, high conductive films with a low sheet resistance on the order of $10^3 \Omega/\text{sq}$ and high transparency (80% at 550 nm) were obtained. Thermally annealed CCG film showed a sheet resistance that was lower than that of the thermally annealed GO films, apparently due to the greater extent restoration of the sp² carbon networks during the two-step reduction of the CCG films. Devices prepared with the CCG films as transparent electrodes exhibited PCE of $1.01 \pm 0.05\%$, which correspond to half the efficiency of solar cell devices in which the electrode was made using ITO [51].

Table 1 summarizes the best PCE achieved by the different research groups presented in the previous section as well as the device conformation that rendered such PCE.

Although the overall PCE obtained by devices using graphene-based materials as anode has not surpassed that of cells using traditional materials, research groups around the world have already identified the main aspects to improve graphene-based materials performance. It has been pointed out that lowering graphene sheet resistance will increase the overall PCE of the BHJ devices. In order to lower the sheet resistance, different strategies can be followed, for example, increasing the thickness of the graphene film. This goal can be achieved following a simple procedure that consists in the modification of the solution concentration from which the film is obtained. This route constitutes a very good option due to its simplicity and to the fact that no additional chemicals are needed, contrary to other techniques that require highly dangerous chemical agents to dope graphene. Thickness control also has an impact on the transparency of the film. A higher transparency will originate a better light transmission and a higher PCE. Thus, a proper balance between transparency and sheet resistance needs to be achieved to improve the performance of the device. Scientists have also identified that the optimization of the graphene conductivity and graphene films surface wetting has a positive effect on the performance of graphene-based electrodes. Thermal treatments (i.e., annealing) also play an important role regarding final efficiency; by this simple procedure, notable increments

TABLE 2: PCE of BHJ OSCs using graphene as cathode.

Material	Device conformation	Highest PCE	Reference
MLG	MLG/WPF-6-oxy-F/P3HT : PCBM/PEDOT : PSS/Al	1.23%	[14]
MLG	Glass/ITO/ZnO/P3HT : PCBM/MLG	2.50%	[52]
SLG	ITO/PEDOT/CuPC : C ₆₀ : TPBi/SLG	0.22%	[53]
rGO	PET : alkali + rGO-SWCNT/P3HT : PCBM/V ₂ O ₅ /Al	1.27%	[55]
SLG	Glass/ITO/ZnO/P3HT : PCBM/PEDOT : PSS/Au + SLG	2.7%	[54]

have been achieved. In the specific case of anode-materials, graphene constitutes a viable option to substitute traditional materials, first due to its higher abundance compared to indium and second to the considerable PCE reached so far.

2.2. Cathode. Although several studies have reported on the graphene-based electrode for replacing the ITO bottom electrode in organic photovoltaic devices, the use of the graphene top electrode is still very limited [52]. The following section presents the research works related to this topic found in the scientific literature. Table 2 summarizes the best PCE achieved by devices using graphene as cathode.

Lee et al. [52] reported a simple lamination process for depositing a graphene electrode on top of a polymer photovoltaic device replacing the conventional metal electrode, resulting in a semitransparent inverted polymer solar cell with a PCE of over 75% of that of the standard opaque device using an Ag metal electrode, which was fabricated for comparison. For the preparation of the graphene top electrode, a graphene film was grown on copper foil using CVD processes. Since a single layer of graphene does not have sufficiently high sheet conductivity, multilayer stacking of the graphene film was required to obtain higher sheet conductance. The Ag-based device yielded a PCE of 3.30% and in the best case (10-layers device) the semitransparent device achieved a PCE of 2.50% when illuminated (AM1.5, 100 mW/cm²) from the ITO side. By contrast, while illuminated from the graphene side, the semitransparent device consisting of 8 layers of graphene exhibited an optimal PCE of 2.04% [52].

Jo et al. [14] fabricated inverted-structure OSCs with graphene cathodes. The graphene film used in this work was work function-engineered with an interfacial dipole layer to reduce the work function of graphene, which resulted in an increase in the built-in potential and enhancement of the charge extraction, thereby enhancing the overall device performance. MLG film was grown through CVD on nickel films as reported elsewhere. The work function of the untreated MLG film was 4.58 ± 0.08 eV, which is close to the work function of highly ordered pyrolytic graphite (4.5 eV). The work function of the MLG film was reduced by the use of different interfacial layers made of poly-ethylene oxide (PEO), poly[9,9-bis((6-(N,N,N-trimethylammonium) hexyl)-2,7-fluorene)-alt-(9,9-bis(2-(2-(2-methoxyethoxy) ethoxy)ethyl)-9-fluorene)] dibromide (denoted by WPF-6-oxy-F), and Cs₂CO₃. These interfacial layers formed interfacial dipoles that pointed away from the MLG surface, thereby decreasing the MLG work function. WPF-6-oxy-F

was found as the best material because it reduces the effective work function of MLG to a value that is close to the LUMO of the acceptor material. Therefore, the best PCE (1.23%) was obtained with WPF-6-oxy-F as the interfacial layer. The performance of the OSCs with MLG electrodes is expected to depend strongly on the quality and properties of the MLG film. The CVD-synthesized MLG films exhibited high sheet resistance in the range of 850 to 520 Ω/sq, while the transmittance changed from 90% to 85% at a wavelength of 450 nm [14].

Cox et al. [53] demonstrated that a laminated single-layer graphene (SLG) grown through chemical vapor deposition can be used as a cathode for organic photovoltaic devices. The PCE of graphene devices was limited by their series resistance, indicating that the preparation of graphene samples with lower sheet resistance could improve device performance. In this work, aluminum control devices were used to evaluate the performance of the graphene OSCs. The graphene devices exhibited a PCE of 0.02% and the aluminum controls showed a PCE of 0.41%. The V_{oc} for both types of instruments was approximately 0.45 V. This large efficiency disparity in conjunction with similar V_{oc} 's indicated that parasitic series resistance dominated the characteristics of the graphene devices. To minimize the influence of the parasitic series resistance, the devices were studied under low-intensity monochromatic illumination. At incident power of 4.6 mW/cm², the graphene device exhibits a PCE of 0.22% [53].

Liu et al. [54] reported the fabrication of a semitransparent device with a SLG synthesized on copper foils with CVD method used as top electrode. The device was optimized by tuning the active layer thickness and changing the conductance and the work function of single-layer graphene by doping Au nanoparticles and PEDOT : PSS. For each synthesis condition, three identical cells were fabricated and the average PCE was calculated. The devices were illuminated on each side under an AM1.5 solar simulator with the intensity of 100 mW/cm². The maximum PCE of the semitransparent cell was 2.7% for an active area of 20 mm² when illuminated from the graphene side, which is much higher than the value from the ITO side (2.2%). It was also found that the PCE of the device decreased from 3% to 2.3% with the increase of the size from 6 to 50 mm², which was attributed to both the increased series resistance and the decreased edge effect of the device [54].

Huang et al. [55] found that the work functions (ϕ_w) of solution-processable, functional graphene/carbon nanotube-based transparent conductors were readily manipulated,

TABLE 3: PCE of BHJ OSCs using graphene as acceptor material.

Material	Device conformation	Highest PCE	Reference
SPFGraphene	ITO/PEDOT : PSS/P3OT : SPFGraphene/LiF/Al	1.40%	[56]
SPFGraphene	Glass/ITO/PEDOT : PSS/P3HT : SPFGraphene/LiF/Al	0.69%	[58]
SPFGraphene	ITO/PEDOT : PSS/P3HT : SPFGraphene/LiF/Al	1.10%	[64]
SPFGraphene	Glass/ITO/PEDOT : PSS/P3HT : SPFGraphene/LiF/Al	0.88%	[61]
Graphene	Glass/ITO/PEDOT : PSS/P3HT : PDI-G hybrid/LiF/Al	1.04%	[63]
SPFGraphene	Glass/ITO/PEDOT : PSS/P3HT : SPFGraphene/LiF/Al	1.046%	[66]
SPFGraphene	ITO/PEDOT : PSS/P3HT : PCBM : SPFGraphene/Al	1.40%	[67]
Graphene	Glass/ITO/PEDOT : PSS/C ₆₀ -G : P3HT/Al	1.22%	[62]
BCFG-F	Glass/ITO/PEDOT : PSS/P3HT : BCFG-F/LiF/Al	1.10%	[60]
SPFGraphene	Glass/ITO/PEDOT : PSS/P3HT : MDMO-PPV : SPFGraphene/LiF/Al	1.506%	[65]
Graphene	Glass/ITO/PEDOT : PSS/P3HT : PCBM : graphene/LiF/Al	0.70%	[59]

varying between 5.1 and 3.4 eV, depending on the nature of the doping alkali carbonate salt used. Highly conductive and transparent graphene-based electrodes with tunable work functions were prepared by combining single walled carbon nanotubes (SWCNTs) with chemically reduced graphene (rGO). Composite films were doped with alkali carbonates, which were decomposed into alkali oxides by means of thermal annealing that covered the carbon-based materials. Graphene-based electrodes possessing lower values of ϕ_w were used as cathodes in inverted-architecture polymer photovoltaic devices to effectively collect electrons. As expected, increasing the number of spin-layers from one to five provided thicker carbon composite films, thereby decreasing the optical transmittance at 550 nm from 88.8 (1 layer) to 58.7% (5 layers). Therefore, an optimal rGO-SWCNT thickness exists for optimal PV performance. The best PCE of the P3HT : PCBM photovoltaic device was achieved when incorporating the four-layer rGO-SWCNT (1.27%) [55].

According to the results presented in the previous section, the control of the work function of graphene layers constitutes the main strategy to improve the conductivity and the overall power conversion efficiency of BHJ solar cells using graphene as cathode material. This goal may be achieved following different procedures, for example, using interfacial layers or doping graphene films with different kind of agents. Other strategies to enhance the PCE include the tuning of the active layer thickness to maximize light absorption and charge transport. Regarding the preparation of the graphene electrode, CVD is the most used route, while lamination is the most commonly method used to deposit the electrode. However, the high processing temperature required for CVD limits the growth of graphene to a restricted number of substrates, which could have a negative impact on the performance of the BHJ device. Thus, it is clear that further enhancement in the conductivity of the graphene electrode is needed and constitutes the next step in order to increase the overall performance of the cathode-graphene-based devices. In the same way, the development of alternative methods for preparing large-area graphene films is required, since massive preparation of graphene films would be needed to satisfy global demand.

3. Active Layer Material

The active layer of an ideal BHJ solar cell is defined as a bicontinuous interpenetrating network of donor and acceptor at the nanometer scale with maximum interfacial area. In this case, excitons can always reach the D/A interface within their limited diffusion length and charge separation can occur efficiently. So far, the most successful active layer with BHJ architecture is based on either soluble P3HT or poly-3-octylthiophene (P3OT) as the donor and PCBM or PC₇₀BM (6,6-phenyl-C₇₀-butyric acid methyl ester) as the acceptor. Solar cells based on P3HT have exhibited PCE values approaching 5%, depending on the architecture of the device. On the other hand, it is known that PCBM is not the optimum acceptor material and limits the efficiency of the organic devices. Thus, new materials for both donor and acceptor with better HOMO/LUMO matching, stronger light absorption, and higher charge mobility with good stability are much needed [6, 56, 57]. In this section, the use of graphene as acceptor material is described, and the PCE and the conformation of BHJ devices using graphene are summarized in Table 3.

Liu et al. [58] used graphene as the acceptor material in BHJ organic photovoltaic cells. To achieve good dispersion of graphene, a solution-processable functionalized graphene (SPFGraphene) was prepared by a two-step method consisting of an oxidation step followed by an organic functionalization step. The oxidation treatment using a modified Hummers' method of the flake gave out graphene oxide sheets having a thickness of ~0.7 nm and a dimension of several hundreds of nanometers. Then, a phenyl isocyanate treatment gave out SPFGraphene that could be dissolved in organic solvent. The active layer was prepared by spin-coating using a P3HT/SPFGraphene solution in 1,2-dichlorobenzene (SPFGraphene content: 0%, 2.5%, 5%, 10%, and 15%). The current-voltage (J - V) curves of the photovoltaic devices were determined using an AM1.5G standard operating with an illumination intensity of 100 mW/cm². Under illumination, the device based on pristine P3HT gave PCE of 0.005%, while the P3HT/10%-SPFGraphene based device gave a maximum PCE value of 0.15%, which is much higher than that of the control device based on pristine P3HT. The authors

also reported that after annealing at 160°C for 10 min a top PCE of 0.69% for the P3HT/5%-SPFGraphene was registered [58].

Yu and Kuppa [59] investigated BHJ devices employing graphene nanosheets in the active layer. Solar cells based on P3HT:PCBM:graphene showed device physics significantly different from traditional BHJs and displayed a monotonic increase in performance with graphene concentration. The PCE of a device based on a P3HT:PCBM blend at a 20:2 concentration ratio was about 0.2%, while the addition of only small amounts of graphene (concentration ratio 20:2:0.01 for P3HT:PCBM:graphene) led to a better performance of about 0.7%. Hence, although the introduction of graphene sheets may have had a slightly negative effect on the V_{oc} and FF, the subsequent improvement in charge mobility and increase in J_{sc} compensated more for these drawbacks and led to an increase in efficiency [59].

Ye et al. [60] grafted a benzoic acid group onto pristine graphene (BCFG, graphene functionalized with benzoic acid) to improve its solubility and open a band gap of the resultant graphene. BCFG was esterified with 1H,1H,2H,2H-perfluoro-1-octanol to obtain BCFG-F, which was blended with P3HT to be used as the active layer in BHJ devices. Solar cells of P3HT/BCFG-F with functionalized graphene content of 5 wt%, 7.5 wt%, 10 wt%, and 12.5 wt% (ratio to P3HT) were fabricated. PCEs of 0.24, 0.46, 1.1, and 0.48 were obtained for these devices, respectively. In order to realize the dependence of the photovoltaic performance on the BCFG-F content, the surface morphology of the composites used as active layer was investigated. It was found that, in composite films containing 5 wt% of BCFG-F, only a few functionalized graphene sheets could be seen embedded in the P3HT matrix. Therefore, for low BCFG-F content, it cannot form enough P3HT/BCFG-F interfaces, at which the separation of excitons occurs, and continuous pathways in the P3HT matrix for the effective electron transport. In the composite film with 10 wt% BCFG-F, there were more graphene sheets than in the film with 5 wt% and they were well dispersed in the P3HT matrix, to form abundant P3HT/BCFG-F interfaces for charge generation and interpenetrating networks. Finally, for the film of the composite with a 15 wt% content, the morphology of the film demonstrated great agglomerated forms by aggregated graphene sheets, which had a deleterious effect on exciton separation and charge transport in the active layer [60].

Liu et al. [61] designed an organic photovoltaic device based on an acceptor of solution-processable functionalized graphene (SPFGraphene). The tested devices were based on heterostructure polymer- (P3HT-) graphene composite layers as active layer. Different active layers were synthesized by means of spin-coating from a solution of 15 mg/mL P3HT in chlorobenzene with SPFGraphene content of 0 wt%, 1 wt%, 2.5 wt%, 5 wt%, 10 wt%, 12.5 wt%, and 15 wt%. Doping of graphene into P3HT resulted in appropriate energetic distance between HOMO and LUMO of the donor/acceptor for a high open circuit voltage and provided higher exciton dissociation volume mobility of carrier transport for a large short-circuit current density. The device containing only 10 wt% of graphene showed the best PCE (0.88%), an open

circuit voltage of 0.77 V, and a short-circuit current density of 3.72 mA/cm². SPFGraphene content was the main factor improving PCE. For smaller concentrations, such as 1 wt% and 2.5 wt%, the SPFGraphene film was too small to form a continuous donor/acceptor interface and the transport pathway for the active layer P3HT matrix. Therefore, the electron cannot effectively meet the donor/acceptor interface and transport smoothly through the active layer. However, if SPFGraphene is further increased to a concentration of 10 wt%, the SPFGraphene film can form a continuous donor/acceptor interface and produce a better way to be transported smoothly through P3HT matrix, improving the electronic transport. However, if there is a further increase in the concentration of SPFGraphene, such as 12.5 wt% and 15 wt%, then the aggregation of SPFGraphene occurred, reducing hole mobility and decreasing the number of extracted carriers [61].

Yu et al. [62] developed a lithiation reaction to covalently attach monosubstituted fullerene (C₆₀) onto graphene (G) nanosheets to be used as electron acceptors in P3HT-based BHJ solar cells. Graphene nanosheets were produced through reduction of GO in pure hydrazine and purified with toluene and methanol. Using C₆₀-G:P3HT (1:1 wt/wt), C₆₀:P3HT (1:1 wt/wt), and C₆₀/G mixture (i.e., 12 wt% graphene, physical blend without chemical functionalization):P3HT (1:1 wt/wt) as a control, the device performance of a series of BHJ solar cells using such materials as active layer was tested under AM1.5 illumination. A PCE of 0.47% was obtained for the C₆₀:P3HT system, while the C₆₀-G:P3HT system showed a PCE of 1.22%. The observed enhancement could be attributed to the improved electron transport due to the presence of the C₆₀-grafted graphene. In the case of the C₆₀:graphene device, the simple blending of C₆₀ with the graphene cannot ensure a good interfacial contact to facilitate strong electronic interactions for efficient electron transport between the two components. To make it even worse, graphene sheets easily aggregated in the composite film, due to poor miscibility, to show a detrimental effect on the charge separation/transport. Therefore, the overall device efficiency was not improved (0.44%) [62].

Liu et al. [56] reported the fabrication and performance of devices with BHJ structure using an organic SPFGraphene as electron-acceptor material and P3OT (poly(3-octylthiophene 2,5 diyl)) and P3HT as donor material. Devices with SPFGraphene content of 1 wt%, 5 wt%, and 15 wt% (ratio to P3OT) were fabricated. The authors indicated that the functionalized graphene material could be dispersed into organic solvent to form a homogeneous solution. Controlled annealing improved the device performance, and the best PCE of 1.4% (5 wt% SPFGraphene) was obtained using simulated 100 mW/cm² AM1.5G illumination after annealing during 20 min at 160°C. Although the reported PCE is moderate, it is comparable with most of the best devices using materials other than fullerenes as electron acceptors. Furthermore, there is much room for improvement, such as optimizing the graphene content, annealing temperature, and time further controlling the size and functionalized degree of graphene sheets and the device fabrication and structure [56].

Wang et al. [63] studied the role of graphene (rGO) as atomic and structural scaffold in the nucleation and assembly of organic nanostructures. The photovoltaic properties of the PDI (*N,N'*-dioctyl-3,4,9,10-perylenedicarboximide) and graphene hybrids were investigated to determine whether they offer enhanced performances over those of the individual constituents like PDI and G. PDI-G hybrids were prepared by the hydrothermal treatment of GO and PDI in DMF. The authors also investigated the performance of physically mixed PDI + G composites made of PDI and G; this system was used as a control to compare with the PDI-G hybrid wires in order to find out if the coating of G around the PDI wires offers any enhanced performance. Using BHJ cells tested under 100 mW/cm² AM1.5 illumination, it was found that PDI-G hybrid wires based cells showed a PCE of 1.04%, while PDI cells presented a PCE of only 0.064% [63].

Liu et al. [64] studied a BHJ device with an active layer consisting of P3HT and SPFGGraphene. According to their results, adding graphene to the P3HT induced a great quenching of the photoluminescence of the P3HT, indicating a strong electron/energy transfer from the P3HT to the graphene. The device containing only 10 wt% of graphene showed the best performance with a PCE of 1.1% under simulated AM1.5G conditions at 100 mW/cm² after an annealing treatment at 160°C for 10 min. The annealing treatment at 160°C greatly improved the device performance. However, overgenerous conditions such as those at 210°C resulted in a decrease in the device efficiency (0.57%) [64].

Wang et al. [65] reported on the fabrication of BHJ devices based on P3HT:SPFGGraphene doped with poly-2-methoxy-5-(30,70-dimethyloctyloxy)-1,4-phenylenevinylene (MDMO-PPV) and P3OT. In this work, the amount of MDMO-PPV incorporated to the P3HT:SPFGGraphene active layer was varied from 0 to 2 mg, while the amount of P3OT varied in the range from 0 to 3 mg. For further characterization, the solar cells were illuminated through the side of the ITO-coated glass plate. AM1.5G standard operating with an illuminated intensity of 100 mW xenon lamp was used as a broadband light source. The authors pointed out that nondoped P3HT:SPFGGraphene showed an efficiency of 1.046%. By incorporating different amounts of P3OT, the best efficiency obtained was of 1.12% when 1 mg of P3OT was added. On the other hand, a top efficiency of 1.506% was registered when 1.5 mg of MDMO-PPV was used [65].

Wang et al. [66] fabricated solar cell devices based on SPFGGraphene oxide and P3HT with different contents of SPFGGraphene oxide (0%, 2.5%, 5%, 7.5%, 10%, 12.5%, and 15%). The π -conjugation of graphene enables the polymers to be used as an active material for various functional devices, including photovoltaic devices. The pure P3HT thin film showed strong photoluminescence between 600 and 800 nm with excitation at 450 nm; however, the photoluminescence is remarkably reduced after doping of SPFGGraphene oxide, showing that efficient energy transfer occurred along the P3HT/SPFGGraphene oxide interface. The overall performance of the P3HT/SPFGGraphene oxide based devices was much higher than that of the pristine P3HT-based one. The improved photovoltaic performance was attributed to

the addition of the SPFGGraphene oxide, stating that there is an obvious charge transfer from the P3HT donor to the SPFGGraphene oxide acceptor. To recover the conjugated structure and conductivity of the graphene sheet through removing the organic functional groups from the SPFGGraphene oxide sheet, a thermal annealing process was carried out at 160°C at different times. The best PCE was obtained for a device containing 10 wt% of SPFGGraphene annealed during 10 min (1.046%) [66].

Liu et al. [67] tested a SPFGGraphene in P3HT/PCBM photovoltaic devices. Tested devices took advantage of the electron-accepting feature of fullerenes and the high electron transport capability of graphene. The photovoltaic performance was investigated for devices containing 0%, 1%, 2.5%, 5%, 10%, 12.5%, and 15% of graphene. The best results were obtained with P3HT:PCBM (1:1) mixture with 10 wt% of graphene with a PCE of 1.4% at illumination at 100 mW/cm² AM1.5. Results indicated that the addition of graphene enhanced the performance of polymer photovoltaic devices [67].

Different methods to obtain graphene-based materials have been developed (e.g., adhesive tape, epitaxial growth, and micromechanical cleavage). However, most of these methods are not suitable for low-cost, large-area optoelectronics. In this tenor, organic solution-processable materials are preferred for electronic applications due to their solubility using common solvents, which allow them to be used in polymer-composite based materials preparation. Solution-processable functionalized graphene (SPFGGraphene) is by far the most used functionalized graphene-based (Figure 4) material employed in the development of BHJ devices. Although the performance of the cells using this material is lower than the most efficient BHJ cells tested, it is clear that the use of graphene significantly increases the efficiency compared to the reference devices (i.e., without graphene) reported in each experiment. The key to improve the PCE of SPFGGraphene based materials seems to be related to the improvement of its miscibility, which will assure a good dispersion of the graphene in the polymer matrix. A better miscibility will also avoid agglomeration and its detrimental effects on charge separation/transport. Thus, in this way, the hole mobility and the number of extracted carriers will be increased. An improved solubility will also ensure a good interfacial contact to facilitate strong electronic interactions for a better charge generation. Another important factor to be considered is the graphene content that needs to be enough to form a continuous donor/acceptor interface and an efficient transport pathway for the active layer. Finally, annealing has proved to be an efficient treatment to increase power conversion efficiency since it considerably increases the V_{oc} of the device.

4. Transport/Extraction Layer Material

The interfaces between active layer and anode and cathode play an essential role in determining the overall device performance of organic electronics [68]. In a simple BHJ device, both the donor and acceptor phases are in direct

TABLE 4: PCE of BHJ OSCs using graphene as HTLs and EELs.

Material	Function	Device conformation	Highest PCE	Reference
GO	HTLs	ITO/GO/P3HT : PCBM/Al	3.50%	[78]
GO	HTLs	ITO/PEDOT : PSS : GO/P3HT : PCBM/LiF/Al	3.80%	[86]
GO	HTLs	ITO/GO : NiO _x /P3HT : PCBM/LiF/Al	3.48%	[79]
FLGs	HTLs	Glass/ITO/FLGs-PEDOT : PSS/P3HT : PCBM/Ca/Al	3.70%	[85]
mrGO	HTLs	Glass/ITO/mrGO/P3HT : PCBM/LiF/Al	3.98%	[81]
GO-OSO ₃ H	HTLs	ITO/GO-OSO ₃ H/P3HT : PCBM/Ca/Al	4.37%	[82]
GO	HTLs	ITO/GO/P3HT : PCBM/LiF/Al	3.25%	
GO-Cs	EELs	ITO/PEDOT : PSS/P3HT : PCBM/GO-Cs/Al	3.08%	[83]
GO/GO-Cs	HTLs/EELs	ITO/GO/P3HT : PCBM/GO-Cs/Al	3.67%	
UV/ozone-G	HTLs	ITO/UV/ozone-G/P3HT : PCBM/LiF/Al	3.00%	[80]
rGO	EELs	Glass/ITO/PEDOT : PSS/P3HT : PCBM/rGO-pyrene : PCBM/Al	3.89%	[84]

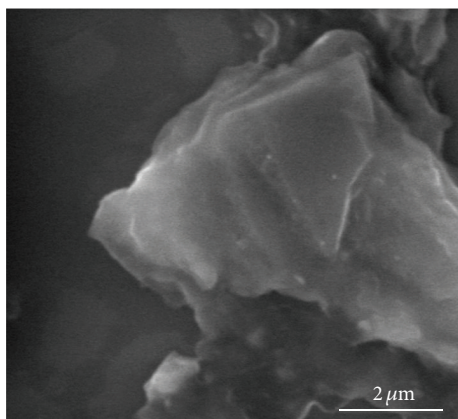


FIGURE 4: SEM micrograph of SPF Graphene.

electrical contact with the cathode and anode electrodes, leading to recombination of carriers and current leakage. To minimize such detrimental effects, hole transport layers (HTLs) and electron extraction layers (EELs) are used. HTLs must be wide band gap p-type materials; in this respect, several inorganic transition metal oxides such as molybdenum, nickel, rhenium, vanadium, or tungsten oxides (V₂O₅, ReO₃, WO₃, and MoO₃ with NiO being the most effective) have been reported yielding efficiencies greater than 5%. In a detrimental manner, inorganic HTLs are deposited using vacuum deposition methods that are incompatible with solution-processable printable electronic techniques used to fabricate photovoltaic devices [69–71].

The most commonly employed material used as HTLs in polymer solar cells is semiconducting PEDOT : PSS, which is used between the ITO anode and the active layer. PEDOT : PSS has the advantages of being deposited from solution and serve to minimize the detrimental effects of ITO roughness and to align the work function of P3HT and ITO for more efficient collection of holes. However, it is usually deposited from highly acidic aqueous suspensions that are known to corrode ITO at elevated temperatures and can also introduce water into the active layer, degrading the device performance [68, 72, 73].

On the other hand, certain metal fluorides, n-type semiconductors (e.g., TiO₂, TiO_x, and ZnO), n-type organic semiconductors (e.g., 2,9-dimethyl-4,7-diphenyl-1,10-phenanthroline, BCP), and conjugated polymer electrolytes have been used as the EELs [74–77]. Materials used as EELs need to have a low work function for electrons to be efficiently transported to the cathode.

Thus, several research groups, motivated by the need to overcome the limitations of PEDOT : PSS as the conventional HTLs by finding a suitable solution-processable alternative that is compatible with OSCs materials and fabrication techniques and by the need to find new materials to serve as both HTLs and EELs that could not only simplify the materials design and device fabrication but also allow for a precise control of the energy barrier for electron and hole extraction by tuning its work function via, for example, controlled functionalization, have reported their findings, which are summarized in the following section and in Table 4.

Li et al. [78] used graphene oxide thin films as the hole transport and electron extraction layer in OSCs. To evaluate the performance of GO devices, a set of two other devices was fabricated for comparison. One set was ITO-only control devices, and the other was the conventional OSCs incorporating PEDOT : PSS as the hole transport layer. The photovoltaic characteristics of the fabricated devices were characterized under simulated AM1.5 illumination at 100 mW/cm². ITO-only device exhibited an average PCE of 1.8%. The insertion of a 2 nm thick GO thin film between ITO and P3HT : PCBM led to an enhancement in the PCE to 3.5%, while the typical PEDOT : PSS typical device had shown a 3.6% PCE. Thus, the incorporation of GO deposited from neutral solutions between the photoactive P3HT : PCBM layer and the transparent and conducting ITO led to a decrease in recombination of electrons and holes and leakage currents, resulting in a dramatic increase in the device PCE to values that are comparable to devices fabricated with PEDOT : PSS as the hole transport layer. [78].

Ryu and Jang [79] reported a solution processed GO, NiO_x, and GO/NiO_x bilayer used as an anode interfacial layer in a BHJ device. In order to obtain the optimized thickness of GO layer, cells with different numbers of GO layers were fabricated by spin-coating. The best cell performance was

achieved for the cell with 3 GO layers, exhibiting a PCE of 2.75%, which was superior to that of the cell without HTL (2.33%). On the other hand, the device with a solution processed NiO_x layer showed an improved PCE of 3.10%. To further enhance cell performance of the device with GO and NiO_x , devices with GO/ NiO_x and NiO_x /GO were fabricated. Cell performance of the OSC with NiO_x /GO as HTLs was similar to the device with a NiO_x . However, the device with a GO/ NiO_x layer showed an enhanced cell performance, indicating a 15% increase in PCE, compared to the cell without HTL. These results indicated that the NiO_x functions both as a hole transport and an electron extraction layer. The device with a GO/ NiO_x showed a PCE of 3.48%. The cell efficiency is correlated with the matching of energy levels between ITO, hole transport layer, and P3HT and thus a well-matched GO/ NiO_x showed the best PCE [79].

Kwon et al. [80] fabricated organic devices using UV/ozone-treated graphene sheets as HTLs. A PEDOT:PSS-coated ITO device was used as reference and, in the case of the UV/ozone-treated graphene devices, the graphene was transferred onto the ITO glass following exposure to UV-ozone with a power of 30 mW/cm^2 for 1, 3, 5, 7, and 9 min. Cells were tested under AM1.5G 100 mW/cm^2 illumination. In the best case (UV-ozone treated device for 9 min), the sheet resistance increased from $1.1 \text{ k}\Omega/\text{sq}$ to infinity and the transmittance at 550 nm decreased from 95.2% to 93.8% due to the formation of carbon-oxygen functionalization layers. Although the device with 9 min treated graphene was expected to show the best efficiency (PCE of 1.46%) due to its highest work function (4.85 eV), the best PCE was obtained from the cell with 5 min treated graphene (3.00%) probably because the graphene sheet was damaged by UV-ozone exposure after 7 min, which roughened the surface creating defects [80].

Jeon et al. [81] used moderately reduced graphene oxide (mrGO) as an alternative to the PEDOT:PSS HTL in BHJ OSCs. mrGO films were fabricated by simple and fast thermal treatment of solution processed mrGO. Spin-coated mrGO layers were thermally treated at 150, 250, and 350°C for 10 min in air. Devices without and with thermal treatment at 150 and 250°C showed a well-formed 2-dimensional nanosheet. On the other hand, in the case of mrGO films thermally treated at 350°C , some aggregation of nanosheets and relatively nonuniform morphologies were observed. The thicknesses of nanosheets of mrGO without and with thermal treatment at 150, 250, and 350°C were estimated to 1.18, 1.07, 0.87, and 0.85 nm, respectively. The decrease in the thickness of single sheet resulted from the removal of oxygen groups, indicating that solution processed mrGO films were reduced by simple thermal treatment. Devices with thermally treated mrGO at 250°C exhibited the best PCE (3.98%) compared to devices containing conventional PEDOT:PSS HTLs, which showed 3.85%. Furthermore, mrGO-based cells showed superior stability compared to conventional devices under atmosphere condition without any encapsulation process [81].

Liu et al. [82] developed a sulfated graphene oxide (GO- OSO_3H) with $-\text{OSO}_3\text{H}$ groups attached to the carbon basal plane of reduced GO surrounded with edge-functionalized

$-\text{COOH}$ groups to be used as HTLs. Different devices based on GO and GO- OSO_3H were fabricated varying the thickness of the HTLs from 2 to 6 nm. The best results were obtained when using 2 nm thick HTLs. Because of the poor conductivity of GO, an increase in the GO thickness from 2 to 6 nm increased the series from 3.1 to $6.4 \Omega \text{ cm}^2$ and hence decreased the PCE. By contrast, the performance of the GO- OSO_3H -based devices is nearly independent of the HTLs thickness over the range from 2 to 6 nm. Compared to that of GO, the better conductivity of GO- OSO_3H led to an improved PCE of 4.37% versus 3.34% of GO. The control devices based on PEDOT:PSS exhibited a PCE of 4.39%. The relatively poor photovoltaic performance observed for the GO device can be attributed to high series resistance associated with the insulating GO. Compared with the GO-based devices, their GO- OSO_3H counterparts exhibited a much lower series resistance and hence a significantly improved PCE [82].

Liu et al. [83] reported on the functionalization of GO to produce both hole and electron extraction materials for BHJ solar cells. GO was tested as HTLs and GO-Cs, in which the periphery $-\text{COOH}$ groups in GO were replaced by $-\text{COOCs}$, as EELs. GO itself has a work function of 4.7 eV, which matches the HOMO level of P3HT for hole extraction. By replacing the periphery $-\text{COOH}$ with the $-\text{COOCs}$ groups through charge neutralization, the work function of the GO-Cs can be reduced to 4.0 eV, which matches the LUMO level of PCBM for efficient electron extraction. To investigate the hole extraction ability of GO, three different devices with the same active layer, cathode, and EELs were compared. The device with GO as HTLs showed a PCE of 3.25%, which was superior to that of the device using PEDOT:PSS (3.15%), implying that GO is an excellent hole extraction material for BHJ solar cells. Similarly, to evaluate the ability of GO-Cs as the electron extraction layer, four devices were fabricated with the same anode, hole extraction layer, active layer, and cathode. In this case, the device using LiF showed the best PCE (3.15%). However, the cell based on GO-Cs exhibited a fairly comparable PCE (3.08%) showing the great capability of GO-Cs as electron extraction material in BHJ solar cells. Finally, based on the excellent capabilities demonstrated for GO and GO-Cs, a pair of BHJ devices with both materials was fabricated. For this purpose, both the normal and inverted configurations were investigated. In both cases, the devices exhibited a better performance (3.67% and 2.97%, resp.) than that of the control device (1.20%) based on Cs_2CO_3 and PEDOT:PSS [83].

Qu et al. [84] reported a graphene fullerene composite (rGO-pyrene-PCBM), in which PCBM was attached onto rGO via the noncovalent functionalization approach. rGO-pyrene-PCBM was successfully applied as EELs for P3HT:PCBM BHJ devices, affording a PCE of 3.89%, which is enhanced by $\sim 15\%$ compared to that of the reference device without EELs (3.39%). Additionally, the comparative devices incorporating the rGO or pyrene-PCBM component as EELs showed dramatically decreased PCE, 2.53% and 2.18%, respectively, which are much lower than that of the reference device, indicating the importance of composite

formation between rGO and pyrene-PCBM components for its electron extraction property [84].

Nguyen et al. [85] demonstrated the use of a few-layered graphene nanosheets- (FLGs-) PEDOT : PSS composite as an effective HTL that improves the hole transporting ability in an organic device, with which the PCE was enhanced from 3.10% to 3.70%. FLGs are considered to be a class of graphene materials, namely, 2D graphitic crystals, with extraordinary electronic transport properties varied systematically by the number of graphene layers. FLGs were synthesized via exfoliation from expanded graphite, since this method produces a low defects material with an excellent conductivity. To demonstrate the application of the FLGs-PEDOT : PSS composite as HTLs, FLGs and PEDOT : PSS were mixed at different volume ratios (1/1, 2/1,) as a part of a BHJ device based on P3HT : PCBM. All samples were measured under light illumination of AM1.5 (100 mW/cm²). By increasing the v/v ratio of FLGs and PEDOT : PSS, PCE increased to 3.47% (1/1) and 3.70% (2/1). Due to partially containing oxygen groups on the graphene edges of FLGs, it was expected that the work function of the FLGs was in the range of 4.4 eV (graphite) to 5.1 eV (acid-oxidized MWCNTs), therefore possessing an energy level close to that of P3HT. Furthermore, no significant differences were found in surface roughness between the pure PEDOT : PSS and the FLGs-PEDOT : PSS composite films, indicating that the contact resistance between the active layer and the hole transport layer was unchanged in all devices. As a result, the significant improvement of current density is attributed to higher hole mobility of FLGs as compared with PEDOT : PSS [85].

Yin et al. [86] reported a high-efficiency device made with hydrophilic GO doped in PEDOT : PSS composites used as HTLs. The PCE of the nondoped composites was of 2.1% and increased to 3.8% for the doped composites under AM1.5G 100 mW/cm² illumination in air. Preannealing of GO made PCE 1.8 times that of the device based on PEDOT : PSS. The low price and ease of preparation make soluble graphene a promising layer to be used in photovoltaic applications [86].

GO-based materials are the most used replacement for PEDOT : PSS, which is the most commonly used hole transport layer material despite its highly acidic nature and hygroscopic properties which leads to a poor long term stability of the device. A major advantage of GO-based materials relies on the fact that they can be deposited from neutral aqueous suspensions and yield efficiency values that are comparable to devices fabricated with PEDOT : PSS, not to mention that the term stability of the device is not compromised using this type of suspensions. On the other hand, the removal of oxygen from the structure of GO induces the transition of GO from an electrical insulator to a semiconductor. Thus, strategies to obtain functionalized GO using reagents with low toxicity constitute one of the main trends in this field research. Regarding EELs materials, the main goal seems to be to obtain low work function highly conductive materials to improve electrons mobility, which can achieve doping graphene with different chemical agents.

5. Conclusions

In this report, the various applications of graphene as a constituent of BHJ OSCs were discussed focusing on the PCE achieved by the graphene-based devices. Results indicate that there is a great room and need for the improvement of BHJ devices to compete with inorganic cells. However, there is also evidence that graphene and its derivatives can be successfully used as a main component of the different layers that constitute OSCs, giving the possibility to reduce the dependence on the materials traditionally employed. As for transparent electrode material, graphene has demonstrated great potential without the detrimental aspects of its traditional analogues; the main key to achieve a better performance relies on increasing the transparency and decreasing the sheet resistance of the graphene films. As for cathode material, the main aim is to control the work function mainly using interfacial layers or doping graphene films. Furthermore, its outstanding properties such as its band structure and dispersion ability have made it also adequate to be used as an acceptor material. The improvement of graphene miscibility to assure a good dispersion represents an important issue in order to increase the performance of the devices using graphene as a main constituent of the active layer. Additionally, its excellent charge extraction performance has made it viable to be used as transport/extraction material in BHJ cells. The main goal in this area is to obtain HTL-materials that can be deposited from neutral aqueous suspensions and highly conductive EEL-materials using different functionalization agents.

Conflict of Interests

The authors declare that there is no conflict of interests regarding the publication of this paper.

References

- [1] B. C. Thompson and J. M. J. Fréchet, "Polymer-fullerene composite solar cells," *Angewandte Chemie—International Edition*, vol. 47, no. 1, pp. 58–77, 2008.
- [2] X. Wan, G. Long, L. Huang, and Y. Chen, "Graphene—a promising material for organic photovoltaic cells," *Advanced Materials*, vol. 23, no. 45, pp. 5342–5358, 2011.
- [3] T. L. Benanti and D. Venkataraman, "Organic solar cells: an overview focusing on active layer morphology," *Photosynthesis Research*, vol. 87, no. 1, pp. 73–81, 2006.
- [4] M. Jørgensen, J. E. Carlé, R. R. Søndergaard et al., "The state of organic solar cells—a meta analysis," *Solar Energy Materials and Solar Cells*, vol. 119, pp. 84–93, 2013.
- [5] Z. Abidin, M. A. Alim, R. Saidur et al., "Solar energy harvesting with the application of nanotechnology," *Renewable and Sustainable Energy Reviews*, vol. 26, pp. 837–852, 2013.
- [6] E. Bundgaard and F. C. Krebs, "Low band gap polymers for organic photovoltaics," *Solar Energy Materials and Solar Cells*, vol. 91, no. 11, pp. 954–985, 2007.
- [7] N. Yeh and P. Yeh, "Organic solar cells: their developments and potentials," *Renewable and Sustainable Energy Reviews*, vol. 21, pp. 421–431, 2013.
- [8] A. K. Geim, "Graphene: status and prospects," *Science*, vol. 324, no. 5934, pp. 1530–1534, 2009.

- [9] M. Yang, Y. Hou, and N. A. Kotov, "Graphene-based multilayers: critical evaluation of materials assembly techniques," *Nano Today*, vol. 7, no. 5, pp. 430–447, 2012.
- [10] Z. Liu, D. He, Y. Wang, H. Wu, J. Wang, and H. Wang, "Improving photovoltaic properties by incorporating both SPFG-Graphene and functionalized multiwalled carbon nanotubes," *Solar Energy Materials and Solar Cells*, vol. 94, no. 12, pp. 2148–2153, 2010.
- [11] S. Stankovich, D. A. Dikin, G. H. B. Dommett et al., "Graphene-based composite materials," *Nature*, vol. 442, no. 7100, pp. 282–286, 2006.
- [12] G. Jo, M. Choe, C.-Y. Cho et al., "Large-scale patterned multilayer graphene films as transparent conducting electrodes for GaN light-emitting diodes," *Nanotechnology*, vol. 21, no. 17, Article ID 175201, 2010.
- [13] Y. Zhu, S. Murali, W. Cai et al., "Graphene and graphene oxide: synthesis, properties, and applications," *Advanced Materials*, vol. 22, no. 35, pp. 3906–3924, 2010.
- [14] G. Jo, S. Na, S. Oh et al., "Tuning of a graphene-electrode work function to enhance the efficiency of organic bulk heterojunction photovoltaic cells with an inverted structure," *Applied Physics Letters*, vol. 97, no. 21, pp. 213301–213303, 2010.
- [15] G. V. Dubacheva, C.-K. Liang, and D. M. Bassani, "Functional monolayers from carbon nanostructures—fullerenes, carbon nanotubes, and graphene—as novel materials for solar energy conversion," *Coordination Chemistry Reviews*, vol. 256, no. 21–22, pp. 2628–2639, 2012.
- [16] A. Iwan and A. Chuchmała, "Perspectives of applied graphene: polymer solar cells," *Progress in Polymer Science*, vol. 37, no. 12, pp. 1805–1828, 2012.
- [17] X. Du, I. Skachko, A. Barker, and E. Y. Andrei, "Approaching ballistic transport in suspended graphene," *Nature Nanotechnology*, vol. 3, no. 8, pp. 491–495, 2008.
- [18] X. Wan, Y. Huang, and Y. Chen, "Focusing on energy and optoelectronic applications: a journey for graphene and graphene oxide at large scale," *Accounts of Chemical Research*, vol. 45, no. 4, pp. 598–607, 2012.
- [19] R. Sengupta, M. Bhattacharya, S. Bandyopadhyay, and A. K. Bhowmick, "A review on the mechanical and electrical properties of graphite and modified graphite reinforced polymer composites," *Progress in Polymer Science*, vol. 36, no. 5, pp. 638–670, 2011.
- [20] M. Eizenberg and J. M. Blakely, "Carbon monolayer phase condensation on Ni(111)," *Surface Science*, vol. 82, no. 1, pp. 228–236, 1979.
- [21] T. Aizawa, R. Souda, S. Otani, Y. Ishizawa, and C. Oshima, "Anomalous bond of monolayer graphite on transition-metal carbide surfaces," *Physical Review Letters*, vol. 64, no. 7, pp. 768–771, 1990.
- [22] K. S. Novoselov, A. K. Geim, S. V. Morozov et al., "Electric field in atomically thin carbon films," *Science*, vol. 306, no. 5696, pp. 666–669, 2004.
- [23] C. Berger, Z. Song, X. Li et al., "Electronic confinement and coherence in patterned epitaxial graphene," *Science*, vol. 312, no. 5777, pp. 1191–1196, 2006.
- [24] S. J. Park and R. S. Ruoff, "Chemical methods for the production of graphenes," *Nature Nanotechnology*, vol. 4, no. 4, pp. 217–224, 2009.
- [25] P. Steurer, R. Wissert, R. Thomann, and R. Mülhaupt, "Functionalized graphenes and thermoplastic nanocomposites based upon expanded graphite oxide," *Macromolecular Rapid Communications*, vol. 30, no. 4–5, pp. 316–327, 2009.
- [26] H. C. Schniepp, J.-L. Li, M. J. McAllister et al., "Functionalized single graphene sheets derived from splitting graphite oxide," *The Journal of Physical Chemistry B*, vol. 110, no. 17, pp. 8535–8539, 2006.
- [27] M. J. McAllister, J.-L. Li, D. H. Adamson et al., "Single sheet functionalized graphene by oxidation and thermal expansion of graphite," *Chemistry of Materials*, vol. 19, no. 18, pp. 4396–4404, 2007.
- [28] J.-M. Yun, J.-S. Yeo, J. Kim et al., "Solution-processable reduced graphene oxide as a novel alternative to PEDOT:PSS hole transport layers for highly efficient and stable polymer solar cells," *Advanced Materials*, vol. 23, no. 42, pp. 4923–4928, 2011.
- [29] V. Yong and J. M. Tour, "Theoretical efficiency of nanostructured graphene-based photovoltaics," *Small*, vol. 6, no. 2, pp. 313–318, 2010.
- [30] T. Winzer, A. Knorr, and E. Malic, "Carrier multiplication in graphene," *Nano Letters*, vol. 10, no. 12, pp. 4839–4843, 2010.
- [31] P. V. Kamat, "Graphene-based nanoarchitectures. Anchoring semiconductor and metal nanoparticles on a two-dimensional carbon support," *Journal of Physical Chemistry Letters*, vol. 1, no. 2, pp. 520–527, 2010.
- [32] Y. H. Hu, H. Wang, and B. Hu, "Thinnest two-dimensional nanomaterial—graphene for solar energy," *Chem Sus Chem*, vol. 3, no. 7, pp. 782–796, 2010.
- [33] S. Bae, H. Kim, Y. Lee et al., "Roll-to-roll production of 30-inch graphene films for transparent electrodes," *Nature Nanotechnology*, vol. 5, no. 8, pp. 574–578, 2010.
- [34] Z. Yin, S. Sun, T. Salim et al., "Organic photovoltaic devices using highly flexible reduced graphene oxide films as transparent electrodes," *ACS Nano*, vol. 4, no. 9, pp. 5263–5268, 2010.
- [35] J. Wu, H. A. Becerril, Z. Bao, Z. Liu, Y. Chen, and P. Peumans, "Organic solar cells with solution-processed graphene transparent electrodes," *Applied Physics Letters*, vol. 92, Article ID 263302, 2008.
- [36] Y. Wang, S. W. Tong, X. F. Xu, B. Özyilmaz, and K. P. Loh, "Interface engineering of layer-by-layer stacked graphene anodes for high-performance organic solar cells," *Advanced Materials*, vol. 23, no. 13, pp. 1514–1518, 2011.
- [37] F. C. Krebs, M. Jørgensen, K. Norrman et al., "A complete process for production of flexible large area polymer solar cells entirely using screen printing—First public demonstration," *Solar Energy Materials and Solar Cells*, vol. 93, no. 4, pp. 422–441, 2009.
- [38] R. R. Nair, P. Blake, A. N. Grigorenko et al., "Fine structure constant defines visual transparency of graphene," *Science*, vol. 320, no. 5881, p. 1308, 2008.
- [39] Y. Zhang, Y.-W. Tan, H. L. Stormer, and P. Kim, "Experimental observation of the quantum Hall effect and Berry's phase in graphene," *Nature*, vol. 438, no. 7065, pp. 201–204, 2005.
- [40] A. K. Geim and K. S. Novoselov, "The rise of graphene," *Nature Materials*, vol. 6, no. 3, pp. 183–191, 2007.
- [41] K. Naito, N. Yoshinaga, E. Tsutsumi, and Y. Akasaka, "Transparent conducting film composed of graphene and silver nanowire stacked layers," *Synthetic Metals*, vol. 175, pp. 42–46, 2013.
- [42] X. Wang, L. Zhi, and K. Müllen, "Transparent, conductive graphene electrodes for dye-sensitized solar cells," *Nano Letters*, vol. 8, no. 1, pp. 323–327, 2008.
- [43] C. Gómez-Navarro, R. T. Weitz, A. M. Bittner et al., "Electronic transport properties of individual chemically reduced graphene oxide sheets," *Nano Letters*, vol. 7, no. 11, pp. 3499–3503, 2007.

- [44] Y. Wang, X. Chen, Y. Zhong, F. Zhu, and K. P. Loh, "Large area, continuous, few-layered graphene as anodes in organic photovoltaic devices," *Applied Physics Letters*, vol. 95, no. 6, Article ID 063302, 2009.
- [45] Y. Xu, G. Long, L. Huang et al., "Polymer photovoltaic devices with transparent graphene electrodes produced by spin-casting," *Carbon*, vol. 48, no. 11, pp. 3308–3311, 2010.
- [46] X. Wang, L. Zhi, N. Tsao, Ž. Tomović, J. Li, and K. Müllen, "Transparent carbon films as electrodes in organic solar cells," *Angewandte Chemie*, vol. 47, no. 16, pp. 2990–2992, 2008.
- [47] L. Gómez De Arco, Y. Zhang, C. W. Schlenker, K. Ryu, M. E. Thompson, and C. Zhou, "Continuous, highly flexible, and transparent graphene films by chemical vapor deposition for organic photovoltaics," *ACS Nano*, vol. 4, no. 5, pp. 2865–2873, 2010.
- [48] Y. U. Jung, S. Na, H. Kim, and S. Jun Kang, "Organic photovoltaic devices with low resistance multilayer graphene transparent electrodes," *Journal of Vacuum Science & Technology A: Vacuum, Surfaces, and Films*, vol. 30, no. 5, Article ID 050604, 2012.
- [49] M. Choe, B. H. Lee, G. Jo et al., "Efficient bulk-heterojunction photovoltaic cells with transparent multi-layer graphene electrodes," *Organic Electronics*, vol. 11, no. 11, pp. 1864–1869, 2010.
- [50] Y.-Y. Choi, S. J. Kang, H.-K. Kim, W. M. Choi, and S.-I. Na, "Multilayer graphene films as transparent electrodes for organic photovoltaic devices," *Solar Energy Materials and Solar Cells*, vol. 96, no. 1, pp. 281–285, 2012.
- [51] J. Geng, L. Liu, S. B. Yang et al., "A simple approach for preparing transparent conductive graphene films using the controlled chemical reduction of exfoliated graphene oxide in an aqueous suspension," *Journal of Physical Chemistry C*, vol. 114, no. 34, pp. 14433–14440, 2010.
- [52] Y.-Y. Lee, K.-H. Tu, C.-C. Yu et al., "Top laminated graphene electrode in a semitransparent polymer solar cell by simultaneous thermal annealing/releasing method," *ACS Nano*, vol. 5, no. 8, pp. 6564–6570, 2011.
- [53] M. Cox, A. Gorodetsky, B. Kim et al., "Single-layer graphene cathodes for organic photovoltaics," *Applied Physics Letters*, vol. 98, no. 12, Article ID 123303, 2011.
- [54] Z. Liu, J. Li, Z.-H. Sun, G. Tai, S.-P. Lau, and F. Yan, "The application of highly doped single-layer graphene as the top electrodes of semitransparent organic solar cells," *ACS Nano*, vol. 6, no. 1, pp. 810–818, 2012.
- [55] J.-H. Huang, J.-H. Fang, C.-C. Liu, and C.-W. Chu, "Effective work function modulation of graphene/carbon nanotube composite films as transparent cathodes for organic optoelectronics," *ACS Nano*, vol. 5, no. 8, pp. 6262–6271, 2011.
- [56] Z. Liu, Q. Liu, Y. Huang et al., "Organic photovoltaic devices based on a novel acceptor material: graphene," *Advanced Materials*, vol. 20, no. 20, pp. 3924–3930, 2008.
- [57] B. Thompson and J. Fréchet, "Polymer–fullerene composite solar cells," *Angewandte Chemie International Edition*, vol. 47, no. 1, pp. 58–77, 2008.
- [58] Q. Liu, Z. Liu, X. Zhang et al., "Organic photovoltaic cells based on an acceptor of soluble graphene," *Applied Physics Letters*, vol. 92, no. 22, Article ID 223303, 2008.
- [59] F. Yu and V. K. Kuppala, "Enhancement in the performance of organic photovoltaic devices with pristine graphene," *Materials Letters*, vol. 99, pp. 72–75, 2013.
- [60] L. Ye, T. Xiao, N. Zhao et al., "Derivatization of pristine graphene for bulk heterojunction polymeric photovoltaic devices," *Journal of Materials Chemistry*, vol. 22, no. 33, pp. 16723–16727, 2012.
- [61] Z. Liu, D. He, Y. Wang, H. Wu, and J. Wang, "Solution-processable functionalized graphene in donor/acceptor-type organic photovoltaic cells," *Solar Energy Materials and Solar Cells*, vol. 94, no. 7, pp. 1196–1200, 2010.
- [62] D. Yu, K. Park, M. Durstock, and L. Dai, "Fullerene-grafted graphene for efficient bulk heterojunction polymer photovoltaic devices," *The Journal of Physical Chemistry Letters*, vol. 2, no. 10, pp. 1113–1118, 2011.
- [63] S. Wang, B. M. Goh, K. K. Manga, Q. Bao, P. Yang, and K. P. Loh, "Graphene as atomic template and structural scaffold in the synthesis of graphene-organic hybrid wire with photovoltaic properties," *ACS Nano*, vol. 4, no. 10, pp. 6180–6186, 2010.
- [64] Q. Liu, Z. Liu, X. Zhang et al., "Polymer photovoltaic cells based on solution-processable graphene and P3HT," *Advanced Functional Materials*, vol. 19, no. 6, pp. 894–904, 2009.
- [65] J. Wang, Y. Wang, D. He et al., "Polymer bulk heterojunction photovoltaic devices based on complex donors and solution-processable functionalized graphene oxide," *Solar Energy Materials and Solar Cells*, vol. 96, no. 1, pp. 58–65, 2012.
- [66] J. Wang, Y. Wang, D. He et al., "Composition and annealing effects in solution-processable functionalized graphene oxide/P3HT based solar cells," *Synthetic Metals*, vol. 160, no. 23–24, pp. 2494–2500, 2010.
- [67] Z. Liu, D. He, Y. Wang, H. Wu, and J. Wang, "Graphene doping of P3HT:PCBM photovoltaic devices," *Synthetic Metals*, vol. 160, no. 9–10, pp. 1036–1039, 2010.
- [68] H. Ma, H. Yip, F. Huang, and A. K. Jen, "Interface engineering for organic electronics," *Advanced Functional Materials*, vol. 20, no. 9, pp. 1371–1388, 2010.
- [69] V. Shrotriya, G. Li, Y. Yao, C.-W. Chu, and Y. Yang, "Transition metal oxides as the buffer layer for polymer photovoltaic cells," *Applied Physics Letters*, vol. 88, no. 7, Article ID 073508, 2006.
- [70] M. D. Irwin, D. B. Buchholz, A. W. Hains, R. P. H. Chang, and T. J. Marks, "p-Type semiconducting nickel oxide as an efficiency-enhancing anode interfacial layer in polymer bulk-heterojunction solar cells," *Proceedings of the National Academy of Sciences of the United States of America*, vol. 105, no. 8, pp. 2783–2787, 2008.
- [71] J. Meyer, R. Khalandovsky, P. Görrn, and A. Kahn, "MoO₃ films spin-coated from a nanoparticle suspension for efficient hole-injection in organic electronics," *Advanced Materials*, vol. 23, no. 1, pp. 70–73, 2011.
- [72] Y.-H. Kim, S.-H. Lee, J. Noh, and S.-H. Han, "Performance and stability of electroluminescent device with self-assembled layers of poly(3,4-ethylenedioxythiophene)–poly(styrenesulfonate) and polyelectrolytes," *Thin Solid Films*, vol. 510, no. 1–2, pp. 305–310, 2006.
- [73] J. Van De Lagemaat, T. M. Barnes, G. Rumbles et al., "Organic solar cells with carbon nanotubes replacing In₂O₃:Sn as the transparent electrode," *Applied Physics Letters*, vol. 88, no. 23, Article ID 233503, 2006.
- [74] R. Steim, F. R. Kogler, and C. J. Brabec, "Interface materials for organic solar cells," *Journal of Materials Chemistry*, vol. 20, no. 13, pp. 2499–2512, 2010.
- [75] J. Y. Kim, S. H. Kim, H.-H. Lee et al., "New architecture for high-efficiency polymer photovoltaic cells using solution-based titanium oxide as an optical spacer," *Advanced Materials*, vol. 18, no. 5, pp. 572–576, 2006.
- [76] T.-Y. Chu, J. Lu, S. Beaupré et al., "Bulk heterojunction solar cells using thieno[3,4-c]pyrrole-4,6-dione and dithieno[3,2-b:2',3'-d]silole copolymer with a power conversion efficiency of 7.3%,"

- Journal of the American Chemical Society*, vol. 133, no. 12, pp. 4250–4253, 2011.
- [77] Z. He, C. Zhong, X. Huang et al., “Simultaneous enhancement of open-circuit voltage, short-circuit current density, and fill factor in polymer solar cells,” *Advanced Materials*, vol. 23, no. 40, pp. 4636–4643, 2011.
- [78] S.-S. Li, K.-H. Tu, C.-C. Lin, C.-W. Chen, and M. Chhowalla, “Solution-processable graphene oxide as an efficient hole transport layer in polymer solar cells,” *ACS Nano*, vol. 4, no. 6, pp. 3169–3174, 2010.
- [79] M. S. Ryu and J. Jang, “Effect of solution processed graphene oxide/nickel oxide bi-layer on cell performance of bulk-heterojunction organic photovoltaic,” *Solar Energy Materials and Solar Cells*, vol. 95, no. 10, pp. 2893–2896, 2011.
- [80] K. C. Kwon, W. J. Dong, G. H. Jung, J. Ham, J.-L. Lee, and S. Y. Kim, “Extension of stability in organic photovoltaic cells using UV/ozone-treated graphene sheets,” *Solar Energy Materials & Solar Cells*, vol. 109, pp. 148–154, 2013.
- [81] Y.-J. Jeon, J.-M. Yun, D.-Y. Kim, S.-I. Na, and S.-S. Kim, “High-performance polymer solar cells with moderately reduced graphene oxide as an efficient hole transporting layer,” *Solar Energy Materials and Solar Cells*, vol. 105, pp. 96–102, 2012.
- [82] J. Liu, Y. Xue, and L. Dai, “Sulfated graphene oxide as a hole-extraction layer in high-performance polymer solar cells,” *Journal of Physical Chemistry Letters*, vol. 3, no. 14, pp. 1928–1933, 2012.
- [83] J. Liu, Y. Xue, Y. Gao, D. Yu, M. Durstock, and L. Dai, “Hole and electron extraction layers based on graphene oxide derivatives for high-performance bulk heterojunction solar cells,” *Advanced Materials*, vol. 24, no. 17, pp. 2228–2233, 2012.
- [84] S. Qu, M. Li, L. Xie et al., “Noncovalent functionalization of graphene attaching [6,6]-phenyl-C61-butyric acid methyl ester (PCBM) and application as electron extraction layer of polymer solar cells,” *ACS Nano*, vol. 7, no. 5, pp. 4070–4081, 2013.
- [85] D. D. Nguyen, N. H. Tai, Y. L. Chueh et al., “Synthesis of ethanol-soluble few-layer graphene nanosheets for flexible and transparent conducting composite films,” *Nanotechnology*, vol. 22, no. 29, Article ID 295606, 2011.
- [86] B. Yin, Q. Liu, L. Yang et al., “Buffer layer of PEDOT:PSS/graphene composite for polymer solar cells,” *Journal of Nanoscience and Nanotechnology*, vol. 10, no. 3, pp. 1934–1938, 2010.

Research Article

Synthesis of Carbon Encapsulated Mono- and Multi-Iron Nanoparticles

M. Reza Sanaee and Eric Bertran

FEMAN Grupo, Instituto de Nanociencia y Nanotecnología (IN2UB), Departament de Física Aplicada i Òptica, Universitat de Barcelona, Martí i Franquès 1, 08028 Barcelona, Spain

Correspondence should be addressed to M. Reza Sanaee; mreza_sanaee@yahoo.com

Received 16 December 2014; Revised 8 February 2015; Accepted 19 February 2015

Academic Editor: Dan Xia

Copyright © 2015 M. R. Sanaee and E. Bertran. This is an open access article distributed under the Creative Commons Attribution License, which permits unrestricted use, distribution, and reproduction in any medium, provided the original work is properly cited.

Core-shell nanostructures of carbon encapsulated iron nanoparticles (CEINPs) show unique properties and technological applications, because carbon shell provides extreme chemical stability and protects pure iron core against oxidation without impairing the possibility of functionalization of the carbon surface. Enhancing iron core magnetic properties and, in parallel, improving carbon shell sealing are the two major challenges in the synthesis of CEINPs. Here, we present the synthesis of both CEINPs and a new carbon encapsulated multi-iron nanoparticle by a new modified arc discharge reactor. The nanoparticle size, composition, and crystallinity and the magnetic properties have been studied. The morphological properties were observed by scanning electron microscopy and transmission electron microscopy. In order to evaluate carbon shell protection, the iron cores were characterized by selected area diffraction and fast Fourier transform techniques as well as by electron energy loss and energy dispersive X-ray spectroscopies. Afterward, the magnetic properties were investigated using a superconducting quantum interference device. As main results, spherical, oval, and multi-iron cores were controllably synthesized by this new modified arc discharge method. The carbon shell with high crystallinity exhibited sufficient protection against oxidation of pure iron cores. The presented results also provided new elements for understanding the growth mechanism of iron core and carbon shell.

1. Introduction

There has been an increasing interest in fabrication of magnetic based nanomaterials due to their potential applications in data storage [1], Li-ion battery [2], highly sensitive magnetic sensors [3], and spintronics devices [4]. Moreover, magnetic nanoparticles are attracting attention in both the medical and biological fields for applications including magnetic separation of biological entities [5], tissue engineering [6], food analysis [7], therapeutic drug delivery [8], hyperthermia for tumor therapy [9], contrast enhancement agents for magnetic resonance imaging applications [10, 11], water purification [12], and catalysis [13, 14]. Most of the studies in these areas focus on particles based on oxides since magnetic nanoparticles which are based on pure metallic materials are very sensitive to oxidation given their high specific surface area and reactivity [15].

The key point of using magnetic nanoparticles is the possibility and capability to control them by external magnetic field. Naked metallic nanoparticles are chemically highly active and are easily oxidized in air, resulting in negative effects on magnetic properties. To avoid such consequences, well developed graphitic carbon layers can provide an effective barrier to maintain magnetic properties. Coating metallic cores by silica [16], carbon [17–20], and precious-metal [21] is an example of popular inorganic coating approaches. Compared to the polymer, silica, or Au layer, the carbon layer has many advantages, such as higher chemical and thermal stability, better conductivity, and higher biocompatibility [22–24]. Moreover, carbon-coated nanoparticles are usually in the metallic state, and, compared to the corresponding oxides, they have a higher magnetic moment [25]. In particular, at present, a hot topic is magnetic carbon-coated metal (such as Fe, Co, Ni, and Mn) composites that are always

metal phase as the nucleus of core-shell structural composite nanomaterials [26].

In this research study, carbon encapsulated iron nanoparticles (CEINPs) were designed and produced in a way to make them suitable nanocarriers for biomedical applications. So far, different methods including arc discharge [27–29], hydrothermal reaction [30], chemical vapor deposition [31], detonation synthesis [32], chemical vapor condensation [33], magnetron and iron-beam cosputtering [34], laser ablation [35], and cocarbonization [36] are used to synthesize core-shell structures in which metallic nanoparticles are encapsulated by precious metals, polymers, silica, or carbon. However, each of these methods has particular advantages and disadvantages comparing to our method for synthesis of CEINPs. Until now, all reported studies have been only on monoiron nanoparticles and the synthesis of multi-iron core at carbon shell has not yet been reported [37–47].

In current nanoparticle fabrication processes, control of the particle size and composition is still empirical, which means that a large number of experimental trials are required to optimize any given process [48]. Plasma properties such as size, gradient temperature, thermal conductivity, and cooling rate mainly depend on the used inert gases. Consequently, all parameters are kept constant to study the influences of helium and nitrogen on morphologies properties as well as magnetic properties. Here, we present the synthesis of both CEINPs and carbon encapsulated multi-iron nanoparticles. The morphological properties were studied by scanning electron microscopy (SEM) and transmission electron microscopy (TEM). In order to verify the absence of iron oxide, the samples were analyzed by selected area diffraction (SAED), electron energy loss spectroscopy (EELS), and energy-dispersive X-ray spectroscopy (EDX) techniques as well as fast Fourier transform (FFT). In addition, carbon shell crystallinity was investigated by Raman spectroscopy. Afterward, the magnetic properties were obtained from superconducting quantum interference device (SQUID) characterization technique.

2. Experimental Details

A modified arc discharge reactor was utilized [49–51]. Nitrogen, helium, and their mixtures were used to synthesize each sample, from 0% to 100% of N_2 . Accordingly, each nanoparticle sample was named based on the nitrogen content; that is, 75% N + 25% H is N75. Two carbon graphite rods (99.99%) with mm thickness were prepared as cathode and anode. The cathode electrode was sharpening at an angle near to 20° . Both electrodes were placed in perpendicular position, in order to generate plasma between them. A needle was placed on top of them to deliver the precursor droplets. A spherical glass covered the whole reactor. Then, the precursor was prepared by dissolving ferrocene (0.5 wt %) in isooctane. Initially, rotary vane pump was used for making vacuum inside the glass chamber up to a pressure of 1 Pa. Afterward, the gases were introduced inside the glass chamber (continuous flow, 1.6 l/min). The pressure was kept at near atmospheric pressure condition by a micro valve. An arc was generated between anode and cathode by a programmable constant power supply which was set at 40 A for each production run

of 5 min. A syringe pump along with an injector regulates the droplets flow of precursor to the plasma zone (droplet flow rate 1 mL/min). Consequently, the synthesis process took place inside the glass chamber. Afterwards, by using ethanol, the nanoparticles were collected from the glass walls. Finally, nanoparticles were separated from ethanol through a magnetic filtration.

3. Results and Discussion

Influences of nitrogen and helium mixtures on CEINPs morphologies and magnetic properties were studied. As it is shown in Figure 1(a), SEM image reflects the CEINPs in spherical and agglomeration form. TEM images in Figures 1(b), 1(c), 1(d), 1(e), and 1(f) show geometry of each individual nanoparticle from N0, N25, N50, N75, and N100 samples, respectively. Spherical iron nanoparticles were observed with mean diameter of 7.5 nm in N0 samples. By adding 25% and 50% nitrogen, mainly oval shape iron nanoparticles with mean dimensions of 7.6×6.5 nm and $8 \text{ nm} \times 5.6$ nm were obtained in N25 and N50 samples, respectively. Afterwards, by adding 25% more nitrogen, iron nanoparticles tended to form comparatively smaller oval iron core with mean dimensions of $7.8 \text{ nm} \times 4.7$ nm in N75 sample. Using only nitrogen led to the formation of carbon encapsulated multi-iron nanoparticles (CEMINPs). Consequently, in case of N100 sample, the majority of nanoparticles have small multi-iron cores. CEMINPs mainly consisted of 1 nm and 2 nm spherical iron and one or two oval shaped $4.3 \text{ nm} \times 2.5$ nm iron nanoparticles. Figures 2(a) and 2(b) represent TEM images from N100 samples. However, as it is shown in Figure 2(c), iron particles with single oval shape and dimensions of $3 \text{ nm} \times 9$ nm were observed in N100 sample as well. In general, according to the TEM observations as we increased nitrogen gas percentage versus helium to generate plasma, the iron cores were forming oval shape. Based on TEM observations extremely small iron particles of 1 to 3 nm do not form a bigger single iron core and instead formed multi-iron core at carbon shell nanoparticle. Gutsch et al. discussed coalescence effect, which merges nanoparticles to form a bigger one in gas phase production of nanoparticles [52]. The condition of nucleation occurs in iron supersaturation vapor, which permits obtaining the particles with stable growth. Afterwards, coalescence occurs when the concentration is high enough. Once the carbon shell formation begins, the iron cores growth and coalescence are finished. Obtained results highlighted the coalescence effects on formation of iron nanoparticles from sample N100 to N0. The presence of oval iron nanoparticles and multi-iron cores shows the coalescence of the nucleus before starting carbon shell formation. The coalescence of only two iron particles was observed. This can be probably due to surpassing of the critical radius of carbon shell for the growth after the first iron coalescence.

The effect of nitrogen and helium in growth formation can be attributed to their differences in thermal conductivity and plasma temperature. Thermal conductivity of nitrogen is about 9 times smaller than helium. Thermal conductivity regulates the cooling rate and gradient of temperature.

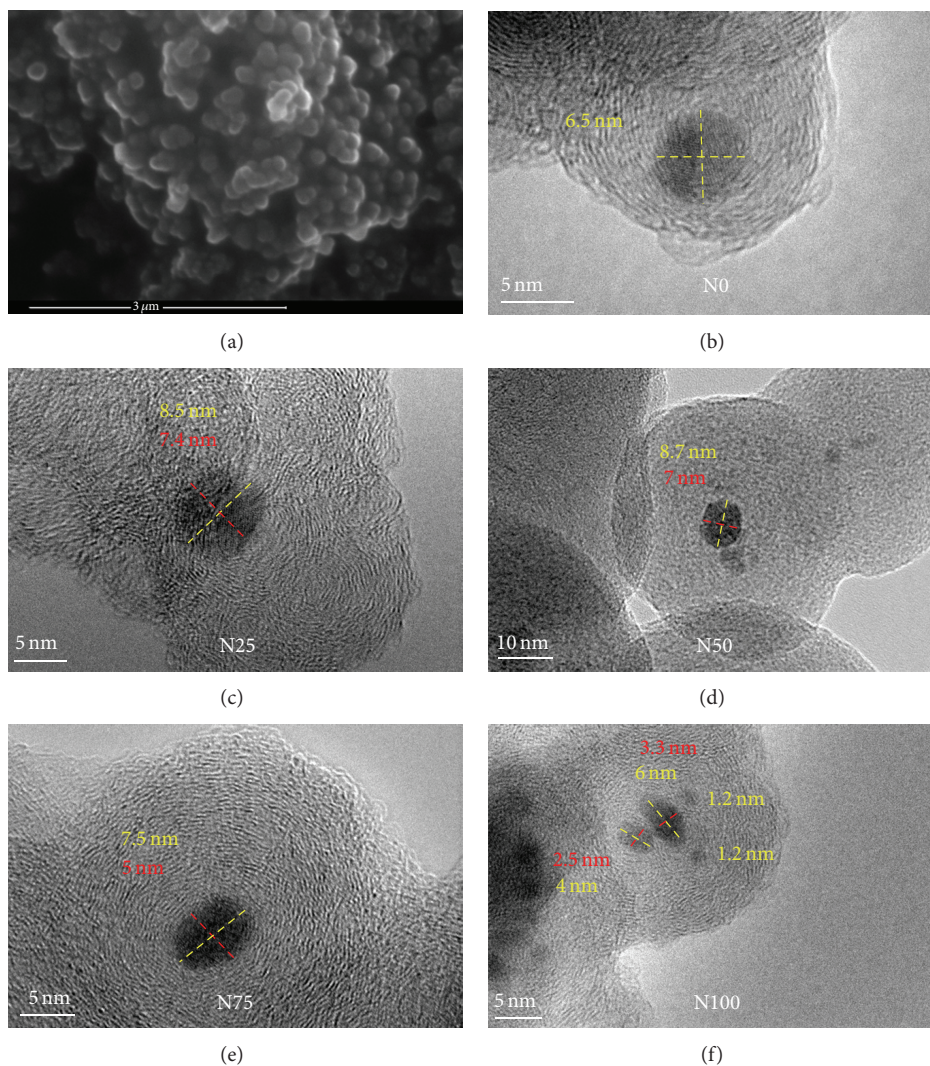


FIGURE 1: (a) SEM image shows agglomeration of CEINPs produced under nitrogen. (b), (c), (d), (e), and (f) TEM images of CEINPs and CEMINPs are shown from N0, N25, N50, N75, and N100 samples, respectively. It is evident that the morphologies of carbon and iron were changed by increasing nitrogen ratio over helium. The increasing trend in carbon shell formation and the decreasing trend in iron formation are remarkable. Merge and formation of iron nanoparticles from N100 to N0 revealed the role and effect of coalescence in formation of CEINPs and CEMINPs.

Thus comparatively nitrogen exhibits lower cooling rate and longer gradient of temperature over highly supersaturated vapor. Supersaturated vapor results in rapid production of numerous nanoparticles. In addition, relatively more carbon species are available in supersaturated vapor for carbon shell formation at higher temperature generated by nitrogen plasma rather than helium plasma. Accordingly, a decrease trend in carbon shell formation is obvious from sample N100 to N0 in Figure 1. It should be noted that the carbon shell formation limits the critical radius of iron. According to our observation when iron particles are small enough (1–3 nm) they are trapped into a single carbon shell.

Since nitrogen is diatomic gas, its plasma has higher energy contents for a given temperature than the atomic gases such as helium [53]. Because of high electronegativity of nitrogen, more energetic electrons are necessary to

produce self-sustained arc discharge. Consequently, when nitrogen is used due to the high temperature the carbon electrodes were deformed during the experiment (Figure S1 in Supplementary Material available online at <http://dx.doi.org/10.1155/2015/450183>). Regardless of inert gas type, in this arc discharge reactor the electron bombardment begins from cathode to anode and therefore the carbon from the anode electrode was consumed and deformed. This deformation caused changes in plasma shape, made it unstable and prevented continuous synthesis. Moreover, it has negative effect on formation and size distributions of CEINPs and CEMINPs. The size distributions of each sample are shown in Figure S2. N0 sample reveals the best iron size distribution comparing to the other samples, because by using only helium the carbon electrodes show smaller deformation. In spite of usefulness of presented method

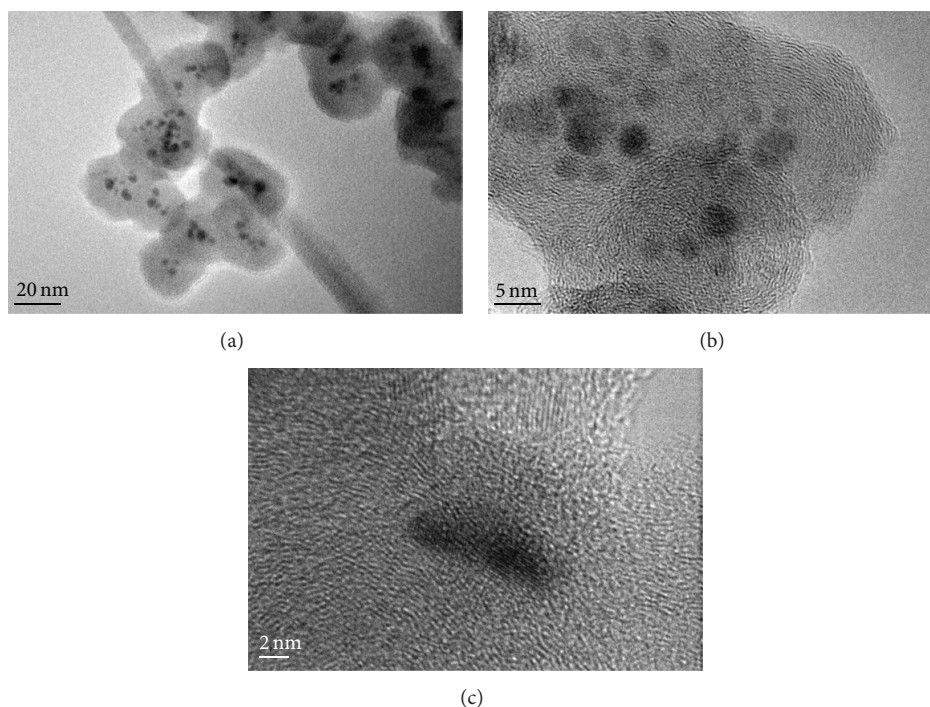


FIGURE 2: (a) Illustration of CEMINPs; the iron cores are located very close to each other. (b) Close observation of a few individual multi-iron cores at carbon shell nanoparticles. (c) Appearance of single oval shape iron nanoparticle in N100 samples; this is probably due to the coalescence between two particles.

for CEINPs and CEMINPs synthesis, plasma instability and discontinuous synthesis are the chief drawbacks. A brief investigation on the deformed carbon electrode by SEM has been done. SEM image from carbon piece taken from anode electrode is presented in Figure 3 and it revealed formation and deposition of spherical carbon particles on top of each other. Spaces between particles are visible clearly; therefore possibly this technique can be used for the synthesis and formation of carbon porous materials. Structure of carbon piece on anode suggests a mechanism of growth, which is large cross section of nanoparticles that facilitates the attachment of free electrons to the nanoparticles in the plasma region, therefore becoming attracted by anode due to the electrostatic forces. This contributes to forming very structured carbon deposition on anode electrode in Figure 3. Thinner carbon deposition on cathode was observed probably due to the neutral nanoparticles and negative radicals of carbon. Moreover, the cathode suffers a significant ion bombardment (e.g., CH_3^+ [54]). In addition, according to the given growth mechanism of CEINPs, the nitrogen plasma has higher temperature compared to helium plasma, which results in higher availability of carbon species. According to our observation, higher contribution of nitrogen shows an increase in deposition of carbon related structure on the electrodes.

Due to the importance of iron core sufficient protection and in order to show the efficiency of carbon shells against the oxidation of core, samples were evaluated by SAED and FFT techniques. SAED is shown in Figure 4(a); diffraction points of iron are indexed to α -Fe crystal structure as identified by diffraction rings corresponding to the $(-1, 0, 1)$ and

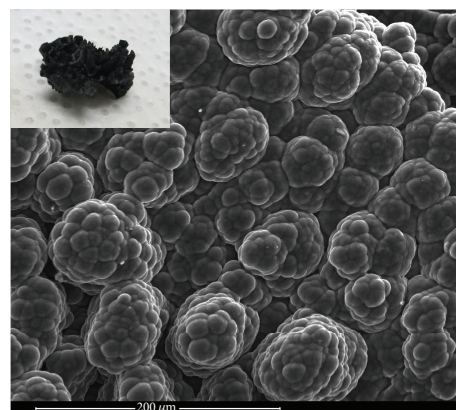


FIGURE 3: SEM image of CEINPs deposited on anode electrode when nitrogen plasma is used. The inset image is the carbon piece in question. Carbon spherical formation and the pores between them are clearly visible. Possibly nanopores also exist but cannot be observed at this resolution.

$(0, -1, 1)$ planes. However, as it is shown in Figure 4(b) from FFT analysis, trace of iron carbide was detected in interface between core and shell. Most importantly, diffraction points of iron oxides were not detected in any of our samples. In addition, nanoparticles were analyzed by EELS and EDX analysis along with chemical mapping. Figure 5 represents an example of EELS analysis at nanoscale and EDX together with chemical mapping at micro scale. As a result, absence of oxygen are confirmed in iron cores; therefore carbon shell

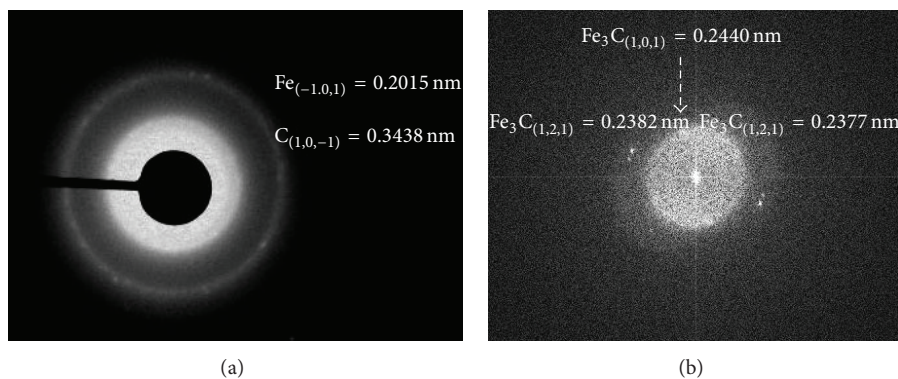


FIGURE 4: (a) SAED image reveals diffuse rings due to the presence of both nanocrystalline and amorphous phases. (b) FFT analysis shows trace of iron carbide.

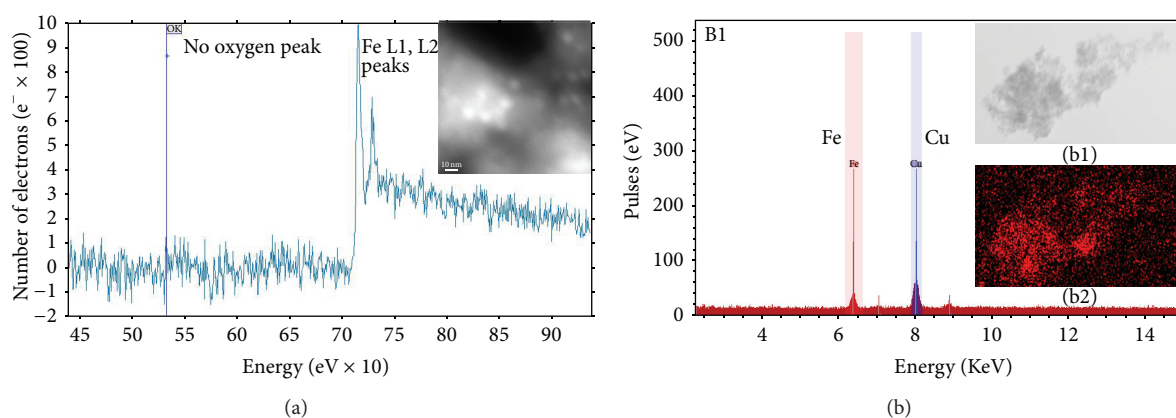


FIGURE 5: (a) Spectra of EELS analysis at nanoscale and associated TEM image are in the inset; EELS analysis shows no oxygen peak. (b) EDX analysis at microscale shows only Fe peak without oxygen peak as well (Cu peak is due to the grid). EDX associated TEM image is in (b1) inset, and associated chemical mapping is in (b2) inset; Red spots represent Fe.

properly sealed the iron cores in all samples. In addition, the fewer defects in carbon shell provide higher protection efficiency. Accordingly, carbon shells order/disorder structure was analyzed by RAMAN spectroscopy. The D-band of metal/C nanoparticles is considered to be a disorder-induced feature owing to lattice distortion or amorphous carbon background signal [55]. The peak intensity ratio I_D/I_G is often used to determine the extent of structural disorder in graphite and/or the size of the graphitic domains [56]. Thus, the decoupled I_D/I_G are considered. D and G peaks are located near ~ 1350 and ~ 1600 cm^{-1} , respectively. RAMAN spectra peak–height ratios I_D/I_G were determined from Lorentzian fittings as the example spectra shown in Figure 6(a). The carbon shells crystallinities degree (I_D/I_G) was obtained for each sample accordingly and was less than one for all samples, indicating high carbon crystallinity. Comparison of I_D/I_G of each sample in Figure 6(b) reveals slight decrease in I_D/I_G ratio as more nitrogen is used. This means that the graphitization degree of the samples increases slightly with increasing nitrogen gas concentration. Zhao et al. studied carbon nanostructures production by AC arc discharge plasma process at atmospheric pressure and concluded that the value of I_D/I_G decreases from 1.2 to 0.6 with the increasing arc

discharge current [57]. In their study, the temperature has been increased by increasing arc discharge electric current, while in our study the electric current was kept constant and the temperature was regulated according to the gas mixture of N_2/He at near atmospheric pressure. Nitrogen exhibits higher plasma temperature in comparison with helium plasma; the lowest I_D/I_G corresponds to N100 sample ($I_D/I_G \sim 0.81$), when only nitrogen is used.

Afterwards, the magnetic properties were characterized by superconducting quantum interference device (SQUID). CEINPs and CEMINPs magnetic behaviors were investigated at 300 K. Figure 7(a) represents comparison of normalized hysteresis curve for N100, N75, N50, N25, and N0 samples. The saturation magnetization for the nanocrystalline ferrites, in general, is found to be lower compared to their bulk value, which is attributed to surface spin effects [58]. Saturation magnetization largely depends on size, shape, metal composition, and crystalline magnetic anisotropy energy, as well as coating by nonmagnetic materials [52, 59]. N0 sample exhibits higher saturation magnetization than samples generated in presence of nitrogen. Therefore, from morphological point of view, as the iron cores are reforming from spherical shape to smaller oval shape, the saturation magnetization is

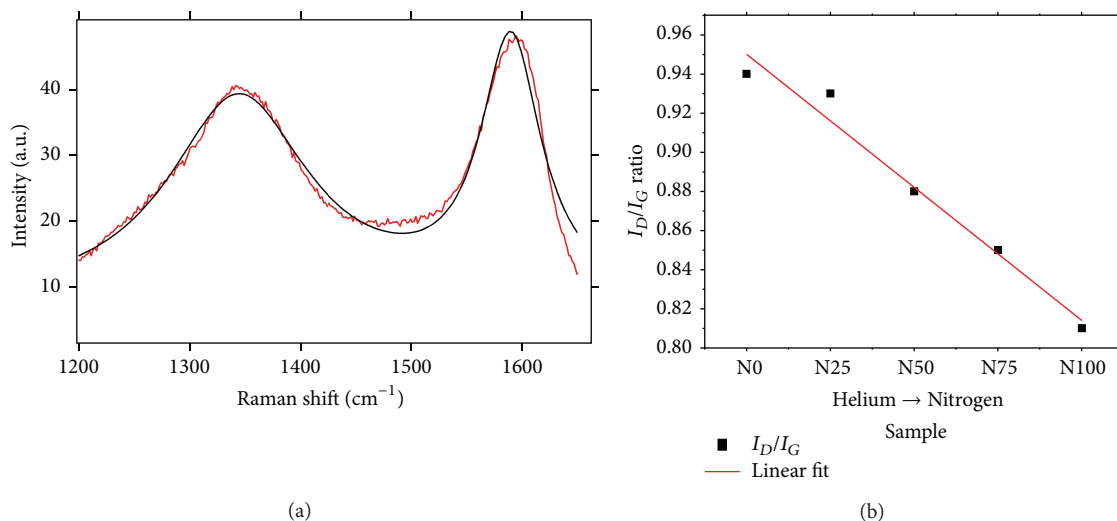


FIGURE 6: (a) Micro-Raman spectra of N100 sample fitted to Lorentzian function; D and G peaks are located near ~ 1350 and ~ 1600 cm^{-1} . (b) This graph shows comparison between I_D/I_G ratios for each sample. By using only helium (N0), the number of defects is always higher than samples that were obtained by using nitrogen and/or its mixture with helium.

decreasing. Size dependency of saturation magnetization is reported in the literature [60–62]. Interestingly, in spite of smaller iron cores, the multi-iron cores nanoparticles (N100 sample) exhibit higher saturation magnetization than single oval shape nanoparticles in N75 sample. Jafari et al. studied the effect of carbon shell on the structural and magnetic properties of Fe_3O_4 and concluded that the magnetization of Fe_3O_4 nanoparticles was reduced after coating with carbon [63]. Bittova et al. carried out a research study on the effects of coating on dipolar interparticle interactions and showed the reduction of saturation magnetization after coating as well [64]. In our samples, the single iron cores are mainly located in the center of a large carbon shell while the multi-iron cores are distributed in a carbon shell; therefore probably carbon shell has less negative magnetic effect to multi-iron cores comparatively due to higher average distance between center iron cores. Increasing the saturation magnetization of magnetic nanoparticles may permit more effective development of multifunctional agents for simultaneous targeted cell delivery, magnetic resonance imaging contrast enhancement, and targeted cancer therapy in the form of local hyperthermia [65]. Zero-field-cooling (ZFC) and field-cooling (FC) curves exhibit the main attribute of superparamagnetic system. ZFC and FC magnetization from N100 sample are plotted in Figure 7(b). All the samples were in superparamagnetic state at room temperature. Multi-iron cores nanoparticles blocking temperature (T_B) value (30 K) is lowest among the others, followed by N75, N50 43 K, N25, and N0 with 36 K, 43 K, 45 K, and 55 K, respectively. The T_B values versus median size from size distribution analysis are plotted in Figure 7(c). The finding that T_B decreases as the size of the nanoparticles decreases is consistent with conventional Stoner-Wohlfarth theory [66]: the energy barrier, over which the magnetization of the nanoparticles should be thermally activated, increases as the size of the nanoparticles increases. Consequently, the lowest T_B value of CEMINPs confirms the existence of

smaller iron nanoparticles comparing to other samples. The sum of multi-iron cores in each carbon shell is greater than a single oval shape in N75 sample but its T_B value is lower. This is an interesting characteristic of CEMINPs. The result of low T_B value opens the possibility of using superparamagnetic particles in applications that required high standard and needs to operate at very low temperatures such as sensors in aerospace industry. Moreover, magnetic properties results of presented CEMINPs and CEINPs are important because in principle interests in magnetic particles are all due to the possibility to governing, heating, and detecting them by external magnetic field for biomedical applications.

4. Conclusion

Mono- and multi-iron nanoparticles encapsulated in carbon shell were controllably synthesized using a new modified arc discharge reactor. Influence of nitrogen on plasma evidenced higher concentration of carbon species and changes the morphologies of CEINPs and CEMINPs. Moreover, the nature of gas has influences on yield of nanoparticles; in particular, nitrogen plasma provided highest yield in our study. The diffraction points of iron oxide were not detected from SAED and FFT techniques. In addition, EELS analysis at nanoscale and EDX analysis at microscale showed no trace of oxygen in iron cores; hence samples were well protected by carbon shells. Based on the Raman spectroscopy results, best carbon crystallinity is observed when only nitrogen is used. Sufficient iron core protection along with low defects of carbon shell structure promotes very small pores and therefore minimizes the possibility of iron oxidation, degradation, and/or possible toxicity; hence both CEINPs and CEMINPs are suitable for highly chemically active environment. All the particles show a superparamagnetic behavior at room temperature as determined by SQUID measurements. Lowest blocking temperature of 30 K evidenced the synthesis of smaller multicores

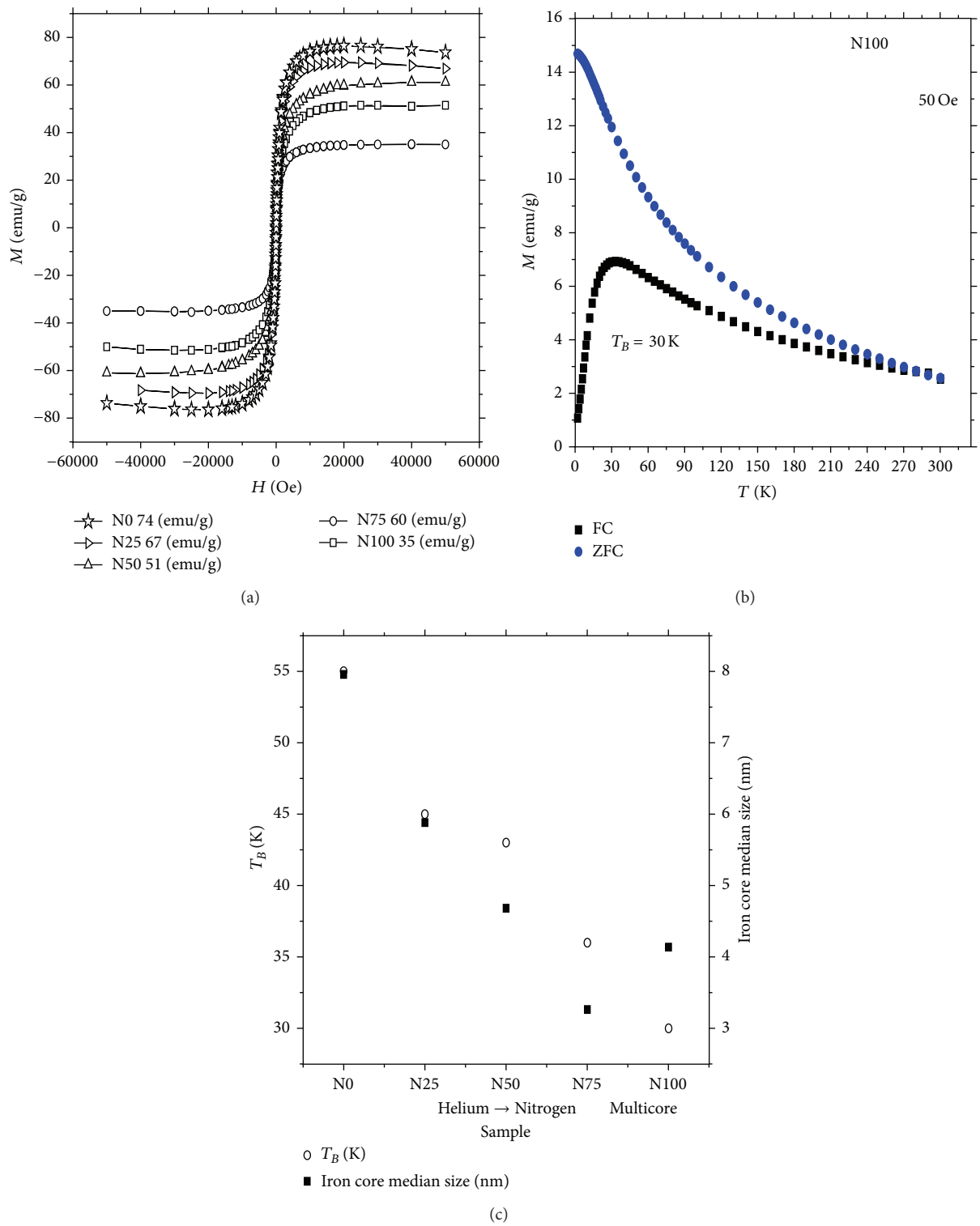


FIGURE 7: (a) Hysteresis curve comparison of N0, N25, N50, N75, and N100 samples and the saturation magnetization are 74, 67, 60, 35, and 51 (emu/g), respectively. (b) Zero-field-cooled and field-cooled magnetization curve of multi-iron core nanoparticles measured in 50 Oe. This type of nanoparticles exhibited low blocking temperature (30 K) and is in superparamagnetic state above 240 K. (c) This graph shows the changes between blocking temperature and iron median size for each sample.

than monocoresh nanoparticles. Interestingly, although multi-iron cores are smaller than iron core in CEINPs (N75), they exhibit higher saturation magnetization; one of the reasons can be the existence of a few iron cores in a single carbon shell and therefore carbon shell has lower negative effect on magnetic properties. Owing to the extremely close distance (around 2 nm) between iron cores in CEMINPs, there will be higher visibility comparing to CEINPs and therefore this type of nanoparticles has more priority to be used as contrast agent. On the other hand it is noteworthy to mention that, due to the carbon shell spherical shape and iron superparamagnetic behavior, their movement in body fluid can be smooth and controllable and hence the CEINPs can be potentially used in drug delivery. It is concluded that the gas nature of the reactor plasma used in the research project has significant effect on the morphological properties of CEINPs. Accordingly, by this method, CEINPs and CEMINPs can be synthesized based on the desired applications.

Conflict of Interests

The authors declare that there is no conflict of interests regarding the publication of this paper.

Acknowledgments

The authors acknowledge Centres Científics i Tecnològics of Universitat de Barcelona (CCIT-UB). This work was partially financed by the MICYN of Spanish Government, under Contract MAT2010 20468, and by AGAUR of Generalitat de Catalunya, under Contracts 2009SGR00185 and 2014SGR0948.

References

- [1] G. Reiss and A. Hütten, "Magnetic nanoparticles: applications beyond data storage," *Nature Materials*, vol. 4, no. 10, pp. 725–726, 2005.
- [2] Z. Yang and S. Wang, "High cycling performance cathode material: interconnected LiFePO₄/carbon nanoparticles fabricated by sol-gel method," *Journal of Nanomaterials*, vol. 2014, Article ID 801562, 7 pages, 2014.
- [3] L.-G. Zamfir, I. Geana, S. Bourigua et al., "Highly sensitive label-free immunosensor for ochratoxin A based on functionalized magnetic nanoparticles and EIS/SPR detection," *Sensors and Actuators B: Chemical*, vol. 159, no. 1, pp. 178–184, 2011.
- [4] S. Singamaneni, V. N. Bliznyuk, C. Binek, and E. Y. Tsybal, "Magnetic nanoparticles: recent advances in synthesis, self-assembly and applications," *Journal of Materials Chemistry*, vol. 21, no. 42, pp. 16819–16845, 2011.
- [5] M. Colombo, S. Carregal-Romero, M. F. Casula et al., "Biological applications of magnetic nanoparticles," *Chemical Society Reviews*, vol. 41, no. 11, pp. 4306–4334, 2012.
- [6] M. Ishii, R. Shibata, Y. Numaguchi et al., "Enhanced angiogenesis by transplantation of mesenchymal stem cell sheet created by a novel magnetic tissue engineering method," *Arteriosclerosis, Thrombosis, and Vascular Biology*, vol. 31, no. 10, pp. 2210–2215, 2011.
- [7] M. Cao, Z. Li, J. Wang et al., "Food related applications of magnetic iron oxide nanoparticles: enzyme immobilization, protein purification, and food analysis," *Trends in Food Science & Technology*, vol. 27, no. 1, pp. 47–56, 2012.
- [8] O. Veisheh, J. W. Gunn, and M. Zhang, "Design and fabrication of magnetic nanoparticles for targeted drug delivery and imaging," *Advanced Drug Delivery Reviews*, vol. 62, no. 3, pp. 284–304, 2010.
- [9] S. Yanase, J. Nomura, Y. Matsumura, H. Kato, and T. Tagawa, "Hyperthermia enhances the antitumor effect of photodynamic therapy with ALA hexyl ester in a squamous cell carcinoma tumor model," *Photodiagnosis and Photodynamic Therapy*, vol. 9, no. 4, pp. 369–375, 2012.
- [10] H. B. Na, I. C. Song, and T. Hyeon, "Inorganic nanoparticles for MRI contrast agents," *Advanced Materials*, vol. 21, no. 21, pp. 2133–2148, 2009.
- [11] A. Ruiz, G. Salas, M. Calero et al., "Short-chain PEG molecules strongly bound to magnetic nanoparticle for MRI long circulating agents," *Acta Biomaterialia*, vol. 9, no. 5, pp. 6421–6430, 2013.
- [12] R. D. Ambashta and M. Sillanpää, "Water purification using magnetic assistance: a review," *Journal of Hazardous Materials*, vol. 180, no. 1–3, pp. 38–49, 2010.
- [13] X. Zuo, C. Peng, Q. Huang et al., "Design of a carbon nanotube/magnetic nanoparticle-based peroxidase-like nanocomplex and its application for highly efficient catalytic oxidation of phenols," *Nano Research*, vol. 2, no. 8, pp. 617–623, 2009.
- [14] S. C. Tsang, V. Caps, I. Paraskevas, D. Chadwick, and D. Thompsett, "Magnetically separable, carbon-supported nanocatalysts for the manufacture of fine chemicals," *Angewandte Chemie*, vol. 43, no. 42, pp. 5645–5649, 2004.
- [15] M. Bystrzejewski, R. Klingeler, T. Gemming, B. Büchner, and M. H. Rummeli, "Synthesis of carbon-encapsulated iron nanoparticles by pyrolysis of iron citrate and poly(vinyl alcohol): a critical evaluation of yield and selectivity," *Nanotechnology*, vol. 22, no. 31, Article ID 315606, 2011.
- [16] A. G. Roca, D. Carmona, N. Miguel-Sancho et al., "Surface functionalization for tailoring the aggregation and magnetic behaviour of silica-coated iron oxide nanostructures," *Nanotechnology*, vol. 23, no. 15, Article ID 155603, 2012.
- [17] A. M. Nowicka, A. Kowalczyk, M. Bystrzejewski, M. Donten, and Z. Stojek, "Carbon-encapsulated iron nanoparticles used to generate magnetic field and to enhance substrate transport at electrode surface," *Electrochemistry Communications*, vol. 20, no. 1, pp. 4–6, 2012.
- [18] M. Reza Sanaee and E. Bertran, "Synthesis of carbon encapsulated iron nanoparticles for applications in biomedicine," *Journal of Nanomedicine and Nanotechnology*, vol. 4, no. 6, p. 219, 2013.
- [19] M. Reza Sanaee, V. M. Freire, N. Aguil, E. Bertran, and N. Aguiló-Aguayo, "Design and synthesis of carbon encapsulated iron nanoparticle for drug delivery," in *Proceedings of the 10th International Conference on Nano Bio and Med*, pp. 212–213, Phantoms Foundation, Bilbao, Spain, 2013.
- [20] K. Wang, Y. Huang, T. Han, Y. Zhao, H. Huang, and L. Xue, "Facile synthesis and performance of polypyrrole-coated hollow Zn₂SnO₄ boxes as anode materials for lithium-ion batteries," *Ceramics International*, vol. 40, no. 1, pp. 2359–2364, 2014.
- [21] W. Schärtl, "Current directions in core-shell nanoparticle design," *Nanoscale*, vol. 2, no. 6, pp. 829–843, 2010.
- [22] P. Wu, N. Du, H. Zhang, J. Yu, and D. Yang, "Carbon nanocapsules as nanoreactors for controllable synthesis of encapsulated iron and iron oxides: magnetic properties and reversible lithium

- storage,” *The Journal of Physical Chemistry C*, vol. 115, no. 9, pp. 3612–3620, 2011.
- [23] F. Avalos-Belmontes, L. F. Ramos-Devalle, E. Ramírez-Vargas, S. Sánchez-Valdes, J. Méndez-Nonel, and R. Zitzumbo-Guzmán, “Nucleating effect of carbon nanoparticles and their influence on the thermal and chemical stability of polypropylene,” *Journal of Nanomaterials*, vol. 2012, Article ID 406214, 8 pages, 2012.
- [24] Y. R. Uhm and C. K. Rhee, “Synthesis and magnetic properties of Ni and carbon coated Ni by levitational gas condensation (LGC),” *Journal of Nanomaterials*, vol. 2013, Article ID 427489, 6 pages, 2013.
- [25] Z. Chen, G. Hong, H. Wang et al., “Graphite-coated magnetic nanoparticle microarray for few-cells enrichment and detection,” *ACS Nano*, vol. 6, no. 2, pp. 1094–1101, 2012.
- [26] N. Luo, K. Liu, Z. Liu et al., “Controllable synthesis of carbon coated iron-based composite nanoparticles,” *Nanotechnology*, vol. 23, no. 47, Article ID 475603, 2012.
- [27] “Study of carbon encapsulated iron nanoparticles produced by a modified arc discharge by applying nitrogen, argon and helium,” in *Proceedings of the International Conference on Nanoscience and Nanotechnology*, pp. 160–161, Phantoms Foundation, Bilbao, Spain, 2013.
- [28] M. R. Sanaee, N. Aguiló-Aguayo, and E. Bertran, “Influences of argon-helium mixtures on the carbon-coated iron nanoparticles produced by a modified arc discharge,” in *Proceedings of the 9th International Conference on Nanoscience and Nanotechnologies*, p. 12, Artion, Thessaloniki, Greece, 2012.
- [29] L. Shen and N. Wang, “Effect of nitrogen pressure on the structure of Cr-N, Ta-N, Mo-N, and W-N nanocrystals synthesized by arc discharge,” *Journal of Nanomaterials*, vol. 2011, Article ID 781935, 5 pages, 2011.
- [30] S. Zhang, H. Niu, Z. Hu, Y. Cai, and Y. Shi, “Preparation of carbon coated Fe₃O₄ nanoparticles and their application for solid-phase extraction of polycyclic aromatic hydrocarbons from environmental water samples,” *Journal of Chromatography A*, vol. 1217, no. 29, pp. 4757–4764, 2010.
- [31] H. Cao, G. Huang, S. Xuan, Q. Wu, F. Gu, and C. Li, “Synthesis and characterization of carbon-coated iron core/shell nanostructures,” *Journal of Alloys and Compounds*, vol. 448, no. 1-2, pp. 272–276, 2008.
- [32] Y. Lu, Z. Zhu, and Z. Liu, “Carbon-encapsulated Fe nanoparticles from detonation-induced pyrolysis of ferrocene,” *Carbon*, vol. 43, no. 2, pp. 369–374, 2005.
- [33] Z. H. Wang, Z. D. Zhang, C. J. Choi, and B. K. Kim, “Structure and magnetic properties of Fe(C) and Co(C) nanocapsules prepared by chemical vapor condensation,” *Journal of Alloys and Compounds*, vol. 361, no. 1-2, pp. 289–293, 2003.
- [34] J. Nishijo, C. Okabe, J. Bushiri, K. Kosugi, N. Nishi, and H. Sawa, “Formation of carbon-encapsulated metallic nanoparticles from metal acetylides by electron beam irradiation,” *The European Physical Journal D—Atomic, Molecular, Optical and Plasma Physics*, vol. 34, no. 1-3, pp. 219–222, 2005.
- [35] J. B. Park, S. H. Jeong, M. S. Jeong, J. Y. Kim, and B. K. Cho, “Synthesis of carbon-encapsulated magnetic nanoparticles by pulsed laser irradiation of solution,” *Carbon*, vol. 46, no. 11, pp. 1369–1377, 2008.
- [36] J. Huo, H. Song, and X. Chen, “Preparation of carbon-encapsulated iron nanoparticles by co-carbonization of aromatic heavy oil and ferrocene,” *Carbon*, vol. 42, no. 15, pp. 3177–3182, 2004.
- [37] R. P. Chaudhary, S. K. Mohanty, and A. R. Koymen, “Novel method for synthesis of Fe core and C shell magnetic nanoparticles,” *Carbon*, vol. 79, pp. 67–73, 2014.
- [38] M. Zhao, H. Song, X. Chen, and W. Lian, “Large-scale synthesis of onion-like carbon nanoparticles by carbonization of phenolic resin,” *Acta Materialia*, vol. 55, no. 18, pp. 6144–6150, 2007.
- [39] N. Luo, X. Li, X. Wang, H. Yan, C. Zhang, and H. Wang, “Synthesis and characterization of carbon-encapsulated iron/iron carbide nanoparticles by a detonation method,” *Carbon*, vol. 48, no. 13, pp. 3858–3863, 2010.
- [40] M. Bystrzejewski, “Synthesis of carbon-encapsulated iron nanoparticles via solid state reduction of iron oxide nanoparticles,” *Journal of Solid State Chemistry*, vol. 184, no. 6, pp. 1492–1498, 2011.
- [41] Y. V. Fedoseeva, L. G. Bulusheva, A. V. Okotrub et al., “Effect of oxidation and heat treatment on the morphology and electronic structure of carbon-encapsulated iron carbide nanoparticles,” *Materials Chemistry and Physics*, vol. 135, no. 1, pp. 235–240, 2012.
- [42] Z. Abdullaeva, E. Omurzak, C. Iwamoto et al., “Onion-like carbon-encapsulated Co, Ni, and Fe magnetic nanoparticles with low cytotoxicity synthesized by a pulsed plasma in a liquid,” *Carbon*, vol. 50, no. 5, pp. 1776–1785, 2012.
- [43] V. Gupta, M. K. Patra, A. Shukla et al., “Synthesis of core-shell iron nanoparticles from decomposition of Fe-Sn nanocomposite and studies on their microwave absorption properties,” *Journal of Nanoparticle Research*, vol. 14, no. 12, article no. 1271, 2012.
- [44] M. Sharma, S. Mantri, and D. Bahadur, “Study of carbon encapsulated iron oxide/iron carbide nanocomposite for hyperthermia,” *Journal of Magnetism and Magnetic Materials*, vol. 324, no. 23, pp. 3975–3980, 2012.
- [45] H. Zhang, C. Liang, J. Liu, Z. Tian, and G. Shao, “The formation of onion-like carbon-encapsulated cobalt carbide core/shell nanoparticles by the laser ablation of metallic cobalt in acetone,” *Carbon*, vol. 55, pp. 108–115, 2013.
- [46] O. Łabędź, A. Grabias, W. Kaszuwara, and M. Bystrzejewski, “Influence of Al on synthesis and properties of carbon-encapsulated iron nanoparticles,” *Journal of Alloys and Compounds*, vol. 603, pp. 230–238, 2014.
- [47] A. Mostofizadeh, Y. Li, B. Song, and Y. Huang, “Synthesis, properties, and applications of low-dimensional carbon-related nanomaterials,” *Journal of Nanomaterials*, vol. 2011, Article ID 685081, 21 pages, 2011.
- [48] M. Shigeta and A. B. Murphy, “Thermal plasmas for nanofabrication,” *Journal of Physics D: Applied Physics*, vol. 44, no. 17, Article ID 174025, 2011.
- [49] E. Bertran-Serra and M. J. Inestrosa-Izurrieta, “Method and reactor for the production of carbon-coated nanoparticles,” Patent, Barcelona, Spain, 2012.
- [50] M. R. Sanaee, O. Arteaga, and E. Bertran, “Influence of plasma reactor parameters on carbon coating of iron nanoparticle,” in *Proceedings of the International Conference on Nanoscience and Nanotechnology*, p. 9, Phantoms Foundation, Madrid, Spain, 2014.
- [51] N. Aguiló-Aguayo, Z. Liu, E. Bertran, and J. Yang, “Thermal-induced structural evolution of carbon-encapsulated iron nanoparticles generated by two different methods,” *The Journal of Physical Chemistry C*, vol. 117, no. 37, pp. 19167–19174, 2013.
- [52] A. Gutsch, M. Krämer, G. Michael, H. Mühlenweg, M. Pridöhl, and G. Zimmermann, “Gas-phase production of nanoparticles,” *KONA Powder and Particle Journal*, vol. 20, pp. 24–37, 2002.

- [53] A. D. Gerdeman, *Arc Plasma Technology in Materials Science*, Springer, Berlin, Germany, 1972.
- [54] B. F. Gordiets, M. J. Inestrosa-Izurietta, A. Navarro, and E. Bertran, "Nanoparticles in SiH₄-Ar plasma: modelling and comparison with experimental data," *Journal of Applied Physics*, vol. 110, no. 10, Article ID 103302, 2011.
- [55] S. J. Lee, J. Jung, M. A. Kim, Y.-R. Kim, and J. K. Park, "Synthesis of highly stable graphite-encapsulated metal (Fe, Co, and Ni) nanoparticles," *Journal of Materials Science*, vol. 47, no. 23, pp. 8112–8117, 2012.
- [56] V. A. Sethuraman, L. J. Hardwick, V. Srinivasan, and R. Kostecki, "Surface structural disordering in graphite upon lithium intercalation/deintercalation," *Journal of Power Sources*, vol. 195, no. 11, pp. 3655–3660, 2010.
- [57] S. Zhao, R. Hong, Z. Luo, H. Lu, and B. Yan, "Carbon nanostructures production by AC arc discharge plasma process at atmospheric pressure," *Journal of Nanomaterials*, vol. 2011, Article ID 346206, 6 pages, 2011.
- [58] S. S. Kader, D. P. Paul, and S. M. Hoque, "Effect of temperature on the structural and magnetic properties of CuFe₂O₄ nano particle prepared by chemical co-precipitation method," *International Journal of Materials, Mechanics and Manufacturing*, vol. 2, no. 1, pp. 5–8, 2014.
- [59] T. Sato, T. Iijima, M. Seki, and N. Inagaki, "Magnetic properties of ultrafine ferrite particles," *Journal of Magnetism and Magnetic Materials*, vol. 65, no. 2-3, pp. 252–256, 1987.
- [60] P. Dutta, S. Pal, M. S. Seehra, N. Shah, and G. P. Huffman, "Size dependence of magnetic parameters and surface disorder in magnetite nanoparticles," *Journal of Applied Physics*, vol. 105, no. 7, Article ID 07B501, 2009.
- [61] R. D. Sánchez, J. Rivas, P. Vaqueiro, M. A. López-Quintela, and D. Caeiro, "Particle size effects on magnetic properties of yttrium iron garnets prepared by a sol-gel method," *Journal of Magnetism and Magnetic Materials*, vol. 247, no. 1, pp. 92–98, 2002.
- [62] M. S. Seehra, V. Singh, P. Dutta et al., "Size-dependent magnetic parameters of fcc FePt nanoparticles: applications to magnetic hyperthermia," *Journal of Physics D: Applied Physics*, vol. 43, no. 14, Article ID 145002, 2010.
- [63] A. Jafari, K. Boustani, and S. F. Shayesteh, "Effect of carbon shell on the structural and magnetic properties of Fe₃O₄ superparamagnetic nanoparticles," *Journal of Superconductivity and Novel Magnetism*, vol. 27, no. 1, pp. 187–194, 2014.
- [64] B. Bittova, J. Poltiero-Vejpravova, A. Roca, M. Morales, and V. Tyrpekl, "Effects of coating on magnetic properties in iron oxide nanoparticles," *Journal of Physics: Conference Series*, vol. 200, Article ID 072012, 2010.
- [65] C. G. Hadjipanayis, M. J. Bonder, S. Balakrishnan, X. Wang, H. Mao, and G. C. Hadjipanayis, "Metallic iron nanoparticles for MRI contrast enhancement and local hyperthermia," *Small*, vol. 4, no. 11, pp. 1925–1929, 2008.
- [66] Y. Lee, J. Lee, C. J. Bae et al., "Large-scale synthesis of uniform and crystalline magnetite nanoparticles using reverse micelles as nanoreactors under reflux conditions," *Advanced Functional Materials*, vol. 15, no. 3, pp. 503–509, 2005.

Research Article

Synthesis and Properties of Magnetic Carbon Nanocages Particles for Dye Removal

Hengfei Qin,¹ Yongkui Huang,¹ Siyu Liu,¹ Yao Fang,¹ Xi Li,¹ and Shifei Kang²

¹Department of Environmental Science and Engineering, Fudan University, Shanghai 200433, China

²Department of Environmental Science and Engineering, University of Shanghai for Science and Technology, Shanghai 200093, China

Correspondence should be addressed to Xi Li; xi_li@fudan.edu.cn and Shifei Kang; karmatimes@126.com

Received 30 May 2015; Revised 21 July 2015; Accepted 29 July 2015

Academic Editor: Yuan Chen

Copyright © 2015 Hengfei Qin et al. This is an open access article distributed under the Creative Commons Attribution License, which permits unrestricted use, distribution, and reproduction in any medium, provided the original work is properly cited.

Magnetic carbon nanocages (MCNCs) with multiform pore structure have been synthesized by a simple low temperature carbonization process. Biorenewable lignin was used as a cheap and carbon-rich precursor for the first time. The products were characterized by X-ray diffraction (XRD), nitrogen adsorption-desorption, energy dispersive X-ray spectroscopy (EDS), vibrating sample magnetometer (VSM), transmission electron microscopy (TEM), and Raman spectrum. XRD pattern and Raman spectrum showed that the product has a high degree of graphitization crystallinity. TEM micrograph indicated that the synthesized MCNCs have the hierarchical pore and cage structure. Due to these characteristics, the obtained magnetic carbon nanocages can be used as efficient and recycled adsorbents in the removal of dye staff from textile wastewater.

1. Introduction

Carbon materials, in their various forms such as carbon nanocages [1], porous materials [2], graphene [3], nanotubes [4], fibers [5], and activated carbons [6], had good adsorption, low density, high surface area, excellent electrical conductivity, and efficient catalytic activity. Among them are carbon nanocages (CNCs), an emerging engineered material, generally used as catalyst supports [7–11], adsorbents [12], electrode materials [13], lithium-ion batteries [14–19], supercapacitors [20, 21], drug delivery [22, 23], and sensors [24].

To date, various synthesis methods, for instance, chemical vapor deposition (CVD) [25], arc discharge, template approach [26], pyrolysis of organic precursors [27], and sol-gel method [28], had been developed to fabricate carbon nanocages. However, in most of these synthesis approaches, acetylene, ethanol, and pyridine were used as carbon sources, which are expensive and unsustainable fossil fuels; they may not be sufficient in near future. Furthermore, energy and environmental concerns have initiated and energized the research on the development of CNCs from renewable carbon

sources. As a result, it is crucial to switch over to the cheap and biorenewable carbon source.

Lignin, a cheap, nontoxic, and carbon-rich renewable resource, is the second most abundant biopolymer after cellulose in the nature [29]. Lignin is usually a waste discharged from paper and biomass bioethanol factories. However, the molecular structure of lignin consists of repeating units of the p-hydroxyphenyl (H), guaiacyl (G), and syringyl (S) (Figure 1) [30], which had a highly cross-linked structure close to the network of phenol resin [31, 32]. Thus, the reaction activity of lignin is similar to phenol. Phenol is a kind of toxic chemical intermediates, which was used to synthesize carbon materials [33–35]. Clearly, nontoxic and carbon-rich renewable lignin could replace the phenol as the precursor of carbon materials. Therefore, there are numerous reports of the use of lignin for the preparation of carbon fibers [36], activated carbons [37], carbon nanotube [38], and porous carbon materials [39]. Nevertheless, to the best of our knowledge, the carbon nanocages prepared by lignin have not yet been reported.

Herein, in this paper, for the first time we report a simple, low-cost, and environment-friendly method for preparing

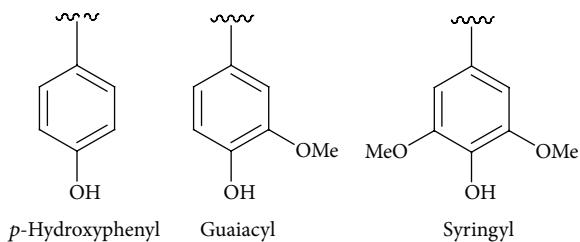


FIGURE 1: Lignin monomeric units.

magnetic carbon nanocages (MCNCs) by a low temperature carbonization process using lignin as the precursor. The structural properties of the obtained samples were characterized by nitrogen adsorption-desorption, X-ray diffraction, transmission electron microscopy, and Raman spectroscopy. Furthermore, lignin-based multiform pore structure and magnetic carbon nanocages used as the adsorbents of methyl orange were investigated.

2. Experimental

2.1. Synthesis of Magnetic Carbon Nanocages. All the chemicals were used as received without further purification. In a typical synthesis process: 1.0 g of lignin was added to 0.35 g of 20 wt% NaOH solution under stirring at 50°C, after 10 min, 1.15 g of formalin solution (37 wt% formalin) was added dropwise, and the reaction mixture was stirred at 70°C for 60 min. Upon cooling the mixture to 30°C, 0.21 g Fe(NO₃)₂·9H₂O was added to the mixture. After stirring for 30 min, the dark-brown oligomer was further polymerized at 100°C for 12 h and then peeled off and pyrolyzed at 600°C for 3 h with a ramping rate of 1°C/min under argon flow. Finally, the obtained material was washed with excess amounts of 1 M HNO₃ aqueous solution, deionized water and ethanol until a neutral pH, and dried in air at 100°C for 12 h. The produced sample was denoted as MCNCs. Commercial activated carbon (AC, Hebei Hua Jing activated Carbon Co., Ltd, S_{BET}: 800 m²·g⁻¹) was used as the reference material.

2.2. Measurements and Characterizations. The structural properties of the obtained MCNCs materials were identified using a Rigaku D/Max2rB-II X-ray diffractometer (XRD, CuK1 radiation, λ = 1.5406 Å), operated at 40 kV and 100 mA (scanning step 8°/s). Transmission electron microscope (TEM) images were recorded using a JEOL JEM-2010 electron microscope with an acceleration voltage of 200 kV. The Raman spectrum was recorded on a Horiba XploRA Raman microscope using a 532 nm argon ion laser. Nitrogen sorption isotherms were measured at -196°C on a Micromeritics ASAP 2000 apparatuses. The Brunauer-Emmett-Teller (BET) method was utilized to calculate the specific surface areas. The pore size distributions were derived from the desorption branches of the isotherms using the Barrett-Joyner-Halenda (BJH) method. VSM measurements were performed by using a vibrating sample magnetometer (Lake Shore 7410 VSM), and the magnetic property of nanocomposite is measured by a strong magnet. The absorbance of methyl orange was

measured by 752 type spectrophotometer whose operating voltage was AC 220 V/50 Hz.

2.3. Adsorption of Methyl Orange. In order to investigate the effect of important parameters (e.g., contact time and initial dye concentration) for the removal of MO dye, batch experiments were conducted. For each experimental run, the adsorbent (50 mg) and MO (50 mL) stock solutions were taken in a 250 mL stopper conical flask. This mixture was stirred at a constant speed for 4 hours at room temperature and then the mixture was separated by magnetic separation and the obtained supernatants were tested using a spectrophotometer at wavelength 461.0 nm. Particularly, the representative adsorbent (MCNCs) was withdrawn at different time intervals (0–200 min), separated, and analyzed for remaining dye concentration.

According to the decolorization rate formula for calculation and analysis, the corresponding curve was drawn and then the saturated adsorption capacity was calculated. The removal percentage, defined as the ratio of difference in initial MO concentration before and after adsorption ($C_0 - C$) to the initial MO concentration in the aqueous solution (C_0), was calculated using the following equation, while A_0 and A , respectively, represent the absorbance of MO before and after the adsorption [40, 41]:

$$Q = \left(1 - \frac{C}{C_0}\right) \times 100\% = \left(1 - \frac{A}{A_0}\right) \times 100\%. \quad (1)$$

Besides, the equilibrium adsorption capacities (Q_e) were determined according to the following formula [42]:

$$Q_e = \frac{(C_i - C_e)V}{M}, \quad (2)$$

wherein C_i is the initial concentration, C_e is the residual concentration, V is the volume of the solution, and M is the mass of the adsorbent.

In research on magnetic separability, 25 mg of adsorbent was added to 25 mL of MO dye solution (50 mg/L) in a bottle. The resulting mixture was stirred at room temperature for 60 min to reach adsorption equilibrium. Subsequently, a conventional laboratory magnet was placed near the glass bottle, and the solid-liquid separation was achieved within few minutes [41].

3. Results and Discussion

The magnetic carbon nanocages (MCNCs) with graphitic framework were evidenced by TEM analysis as shown in Figure 2. As can be seen, the sample consists of nanocages. The size and shape of the nanocages were not uniform, and the size of the nanocages was estimated to be 30–70 nm (Figure 2(a)). After acid treatment, a great deal of iron phase was eliminated, leaving a graphitic carbon nanocages structure as shown in Figure 2(b), but a small part of iron still residue in the graphitic carbon nanocages. Particularly, the Fe₃C particles remain within the cages as it is not in an ionic form after the acid treatment of Fe₃C by HNO₃.

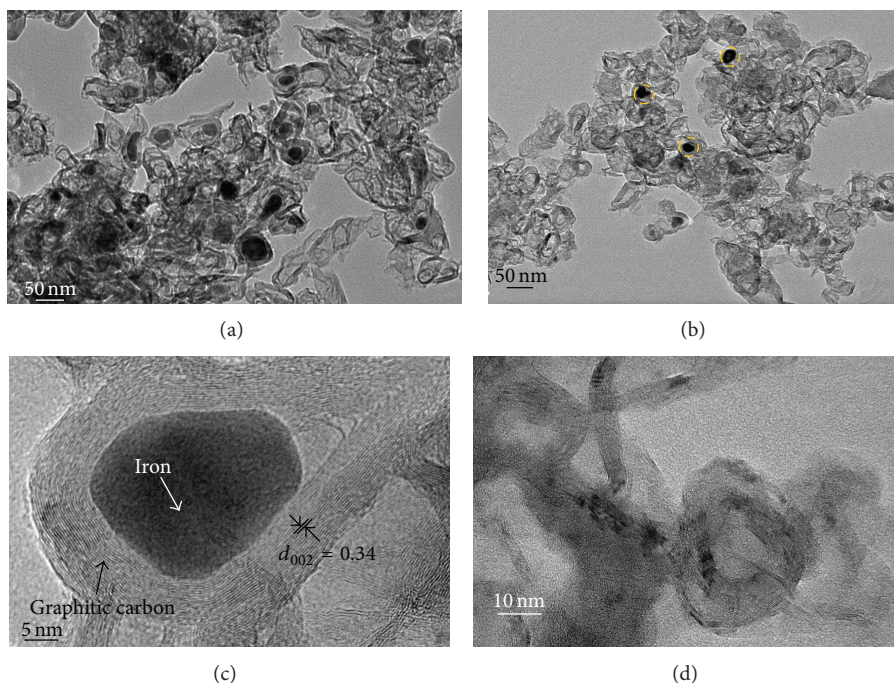


FIGURE 2: (a) TEM and (c) HRTEM image of magnetic carbon nanocages before acid treatment; (b) TEM and (d) HRTEM image of magnetic carbon nanocages after acid treatment.

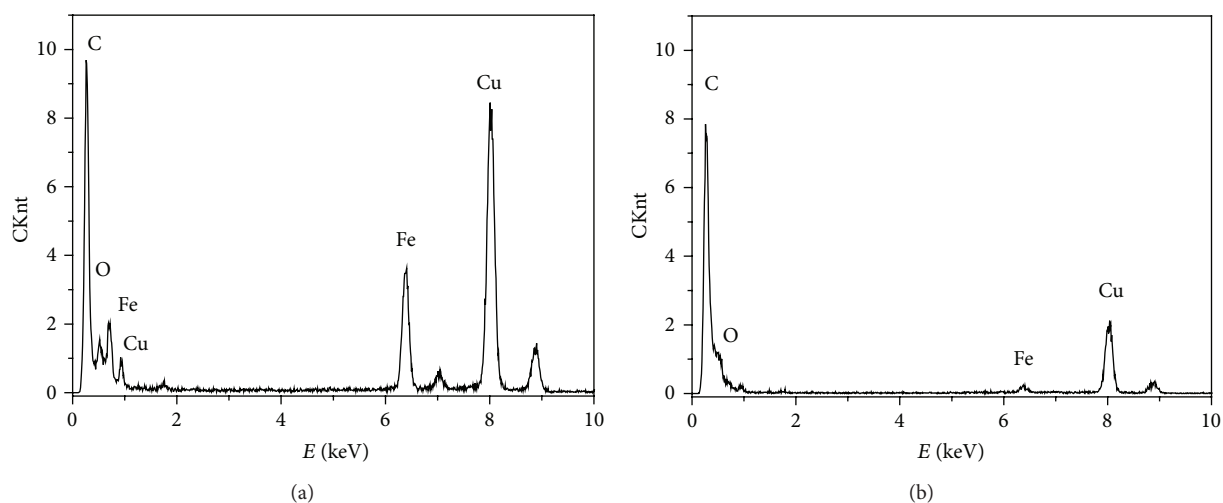


FIGURE 3: Energy dispersive X-ray spectroscopy (EDS) analysis of magnetic carbon nanocages before (a) and after (b) acid treatment, respectively.

The magnetic carbon nanocages had an average size of about 50 nm and a shell thickness ranging from 5 to 10 nm. HRTEM image illustrates that the nanocage shell was composed of about 28 well-defined graphitic layers with a spacing of 0.34 nm (Figures 2(c) and 2(d)), which is consistent with the (002) plane of graphite (Figure 4(a) JCPDS Card number 41-1487). The graphitization degree of the present MCNCs (Figure 2(d)) corresponded well to the results of XRD pattern and Raman spectrum (see below), which are similar to the previous work [43].

The structure of the magnetic carbon nanocages was studied using energy dispersive X-ray spectroscopy (EDX). The resulting spectrum is shown in Figure 3. As shown in this figure, the iron particles are present at 0.69, 6.41, and 6.38 keV before and after acid treatment, respectively. The peak at 6.38 keV (Figure 3(b)) can be attributed to the phase of iron particles after acid treatment. Energy dispersive X-ray spectroscopy (EDS) analysis (Figure 3(b)) confirmed the TEM result of the few iron nanoparticles residue in MCNCs (Figure 2(b)).

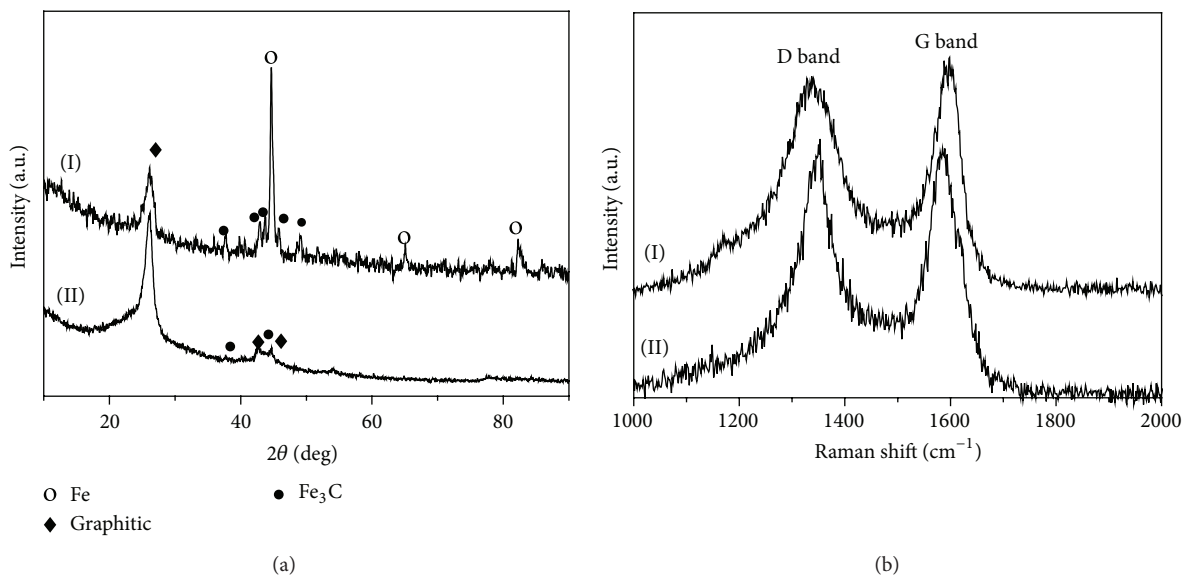


FIGURE 4: (a) XRD pattern and (b) Raman spectrum of the magnetic carbon nanocages before (I) and after treatment (II).

Figure 4(a) shows the wide-angle X-ray diffraction (XRD) pattern of magnetic carbon nanocages before and after acid treatment; the peaks at around 26.3° , 42.2° , and 44.3° can be indexed as (002), (100), and (101) diffraction planes of the graphite (JCPDS Card number 41-1487), respectively. The weak peaks located at about 37.4° , 42.7° , and 43.5° can be, respectively, indexed to the (121), (211), and (102) reflections of Fe₃C phases (JCPDS Card number 65-0393), while the other intense peaks at around 44.6° , 65.1° , and 82.3° can be indexed as (110), (200), and (211) diffraction planes of Fe (Figure 4(a), I, JCPDS Card number 65-4899). Compared with the original sample without acid treatment, the peaks of 44.6° , 65.1° , and 82.3° corresponding to Fe phases were no longer observed in the acid-treated sample, suggesting that the Fe was removed, but graphitic layers on the outer surface remained after acid treatment. The reflections of graphitic and Fe₃C planes were still visible on the XRD pattern of the after acid-treated sample; meanwhile, the peaks of 26.3° were intense (Figure 4(a), II). Maybe the iron carbides in graphite layers (Fe₃C@C) are difficult to be acid-treated.

To further investigate the graphitization state of magnetic carbon nanocages before and after acid treatment, Raman spectroscopy test was carried out to define the vibration of carbon species. As shown in Figure 4(b), the magnetic carbon nanocages exhibited a D band at 1338 cm^{-1} and a G band at 1586 cm^{-1} ; the D band is attributed to an A_{1g} vibration mode of carbon atoms with dangling bonds in plane terminations of disordered graphite [44]. The G band corresponds to the E_{2g} mode of hexagonal graphite and is related to the vibration of sp² hybridized carbon atoms in the graphite layer. The relative intensity of these two bands (I_D/I_G) can be used to reflect the degree of graphitization, which are calculated to be 1.72, 1.10 for before and after acid treatment, respectively. The greater the ratio of I_D/I_G is, the higher the disorder degree for graphite is. The relatively lower I_D/I_G value (1.10) combined

with a broad D band confirms that the after acid-treated magnetic carbon nanocages had better graphitization degree [45], which can be confirmed by its XRD pattern (Figure 4(a), II).

Nitrogen sorption isotherms were recorded to investigate the before and after acid treatment of the samples. Figure 5 gives the N₂ adsorption-desorption isotherm and corresponding pore size distribution curve of MCNCs. The isotherms (Figure 5(a)) exhibit a clear H₁-type hysteresis loop at a relative pressure of 0.5–0.7, indicating mesoporous characteristics with a capillary condensation phenomenon. The pore size distribution obtained from an analysis of desorption branch of the isotherms is shown in Figure 5(b). It can be seen that the MCNCs sample has bimodal pore size distributions centered at about 4.1, 30–65 nm and 0.57, 3.1, 30–65 nm of magnetic carbon nanocages before and after acid treatment, respectively. These sizes are close to the diameters of the nanocages observed by TEM (Figure 2). Specifically, the pores size 0.57 nm may be produced by the acid treatment for removal of the metallic iron nanoparticles. These magnetic carbon nanocages generally have high BET surface areas ($307.9, 420.5\text{ m}^2\cdot\text{g}^{-1}$) and large pore volumes ($0.69, 0.71\text{ cm}^3\cdot\text{g}^{-1}$); both are increasing with the removal of iron nanoparticles by acid treatment.

The magnetic properties of the synthesized carbon nanocages particles (Fe₃C) were characterized by magnetic hysteresis loops with varying magnetic field at room temperature and the obtained magnetization hysteresis loop is shown in Figure 6(a). The hysteresis loop of the carbon nanocages particles (Fe₃C) measured at 300 K shows typical soft magnetic behavior of the composite with a high saturation magnetization up to $19.1\text{ emu}\cdot\text{g}^{-1}$, low coercivity of 136.4 Oe , and low remanence of $2.5\text{ emu}\cdot\text{g}^{-1}$. Figure 6(a) (inset) shows the thermogravimetric analysis (TGA) of the magnetic carbon nanocages materials under the air atmosphere. From

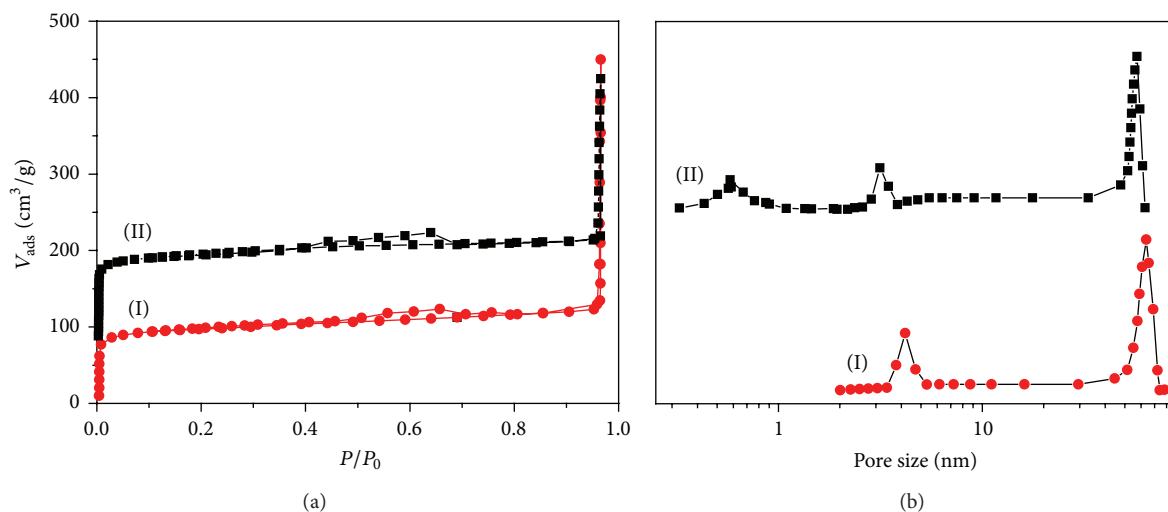


FIGURE 5: (a) N_2 adsorption-desorption isotherms and (b) pore size distribution curves of the magnetic carbon nanocages before (I) and after acid treatment (II).

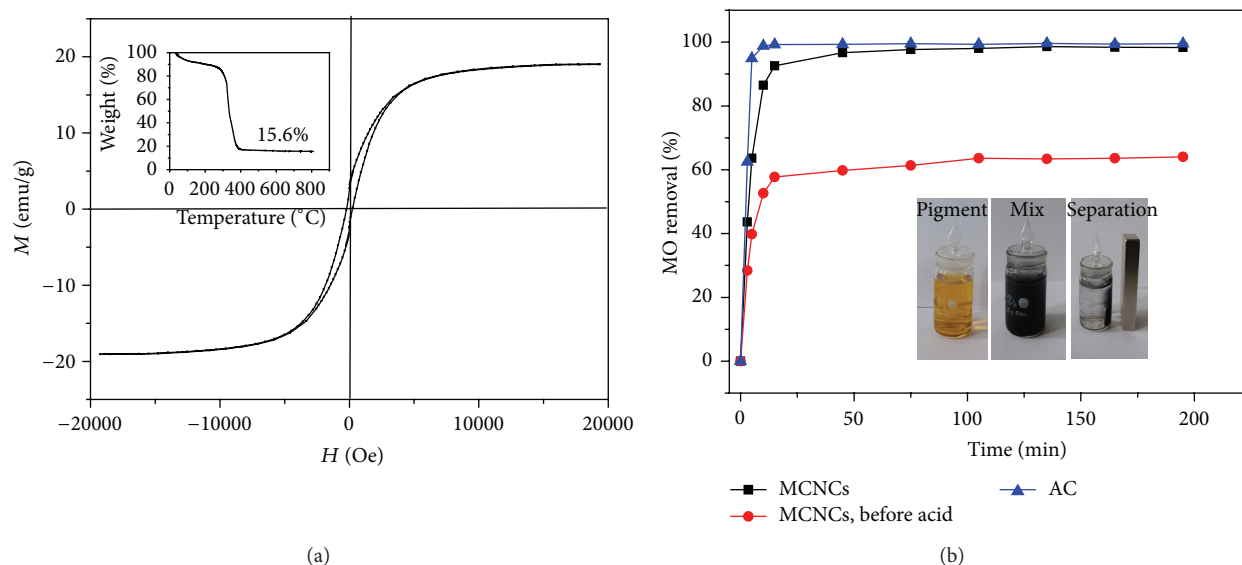


FIGURE 6: (a) Magnetization curves of the MCNCs and (b) the adsorption kinetics of MO onto the representative AC and MCNCs. The inset in (a) is the TGA curve of MCNCs. The inset in (b) is a photograph of dispersed MCNCs in MO solution after being attracted by an outer magnet.

TGA results we obtained the iron oxide content which is 15.6% in MCNCs. Based on calculation, the Fe_3C content is 17.5% in MCNCs.

Pollutants, especially textile dyestuffs, have caused overwhelming environmental pollution worldwide, which have triggered many studies' attention. Recent studies showed that magnetic materials with high surface area have a wide potential application for the removal various pollutants in wastewater, notably for textile dyestuffs [46–48]. In order to evaluate the adsorption behavior of magnetic carbon nanocages, we investigate their capacities by adsorbing MO dye from its aqueous solutions. Figure 6(b) presents the adsorption kinetics of MO dye onto the representative

magnetic carbon nanocages with a given initial MO dye concentration of 50 mg/L. MCNCs have obviously better removal ability than that of the MCNCs before acid, with adsorption rates of 43.6%, 63.6% and 28.4%, 39.8% in the first 3, 5 min, respectively. Then the dye was rapidly adsorbed in 15 min (92.6%), and subsequently the adsorption rate decreased gradually and reached equilibrium in about 60 min (97.7%). However, compared with commercial activated carbon, MCNCs adsorption rate is not fast enough, which the adsorption rates of 98.8% in 10 min.

Magnetic carbon nanocages (MCNCs) exhibit a higher adsorption capacity, which may be attributed to the triple synergy effect based on the special hierarchical pore and

nanocages structure of MCNCs. Firstly, dye molecules are easily adsorbed or condensed on the exterior surface of MCNCs. Secondly, When the adsorption of the exterior surface reached saturation, the dye molecules extended into the microporous and were adsorbed by the interior surface of MCNCs. Furthermore, it is conjectured that a certain amount of dye molecules may be adsorbed partially or fully filled in the hollow core of MCNCs.

As displayed in Figure 6(b) (inset), the magnetic carbon nanocages can be well-dispersed in MO solution; there was a change from black to colorless within few minutes by placing a conventional laboratory magnet near the glass bottle. That is to say, the black particles of magnetic carbon nanocages were attracted towards the magnet, and the clear solution could be easily decanted off or removed by pipette. It is proved that magnetic carbon nanocages possessed magnetism and could be potentially used as a magnetic adsorbent to remove organic dyes in liquid phase.

4. Conclusion

In conclusion, we demonstrate a simple route for the synthesis of magnetic carbon nanocages via a direct carbonization process by using biorenewable lignin as a carbon source. XRD, N₂ adsorption-desorption, EDS, VSM, TEM, and Raman results all consistently reveal that the synthesized magnetic carbon nanocages have a multiform pore structure, relative high specific surface area, and relative large pore volume, which are beneficial for the dye molecules diffusion/transfer in the absorbents and thereby result in the improvement of adsorption and separation properties. In addition, the experimental results indicate that the magnetic carbon nanocages exhibited a high capacity for methyl orange adsorption; the excellent adsorption performance of MCNCs can be attributed to its nanocage structure and hierarchical porosity.

Conflict of Interests

The authors declare that there is no conflict of interests regarding the publication of this paper.

Authors' Contribution

Hengfei Qin and Yongkui Huang equally contributed to this paper.

Acknowledgments

This work was carried out with financial supports from National Natural Science Foundation of China (Grant no. 61171008 and no. 21103024). This research was also supported by Yancheng Huanbo Energy Technology Co., Ltd., on field and fund. The authors would like to thank Qinming Liu Professor of Nanjing Forestry University for providing lignin and Chaochuang Yin, Yangling Xu for experimental technique support.

References

- [1] X. X. Wang, Z. H. Tan, M. Zeng, and J. N. Wang, "Carbon nanocages: a new support material for Pt catalyst with remarkably high durability," *Scientific Reports*, vol. 4, pp. 4437–4443, 2014.
- [2] Y. Yang, Z. J. Wei, C. Y. Wang, and Z. Tong, "Lignin-based Pickering HIPEs for macroporous foams and their enhanced adsorption of copper(II) ions," *Chemical Communications*, vol. 49, no. 64, pp. 7144–7146, 2013.
- [3] W. S. Liu, R. Zhou, D. Zhou et al., "Lignin-assisted direct exfoliation of graphite to graphene in aqueous media and its application in polymer composites," *Carbon*, vol. 83, pp. 188–197, 2015.
- [4] M. Y. Chen, Y. B. Huang, H. Pang, X. X. Liu, and Y. Fu, "Hydrodeoxygenation of lignin-derived phenols into alkanes over carbon nanotube supported Ru catalysts in biphasic systems," *Green Chemistry*, vol. 17, no. 3, pp. 1710–1717, 2015.
- [5] X. Xu, J. Zhou, L. Jiang, G. Lubineau, S. A. Payne, and D. Gutschmidt, "Lignin-based carbon fibers: carbon nanotube decoration and superior thermal stability," *Carbon*, vol. 80, no. 1, pp. 91–102, 2014.
- [6] J. Hayashi, K. Muroyama, V. G. Gomes, and A. P. Watkinson, "Fractal dimensions of activated carbons prepared from lignin by chemical activation," *Carbon*, vol. 40, no. 4, pp. 630–632, 2002.
- [7] S. Chen, J. Y. Bi, Y. Zhao et al., "Nitrogen-doped carbon nanocages as efficient metal-free electrocatalysts for oxygen reduction reaction," *Advanced Materials*, vol. 24, no. 41, pp. 5593–5597, 2012.
- [8] A. V. Erokhin, E. S. Lokteva, A. Y. Yermakov et al., "Phenylacetylene hydrogenation on Fe@C and Ni@C core-shell nanoparticles: about intrinsic activity of graphene-like carbon layer in H₂ activation," *Carbon*, vol. 74, pp. 291–301, 2014.
- [9] V. R. Galakhov, A. S. Shkvarin, A. S. Semenova et al., "Characterization of carbon-encapsulated nickel and iron nanoparticles by means of X-ray absorption and photoelectron spectroscopy," *Journal of Physical Chemistry C*, vol. 114, no. 51, pp. 22413–22416, 2010.
- [10] X. Li, F. Gai, B. Guan, Y. Zhang, Y. Liu, and Q. Huo, "Fe@C core-shell and Fe@C yolk-shell particles for effective removal of 4-chlorophenol," *Journal of Materials Chemistry A*, vol. 3, no. 7, pp. 3988–3994, 2015.
- [11] C. Xue, Q. Zhang, J. Li et al., "High photocatalytic activity of Fe₃O₄-SiO₂-TiO₂ functional particles with core-shell structure," *Journal of Nanomaterials*, vol. 2013, Article ID 762423, 8 pages, 2013.
- [12] G. D. Li, H. X. Yu, L. Q. Xu et al., "General synthesis of carbon nanocages and their adsorption of toxic compounds from cigarette smoke," *Nanoscale*, vol. 3, no. 8, pp. 3251–3257, 2011.
- [13] D. Yuan, J. Chen, J. Zeng, and S. Tan, "Preparation of monodisperse carbon nanospheres for electrochemical capacitors," *Electrochemistry Communications*, vol. 10, no. 7, pp. 1067–1070, 2008.
- [14] R. Feng, L. Wang, Z. Lyu et al., "Carbon nanocages supported LiFePO₄ nanoparticles as high-performance cathode for lithium ion batteries," *Acta Chimica Sinica*, vol. 72, no. 6, pp. 653–657, 2014.
- [15] G. D. Li, L. Q. Xu, Q. Hao, M. Wang, and Y. T. Qian, "Synthesis, characterization and application of carbon nanocages as anode materials for high-performance lithium-ion batteries," *RSC Advances*, vol. 2, no. 1, pp. 284–291, 2012.

- [16] K. X. Wang, Z. L. Li, Y. G. Wang et al., "Carbon nanocages with nanographene shell for high-rate lithium ion batteries," *Journal of Materials Chemistry*, vol. 20, no. 43, pp. 9748–9753, 2010.
- [17] S. B. Yang, X. L. Feng, L. J. Zhi, Q. A. Cao, J. Maier, and K. Müllen, "Nanographene-constructed hollow carbon spheres and their favorable electroactivity with respect to lithium storage," *Advanced Materials*, vol. 22, no. 7, pp. 838–845, 2010.
- [18] X. Y. Zheng, W. Lv, Y.-B. He et al., "3D hollow Sn@carbon-graphene hybrid material as promising anode for lithium-ion batteries," *Journal of Nanomaterials*, vol. 2014, Article ID 974285, 6 pages, 2014.
- [19] X. Ji, X. Huang, Q. Zhao, A. Wang, and X. Liu, "Facile synthesis of carbon-coated Zn₂SnO₄ nanomaterials as anode materials for lithium-ion batteries," *Journal of Nanomaterials*, vol. 2014, Article ID 169373, 6 pages, 2014.
- [20] J.-Z. Xia, L.-W. Wang, R.-Z. Hu et al., "Enhancement of supercapacitor performance of carbon nanocages by surface functionalization," *Chinese Journal of Inorganic Chemistry*, vol. 30, no. 9, pp. 2099–2104, 2014.
- [21] Y. Tan, C. Xu, G. Chen et al., "Synthesis of ultrathin nitrogen-doped graphitic carbon nanocages as advanced electrode materials for supercapacitor," *ACS Applied Materials & Interfaces*, vol. 5, no. 6, pp. 2241–2248, 2013.
- [22] C. S. Sharma, S. Patil, S. Saurabh, A. Sharma, and R. Venkataraghavan, "Resorcinol-formaldehyde based carbon nanospheres by electrospinning," *Bulletin of Materials Science*, vol. 32, no. 3, pp. 239–246, 2009.
- [23] C. Manaspon, K. Viravaidya-Pasuwat, and N. Pimpha, "Preparation of folate-conjugated pluronic F127/chitosan core-shell nanoparticles encapsulating doxorubicin for breast cancer treatment," *Journal of Nanomaterials*, vol. 2012, Article ID 593878, 11 pages, 2012.
- [24] A. Markwitz, J. Leveneur, P. Gupta, K. Suschke, J. Futter, and M. Rondeau, "Transition metal ion implantation into diamond-like carbon coatings: development of a base material for gas sensing applications," *Journal of Nanomaterials*, vol. 2015, Article ID 706417, 7 pages, 2015.
- [25] C. N. He, F. Tian, S. J. Liu et al., "Characterization and magnetic property of carbon coated metal nanoparticles and hollow carbon onions fabricated by CVD of methane," *Materials Letters*, vol. 62, no. 21–22, pp. 3697–3699, 2008.
- [26] J. Jang and B. Lim, "Selective fabrication of carbon nanocapsules and mesocellular foams by surface-modified colloidal silica templating," *Advanced Materials*, vol. 14, no. 19, pp. 1390–1393, 2002.
- [27] G. D. Li, C. L. Guo, C. H. Sun et al., "A facile approach for the synthesis of uniform hollow carbon nanospheres," *The Journal of Physical Chemistry C*, vol. 112, no. 6, pp. 1896–1900, 2008.
- [28] D. Kawashima, T. Aihara, Y. Kobayashi, T. Kyotani, and A. Tomita, "Preparation of mesoporous carbon from organic polymer/silica nanocomposite," *Chemistry of Materials*, vol. 12, no. 11, pp. 3397–3401, 2000.
- [29] T. Saito, R. H. Brown, M. A. Hunt et al., "Turning renewable resources into value-added polymer: development of lignin-based thermoplastic," *Green Chemistry*, vol. 14, no. 12, pp. 3295–3303, 2012.
- [30] K. Freudenberg, "Biosynthesis and constitution of lignin," *Nature*, vol. 183, no. 4669, pp. 1152–1155, 1959.
- [31] J. M. Pérez, F. Rodríguez, M. V. Alonso, M. Oliet, and J. M. Echeverría, "Characterization of a novolac resin substituting phenol by ammonium lignosulfonate as filler or extender," *BioResources*, vol. 2, no. 2, pp. 270–283, 2007.
- [32] B. Danielson and R. Simonson, "Kraft lignin in phenol formaldehyde resin. Part I. Partial replacement of phenol by kraft lignin in phenol formaldehyde adhesives for plywood," *Journal of Adhesion Science and Technology*, vol. 12, no. 9, pp. 923–939, 1998.
- [33] Y. P. Zhai, Y. Q. Dou, X. X. Liu, B. Tu, and D. Y. Zhao, "One-pot synthesis of magnetically separable ordered mesoporous carbon," *Journal of Materials Chemistry*, vol. 19, no. 20, pp. 3292–3300, 2009.
- [34] Z. K. Sun, B. Sun, Y. H. Deng, M. H. Qiao, and D. Y. Zhao, "Synthesis of precisely size tunable metallic nanoparticles decorated ordered mesoporous carbon via a general chelate-assisted pathway and their remarkable performance in Fischer-Tropsch synthesis," *Abstracts of Papers of the American Chemical Society*, vol. 243, 2012.
- [35] Z. Sun, B. Sun, M. Qiao et al., "A general chelate-assisted co-assembly to metallic nanoparticles-incorporated ordered mesoporous carbon catalysts for Fischer-Tropsch synthesis," *Journal of the American Chemical Society*, vol. 134, no. 42, pp. 17653–17660, 2012.
- [36] M. Zhang and A. A. Ogale, "Carbon fibers from dry-spinning of acetylated softwood kraft lignin," *Carbon*, vol. 69, pp. 626–629, 2014.
- [37] S. X. Hu and Y. L. Hsieh, "Preparation of activated carbon particulates from lignin and its application as electric supercapacitor," in *Proceedings of the 247th National Spring Meeting of the American-Chemical-Society (ACS '14)*, vol. 247 of *Abstracts of Papers of the American Chemical Society*, Dallas, Tex, USA, March 2014.
- [38] P. Estellé, S. Halefadi, and T. Maré, "Lignin as dispersant for water-based carbon nanotubes nanofluids: impact on viscosity and thermal conductivity," *International Communications in Heat and Mass Transfer*, vol. 57, pp. 8–12, 2014.
- [39] S. Chatterjee, A. Clingenpeel, A. McKenna, O. Rios, and A. Johs, "Synthesis and characterization of lignin-based carbon materials with tunable microstructure," *RSC Advances*, vol. 4, no. 9, pp. 4743–4753, 2014.
- [40] S. J. Dai, S. Y. Yang, and D. Q. Zhou, "The influence of coexisting ions on adsorption-flotation of Pb²⁺ in water by gordona amarae," *Advanced Materials Research*, vol. 433–440, pp. 183–187, 2012.
- [41] Y. Wang, M. Yao, Y. Chen, Y. Zuo, X. Zhang, and L. Cui, "General synthesis of magnetic mesoporous FeNi/graphitic carbon nanocomposites and their application for dye adsorption," *Journal of Alloys and Compounds*, vol. 627, pp. 7–12, 2015.
- [42] J. H. Wang, S. R. Zheng, J. L. Liu, and Z. Y. Xu, "Tannic acid adsorption on amino-functionalized magnetic mesoporous silica," *Chemical Engineering Journal*, vol. 165, no. 1, pp. 10–16, 2010.
- [43] Z. M. Sheng and J. N. Wang, "Thin-walled carbon nanocages: direct growth, characterization, and applications," *Advanced Materials*, vol. 20, no. 5, pp. 1071–1075, 2008.
- [44] M. Ginic-Markovic, J. G. Matosons, R. Cervini, G. P. Simon, and P. M. Fredericks, "Synthesis of new polyaniline/nanotube composites using ultrasonically initiated emulsion polymerization," *Chemistry of Materials*, vol. 18, no. 26, pp. 6258–6265, 2006.
- [45] T.-W. Kim, I.-S. Park, and R. Ryoo, "A synthetic route to ordered mesoporous carbon materials with graphitic pore walls," *Angewandte Chemie International Edition*, vol. 42, no. 36, pp. 4375–4379, 2003.
- [46] A. Banerjee, R. Gokhale, S. Bhatnagar et al., "MOF derived porous carbon-Fe₃O₄ nanocomposite as a high performance,

recyclable environmental superadsorbent,” *Journal of Materials Chemistry*, vol. 22, no. 37, pp. 19694–19699, 2012.

- [47] C. Zhang, Z. L. Mo, P. Zhang, C. Feng, and R. B. Guo, “Facile synthesis of porous carbon@Fe₃O₄ composites and their applications in wastewater treatment,” *Materials Letters*, vol. 106, pp. 107–110, 2013.
- [48] N. Yang, S. M. Zhu, D. Zhang, and S. Xu, “Synthesis and properties of magnetic Fe₃O₄-activated carbon nanocomposite particles for dye removal,” *Materials Letters*, vol. 62, no. 4-5, pp. 645–647, 2008.

Research Article

Highly Sensitive CO Gas Sensor from Defective Graphene: Role of van der Waals Interactions

Yingda Jiang, Sha Yang, Shuang Li, Wei Liu, and Yonghao Zhao

Nano Structural Materials Center, School of Materials Science and Engineering, Nanjing University of Science and Technology, Nanjing, Jiangsu 210094, China

Correspondence should be addressed to Wei Liu; weiliu@njust.edu.cn

Received 20 May 2015; Accepted 11 June 2015

Academic Editor: Xuping Sun

Copyright © 2015 Yingda Jiang et al. This is an open access article distributed under the Creative Commons Attribution License, which permits unrestricted use, distribution, and reproduction in any medium, provided the original work is properly cited.

Layered materials, such as graphene, have attracted increasing interests since they can be extensively used in gas sensors, spintronic devices, and transparent electrodes. Although larger size of graphene sheets has been fabricated, in reality, the existence of the defects in layered materials is almost inevitable during the manufacturing process. Here, we performed the state-of-the-art density-functional theory calculations to study the interactions between CO molecule and the pristine and defective graphene layers, with the aim of designing a CO gas sensor with higher sensitivity. The van der Waals interactions predominate the binding between the CO gas and the sensor, and also significantly enhance the stability of the system. The defective graphene strongly interacts with CO, and thus enhances the sensitivity of the graphene and further tunes the electronic and magnetic properties of the entire system. Our computed results clearly demonstrate that the defective graphene could be a good sensor for gas molecules.

1. Introduction

Carbon-based materials, such as nanotubes and graphene, are widely accepted as a good sensor to monitor small gas molecules, such as CO, NO, NO₂, and NH₃ molecules [1–9]. In particular, the detection of the CO molecule to prevent poisoning is of vital importance, due to the fact that CO is colorless, tasteless, and odorless, but toxic and flammable. Carbon nanotubes were often used as building blocks in gas sensors, which is capable of effectively monitoring extremely low concentrations of gases [10–13]. Since fabrication in 2004 by Novoselov et al. [14], graphene, the two-dimensional material, has attracted increasing interests as a gas sensor, thanks to its huge specific surface area, good electrical conductivity, stable chemical performance, high Young's modulus, and excellent optical performance [3, 8, 15–17]. In particular, Zhang et al. [16] theoretically studied small gas molecules (CO, NO, NO₂, NH₃) adsorption on four graphene layers (pristine, B and N-doped, and defective graphene) using the local-density approximation (LDA) method and exploited their potential applications as gas sensors. Although efforts are being undertaken to enhance the performance of gas

sensor, many challenges remain in the field, such as the low binding energy, low sensitivity, and bad selectivity.

A prerequisite to design an effective sensor is the understanding of the interactions between the gas molecules and the substrate. However, from the point of view of modelling, the accurate description of their interactions remains a big challenge, due to the well-known fact that the gas/substrate binding arises from the dedicated balance between various types of bonding: covalent bonding, van der Waals (vdW) interactions, hydrogen bonding, charge transfer, and Pauli repulsion [15, 18–20]. Thanks to the recent development of vdW-inclusive methods in the framework of density-functional theory (DFT) [21, 22], the role of vdW force between small molecules in the gas phase has been reasonably described and is well understood. Notably, the vdW energy is of extreme importance in two-dimensional materials but is often ignored in previous DFT calculations when studying the gas sensors.

In this contribution, we performed various types of vdW-inclusive DFT calculations to study the interactions between CO molecule and graphene layers. Although larger size of graphene sheets has been fabricated, in reality, the existence

TABLE 1: Adsorption energy (E_{ad} in eV) and equilibrium molecule-substrate distance (d in Å) of the CO adsorbed on different sites.

Systems	Structures	LDA		PBE		PBE + vdW (TS)	
		E_{ad}	d	E_{ad}	d	E_{ad}	d
CO on G	a	-0.10	3.01	0.03	3.14	-0.05	2.84
	b	-0.04	2.72 ^a	0.04	2.97 ^a	-0.03	2.68 ^a
	c	-0.08	2.82	0.02	3.22	-0.03	2.77
	d	-0.03	2.71 ^a	0.05	2.85 ^a	-0.04	2.71 ^a
	e	-0.08	2.61	0.06	2.85	-0.03	2.76
	f	-0.06	2.63 ^a	0.07	2.72 ^a	0.03	2.47 ^a
	g	-0.11	2.86	0.04	3.10	-0.10	2.79
	h	-0.12	2.69	0.04	2.97	-0.11	2.88
	i	-0.12	2.83	0.03	3.09	-0.09	2.85
	j	-0.12	2.82	0.03	3.14	-0.10	2.91
CO on defective G	k	-0.36	2.90	-0.25	3.09	-0.32	2.63
	l	-2.75	1.32 ^b	-2.05	1.33 ^b	-2.15	1.33 ^b

a refers to the distance between the O atom in CO and the C atom in graphene.
b refers to the shortest bond length.

of the defects in layered materials is almost inevitable during the manufacturing process. As such it is of fundamental interests to study the interactions of gas molecules with the defective graphene sheets. Our calculations showed that by introducing defects, even a single point vacancy, in the graphene layers, the sensitivity of the gas sensor can be significantly enhanced. Moreover, the electric and magnetic properties of the system are strongly perturbed upon interaction with the molecules. We demonstrate that the defective graphene would be a highly sensitive sensor for monitoring the CO gas.

2. Methods

DFT calculations were performed using the Vienna ab initio simulation package (VASP) [23]. The interaction between the valence electrons and ionic cores is described by the projector augmented wave (PAW) method [24]. The LDA, the Perdew-Burke-Ernzerhof (PBE) form of the generalized-gradient approximation (GGA) [25], and the PBE + vdW (or TS) [26] are employed to describe electron exchange and correlation. The plane wave energy cut-off is set to 350 eV and the Brillouin zone is sampled with $3 \times 3 \times 1$ k -point mesh. The surfaces are modeled by periodic (5×5) supercell, which is separated by 15 Å of vacuum. A threshold for the convergence criteria of 0.001 eV/Å is used for the final force. For the calculation of density of electronic states (DOS), the k -point is set to $19 \times 19 \times 1$.

The adsorption energy of CO on graphene can be written as

$$E_{\text{ads}} = E_{\text{CO/Graphene}} - E_{\text{Graphene}} - E_{\text{CO}}, \quad (1)$$

where $E_{\text{CO/Graphene}}$, E_{Graphene} , and E_{CO} are the total energies of the relaxed CO on graphene system, free-standing graphene, and the isolated CO molecule, respectively.

To find the most favorable adsorption configuration, a CO molecule is initially placed at different positions above the pristine graphene (G) and the defective graphene (DG) with perpendicular or parallel orientation. We also use other

five vdW-inclusive methods, including DFT-D2 [27], DFT-D3 [28], vdW-DF, optPBE-vdW, and optB88-vdW [29, 30], to revisit the favorable adsorption configurations relaxed from the PBE + vdW method, with the aim of deeply understanding the role of vdW interactions in these adsorption systems.

3. Results and Discussion

Figure 1 shows the optimized configurations after full relaxation. The C-C bond length in graphene from our LDA, PBE, and PBE + vdW calculations ranges from 1.41 to 1.43 Å, in excellent agreement with the experimental data (1.42 Å) [31]. Also, the calculated atomic distance between O and C in CO molecule agrees very well with those from experiments (1.13 to 1.14 Å versus 1.13 Å [32]). The computed adsorption energies (E_{ad}) and the equilibrium molecule-substrate distances (d) are listed in Table 1. The most stable configurations of the CO molecule on pristine graphene and defective graphene are configurations (h) and (l), respectively. The adsorption energy of CO on G is found to be -0.12 eV, along with the CO-substrate distance of 2.69 Å from the LDA functional. We found that the E_{ad} of configurations (g) to (j) are almost identical, suggesting the flat potential-energy surface for CO at the pristine graphene. Notably, our computed adsorption energy at the favorable configuration (h) agrees with that in [16]. The LDA results are close to those from the PBE + vdW method with an E_{ad} of -0.11 eV. In contrast, the PBE adsorption energies are positive, and the adsorption distances are considerably larger than those from LDA and PBE + vdW. Therefore, one could conclude that the GGA-PBE method tends to underestimate the adsorption energy and overestimate the adsorption distance, confirming the essential role of vdW interactions in these systems.

For the defective graphene, the configuration (l) in Figure 1 is found to be the most stable, where the CO tilts to the defective graphene and carbon atom pointing towards the vacancy. When using LDA, the adsorption energy of CO on DG significantly increases to -2.75 eV, with a CO-substrate distance of 1.32 Å. The E_{ad} computed from PBE and

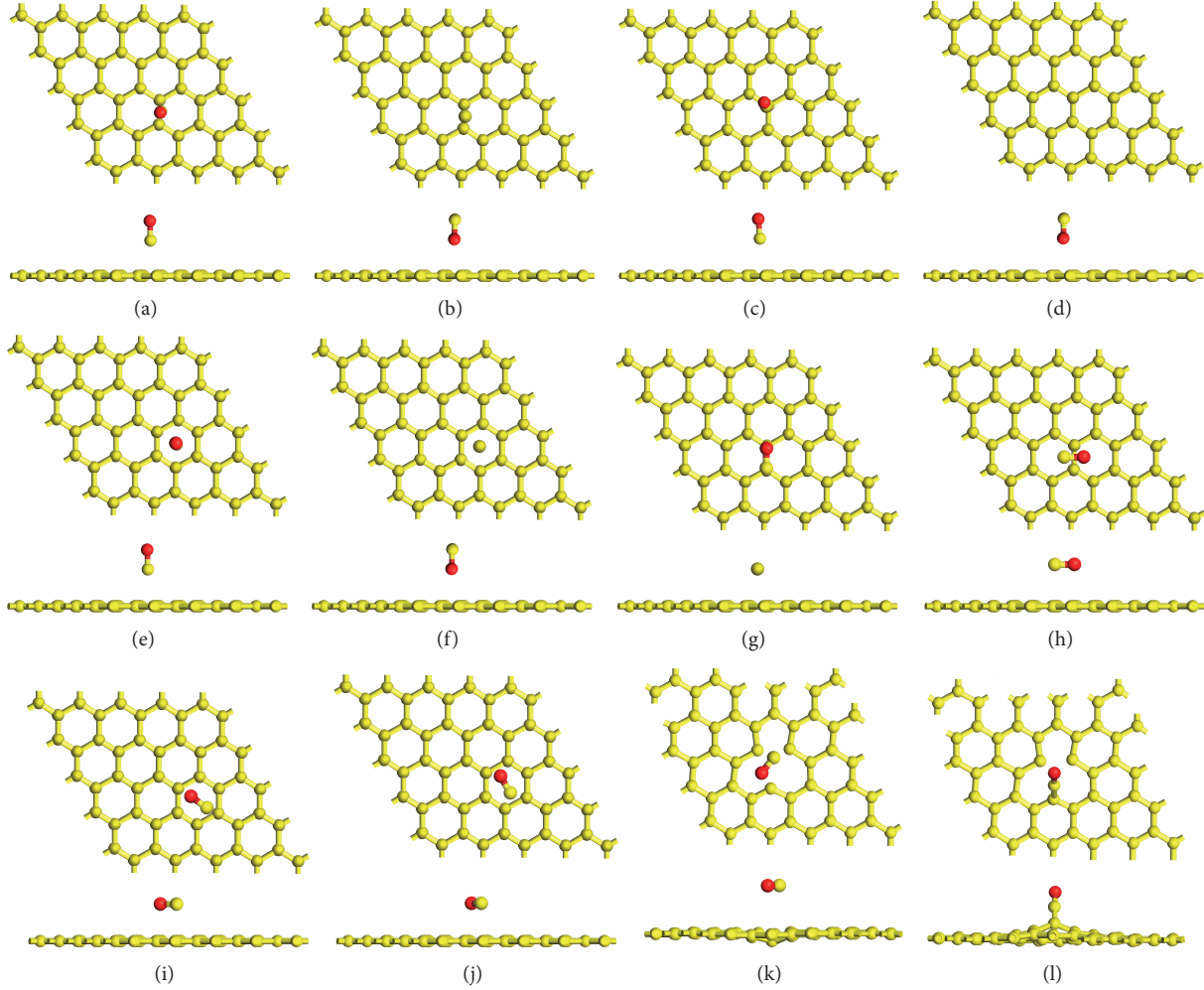


FIGURE 1: Top and side views of the adsorption structures for CO on graphene and defective graphene. (a) to (j) are for graphene and (k) to (l) are for defective graphene.

PBE + vdW are -2.05 and -2.15 eV, respectively, and the d value dramatically decreases to 1.33 Å. The distance is close to the bond length of a C=C double bond (1.34 Å), indicating the formation of the covalent bonds upon CO adsorption. As such, the CO molecule is chemisorbed at the defective graphene, with a significantly larger adsorption energy than for the pristine graphene sheet.

Table 2 shows the comparison of calculated adsorption energy and equilibrium molecule-substrate distance at the most stable sites h and l of G and DG, respectively, between six vdW functionals. For configuration h, the E_{ad} from DFT-D2 (-0.09 eV) and DFT-D3 (-0.10 eV) are lower than that of PBE + vdW (-0.11 eV), and the vdW-DF (-0.14 eV) and optPBE-vdW (-0.16 eV) are higher. The best agreement can be found in the optB88-vdW functional, with an $E_{\text{ad}} = -0.11$ eV. A relatively wide range of E_{ad} (-0.09 to -0.16 eV) can be seen for the vdW-DF-type functionals, while the distance is from 2.77 to 3.02 Å. For configuration l, the E_{ad} values of DFT-D2 (-2.25 eV) and DFT-D3 (-2.17 eV) are higher than that of PBE + vdW (-2.15 eV), the vdW-DF (-1.80 eV), optB88-vdW (-2.04 eV), and optPBE-vdW (-2.01 eV) which

TABLE 2: Comparison of the calculated adsorption energy (E_{ad} in eV) and equilibrium molecule-substrate distance (d in Å) at sites h and l of graphene and defective graphene, between different vdW functionals.

Methods	h		l	
	E_{ad}	d	E_{ad}	d
PBE + vdW	-0.11	2.88	-2.15	1.33
DFT-D2	-0.09	2.87	-2.25	1.33
DFT-D3	-0.10	2.92	-2.17	1.33
vdW-DF	-0.14	3.02	-1.80	1.33
optB88-vdW	-0.11	2.77	-2.04	1.33
optPBE-vdW	-0.16	2.93	-2.01	1.33

are lower. Further analysis of the data in Table 2 shows that different vdW-inclusive methods give a relatively wide range in adsorption energies for the chemisorbed system. More specifically, the PBE + vdW and DFT-D3 give almost identical binding energies, which are about 100 meV larger than those from the DFT-D2 method. This is presumably because the

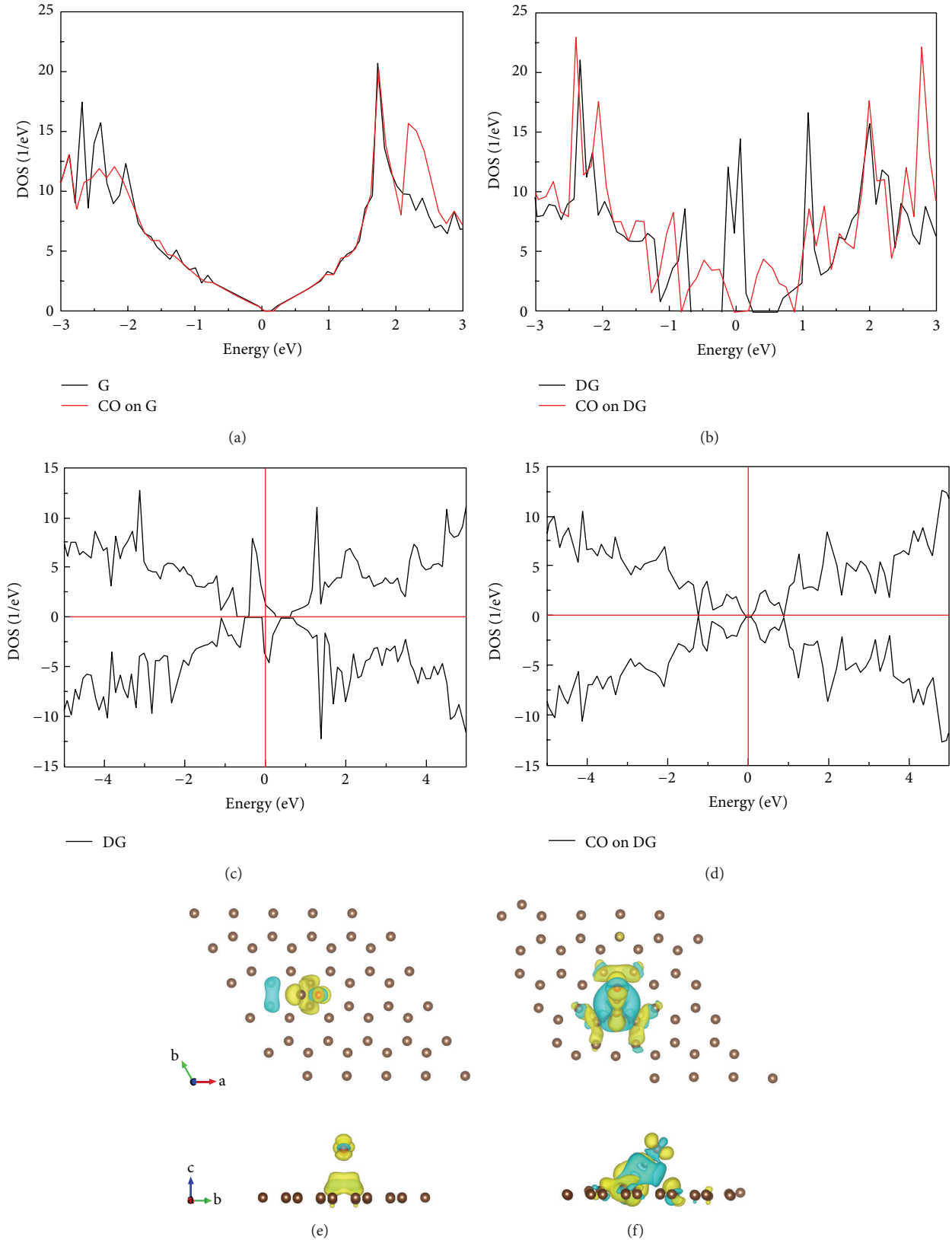


FIGURE 2: The DOS for (a) CO on pristine graphene and (b) CO on defective graphene. Spin-polarized density of states (DOS) for (c) defective graphene and (d) CO on defective graphene. The Fermi level of the system is set to zero. Calculated differential charge densities for (e) CO on pristine graphene and (f) CO on defective graphene. Blue color and yellow color show the areas with $\Delta\rho < 0$ and $\Delta\rho > 0$, respectively. Note that different isosurface levels were used in plots (e) and (f): $0.0002 \text{ e}/\text{\AA}^3$ for the former and $0.002 \text{ e}/\text{\AA}^3$ for the latter.

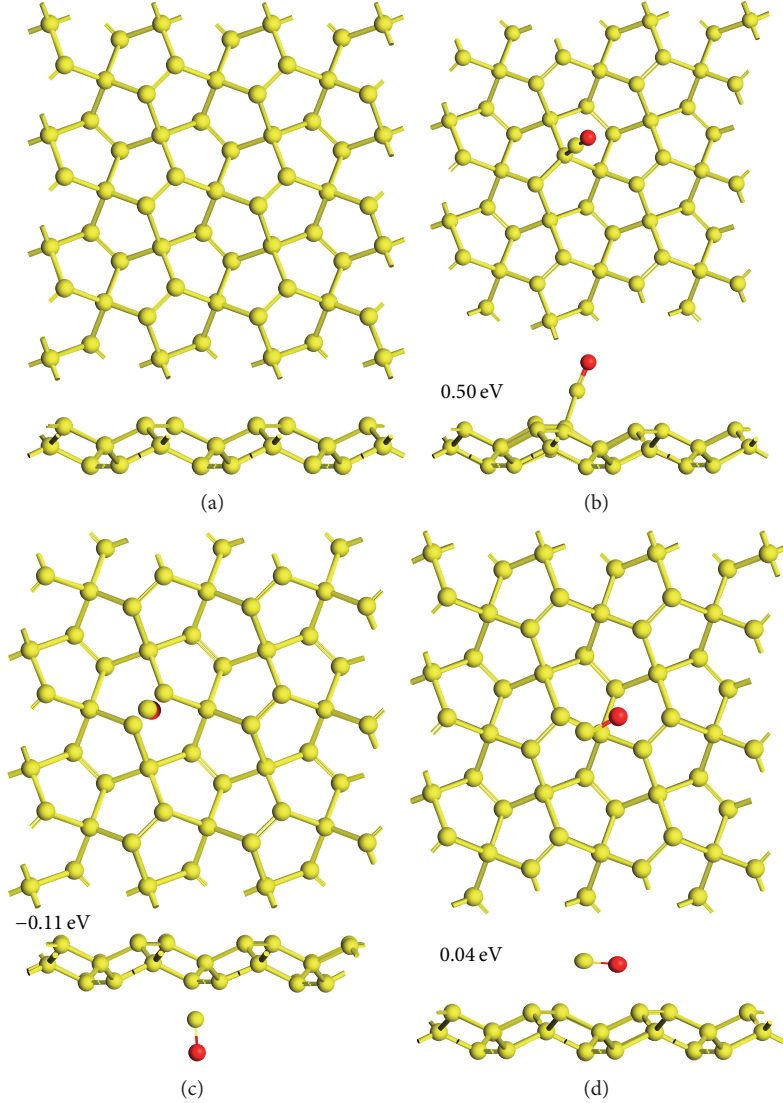


FIGURE 3: Top and side views of (a) the penta-graphene sheet, (b) to (d) CO adsorbed on the penta-graphene sheet at different sites. The adsorption energies are also shown in the figure.

former methods utilized the environmental dependent vdW parameters in DFT calculations. The vdW-DF functional gives the highest binding energy due to the well-known overly repulsive exchange part (revPBE) used in this approach [18]. Although the E_{ad} ranges from -1.80 to -2.25 eV, their related distances for all functionals are the same (1.33 Å). This indicates that the adsorption distance is determined by the covalent bonding, rather than the vdW interactions, for the chemisorbed systems.

To better understand the change in the electronic structure caused by CO adsorption, we computed the electronic density of states (DOS) for CO on G and further compared it with that of CO on DG. As shown in Figure 2(a), almost no electron orbital overlaps between CO molecule and the graphene in the CO on G system due to the physisorptive nature of bonding in this case. On the contrary, the DOS plots of CO and the defective graphene in the CO on DG system are significantly hybridized (Figure 2(b)), clearly implying

the strong chemisorption between the CO molecule and the defective graphene. It is inferred that the adsorption of CO on DG brings apparent perturbation to electronic properties of the defective graphene. Also, the spin-polarized DOS analysis shows that the DG is magnetic (1.68 μB) whilst the magnetism vanishes upon the CO adsorption (see Figures 2(c) and 2(d)).

To obtain the charge redistribution after the adsorption process, we further computed the differential charge densities (DCD), which is defined as

$$\Delta\rho = \rho_{\text{CO/Graphene}} - \rho_{\text{Graphene}} - \rho_{\text{CO}}, \quad (2)$$

where $\rho_{\text{CO/Graphene}}$ represents the total electronic density for the CO/graphene system and ρ_{Graphene} and ρ_{CO} are the densities for the isolated graphene (or defective graphene) and CO molecule, respectively. In Figures 2(e) and 2(f), we present the results of $\Delta\rho$ at the CO-G and CO-DG interfaces.

Very weak charge transfer can be observed from graphene (blue color, $\Delta\rho < 0$) to the CO molecule (yellow color, $\Delta\rho > 0$) in Figure 2(e). For CO-DG in Figure 2(f), a significant charge transfer is observable from CO to defective graphene.

Finally, we made a comparison of graphene with the newly proposed penta-graphene [33] to confirm the better performance for the defective graphene as a CO gas sensor. As shown in Figure 3(a), the penta-graphene possesses 54 C atoms, and the optimized lattice constants are 10.69 Å from PBE + vdW method. The total thickness of the relaxed structure is 1.26 Å and the buckling is 0.63 Å. There are two kinds of C atoms, the sp^3 - and the sp^2 -hybridized C atoms named C1 and C2, respectively. The C1–C2 is 1.53 Å and C2–C2 is 1.33 Å, while the bond angle of C2–C1–C2 is 131.1°. Three different configurations are shown in Figures 3(b) to 3(d). The most favorable configuration is site c with an E_{ad} of -0.11 eV and a distance of 2.19 Å. The remaining two configurations are both unstable due to the positive E_{ad} . Then we calculated the formation energy of the graphene (-9.28 eV) and penta-graphene (-8.39 eV) per atom, respectively. We found the formation energy of graphene is lower than that of penta-graphene.

4. Conclusions

In summary, the interactions between CO molecule and the pristine and defective graphene layers using different vdW-inclusive functionals were investigated. CO is physisorbed on the perfect graphene sheets, along with low adsorption energy and almost no charge transfer. In contrast, the defective graphene is reactive to bond with CO molecule, and their interactions tune the electronic and magnetic properties of the adsorption system. Our calculations demonstrate the potential application of defective graphene as a highly sensitive CO gas sensor.

Conflict of Interests

The authors declare that there is no conflict of interests regarding the publication of this paper.

Acknowledgments

The authors gratefully acknowledge the financial support of National Natural Science Foundation of China (21403113, 51225102, and 2012CB932203), Program for New Century Excellent Talents in University from Chinese Ministry of Education, the Fundamental Research Funds for the Central Universities (30915011330), and a Project Funded by the Priority Academic Program Development of Jiangsu Higher Education Institutions.

References

- [1] O. Leenaerts, B. Partoens, and F. M. Peeters, "Adsorption of H_2O , NH_3 , CO , NO_2 , and NO on graphene: a first-principles study," *Physical Review B*, vol. 77, Article ID 125416, 2008.
- [2] F. Schedin, A. K. Geim, S. V. Morozov et al., "Detection of individual gas molecules adsorbed on graphene," *Nature Materials*, vol. 6, no. 9, pp. 652–655, 2007.
- [3] H. Choi, J. S. Choi, J.-S. Kim et al., "Flexible and transparent gas molecule sensor integrated with sensing and heating graphene layers," *Small*, vol. 10, no. 18, pp. 3685–3691, 2014.
- [4] W. Hu, N. Xia, X. Wu, Z. Li, and J. Yang, "Silicene as a highly sensitive molecule sensor for NH_3 , NO and NO_2 ," *Physical Chemistry Chemical Physics*, vol. 16, pp. 6957–6962, 2014.
- [5] G. Mazzamuto, A. Tabani, S. Pazzagli et al., "Single-molecule study for a graphene-based nano-position sensor," *New Journal of Physics*, vol. 16, Article ID 113007, 2014.
- [6] A. H. Reshak and S. Auluck, "Adsorbing H_2S onto a single graphene sheet: a possible gas sensor," *Journal of Applied Physics*, vol. 116, Article ID 103702, 2014.
- [7] L. Shao, G. Chen, H. Ye et al., "Sulfur dioxide molecule sensors based on zigzag graphene nanoribbons with and without Cr dopant," *Physics Letters A*, vol. 378, no. 7–8, pp. 667–671, 2014.
- [8] G. S. Kulkarni, K. Reddy, Z. Zhong, and X. Fan, "Graphene nanoelectronic heterodyne sensor for rapid and sensitive vapour detection," *Nature Communications*, vol. 5, article 4376, 2014.
- [9] W. Yuan, A. Liu, L. Huang, C. Li, and G. Shi, "High-performance NO_2 sensors based on chemically modified graphene," *Advanced Materials*, vol. 25, no. 5, pp. 766–771, 2013.
- [10] L. Bai and Z. Zhou, "Computational study of B- or N-doped single-walled carbon nanotubes as NH_3 and NO_2 sensors," *Carbon*, vol. 45, no. 10, pp. 2105–2110, 2007.
- [11] C. Matranga, L. Chen, B. Bockrath, and J. K. Johnson, "Displacement of CO_2 by Xe in single-walled carbon nanotube bundles," *Physical Review B*, vol. 70, no. 16, Article ID 165416, 7 pages, 2004.
- [12] L. B. Da Silva, S. B. Fagan, and R. Mota, "Ab initio study of deformed carbon nanotube sensors for carbon monoxide molecules," *Nano Letters*, vol. 4, no. 1, pp. 65–67, 2004.
- [13] J. A. Robinson, E. S. Snow, Ş. C. Badescu, T. L. Reinecke, and F. K. Perkins, "Role of defects in single-walled carbon nanotube chemical sensors," *Nano Letters*, vol. 6, no. 8, pp. 1747–1751, 2006.
- [14] K. S. Novoselov, A. K. Geim, S. V. Morozov et al., "Electric field in atomically thin carbon films," *Science*, vol. 306, no. 5696, pp. 666–669, 2004.
- [15] W. Liu, A. Savara, X. Ren et al., "Toward low-temperature dehydrogenation catalysis: isophorone adsorbed on Pd(111)," *The Journal of Physical Chemistry Letters*, vol. 3, no. 5, pp. 582–586, 2012.
- [16] Y. Zhang, Y. Chen, K. Zhou et al., "Improving gas sensing properties of graphene by introducing dopants and defects: a first-principles study," *Nanotechnology*, vol. 20, no. 18, Article ID 185504, 2009.
- [17] R. Lv, M. C. dos Santos, C. Antonelli et al., "Large-area Si-doped graphene: controllable synthesis and enhanced molecular sensing," *Advanced Materials*, vol. 26, no. 45, pp. 7593–7599, 2014.
- [18] W. Liu, A. Tkatchenko, and M. Scheffler, "Modeling adsorption and reactions of organic molecules at metal surfaces," *Accounts of Chemical Research*, vol. 47, no. 11, pp. 3369–3377, 2014.
- [19] W. Liu, V. G. Ruiz, G.-X. Zhang et al., "Structure and energetics of benzene adsorbed on transition-metal surfaces: density-functional theory with van der Waals interactions including collective substrate response," *New Journal of Physics*, vol. 15, Article ID 053046, 2013.

- [20] W. Liu, J. Carrasco, B. Santra, A. Michaelides, M. Scheffler, and A. Tkatchenko, "Benzene adsorbed on metals: concerted effect of covalency and van der Waals bonding," *Physical Review B—Condensed Matter and Materials Physics*, vol. 86, no. 24, Article ID 245405, 2012.
- [21] P. Hohenberg and W. Kohn, "Inhomogeneous electron gas," *Physical Review B*, vol. 136, no. 3, pp. B864–B871, 1964.
- [22] W. Kohn and L. J. Sham, "Self-consistent equations including exchange and correlation effects," *Physical Review A*, vol. 140, Article ID A1133, 1965.
- [23] G. Kresse and J. Furthmüller, "Efficiency of ab-initio total energy calculations for metals and semiconductors using a plane-wave basis set," *Computational Materials Science*, vol. 6, no. 1, pp. 15–50, 1996.
- [24] P. E. Blöchl, "Projector augmented-wave method," *Physical Review B*, vol. 50, no. 24, pp. 17953–17979, 1994.
- [25] J. P. Perdew, K. Burke, and M. Ernzerhof, "Generalized gradient approximation made simple," *Physical Review Letters*, vol. 77, no. 18, article 3865, 1996.
- [26] A. Tkatchenko and M. Scheffler, "Accurate molecular van der Waals interactions from ground-state electron density and free-atom reference data," *Physical Review Letters*, vol. 102, Article ID 073005, 2009.
- [27] S. Grimme, "Semiempirical GGA-type density functional constructed with a long-range dispersion correction," *Journal of Computational Chemistry*, vol. 27, no. 15, pp. 1787–1799, 2006.
- [28] S. Grimme, J. Antony, S. Ehrlich, and H. Krieg, "A consistent and accurate ab initio parametrization of density functional dispersion correction (DFT-D) for the 94 elements H–Pu," *The Journal of Chemical Physics*, vol. 132, no. 15, Article ID 154104, 2010.
- [29] J. Klimeš, D. R. Bowler, and A. Michaelides, "Chemical accuracy for the van der Waals density functional," *Journal of Physics: Condensed Matter*, vol. 22, no. 2, Article ID 022201, 2010.
- [30] J. Klimeš, D. R. Bowler, and A. Michaelides, "Van der Waals density functionals applied to solids," *Physical Review B*, vol. 83, no. 19, Article ID 195131, 13 pages, 2011.
- [31] D. R. Cooper, B. D'Anjou, N. Ghattamaneni et al., "Experimental review of graphene," *ISRN Condensed Matter Physics*, vol. 2012, Article ID 501686, 56 pages, 2012.
- [32] Y. Luo, *CRC Handbook of Chemistry and Physics*, CRC Press, Boca Raton, Fla, USA, 2010.
- [33] S. Zhang, J. Zhou, Q. Wang, X. Chen, Y. Kawazoe, and P. Jena, "Penta-graphene: a new carbon allotrope," *Proceedings of the National Academy of Sciences*, vol. 112, no. 8, pp. 2372–2377, 2015.

Research Article

Substrate Temperature Effect on the Microstructure and Properties of (Si, Al)/a-C:H Films Prepared through Magnetron Sputtering Deposition

Xiaoqiang Liu,¹ Junying Hao,² Hu Yang,¹ Xiuzhou Lin,¹ and Xianguang Zeng¹

¹Material Corrosion and Protection Key Laboratory of Sichuan Province, Sichuan University of Science and Engineering, Zigong 643000, China

²State Key Laboratory of Solid Lubrication, Lanzhou Institute of Chemical Physics, Chinese Academy of Sciences, Lanzhou 730000, China

Correspondence should be addressed to Junying Hao; jyhao@licp.cas.cn

Received 11 May 2015; Revised 3 August 2015; Accepted 4 August 2015

Academic Editor: Dan Xia

Copyright © 2015 Xiaoqiang Liu et al. This is an open access article distributed under the Creative Commons Attribution License, which permits unrestricted use, distribution, and reproduction in any medium, provided the original work is properly cited.

Hydrogenated amorphous carbon films codoped with Si and Al ((Si, Al)/a-C:H) were deposited through radio frequency (RF, 13.56 MHz) magnetron sputtering on Si (100) substrate at different temperatures. The composition and structure of the films were investigated by means of X-ray photoelectron spectroscopy (XPS), TEM, and Raman spectra, respectively. The substrate temperature effect on microstructure and mechanical and tribological properties of the films was studied. A structural transition of the films from nanoparticle containing to fullerene-like was observed. Correspondingly, the mechanical properties of the films also had obvious transition. The tribological results in ambient air showed that high substrate temperature (>573 K) was disadvantage of wear resistance of the films albeit in favor of formation of ordering carbon clusters. Particularly, the film deposited at temperature of 423 K had an ultralow friction coefficient of about 0.01 and high wear resistance.

1. Introduction

Hydrogenated amorphous carbon (a-C:H) films have been well known for their outstanding mechanical properties such as super-hard (up to 80 GPa) and excellent tribological performance (friction coefficient lower than 0.01 under vacuum) [1]. However, pure a-C:H films have some intrinsic limitations in application as solid lubricant materials, such as high internal stress, low toughness, and high sensitivity of friction coefficient to humidity. In order to overcome those limitations, doping additional elements has been widely applied to fabricate nanocomposite amorphous carbon films. Among those doped elements, silicon has attracted extensive attention due to its effectiveness in improving thermal stability and enhancing corrosion resistance [2]. In particular, the humidity sensitivity of friction coefficient films can be suppressed by incorporating Si into a-C:H films based on the forming silicon hydroxides or silicon oxide during friction process [3]. Aluminum has been regarded as one of the most

effective elements in relaxing internal stress of a-C:H films [4]. Besides, it was reported that the graphitization of a-C:H films during friction would be enhanced by incorporation of Al, so the friction coefficient can be further reduced [5]. Hence, Al would be a good candidate as a doping element of a-C:H films. However, incorporation of such metallic element would inevitably cost some hardness of films.

Recently, a mode of duplex-doping was developed to further comprehensively promote the mechanical and tribological properties of carbon-based solid lubricant films. An optimum combination between mechanical and tribological properties of films can be achieved by tailoring the content ratio of codoped elements and the ratio C/Me [6] (Me is the metal incorporated into amorphous carbon films). Based on this mode, Wilhelmsson et al. [5] firstly proposed a concept for design of low friction nanocomposite films using Ti-Al-C films as a model system. The Ti-Al-C films exhibited good toughness and low internal stress coupled with low friction. Moreover, it was found in our previous

TABLE 1: Deposition parameters of the films.

Parameters	Value
Working pressure (Pa)	1.2
Radio frequency power (W)	700
Negative substrate bias (V)	-200
Substrate current (mA)	100
Bias frequency (KHz)	40
Deposition duration (min)	90

works that Si and Al codoped amorphous carbon films ((Si, Al)/a-C:H) showed superlow friction (<0.01) and superior wear resistance in ambient air with relative humidity of about 40% [7]. Also, both internal stress and the moisture sensitivity of tribological properties of carbon-based films can be significantly lowered by jointly doping Si and Al, which was further validated by the works of Zhao et al. [8].

Furthermore, duplex-doping can be in favor of nanostructure construction in amorphous carbon films. Until the present, amorphous carbon films have been deposited with many kinds of nanostructures including nanoparticle containing structure [5, 9, 10], nanoscale multilayer [11, 12], nanoporous membranes [13], and dual nanostructure [14]. In order to prepare amorphous carbon films with a certain nanostructure through magnetron sputtering deposition methods, there are lots of preparation parameters taken into account, including sputtering power [15], substrate bias voltage [16], and deposition atmosphere [7, 17], which directly influence the growth mode, structure, and properties of amorphous carbon films. In this study, the substrate temperature effect on microstructure and mechanical and tribological properties of the (Si, Al)/a-C:H films was studied. The correlation between the structure and mechanical and tribological properties was discussed.

2. Experimental Details

2.1. Films Deposition. The (Si, Al)/a-C:H films were deposited on Si (100) substrates through sputtering a rectangular target with dimension of $80 \times 240 \text{ mm}^2$, consisting of silicon (99.999 wt.%) and aluminum (≥ 99.5 wt.%) in argon (Ar) and methane (CH_4) mixture plasma. The exposure area ratio of the Si and Al target is 6:1. Before the deposition, the substrates were ultrasonically cleaned in alcohol and acetone for 10 min, respectively. The distance between the target and substrate was about $95 \pm 5 \text{ mm}$. The residual pressure of the deposition chamber was evacuated down to $3.0 \times 10^{-4} \text{ Pa}$ and then the substrates were cleaned using Ar ion bombardment at a pressure of 1.2 Pa and a negative bias voltage of 1000 V with 70% duty factor. Subsequently, the substrates were heated to a scheduled temperature and then the (Si, Al)/a-C:H film was deposited on them. The substrate temperature was controlled at 423 K, 473 K, 573 K, 673 K, and 773 K. The gas flow of methane and argon was 27 sccm and 40 sccm, respectively. Other deposition parameters of the films can be found in Table 1.

TABLE 2: Parameters of tribotests.

Contact load (N)	2.0
Sliding speed (m/s)	0.10 (reciprocating mode)
Sliding time (s)	1800
Relative humidity (%)	30-40
Counter face	Stainless steel ball (AISI 52100), $\Phi = 3 \text{ mm}$, HRC = 62, Ra = $0.02 \mu\text{m}$

2.2. Film Characterization. The thickness and morphology of fractured cross section of the films were surveyed by field emission scanning electron microscopy (FESEM, JSM 6701F). The compositions of the films were analyzed by a PHI-5702 X-ray photoelectron spectroscope (XPS) with monochromatic Al $K\alpha$ radiation at pass energy of 29.4 eV. The residual pressure of the system was lower than $4 \times 10^{-6} \text{ Pa}$. Raman spectra of the films were obtained on a Jobin-Yvon HR 800 Raman microscopy instrument with 532 nm Ar ion laser and a resolution of 1 cm^{-1} . High resolution transmission electron microscopy was operated on FEI Tecnai G2 F20 FE-TEM at 200 kV. The samples for TEM observation were obtained from the as-deposited films on the Si substrate, which mechanically polished and then Ar ion-milled (Gatan 691) at a small angle with respect to the milled surface. The hardness of the films was investigated by a nanoindenter (Hysteron TI950, Hysitron TriboIndenter). The depth of indentation was controlled to 10% of the film thickness to exclude the influence of the substrate. Five indentation tests were made at different locations of the films. The solid lubricity of the films was evaluated by ball-on-disk method in ambient air. The tribotest parameters can be found in Table 2. The wear tracks were surveyed using noncontact method on Micro XAM-3D Surface Profile (ADE Phase Shift, USA). Surface morphology of transfer layer sliding against the films was scrutinized by SEM (JSM-5600LV).

3. Result and Discussion

3.1. Composition and Microstructure. The composition of the films was surveyed by XPS. The results showed that there was no obvious difference in the composition among the films, as shown in Figure 1. Specifically, oxygen should be concerned with the surface oxidation when the samples were exposed to the air. The composition of the films was almost independent of the growth temperature. On the contrary, the thickness of the films which was detected by FESEM, as shown in Figures 2(a)-2(c), decreased with the increase of growth temperature. Specifically, the deposition rate of the films decreased in contrast with increase of the substrate temperature. The change of deposition rate is consistent with that reported by Shinohara et al. [18]. This kind of phenomenon may be concerned with decrease of sticking coefficient of the chemical species generated in the methane plasma or the increase of density caused by ion bombardment. However, we think the latter is more likely since elemental composition of the films, which depend on the sticking and resputtering of the different chemical species, was almost unchanged with

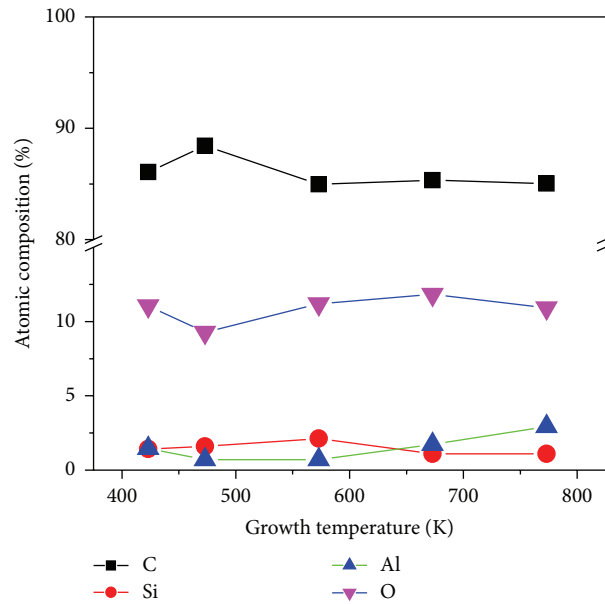


FIGURE 1: The composition of the films deposited at different substrate temperatures.

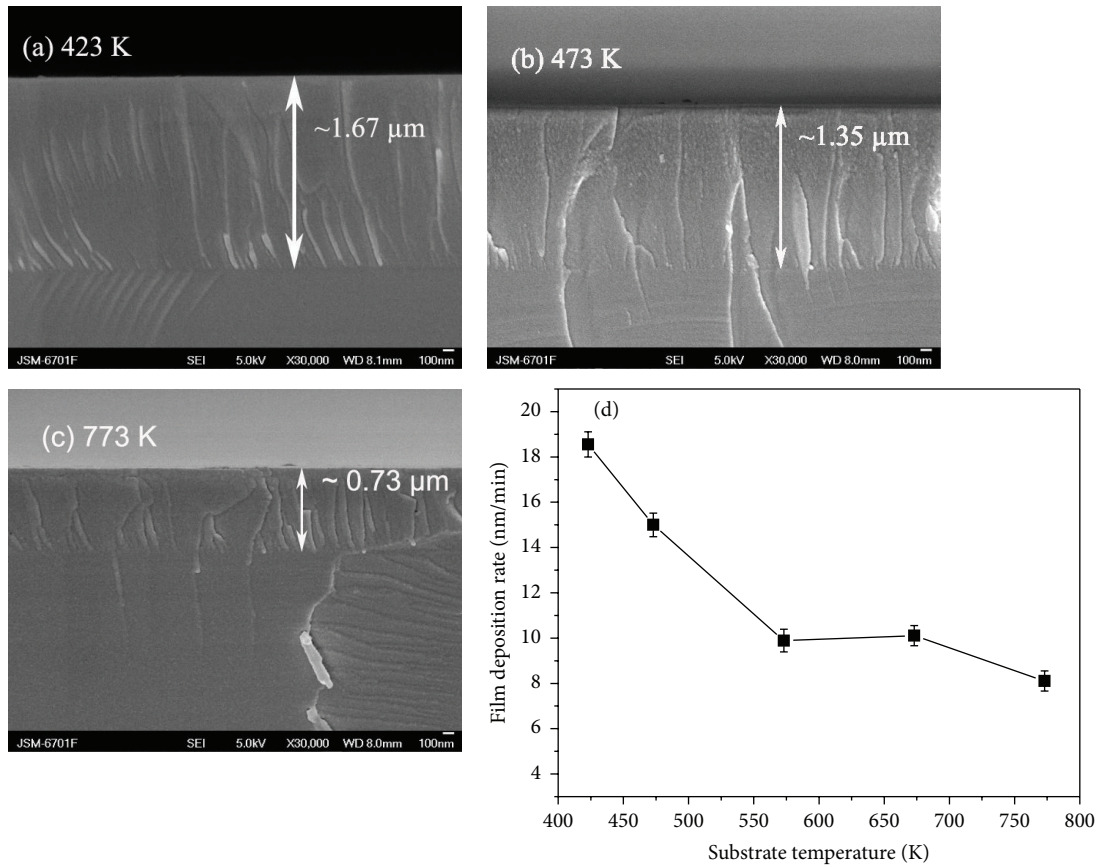


FIGURE 2: (a–c) FESEM images of fractured cross section and (d) total thickness as a function of the substrate temperatures.

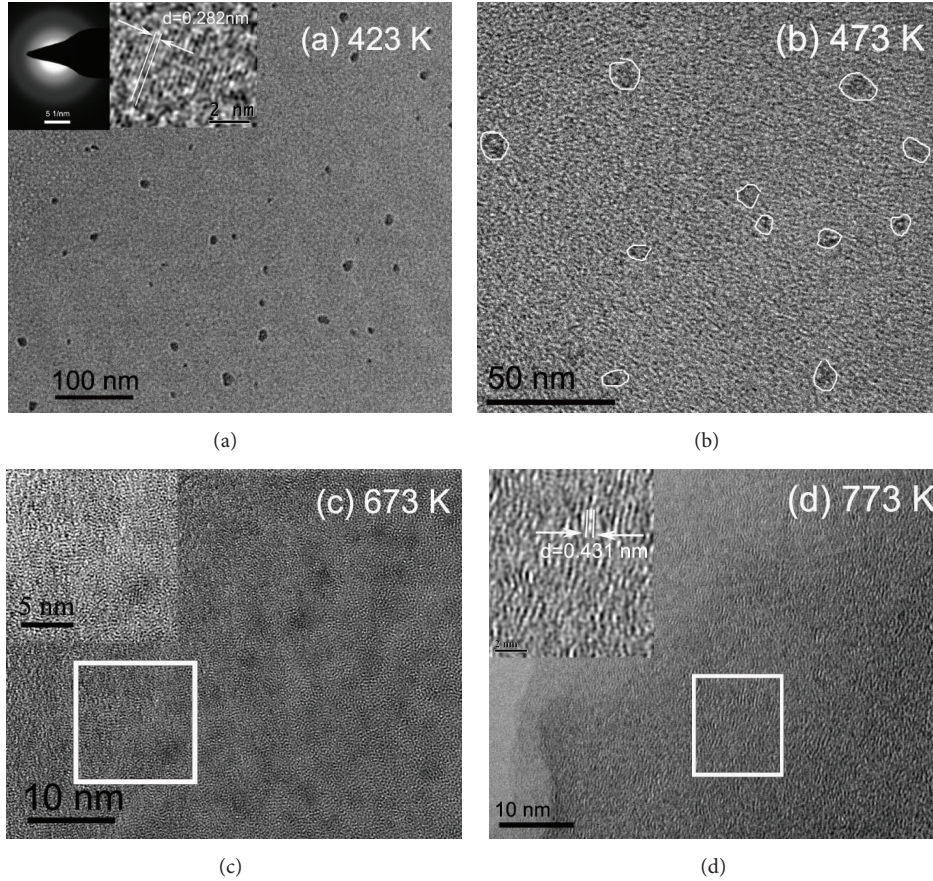


FIGURE 3: Plane-view TEM images taken from the bulk of the films deposited at different substrate temperatures (the insets of (a), (c), and (d) are inversely filtered FFT local images of the area marked by white squares): (a) 423 K, (b) 473 K, (c) 673 K, and (d) 773 K.

the increase of substrate temperature, as shown in Figure 1. Additionally, it also could be observed that all of the films are very dense and the interface between the film and substrate gradually became ambiguous, which could be caused by the increase of diffusion of carbon into the silicon substrate with the temperature increase.

The nanostructure evolution of the films as a function of substrate temperatures was investigated by HRTEM. Obviously, the nanostructures of the films were distinct from each other as different substrate temperatures were applied, as shown in Figures 3(a)–3(d). The film deposited at low temperature exhibited a kind of nanoparticle containing structure. The particles mainly consisted of Si and Al, according to the results of Energy Dispersive X-Ray Spectrum (EDS), and exhibited a lattice space of about 0.282 nm, close to that of Si ($d_{201} = 0.269$ nm). However, the amount of particles was small and they were distributed sparsely in the film, which should be concerned with the low content of doped elements. However, it should be noted that the entire film is amorphous, as suggested by electron diffraction pattern shown in the inset of Figure 3(a). As the substrate was heated up to 673 K, such particles almost did not form. On the other hand, the amorphous carbon matrix of the films gradually graphitized and became relatively ordered with the rising of substrate temperature. As the temperature heightened up to 773 K, as

shown in Figure 3(d), the ordering structure was gradually obvious and the film exhibited a structure of parallel curved fringes and the space of the fringes was about 0.431 nm, which is close to the lattice space of the fullerene ($d_{112} = 0.428$ nm). Commonly, this kind of structure is usually so called fullerene-like structure [19]. Meanwhile, the film did not contain nanoparticle.

The graphitization of amorphous carbon matrix can be further evidenced by the Raman spectra of the films. As well known, visible Raman spectroscopy is an efficient and nondestructive tool for research of structure information of amorphous carbon matrix in films materials based on carbon. As given in Figures 4(a)–4(e), the Raman spectra of the films mainly consisted of the G peak centered around 1560 cm^{-1} and D peak (shoulder peak) around 1340 cm^{-1} , which originate from the breathing modes of rings and the bond stretching of all pairs of sp^2 atoms in rings and chains [20, 21], respectively. It was noted that the D peak became more distinguishable and the “valley” located between the D peak and G peak became deeper with the ascending of the substrate temperature. Additionally, two important parameters of G peak position and the intensity ratio of D and G peaks, $I(\text{D})/I(\text{G})$, were demonstrated in Figure 4(f) as a function of substrate temperatures. As Ferrari and Robertson suggested, the fluctuation of the ratio of sp^3 bonded carbon

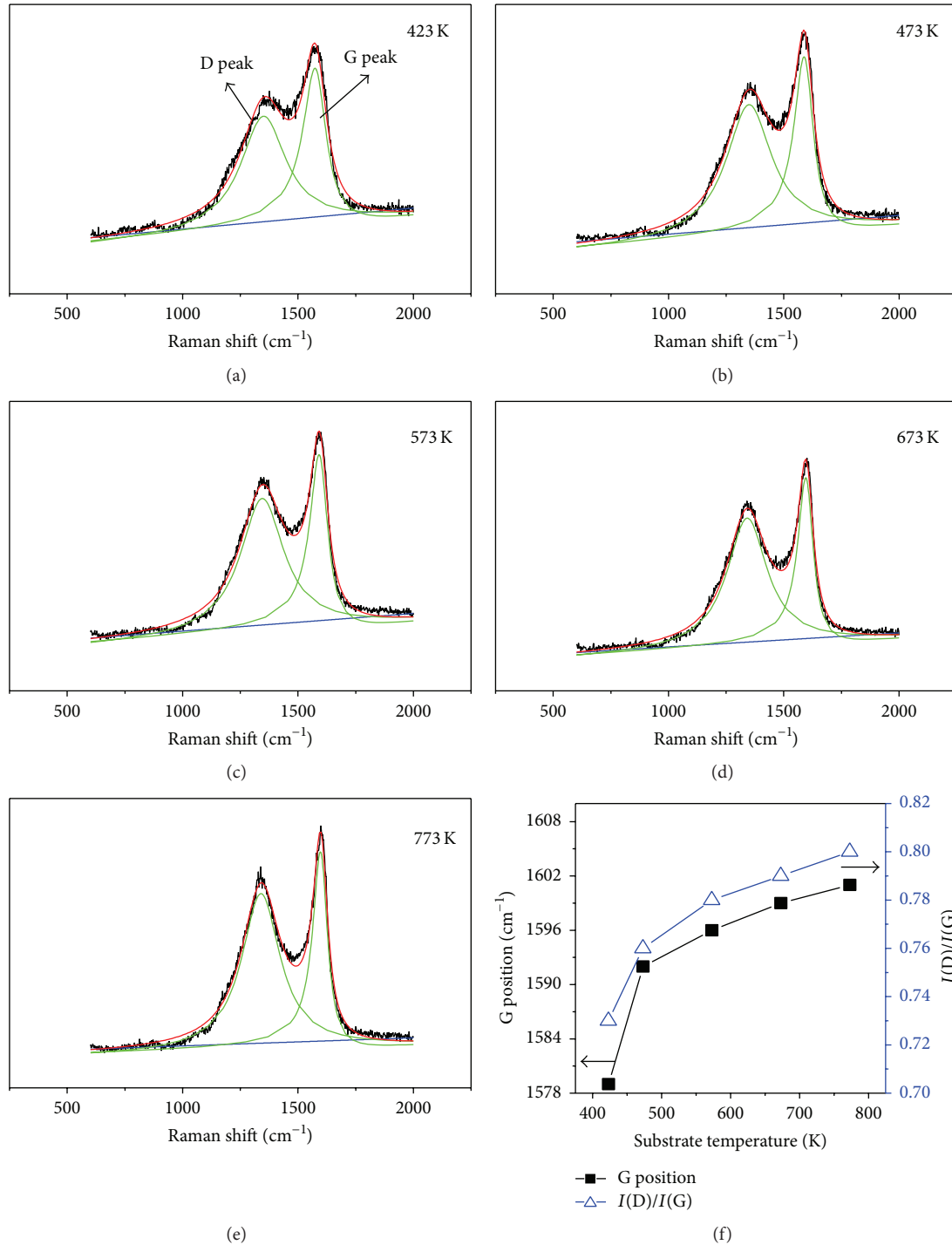


FIGURE 4: (a–e) Raman spectra of the films deposited at different temperatures; (f) G band position and $I(D)/I(G)$ as a function of substrate temperatures.

and sp^2 bonded carbon can be indirectly deduced from the shifting of G peak position and change of $I(D)/I(G)$ of visible Raman spectra of amorphous carbon films: the ratio of sp^2/sp^3 increases with increase of the two parameters [20, 22], and the graphitization degree is proportional to the ratio. Therefore, it was suggested from Figure 4(f) that the ratio of sp^2/sp^3 increases with increase of substrate temperature.

In other words, the carbon matrix gradually graphitized as the substrate temperature heightened, which was in good agreement with the observation of the TEM.

3.2. Mechanical and Tribological Properties. The hardness of the films was determined through an indentation method. Figure 5 shows the hardness for films deposited at different

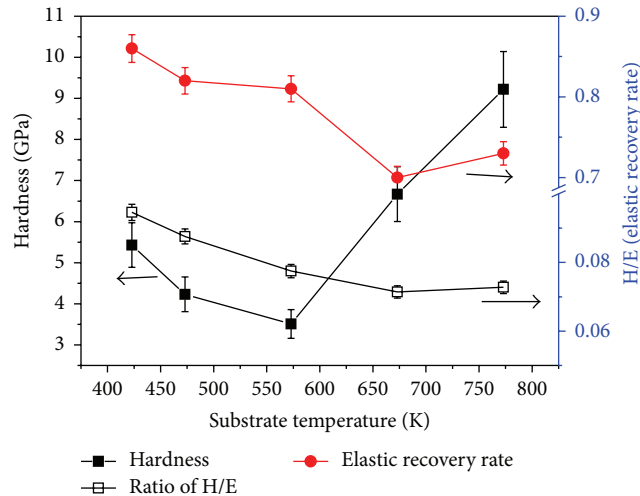


FIGURE 5: The microhardness, ratio of H/E, and elastic recovery rate of the films as a function of substrate temperatures.

TABLE 3: Duration of reaching the lowest friction coefficient (μ) of the films.

Substrate temperature/K	423	473	573	673	773
Lowest μ	0.01	0.03	0.06	0.035	0.04
Duration/second	1700	1300	190	166	30

substrate temperatures. All the films are relatively soft since their hardness is not beyond 10 GPa. As the temperature rises from 423 K to 573 K, the hardness of the films did not change significantly, slightly decreasing from 5.4 GPa to 3.5. With further increase of substrate temperature up to 773 K, the hardness obviously increased from 3.5 GPa to 9.2 GPa. Such enhancement of hardness should be attributed to the unique fullerene-like structure [23, 24]. However, the ratio of H/E and elastic recovery rate (E, elastic modulus), which are important prediction parameters of cracking resistance or toughness of hard films or coatings [7, 25–27], degraded with the increase of substrate temperature. Namely, high substrate temperature should be disadvantage of the toughness and wear resistance of the films.

The results of dry-sliding tribotest showed that the film deposited at temperature of 423 K had a very low and stable friction coefficient of about 0.01 and it increased to about 0.034 as the substrate temperature ascended to 473 K, as given in Figure 6. As substrate temperature heightened up to 573 K and above, the friction coefficient of the films was about 0.065, as shown in the inset of Figure 6, but it lasted a short sliding duration. Meanwhile, it is noted that the duration of reaching the lowest friction coefficient decreases with increase of substrate temperature, as listed in Table 3. Also, the wear resistance of the films was reflected by the wear depth of the sliding tracks, as demonstrated in Figures 7(a)–7(c). In comparison to the films deposited at 423 K and 473 K, the depth of film at 623 K was significantly larger than the thickness of the film. This meant that the film was easily worn through post-dry-sliding duration of about 900 seconds. Thus, it can be found that the wear resistance of the films

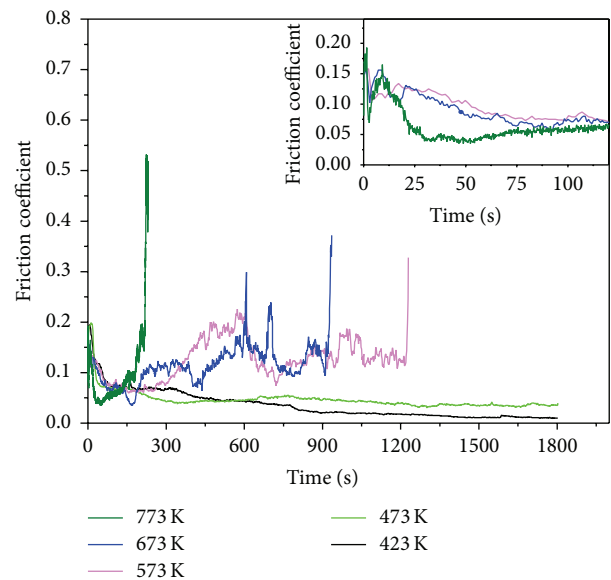


FIGURE 6: Friction curves of the films deposited at different substrate temperatures (the inset displays three friction curves with duration of 120 seconds).

degenerated with the increase of the substrate temperature. Besides, the negative effect caused from increase of substrate temperature on wear resistance was more significant than on the friction coefficient of films.

Mechanically, the decrease of cracking resistance or toughness was indicated by the H/E and elastic recovery rate of the films, and transfer layers could be responsible for the degeneration of tribological properties of the films with increase of substrate temperature. Figures 7(d)–7(f) show the SEM micrographs of transfer layers on counter faces sliding against the films deposited at different substrate temperatures. It has been proved that a continuous and dense transfer layer has positive effects on the high lubrication performance in the ambient air due to the much lower

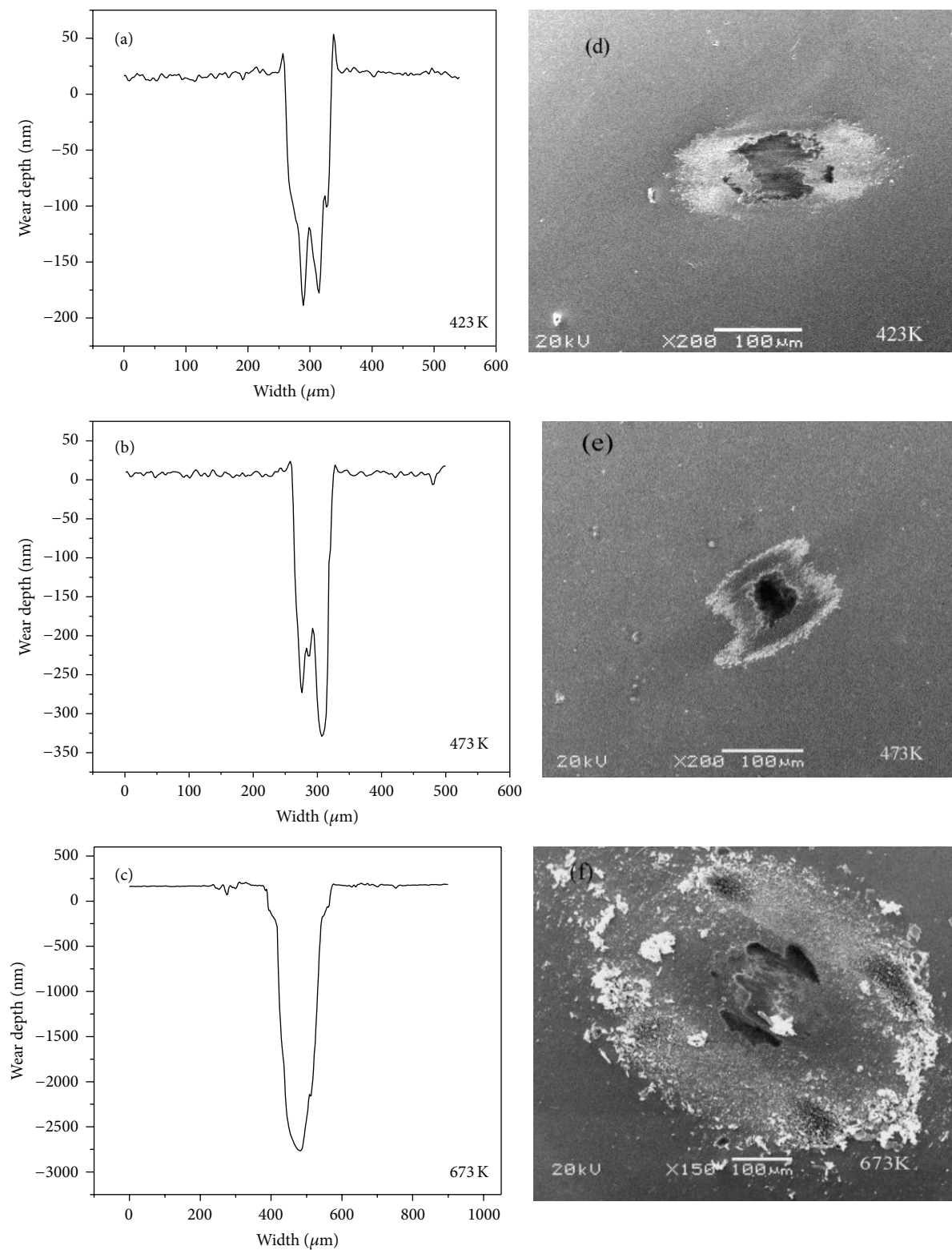


FIGURE 7: Cross-sectional profiles (a–c) of the wear tracks (after sliding time of 1800 s) and corresponding transfer layers (d–f) on the counter faces produced from the dry sliding of the films deposited at different substrate temperatures.

interfacial shear stress between the two carbon surfaces [8, 28], and triboinduced graphitization of sliding interface is beneficial to the reduction of friction coefficient [5, 28, 29]. As a result of increase of graphitization level which is previously verified by the TEM and Raman spectra of the films, the duration of reaching the lowest friction coefficient decreases with increase of substrate temperature. However, because of the low toughness which is indicated by the ratio H/E, the films deposited at high temperature did not last a long duration of low friction state and the films were easily worn through, regardless of formation of transfer layer on counter faces.

4. Conclusions

(Si, Al)/a-C:H films were deposited at different substrate temperatures. The dependence of the microstructure, hardness, and tribological properties of the films on growth temperature was studied. The results of HRTEM and Raman spectra revealed that the films underwent significant microstructure evolution from particle containing to fullerene-like structure as the growth temperature increased from 423 K to 773 K. The graphitization level of the films increased with the substrate temperature, leading to shortening of the duration of reaching the lowest friction coefficient. However, the wear resistance of the films still significantly degenerated since the reduction of toughness of the films, even though the lubricity of the films was not seriously damaged when high substrate temperature was applied.

Conflict of Interests

The authors declare that there is no conflict of interests regarding the publication of this paper.

Acknowledgments

The authors are grateful to financial support of State Key Laboratory of Solid Lubrication (Grant LSL-1303), Sichuan University of Science and Engineering (Grant 2013RC01), Material Corrosion and Protection Key Laboratory of Sichuan Province (Grant 2015CL14), the National Natural Science Foundation of China (Grant 51375471), and 973 projects (2013CB632302) of the Ministry of Science and Technology of China.

References

- [1] J. Robertson, "Diamond-like amorphous carbon," *Materials Science and Engineering: R: Reports*, vol. 37, no. 4-6, pp. 129-282, 2002.
- [2] G. A. Abbas, P. Papakonstantinou, J. A. McLaughlin, T. D. M. Weijers-Dall, R. G. Elliman, and J. Filik, "Hydrogen softening and optical transparency in Si-incorporated hydrogenated amorphous carbon films," *Journal of Applied Physics*, vol. 98, no. 10, Article ID 103505, 2005.
- [3] F. Zhao, H. X. Li, L. Ji et al., "Structural, mechanical and tribological characterizations of a-C: H: Si films prepared by a hybrid PECVD and sputtering technique," *Journal of Physics D: Applied Physics*, vol. 42, no. 16, Article ID 165407, 2009.
- [4] W. Dai and A. Wang, "Deposition and properties of Al-containing diamond-like carbon films by a hybrid ion beam sources," *Journal of Alloys and Compounds*, vol. 509, no. 13, pp. 4626-4631, 2011.
- [5] O. Wilhelmsson, M. Räsander, M. Carlsson et al., "Design of nanocomposite low-friction coatings," *Advanced Functional Materials*, vol. 17, no. 10, pp. 1611-1616, 2007.
- [6] J. Musil, P. Novák, R. Čerstvý, and Z. Soukup, "Tribological and mechanical properties of nanocrystalline-TiC/a-C nanocomposite thin films," *Journal of Vacuum Science & Technology A*, vol. 28, no. 2, pp. 244-249, 2010.
- [7] X. Liu, J. Hao, J. Yang et al., "Preparation of superior lubricious amorphous carbon films co-doped by silicon and aluminum," *Journal of Applied Physics*, vol. 110, no. 5, Article ID 053507, 2011.
- [8] F. Zhao, H. Li, L. Ji, Y. Wang, H. Zhou, and J. Chen, "Ti-DLC films with superior friction performance," *Diamond and Related Materials*, vol. 19, no. 4, pp. 342-349, 2010.
- [9] X. Q. Liu, J. Yang, J. Y. Hao, and W. M. Liu, "Microstructure and properties of nc-TiC/a-C:H films deposited by radio frequency reactive sputtering," *Materials Science and Technology*, vol. 27, no. 11, pp. 1669-1673, 2011.
- [10] A. A. Onoprienko, N. I. Danilenko, and I. A. Kosko, "Structure evolution on annealing of copper-doped carbon film," *Thin Solid Films*, vol. 515, no. 17, pp. 6672-6675, 2007.
- [11] F. J. Li, S. Zhang, J. Kong, Y. Zhang, and W. Zhang, "Multilayer DLC coatings via alternating bias during magnetron sputtering," *Thin Solid Films*, vol. 519, no. 15, pp. 4910-4916, 2011.
- [12] M. Stueber, H. Holleck, H. Leiste, K. Seemann, S. Ulrich, and C. Ziebert, "Concepts for the design of advanced nanoscale PVD multilayer protective thin films," *Journal of Alloys and Compounds*, vol. 483, no. 1-2, pp. 321-333, 2009.
- [13] S. Karan, S. Samitsu, X. Peng, K. Kurashima, and I. Ichinose, "Ultrafast viscous permeation of organic solvents through diamond-like carbon nanosheets," *Science*, vol. 335, no. 6067, pp. 444-447, 2012.
- [14] X. Liu, J. Yang, J. Hao, J. Zheng, Q. Gong, and W. Liu, "A near-frictionless and extremely elastic hydrogenated amorphous carbon film with self-assembled dual nanostructure," *Advanced Materials*, vol. 24, no. 34, pp. 4614-4617, 2012.
- [15] Y. T. Pei, C. Q. Chen, K. P. Shaha et al., "Microstructural control of TiC/a-C nanocomposite coatings with pulsed magnetron sputtering," *Acta Materialia*, vol. 56, no. 4, pp. 696-709, 2008.
- [16] W. M. Liu, X. Pang, J. Hao, P. Wang, and Y. Xia, "Effects of bias voltage on structure and properties of TiAl-doped a-C:H films prepared by magnetron sputtering," *Surface and Interface Analysis*, vol. 43, no. 3, pp. 677-682, 2011.
- [17] W. Gulbiński, S. Mathur, H. Shen, T. Suszko, A. Gilewicz, and B. Warcholiński, "Evaluation of phase, composition, microstructure and properties in TiC/a-C:H thin films deposited by magnetron sputtering," *Applied Surface Science*, vol. 239, no. 3-4, pp. 302-310, 2005.
- [18] M. Shinohara, K. Cho, Y. Matsuda et al., "Substrate temperature effects on amorphous carbon film growth, investigated by infrared spectroscopy in multiple internal reflection geometry," *Journal of Vacuum Science & Technology A*, vol. 27, no. 4, pp. 813-817, 2009.
- [19] I. Alexandrou, H.-J. Scheibe, C. J. Kiely, A. J. Papworth, G. A. J. Amaratunga, and B. Schultrich, "Carbon films with an sp² network structure," *Physical Review B: Condensed Matter and Materials Physics*, vol. 60, no. 15, pp. 10903-10907, 1999.

- [20] A. C. Ferrari and J. Robertson, "Interpretation of Raman spectra of disordered and amorphous carbon," *Physical Review B*, vol. 61, no. 20, pp. 14095–14107, 2000.
- [21] A. C. Ferrari, "Raman spectroscopy of graphene and graphite: disorder, electron-phonon coupling, doping and nonadiabatic effects," *Solid State Communications*, vol. 143, no. 1-2, pp. 47–57, 2007.
- [22] G. Irmer and A. Dorner-Reisel, "Micro-Raman studies on DLC coatings," *Advanced Engineering Materials*, vol. 7, no. 8, pp. 694–705, 2005.
- [23] P. Wang, X. Wang, B. Zhang, and W. Liu, "Structural, mechanical and tribological behavior of fullerene-like carbon film," *Thin Solid Films*, vol. 518, no. 21, pp. 5938–5943, 2010.
- [24] P. Wang, X. Wang, W. Liu, and J. Zhang, "Growth and structure of hydrogenated carbon films containing fullerene-like structure," *Journal of Physics D*, vol. 41, no. 8, Article ID 085401, 2008.
- [25] C. A. Charitidis, "Nanomechanical and nanotribological properties of carbon-based thin films: a review," *International Journal of Refractory Metals & Hard Materials*, vol. 28, no. 1, pp. 51–70, 2010.
- [26] J. Musil and M. Jirout, "Toughness of hard nanostructured ceramic thin films," *Surface & Coatings Technology*, vol. 201, no. 9–11, pp. 5148–5152, 2007.
- [27] A. Leyland and A. Matthews, "On the significance of the H/E ratio in wear control: a nanocomposite coating approach to optimised tribological behaviour," *Wear*, vol. 246, no. 1-2, pp. 1–11, 2000.
- [28] X. Liu, J. Yang, J. Hao, J. Zheng, Q. Gong, and W. Liu, "Microstructure, mechanical and tribological properties of Si and Al co-doped hydrogenated amorphous carbon films deposited at various bias voltages," *Surface and Coatings Technology*, vol. 206, no. 19-20, pp. 4119–4125, 2012.
- [29] A. P. Merkle, A. Erdemir, O. L. Eryilmaz, J. A. Johnson, and L. D. Marks, "In situ TEM studies of tribo-induced bonding modifications in near-frictionless carbon films," *Carbon*, vol. 48, no. 3, pp. 587–591, 2010.